Doctoral Dissertation
博士論文

Search for heavy diboson resonances decaying into semi-leptonic final states in 139 fb^{-1} of $\sqrt{s} = 13$ TeV pp collisions with the ATLAS detector

(ATLAS測定器において収集した重心系エネルギー13 TeVの陽子陽子衝突データ139 fb^{-1}を使った、セミレプトニック終状態を持つ弱ボソン共鳴の探索)

A Disseration submitted for the Degree of Doctor of Philosophy
January 2020

令和２年１月博士（理学）申請

Department of Physics, Graduate School of Science
The University of Tokyo
東京大学大学院理学系研究科物理学専攻
Masahiro Yamatani
山谷　昌大

Abstract

This thesis represents searches for heavy new resonances decaying into dibosons (WW, WZ and ZZ) in semi-leptonic final states ($\nu\nu qq$, $\ell\nu qq$ and $\ell\ell qq$) using proton-proton collision data at a center-of-mass energy of $\sqrt{s} = 13$ TeV. The data, corresponding to an integrated luminosity of 139 fb^{-1}, were recorded with the ATLAS detector between years 2015 and 2018 at the Large Hadron Collider. The searches are performed in final states in which one vector boson decays leptonically (a pair of electrons or muons, a pair of neutrinos, and a pair of an electron (muon) and a neutrino), and the associated W boson or the other Z boson decays hadronically. Several new ideas are introduced to improve the sensitivity e.g. Track-CaloCluster (TCC), which is particle-flow algorithm to achieve better jet substructure performance for high-p_{T} jet, Variable-radius (VR) track-jet b-tagging for the boosted $Z \to bb$ reconstruction and machine learning (ML) based analysis. No evidence for the production of heavy resonances is observed. Upper bounds on the production cross sections of heavy resonances times their decay branching ratios to WW, WZ and ZZ are derived in the mass range from 300 to 5000 GeV, within the context of Standard Model extensions with a heavy vector triplet or warped extra dimensions. Production processes of gluon-gluon-fusion, Drell-Yan or vector-boson-fusion are considered, depending on the assumed model.

To my loving wife Tomomi, and my dear child Naoya.

Acknowledgements

I wish to express my deepest gratitude to my supervisor, Professor Masaya Ishino, who adequately guided and encouraged me to be professional. Without his support, I could not pass the defence in 2020. I also would like to thank my local supervisors, Dr. Tatsuya Masubuchi and Dr. Takuya Nobe, for helping me with VV semi-leptonic analysis and insightfull discussions about an angular analysis and a TCC jet study. I am grateful to Associate Professor Tatsuo Kawamoto, who was my supervisor for the first four years of my PhD course, for his support and encouragement.

I would like to thank the academic researchers at the University of Tokyo, Dr. Yuji Enari for giving delicious cuisines, Dr. Koji Terashi for giving insightfull advisies, Associate Professor Yasuyuki Okumura for giving me a ride when I missed the last bus, Professor J. Tanaka and Associate professor Ryo Sawada for giving me a chance to use a quantum annealing system, and Dr. Tomoyuki Saito for inviting me to CERN relay race. I also would like to express my appreciation to people in ATLAS VV semi-leptonic group.

I am thankfull to my thesis committee members, Yutaka Ushiroda, Koichi Hamaguchi, Susumu Shimoura, Toshinori Mori and Taku Gunji, for their insightful discussions, hard questions during the defence, and joining the defence by video conferencing in this difficult situation with COVID-19.

I really enjoyed my student life with all the ICEPP members. In particular, I would like to express my respectful gratitude to the ICEPP secretaries, Masako Shiota, Yumi Kase, Michiko Takemoto and Sonoko Kaneko for supporting my research life. During my six years at ICEPP, I was able to focus on my research thank to their huge support.

I wish to thank I-Han Chiu for doing desk lunch together, Yuya Kano for an air show in France, Shota Nakaura for inviting me to your wedding ceremony in Lucerne, Naoki Nagakura for playing football together in Tokyo, Yuichi Nishizawa for chatting idly via SNS, Masahiko Saito for Berlioz's Symphonie Fantastique, Tomohiro Yamazaki for giving a moderate break, Yi-Ling Yang for talking on my way to CERN from Saint-Genis-Pouilly.

Finally, the deepest appreciation goes to my family for supporting me all my life.

Contents

List of Figures

List of Tables

Chapter 1

Introduction

1.1 Overview

The discovery of a new scalar particle with a mass of approximately 125 GeV by the ATLAS and CMS collaborations at the Large Hadron Collider (LHC) in the year 2012 [1, 2] represents a major milestone in the understanding of electroweak symmetry breaking. Figure 1.1 shows the distribution of reconstructed invariant mass of diphoton candidates and the combined results of observed local p_0 values as a function of candidate particle mass in the ATLAS experiment. The particle was identified as a scalar boson, and subsequent studies have shown that the properties of the new particle are consistent with the expectations of the last missing piece of the Standard Model (SM), Higgs boson.

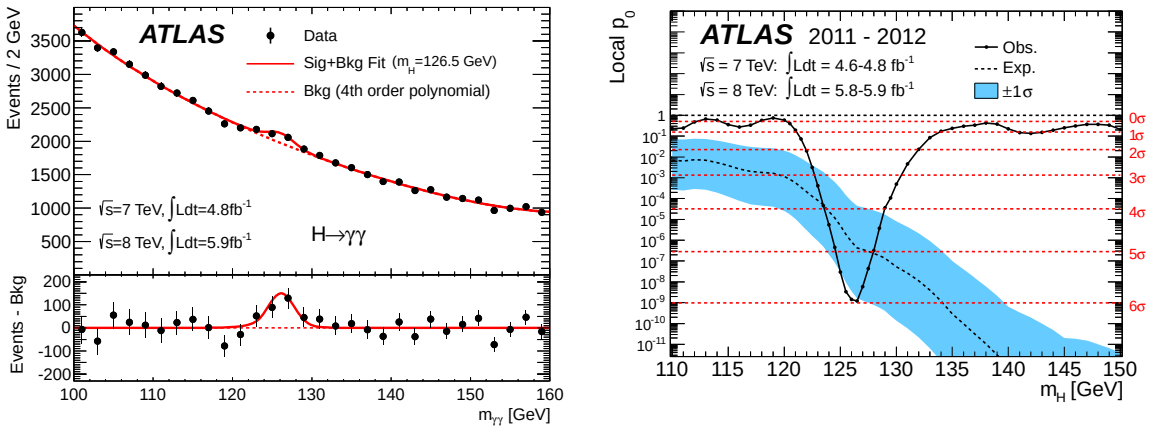

(a) (b)

Figure 1.1: (a) The reconstructed invariant mass distributions of the two photons decaying from candidate Higgs boson and (b) The observed p_0 values from the combination of channels in the ATLAS experiment [1].

Nevertheless, the SM is not the ultimate theory of particle physics since it cannot fully explain underlying problems such as Dark Matter and Hierarchy problem, and therefore we need the extensions of the SM which predict new particles. Motivated by hierarchy and naturalness arguments [3], several new physics models are proposed, such as the Extended Gauge Model (EGM) [4], Extra Dimensions [5, 6], and Technicolor models [7, 8]. They predict new heavy resonances which decay into a pair of vector bosons VV ($V = W, Z$) which can be discovered in the modern technology of particle physics experiments. For instance, a heavy W-like vector boson is predicted by the extended gauge model, and the extra dimension models predict spin-2 Kaluza-Klein (KK) excitations of graviton.

This thesis presents searches for new heavy diboson resonances ($X \to WW$, ZZ or WZ, collectively denoted as $X \to VV$), using pp collision data collected with the ATLAS detector at a center-of-mass energy of $\sqrt{s} = 13\,\text{TeV}$ in years 2015-18 corresponding to an integrated luminosity of $139\,\text{fb}^{-1}$. The search utilizes the semi-leptonic final states of the heavy diboson resonances, where one of the boson pair decays leptonically and the other decays hadronically. It takes advantages of a larger branching ratio from a hadronic vector boson decay and smaller background yields from a leptonic vector boson decay. Therefore the analysis can search for a broader range of the resonance mass from 300 GeV to 5 TeV, while full hadronic (leptonic) analysis can only search for higher (lower) mass regions. Figure 1.2 shows production modes considered in this analysis: gluon-gluon-fusion (ggF), Drell-Yan (DY) and vector-boson-fusion (VBF).

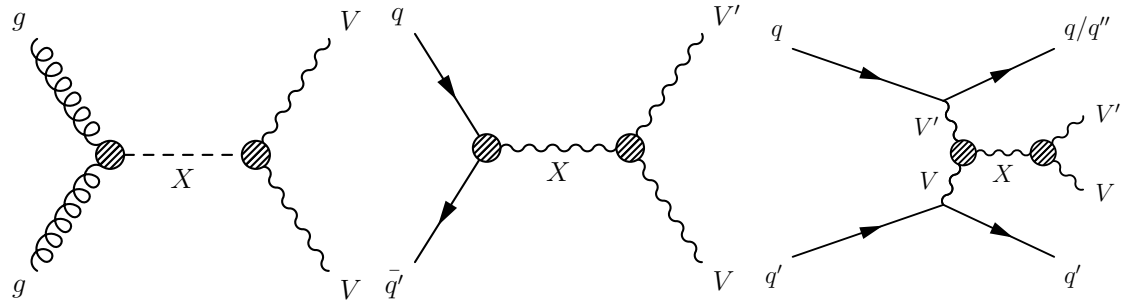

(a) gluon-gluon fusion (b) Drell-Yan (c) vector-boson fusion

Figure 1.2: Representive Feynman diagrams for the production of heavy resonances X with their decays into a pair of vector bosons.

This thesis is organized as follows. Chapter 1 gives an overview of the theoretical background and motivations for heavy diboson resonances search in semi-leptonic final states. Chapter 2 describes the experimental setup, which includes the Large Hadron Collider (LHC) and the ATLAS detector. Chapter 3 describes the accumulated data sample and Monte Carlo simulated samples to model the signals and background events. The details of the object definitions are found in Chapter 4. The details of the Track-Calo Cluster, which are studies for improvement of signal sensitivities, are found in Chapter 5. Event selection and categorization are summarized in Chapter 6. Strategy on the background estimation is discussed in Chapter 7 as well as data/MC comparison studies. Systematic uncertainties are discussed in Chapter 8. After the discussion about the statistical treatment in Chapter 9, results are presented in Chapter 10. Finally, a summary of the work presented is given in Chapter 11.

1.2 The Standard Model of Particle Physics

The Standard Model (SM) of particle physics [9–11] is a relativistic field theory in which the interactions between the *elementary particles (fermions)* are described as the exchange of the *force-mediating particles (gauge bosons)* derived by imposing local gauge symmetries on the natural world. The SM is based on $SU(3)_c \times SU(2)_L \times U(1)_Y$ gauge symmetry group, where the $SU(3)_c$ symmetry defines strong interactions and $SU(2)_L \times U(1)_Y$ symmetry expresses the electroweak interactions. The bosonic gauge fields define the spin-one force-mediating particles and the spin-half elementary particles are described by fermionic Weyl fields.

The simplified lagrangian for the SM can be described as:

$$\begin{aligned}\mathcal{L}_{\mathrm{SM}} = &-\frac{1}{4}F_{\mu\nu}F^{\mu\nu} \\ &+ i\bar{\psi}\not{D}\psi + \mathrm{h.c} \\ &+ |D_\mu\phi|^2 - V(\phi) \\ &+ \psi_i y_{ij}\psi_j\phi + \mathrm{h.c.}\end{aligned} \tag{1.1}$$

The first term of Equation 1.1 is the scalar product of the field strength tensor $F_{\mu\nu}$, corresponding to kinetic terms of force-mediating particles. Under the requirement of the local gauge invariance, the interactions between the elementary particles arise from the kinetic terms of elementary particles described in the second term of Equation 1.1. The third term corresponds to kinetic term of Higgs field and Higgs potential, which explain how massive force-mediating particles acquire their mass. Massive force-mediating particles, $W^\pm$ and Z bosons, are obtained by introducing the scalar filed called the *Higgs filed* [12–15]. The Higgs field has a nonzero Vacuum Expectation Value (VEV) which breaks $SU(2)_L \times U(1)_Y$ to $U(1)_{\mathrm{EM}}$ symmetry. The unbroken $U(1)_{\mathrm{EM}}$ symmetry is identified as electromagnetism. Finally, the mass of elementary particles is

acquired by introducing the last term of Equation 1.1, Yukawa coupling terms, which involve the coupling of elementary particles to the Higgs boson, and thus particles obtain their mass.

All of the SM particles are listed in Table 1.1-1.2. Weak interaction involves all fundamental particles, while electromagnetic interaction of quantum electrodynamics (QED) does not affect neutrinos since they are electronically neutral. In the case of the strong interaction of quantum chromodynamics (QCD), only the quarks receive the interaction because of their color charge. Quarks are never observed as free particles due to asymptotic freedom, a feature of QCD [16, 17]. Therefore quarks are always confined to bound states called hadrons.

Table 1.1: A table of the SM bosons and their properties [18]

Particle	Symbol	$\mathcal{Q}$	spin	mass	gauge symmetry	force
			Vector bosons			
photon	γ	0	1	0	$SU(2)_L \times U(1)_Y$	Electromagnetism
W boson	$W^{\pm}$	± 1	1	80.4 GeV	$SU(2)_L \times U(1)_Y$	Weak
Z boson	Z	0	1	91.2 GeV	$SU(2)_L \times U(1)_Y$	Weak
Gluon	g	0	1	0	$SU(3)_c$	Strong
			Scalar bosons			
Higgs	H	0	0	125 GeV	-	- (Origin of particle mass)

Table 1.2: A table of the SM elementary particles (fermions) and their properties [18]

Particle	Symbol	$\mathcal{Q}$	spin	mass	strong Interaction	electromagnetic Interaction	weak Interaction
			Leptons				
electron	e	-1	1/2	0.51 MeV		✓	✓
electron neutrino	ν_e	0	1/2	<0.2 eV			✓
muon	μ	-1	1/2	105.6 MeV		✓	✓
muon neutrino	ν_μ	0	1/2	<0.2 eV			✓
tau	τ	-1	1/2	1776 MeV		✓	✓
tau neutrino	ν_τ	0	1/2	<0.2 eV			✓
			Quarks				
down	d	-1/3	1/2	4.7 MeV	✓	✓	✓
up	u	+2/3	1/2	2.2 MeV	✓	✓	✓
strange	s	-1/3	1/2	96 MeV	✓	✓	✓
charem	c	+2/3	1/2	1.3 GeV	✓	✓	✓
bottom	b	-1/3	1/2	4.2 GeV	✓	✓	✓
top	t	+2/3	1/2	173 GeV	✓	✓	✓

The SM has been highly successful in predictions. One of the most successful predictions is the Higgs boson, discovered in 2012 by the ATLAS and CMS collaborations [1, 2] at the Large Hadron Collider (LHC) as introduced in Section 1.1. The level of agreement between the background-subtracted data and the expected Higgs boson signal in Figure 1.1a indicates the observed excess is a signal from Higgs boson decay. After the discovery of Higgs boson, the analysis of the data collected at the LHC has led to the observations of various production modes and decay channels predicted by the SM, and it was found that the measurements are consistent with the SM prediction [19–21].

There are 18 free parameters in the SM of particle physics: the masses of nine elementary particles, the three coupling constant describing the strengths of the gauge interactions, vacuum expectation value and the mass of the Higgs boson, and the three mixing angles and the CP-violating phase of Cabibbo-Kobayashi-Maskawa (CKM) matrix. These parameters cannot be determined by the SM itself and we need to put them by hand.

An example of the SM measurements and predictions is the mass and width measurement of the Z boson performed at the LEP collider, which was operated at center-of-mass energies close to the Z mass from 1989 to 1995 [22]. Figure 1.3 shows the measurements of the Z resonance at LEP. From this, the mass and width of the Z boson are determined to be $m_Z = 91.1875 \pm 0.0021$ GeV and $\Gamma_Z = 2.4952 \pm 0.0023$ GeV. Since the total width of the Z boson can be represented as the sum of the particle decay widths for all its decay modes, the number of light neutrino generations can be obtained by the measured particle decay widths for all of its

decay modes except for neutrinos. The obtained number of light neutrino generations is determined to be $N_\nu = 2.9840 \pm 0.0082$ and it indicates the observed data is consistent with three neutrino generations.

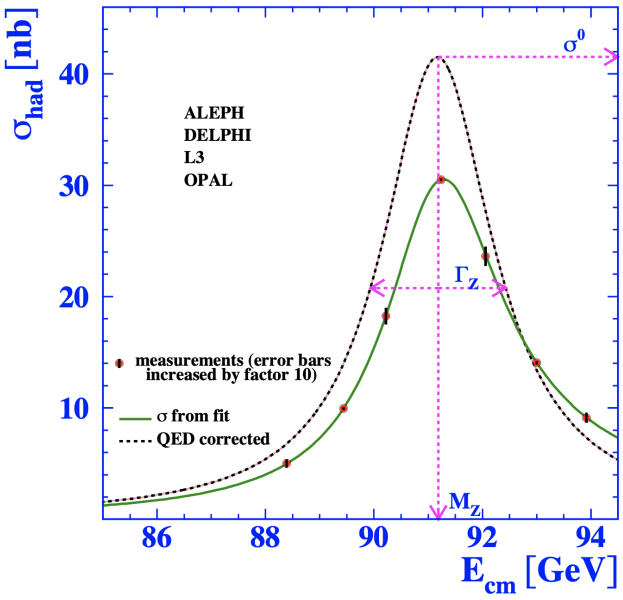

Figure 1.3: The measurements of the $e^+e^- \to q\bar{q}$ cross-section from LEP close to the Z resonance at LEP. The solid and dashed lines show before and after ISR correction, respectively [22].

1.3 Limitations of the Standard Model

Although the SM can provide several predictions, it is also known that there are some critical issues that cannot be explained within the SM framework. This section describes some of the open questions indicating the new physics beyond the SM.

Gravity

As described in Section 1.2, the SM does not include the gravitational interaction. The quantization of gravity faces difficulty at the Planck scale (10^{19} GeV) due to the nonrenormalizability of gravity. There are several potential candidates of the quantum gravity theory like the string theory and the loop quantum gravity.

Dark Matter

Many experimental observations suggest a fraction of the Universe consisting of luminous matter is quite small [23, 24]. The most significant evidence for that is the velocity distributions of stars orbiting around a galactic center. According to our observations of a spiral galaxy, most of the luminous mass is located in the center, and we can calculate the tangential velocity of a star outside the central region based on that,

$$\frac{mv^2}{r} \sim \frac{Gm}{r^2} M(r), \tag{1.2}$$

where $M(r)$ is the total mass within a radius r of a galaxy, and the tangental velocity should decrease as $r^{-1/2}$. However, the observed velocity of the stars is not consistent with the calculated ones, implying that the mass of a galaxy has a significant non-luminous component.

The non-luminous component, things composing the remaining parts of the Universe, are called Dark Matter and Dark Energy. They constitute nearly 95% (68% for Dark Energy and 27% for Dark Matter) of the Universe according to the Standard Model of Cosmology [25]. Dark Matter is expected to be weakly interacting with the SM particles and massive since it interacts gravitationally and is not detected directly yet. Weakly interacting massive particles model (WIMP) is a good candidate for Dark Matter. The WIMP density becomes consistent with the production at the thermal equilibrium if its mass is between 10 GeV and 10 TeV.

Hierarchy problem

As seen from discussions in previous sections, the SM contains several problems and it seems that the physics beyond the Standard Model of particle physics (BSM) exists. From this point of view, the SM can be regarded as the low energy effective theory with the cutoff scale of Λ_{UV}, and the BSM emerges beyond the energy scale.

Experimentally we know that the Higgs boson mass is 125 GeV [19]. When calculating the Higgs boson mass m_H, it receives large radiative corrections due to the coupling with other particles. Figure 1.4 shows one-loop correction to the Higgs boson mass from a fermion and a scalar particle. The correction from fermion

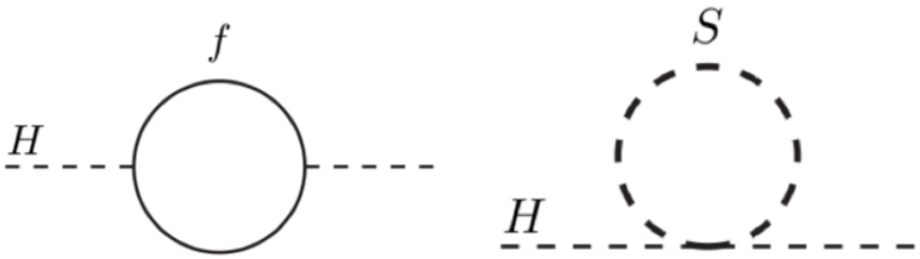

(a) (b)

Figure 1.4: One-loop correction to the Higgs boson mass by (a) a fermion f and (b) a scalar particle S.

couplings is described as

$$\Delta m_H^2 = -\frac{|\lambda_f|^2}{8\pi^2}\Lambda_{\mathrm{UV}}^2 + ... \tag{1.3}$$

where λ_f is a coupling constant to fermion f and Λ_{UV} is the cutoff scale. If we assume the BSM includes gravity, the cutoff scale Λ_{UV} would be at the Planck scale and this brings up the hierarchy problem. In this case, the correction to the Higgs boson mass is extremely high ($\sim 10^{19}$ GeV), which is about 17 orders of magnitude larger than Higgs boson mass. The theory is said to have a naturalness [3] problem since the Higgs boson mass and its correction must be at most of the same order to obtain the Higgs boson mass 125 GeV. The SM fermions are less affected by the Λ_{UV} cutoff since the dependency on Λ_{UV} is logarithm and not quadratic due to the chiral symmetry.

One of the solutions is preparing a counterterm to cancel the correction by introducing a new scalar filed S. The correction is described as

$$\Delta m_H^2 = \frac{\lambda_S}{16\pi^2}[\Lambda_{\mathrm{UV}}^2 - 2m_S^2 \log(\Lambda_{\mathrm{UV}}^2/m_S) + ...]. \tag{1.4}$$

Comparing Equation 1.3 and 1.4, one sees that the large corrections can be cancelled out. Generally, this solution is obtained by adding a new symmetry. Supersymmetry [26–31] can achieve this kind of cancellation by suggesting a symmetry between fermions and bosons. If each SM fermion has a corresponding boson, the Λ_{UV} contribution can be canceled.

The other option is introducing a new phenomenon between the cutoff scale Λ_{UV} and the Planck scale so that we don't need to apply the cutoff scale Λ_{UV} up to the Planck scale. The Extended gauge symmetry model assumes an additional gauge symmetry to introduce new particles [4]. Composite Higgs model is trying to avoid the hierarchy problem by regarding the Higgs boson as a composite particle, referring to the particles like neutron and proton in the context of QCD theory [32]. Extra dimension theory is also a possible solution [33]. These models predict a TeV-scale new particle and it is one of the biggest motivations to search for new particles at the LHC.

1.4 BSM Models and The Interpretation Strategy

Many kinds of BSM models have been proposed to avoid the hierarchy problem. BSM models like an extended gauge symmetry, Minimal Composite Higgs Model, and Bulk Randall-Sundrum Model predict heavy particles that could decay into diboson final states. This section introduces the models predicting new particles that

decay into diboson final states and can be explored by the ATLAS experiment. The interpretation strategies for each model are also discussed in this section.

1.4.1 Heavy Vector Triplet Models

In this section, BSM models predicting spin-1 new particles are discussed. First, two kinds of BSM models are introduced as benchmark models in this analysis: Extended Gauge Symmetry and Minimal Composite Higgs Model. Then the Heavy Vector Triplet (HVT) model, a phenomenological framework for describing spin-1 new particles, is introduced. Finally, the strategy for the signal interpretation is discussed.

Extended Gauge Symmetry

The Extended Gauge Symmetry model describes the new vector particles emerging from the symmetry breaking of $SU(2)_1 \times SU(2)_2 \times U(1)_Y$ to $SU(2)_L \times U(1)_Y$ symmetry throughout a linear σ-model [4]. Here the additional gauge group $SU(2)_2$ symmetry is considered in addition to the SM gauge group symmetry $SU(2)_1 \times U(1)_Y$. The electric charge operator is defined as $Q = T_3 + Y/2 + T_3'$ where T_3' accounts for the additional gauge $SU(2)_2$ symmetry . To achieve the spontaneous symmetry breaking, the scalar field Φ ($T_3 = \frac{1}{2},\ Y = 0,\ T_3' = \frac{1}{2}$) is introduced as a quartet in addition to the SM Higgs doublet H ($T_3 = \frac{1}{2},\ Y = 1,\ T_3' = 0$). The bosonic part of the Lagrangian is

$$\mathcal{L} = -\frac{1}{4g_1^2} W_{1\mu\nu}^a W_1^{a\mu\nu} - \frac{1}{4g_2^2} W_{2\mu\nu}^a W_2^{a\mu\nu} + D_\mu H^\dagger D^\mu H + \mathrm{Tr}(D_\mu \Phi^\dagger D^\mu \Phi) - \mathcal{V}(H, \Phi), \tag{1.5}$$

where a=1,2,3. The potential $\mathcal{V}$ is defined so that H and Φ have vacuum expectaion values.

$$\langle H \rangle = \begin{pmatrix} 0 \\ v \end{pmatrix}, \langle \Phi \rangle = \begin{pmatrix} f & 0 \\ 0 & f \end{pmatrix}. \tag{1.6}$$

The VEV of scalar field Φ breaks $SU(2)_1 \times SU(2)_2$ gauge symmetry to the SM $SU(2)_L$ gauge symmetry. The mass terms of gauge bosons are obtained from the kinetic term of Φ. After the specific field redefinition, we can obtain a new vector triplet V and the SM W boson fields. The kinetic mixing between V and W is obtained from the kinetic term of W_2 and it leads to the decay of V into the SM diboson resonance.

Minimal Composite Higgs Model

The fundamental idea of the Minimal Composite Higgs Model (MCHM) [32] is based on technicolor (TC) [7, 8] in which Higgs arises as a composite pseudo-Nambu-Goldstone boson (PNGB). The electroweak symmetry breaking (EWSB) arises from a strongly interacting new sector, similarly as the chiral symmetry breaking in QCD. Due to the different EWSB mechanism from the SM, TC models need no fundamental scalar particle which is the cause of the hierarchy problem. The problems of TC are that they can not pass the electroweak precision tests (EWPT) at LEP and SLAC colliders, mainly for their large contribution to the Peskin-Takeuchi S parameter [34] allowed by the experimental data.

The MCHM can account for these problems and contributions to electroweak precision observables are below experimental bounds. In the MCHM, the Higgs boson arises as a composite PNGB with a symmetry breaking of a global $SO(5)$ symmetry to an $SO(4)$ subgroup. The top loop effects trigger EWSB dynamically and the Higgs field acquires a VEV, breaking $SO(4)$ down to the custodial $SO(3)$ group. Originally the MCHM is a four-dimensional (4D) conformal field theory (CFT) with Higgs as a composite PNGB of a strongly coupled sector. Since it is a theory of strong dynamics, we cannot determine the values of parameter in the effective Lagrangian for the SM fields. Considering AdS/CFT correspondance [35–37], we can obtain the corresponding five dimensional (5D) AdS theory that leads to the same effective Lagrangian as the original 4D model. By working on the 5D AdS model, the precise parameter values of the effective Lagrangian can be computed and it leads to the compatible predictions with the electroweak precision tests. The existence of heavy vector resonances with electroweak quantum numbers are also predicted by this model.

Interpretation strategy for HVT Models

In this analysis, a simplified model called the HVT model, is introduced to provide a phenomenological parameterization of a broad set of explicit models such as Extended Gauge Symmetry and Minimal Composite Higgs Model.

The HVT model introduces a heavy vector triplet which corresponds to the new heavy vector particles V' ($W'^{\pm}$ and Z') predicted by BSM. In the HVT model, g_q, g_l and g_H correspond to the coupling strengths between the new vector triplet and the quark, lepton and Higgs fields. The triplet also interacts with SM W and Z bosons by the equivalence theorem [38–40]. To capture the features of several kinds of models, the new coupling g_V is introduced. The g_V parametrizes the interaction strength between the heavy vectors and W/Z bosons and is related to other coupling constants as follows. The Higgs coupling and the universal fermion coupling are $g_H = g_V c_H$ and $g_f = g^2 c_F / g_V$, where g is the SM $SU(2)_L$ gauge coupling. $c_{H(F)}$ parameters is a free parameter that can be fixed in explicit models. Generally, $c_{H(F)}$ is of order one.

In the HVT model, a real vector V^a_μ (a=1,2,3) are considered in addition to the SM vector bosons. The additional neutral and charged heavy vector particles are defined by

$$V^{\pm}_\mu = \frac{V^1_\mu \mp i V^2_\mu}{\sqrt{2}}, \quad V^0_\mu = V^3_\mu. \tag{1.7}$$

The dynamics of the new vector are described by a simple phenomenological Lagrangian:

$$\begin{aligned}\mathcal{L}_{\mathcal{V}} = &-\frac{1}{4} D_{[\mu} V^a_{\nu]} D^{[\mu} V^{\nu]a} + \frac{m_V^2}{2} V^a_\mu V^{\mu\ a} \\ &+ i g_V c_H V^a_\mu H^\dagger \tau^a \overleftrightarrow{D^\mu} H + \frac{g^2}{g_V} c_F V^a_\mu J_F^{\mu\ a} \\ &+ \frac{g_\mu}{2} c_{VVV} \epsilon_{abc} V^a_\mu V^b_\nu D^{[\mu} V^{\nu]c} + g_V^2 c_{VVHH} V^a_\mu V^{\mu\ a} H^\dagger H - \frac{g}{2} c_{VVW} \epsilon_{abc} W^{\mu\nu a} V^b_\mu V^c_\nu.\end{aligned} \tag{1.8}$$

The kinetic and mass term of V are contained in the first line. The second line contains direct interaction of V with the Higgs current

$$i H^\dagger \tau^a \overleftrightarrow{D^\mu} H = i H^\dagger \tau^a D^\mu H - i D^\mu H^\dagger \tau^a H, \tag{1.9}$$

and with the SM left-handed fermionic currents

$$J_F^{\mu a} = \sum_f \bar{f}_L \gamma^\mu \tau^a f_L, \tag{1.10}$$

where $\tau^a = \sigma^a/2$. The Higgs current term involves the V interaction with the SM vectors and with the Higgs boson. Therefore the V decay into bosonic channel is controlled by the coefficient c_H. On the other hand, the coefficient c_F describes the direct interaction with fermions. The fermionic current is responsible for the Drell-Yan (DY) production and fermionic decays. To take into account the more general situation, c_F, a universal coupling of V to fermions, are generalized to

$$c_F V \cdot J_F \to c_l V \cdot J_l + c_q V \cdot J_q + c_3 V \cdot J_3. \tag{1.11}$$

The third line of Equation 1.8 contains 3 new operators involving c_{VVV}, c_{VVHH} and c_{VVW}. However, they do not contribute directly to V decays and single production processes since none of them contains vertices of one V with SM fields. Therefore the phenomelogy of interest is described by the five parameters c_H, c_F, c_l, c_q, c_3 and the mass term m_V. The coupling g_V represents the typical strength of V interactions and the dimensionless coefficients "c" parametrize the departures from the typical size of order one. In the case of the fermion couplings, one extract factor of g^2/g_V^2 is introduced. This feature is common to all the explicit heavy vector triplet models we are interested in and the c_F's are of order one.

By tuning the HVT parameters, several kinds of BSMs such as Extended Gauge Symmetry and Minimum Composite Higgs Model can be treated. In this analysis, three explicit parameter sets are chosen as spin-1 new particle benchmarks. The first two correspond to Extended gauge symmetry and Minimum Composite Higgs model, which are produced by DY mechanism. The first DY beanch mark is the weakly coupled model describing the Extended Gauge Symmetry model. In this case $g_V = 1$ and the fermion coupling is assumed to univeral ($g_f = g_q = g_l$). This model is referred to as Model A in this thesis. The second DY scenario reproduces the phenomenology of a strongly coupled model as Minimum Composite Higgs Model. This model is called Model B in this thesis. $g_V = 3$ is adopted in the model. For the DY processes, the branching ratios for decays into individual SM diboson channels are about 2% in Model A, whereas 50% in Model B. As the extreme case, the third model called Model C, is designed to study the rare process of VBF production mode. In this model the couplings are set to $g_H = 1$ and $g_f = 0$. The interpretation can be done for each resonance mass and the two-dimensional parameter space consisting of coupling constants defined above. Signal samples for the HVT (both DY and VBF) are generated with MadGraph5 (MG5) [41] interfaced to

Pythia 8.

1.4.2 RS Graviton and Radion

In this section, BSM models predicting new spin-0/2 particles are discussed. The strategy for the interpretation is also discussed.

Bulk Randall-Sundrum Model

Models with large compactified extra dimension provide an alternative solution to the hierarchy problem [5, 6]. In these models, the effective four-dimensional Planck scale M_{Pl} is determined by the fundamental (4+n)-dimensional Planck scale M and the geometry of the extra dimensions. The relation is described by $M_{\mathrm{Pl}}^2 = M^{n+2}V_n$, where V_n is the volume of the extra dimensions. The large hierarchy between the weak scale and the fundamental scale of gravity can be eliminated if V_n is large enough. Unfortunately, the large extra dimension introduces a new hierarchy, namely between the compactification scale $\mu_c = V_n^{-1/n}$ and M.

Randall-Sundrum model [33] is one of higher dimensional scenarios that can solve the hierarchy problem with small extra dimensions. This model consists of a spacetime with a single S^1/Z_2 [1]orbifold extra dimension ($-\pi \leq \phi \leq \pi$ with ϕ and $-\phi$ identified) and two 4-dimensional branes localized at both $\phi = 0$ ("UV/Planck" brane) and $\phi = \pi$ ("IR/TeV" brane). The resulting spacetime metric is

$$ds^2 = e^{-2kr_c|\phi|}\eta_{\mu\nu}dx^\mu dx^\nu - r_c^2 d\phi^2, \tag{1.12}$$

where r_c is the radius of the compactifed dimension, k is a curvature scale which is assumed to be of order of M, and x_μ are Lorentz coordinates on the four-dimensional surface of constant ϕ. By exploring the four-dimensional effective field theory based on Eq 1.12, we can see

$$M_{\mathrm{Pl}}^2 = \frac{M^3}{k}\left[1 - e^{-2kr_c\pi}\right]. \tag{1.13}$$

This tells that M_{Pl} depends only weakly on r_c in the large kr_c limit and M is compatible with M_{Pl} as fundamental scale. The large hierarchy between TeV physical mass scales and fundamental Planck mass scales are generated by the exponential geometric factor appearing in the metric. This model assumes all SM particles are localized on the "IR/TeV brane" and KK (Kaluza-Klein) gravitation is predicted at the TeV scale. Since KK graviton is also assumed to be localized near the "IR/TeV brane", the entire SM particles have TeV scale coupling to KK graviton. However, the original Randall-Sundrum model leads to the large contributions to flavor changing neutral current (FCNC) and observables related to electroweak precision tests, which is forbidden by experimental observations.

To avoid these problems, "Bulk" RS model, in which the SM fields are allowed to propagate in the extra dimension, had been proposed [42–45]. In this model, 1st and 2nd generation fermions are localized near "UV/Planck brane" so that the contributions to FCNC and electroweak precision tests are suppressed. On the other hand, KK graviton is still localized near the "IR/TeV brane" so that the coupling of KK graviton to light fermions are highly suppressed.

Radion

The problem of the RS model is that it lacks the mechanism of determining the value of r_c dynamically. Radion is a bulk scalar which provides the mechanism of generating a potential to stabilize the value of r_c [46]. The bulk action with the five-dimensional bulk scalar fields Φ is

$$S_b = \frac{1}{2}a\int dx^4 \int_{-\phi}^{\phi} d\phi\sqrt{G}\left(G^{AB}\partial_A\Phi\partial_B\Phi - m^2\Phi^2\right), \tag{1.14}$$

where G_{AB} with $A, B = \mu, \phi$. We can also consider the interactions of scalar fields Φ on "IR/TeV brane" and "UV/Planck brane". The interaction terms on branes cause Φ to develop a ϕ-dependent vacuum expectation value

$$\Phi(\phi) = e^{2\sigma}\left[Ae^{\nu\sigma} + Be^{-\nu\sigma}\right], \tag{1.15}$$

[1] A space obtained by identifications that have fixed points. A circle of raidus r_c with the identification $\phi \sim -\phi$ in this case.

where $\nu = \sqrt{4 + m^2/k^2}$. Putting this back into the scalar field action and integrating over ϕ, an effective four-dimensional potential $V_\Phi(r_c)$ is obtained and it leads to the minimum value of r_c. Therefore the compactified radius r_c is stabilized. This mechanism for stabilizing r_c is caused by the presence of a ϕ-dependent vacuum bulk field and causes the radion field Φ to acquire a mass term and couplings to SM fields [47–49].

Interpretation strategy for Bulk RS graviton

In the bulk RS model described, both gravity and SM fields can propagate into the warped extra dimension and it leads to a tower of KK excitations of gravtion G_{KK} and SM fields. The couplings of G_{KK} to light fermions are suppressed by virtue of avoiding constraints from FCNC and electroweak precision tests. The spin-2 KK gravitons G_{KK} is produced dominantly via gluon-gluon fusion (ggF). The coupling strength depdends on $k/M_{\rm Pl}$, where $M_{\rm Pl}$ is the reduced Planck mass [50]. Consequently both the production cross-section and decay width of the G_{KK} scale as the square of $k/M_{\rm Pl}$. Typically the value of $k/M_{\rm Pl}$ is of order one. In the interpretation, $k/M_{\rm Pl} = 1$ is used so the only free parameter is mass of G_{KK}

Interpretation strategy for Radion

The coupling strength of the radion field to SM fields depends on the model parameter $\Lambda_R = \sqrt{\langle g \rangle} \times ke^{-k\pi r_c}\sqrt{\frac{M_5^3}{k^3}}$ where M_5 is the 5-dimensional Plank mass [47–49], $k\pi r_c = 35$, and $\Lambda_R = 3\,\text{TeV}$. The size of the extra dimension defined as $k\pi r_c$, is another parameter of the model. The coupling of the radion to fermions is proportional to the mass of the fermion while it is proportional to the square of the mass for bosonic fields. This leads to the dominant decay mode for the radion to be a pair of bosons when the radion mass above ~ 1 TeV. Both the production cross-section for the radions and the total width scale like $\sim 1/\Lambda_R^2$.

1.4.3 Signal Parameters

Finally, signal parameters used in the interpretation are summarized in Table.1.3

Table 1.3: List of benchmark signal models. Predictions of cross-section σ, branching ratio BR ($X \to WW/WZ/ZZ$), and intrinsic width divided by the resonance mass Γ/m for the given hypothetical new particle at $m = 500\,\text{GeV}$ and $3\,\text{TeV}$ are summarized.

Model			Spin	$m = 500\,\text{GeV}$			$m = 3\,\text{TeV}$		
				σ [pb]	BR	Γ/m	σ [fb]	BR	Γ/m
Radion ($k\pi r_c = 35$, $\Lambda_R = 3\,\text{TeV}$)		$R \to WW$ $R \to ZZ$	0	1.96 (3.5×10^{-3}) in ggF (VBF)	0.39 0.19	0.001	1.38 (5.5×10^{-3}) in ggF (VBF)	0.44 0.22	0.03
HVT	Model A	$W' \to WZ$ $Z' \to WW$	1	327 157	0.028 0.027	0.027	79 36	0.020	0.025
	Model B	$W' \to WZ$ $Z' \to WW$		– –	– –	–	5.5 2.5	0.47	0.031
	Model C (VBF)	$W' \to WZ$ $Z' \to WW$		0.036 0.023	0.50 0.46	0.0040	1.61×10^{-3} 1.04×10^{-3}	0.50	0.0033
Bulk RS $G_{\rm KK}$ ($k/\overline{M}_{\rm Pl} = 1.0$)		$G_{\rm KK} \to WW$ $G_{\rm KK} \to ZZ$	2	17.2 (0.46) in ggF (VBF)	0.43 0.23	0.037	0.47 (1.6×10^{-2}) in ggF (VBF)	0.20 0.10	0.062

1.5 Heavy Resonance Searches using Early Run2 Data

This section presents the results of the previous round of searches for the new heavy resonance decaying into diboson final states. ATLAS Run-2 data sample correponding to 36.1 fb^{-1} of pp collisions at $\sqrt{s}$=13 TeV collected by the ATLAS detector in 2015-2016 is used [51]. Interpretation results of the spin-1 HVT model, spin-2 Bulk RS model, and a spin-0 new heavy scalar are presented. Based on the number of charged leptons, the semi-leptonic analysis is split into three analysis channels: 0-lepton ($ZZ/ZW \to \nu\nu qq$), 1-lepton ($WW/WZ \to \ell\nu qq$) and 2-lepton ($ZZ/ZW \to \ell\ell qq$) channels. Here ℓ, ν and q denote the charged lepton (e or μ), neutrino, and quark (u, d, c, s, b), respectively. Section 1.5.1 shows upper limits on cross-section times branching ratio as a function of new boson mass using combined searches performed in the VV channels including the semi-leptonic channel; $WZ \to qqqq$, $l\nu qq$, $l\nu ll$; $WW \to qqqq$, $l\nu qq$, $l\nu l\nu$; and $ZZ \to qqqq$, $\nu\nu qq$, $llqq$, $ll\nu\nu$, $llll$. In addition, exclusion contour of signal parameters is also discussed for the HVT models in Section 1.5.2. Detailed event selection and statistical methodology can be found in Refs [51].

1.5.1 Upper limits on the cross-section times branching ratio

Figure 1.5 shows the upper limits on the cross-section times branching ratio of W' for the HVT model. For DY category, the lower limit on the $m(W')$ is 3.6 TeV in the weakly coupled HVT Model A and approximately 4 TeV in the strongly coupled HVT Model B. On the other hand, the lower limit does not reach to an expected theory curve for VBF production at all, and therefore there is room for exploring new particles produced via VBF production mode. In high $m(W')$ region of both DY and VBF categories, $l\nu qq$ and $\nu\nu qq$ channels have dominant lower limits, while $llqq$ channel shows better constraints at low $m(W')$ region. The full leptonic channel ($lll\nu$) presents the best performance at low $m(W')$ region. The full hadronic channel ($qqqq$) indicates the compatible sensitivity with $\ell\nu qq$ and $\nu\nu qq$ channels in high $m(W')$ region, but it can search for only $m(W')$ greater than ~ 1 TeV. In contrast to these situations, the semi-leptonic channels can probe the full range of $m(W')$ by compensating shortages of each channel, and therefore the channel could be the good probe for exploring new physics.

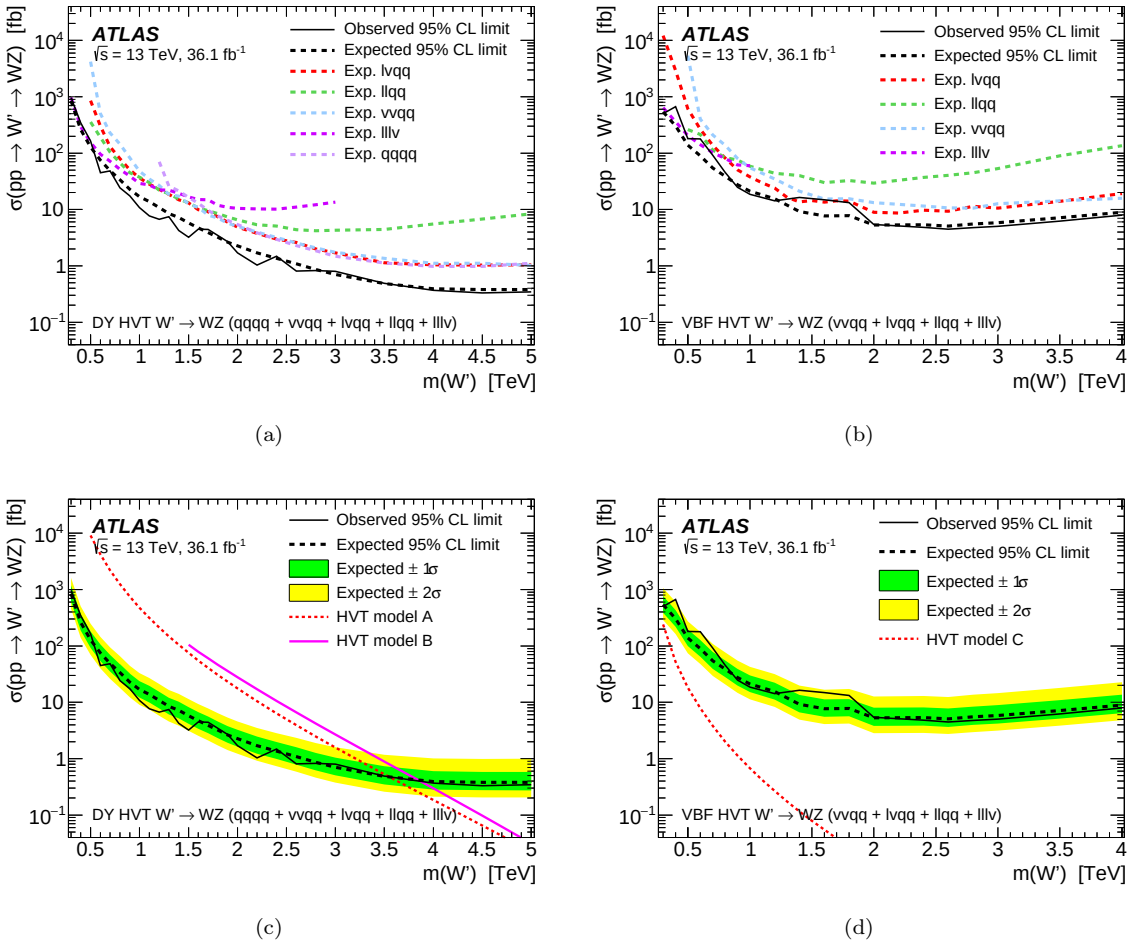

Figure 1.5: Observed and expected 95% CL (confidence level) upper limits on the W' cross-section times branching ratio to WZ for the HVT model. Expected limits for individual channels and their combination are shown for the (a) DY and (b) VBF production mechanisms. The limits for the combined channels for the (c) DY and (d) VBF production mechanisms are also shown, along with predictions for HVT models A, B, and C [51]

Figure 1.6 shows the upper limits on the cross-section times branching ratio of G_{KK} for the Bulk RS model. For $G_{KK} \to WW$ search, the $\ell\nu qq$ outperforms both full leptonic and full hadronic channels over the full range of $m(G_{KK})$. For $G_{KK} \to ZZ$ search, the $\nu\nu qq$ channel has strong constraints at high $m(G_{KK})$ region and the $llqq$ channel shows better constraints at low $m(G_{KK})$ region. The $l\nu qq$ channel does not contribute to this search. As in the case of HVT searches, the semi-leptonic channel demonstrates the outstanding sensitivity to G_{KK} in all $m(G_{KK})$ region. The lower limit on the $m(G_{KK})$ is 1.9 TeV in $G_{KK} \to WW$ and 1.7 TeV in $G_{KK} \to ZZ$.

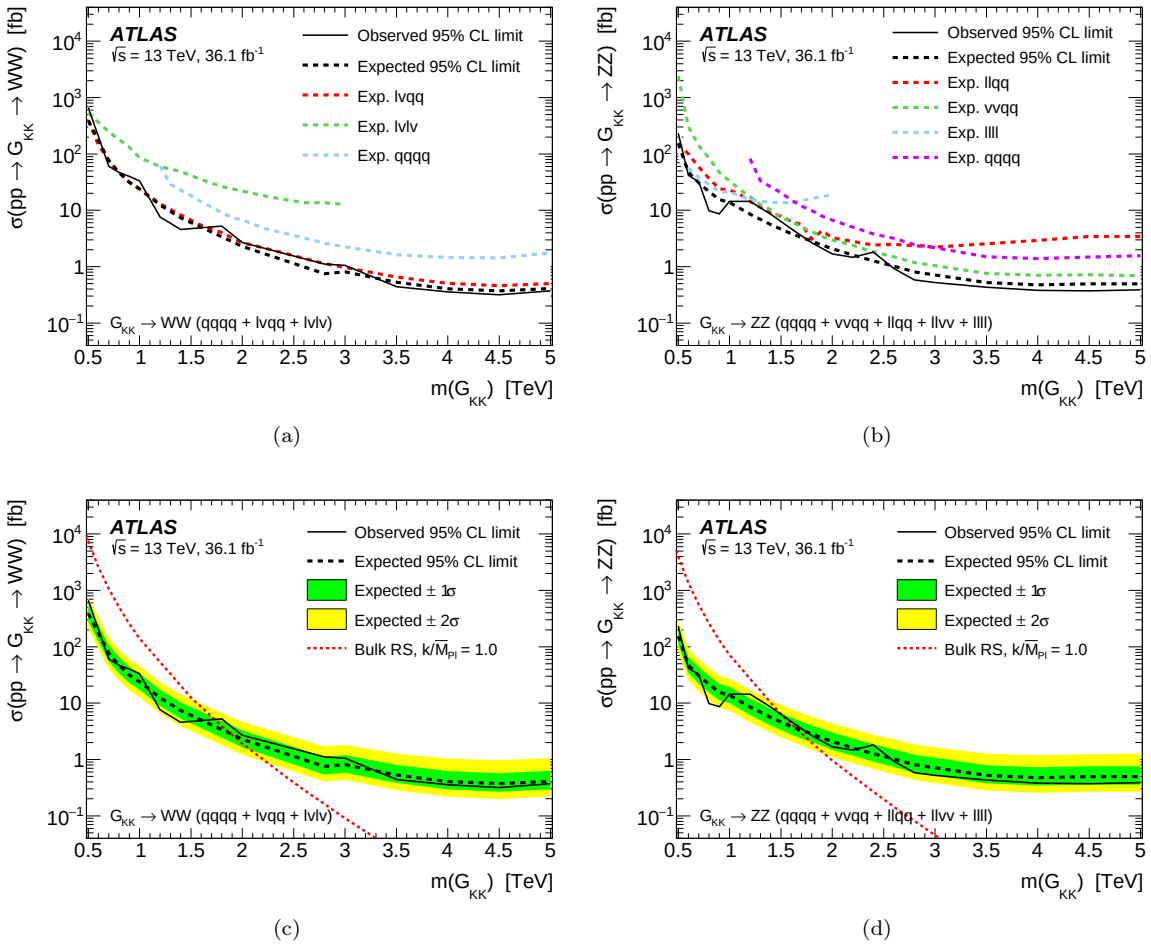

Figure 1.6: Observed and expected 95% CL upper limits on the G_{KK} cross-section times branching ratio to (a) WW and (b) ZZ for the Bulk RS model. Expected limits and their combination for individual channels and their combination are shown, along with (c), (d) predictions for Bulk RS model with $k/\bar{M}_{Pl} = 1$ [51].

Figure 1.7 shows the upper limits on the cross-section times branching ratio for the heavy scalar model. $\ell\nu qq$ and $\nu\nu qq$ channels are dominant in high m(scalar) region, while $llqq$ channel shows better constraints in low m(scalar) region.

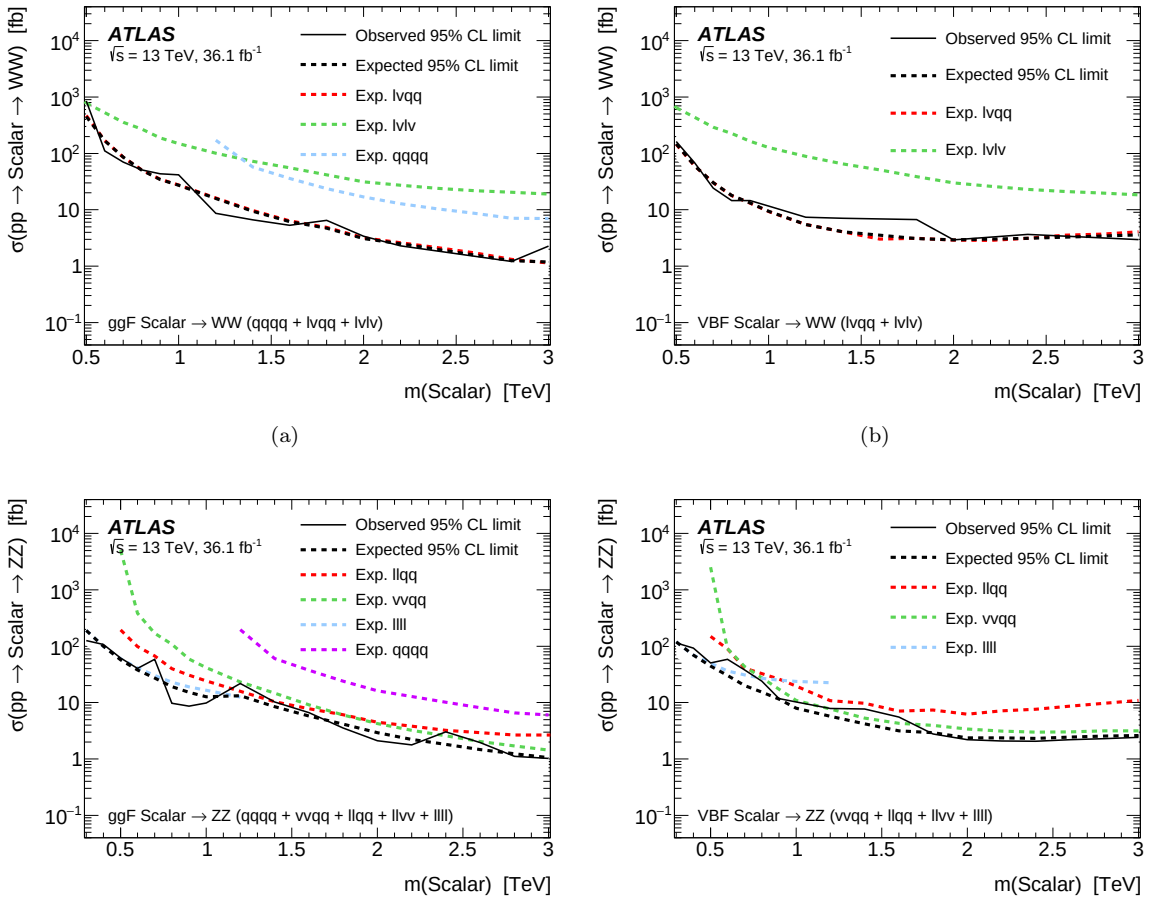

Figure 1.7: Observed and expected 95% CL upper limits on the scalar cross-section times branching ratio for the heavy scalar model. Expected limits for individual channels and their combination are shown for the (a) ggF-WW, (b) VBF-WW, (c) ggF-ZZ and (d) VBF-ZZ production mechanisms [51].

$VV + VH$ combined results of observed and expected 95% CL upper limits on the cross-section times branching ratio for HVT, Bulk RS and heavy scalar models are also discussed in Refs [51]. The upper limits on HVT Model A combined VV, VH and $V' \to \ell\ell/\ell\nu$ decay modes are shown in Figure 1.8. Combined limits exclude HVT Model A up to approximately 4.5 TeV due to stronger dileptonic decay mode.

For the original RS Graviton model with $k/M_{\mathrm{Pl}} = 0.1$, Figure 1.9 shows the limits on the cross-section times branching ratio to two photons as a function of the resonance mass. The RS model with $k/M_{\mathrm{Pl}} = 0.1$ is excluded for m_{G*} below 4.1 TeV, and this is one of the motivations of searching for the Bulk RS model discussed in Section 1.4.2.

1.5.2 Upper limits on coupling strengths

Constraints on the coupling strengths to both quarks and bosons (g_q, g_H) are also provided in the context of HVT models. The constraints are shown in Figure 1.10. In the shaded region, the limits are not valid since resonance would have a width greater than 5% of their mass. This is a region where the width of resonance would exceed the experimental m(VV) resolution, and an assumption of the narrow-width approximation is not valid anymore. The area outside the curves is excluded for each mass point. The resonance couplings to VV and VH decreases as the g_H coupling approaches zero, and production of the resonance tends to zero as the g_f couplings approach zero. This is why the constraints become weak when the couplings for both g_H and g_f decrease. By combining VV+VH+lv/ll channels, only smaller couplings for g_f are not excluded as

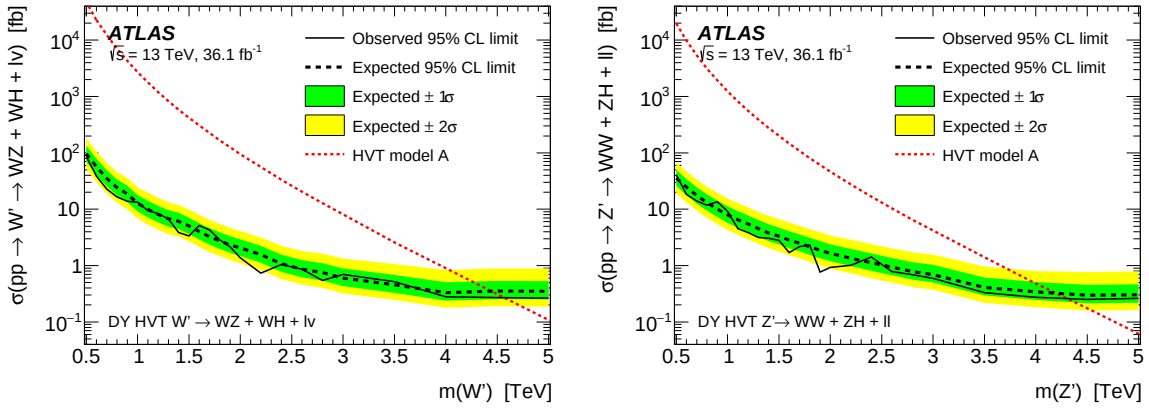

(a) (b)

Figure 1.8: Observed and expected 95% CL upper limits on the V' cross-section times branching ratio to VV, VH, and lepton–antilepton states for (a) W', (b) Z', and (c) V' production, along the predictions for HVT Model A [51].

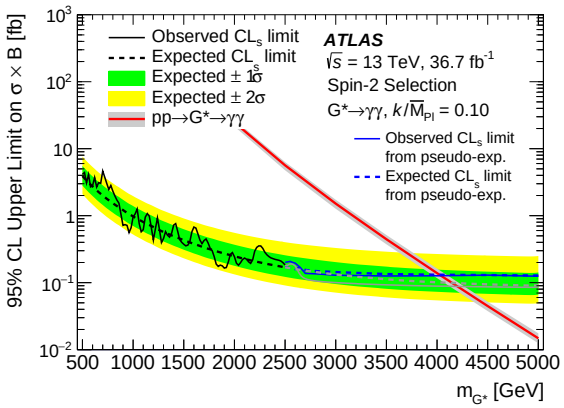

Figure 1.9: Upper limits on the production cross section times branching ratio to two photons at $\sqrt{s} = 13$ TeV of the lightest KK graviton as a function of its mass m_{G^*} for $k/M_{\mathrm{Pl}} = 0.1$. For $m_{G*} > 2500$ GeV, the observed and expected limits are determined with pseudo-experiments shown by the blue solid and dashed lines, respectively. Predictions are shown for the RS1 model, where the grey shaded band represents the PDF uncertainty [52].

described in Figure 1.10b. This motivates a search for a heavy vector like particle produced via VBF, which corresponds to HVT model C ($g_f = 0$) discussed in Section 1.4.1.

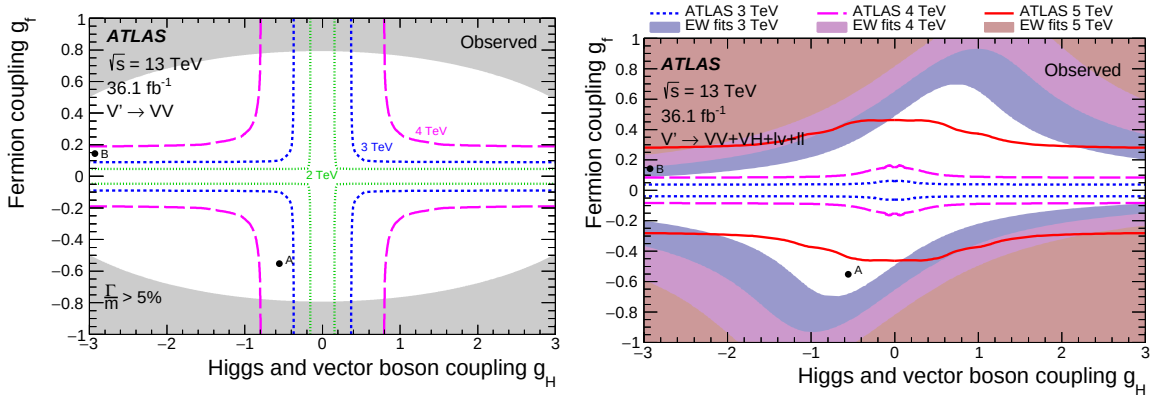

(a) (b)

Figure 1.10: Observed 95% CL exclusion contours in the HVT parameter space $\{g_H, g_f\}$ for resonances of mass 3, 4, and 5 TeV for the combination of (a) VV, and (b) VV+VH+lv/ll channels. The areas outside the curves are excluded, as are the filled regions which show the constraints from precision EW measurements [51].

1.6 Search for heavy diboson resonances in semi-leptonic final states

As introduced briefly in the previous section, the semi-leptonic channel of heavy resonances search has the good sensitivity to new particles over broader range of resonance mass. Furthermore, only this analysis searches for VBF production mode, and most of the resonance mass parameters are not excluded yet. There are still motivations to improve the sensitivity of all mass regions. In ggF production mode, lower mass region is excluded for most of the benchmark models. Hence sensitivity improvements for higher mass region are getting more important. Since the semi-leptonic analysis could be the significant indicator of new physics, the analysis improvement is surely helpful and the author contributed to that by introducing several ideas, which are discussed in Section 5 and 6 in details.

The author introduced several new ideas to improve the sensitivity e.g. Track-Calo Cluster (TCC), which is a particle-flow algorithm for high-p_{T} jet to achieve better jet substructure resolution, variable-radius (VR) track-jet b-tagging for the boosted $Z \to bb$ reconstruction, machine-learning (ML) based analysis. The author contributed in the ATLAS collaboration to these developments, in particular the optimization of boson tagging criteria and the calibration of TCC jets.

In the semi-leptonic analysis, the invariant-mass (for 1-lepton and 2-lepton channels) and transverse mass (for the 0-lepton channel) reconstructed by the final-state boson candidates are used as a final discriminant, and an excess against the estimated SM background is explored. When the resonance mass is significantly greater than the W/Z boson mass, the hadronically decaying W/Z boson from new particle X is highly boosted. Therefore the resulting quark pair can be collimated so that each of quark can not be identified separately. To handle this situation, each lepton channel analysis is split into two categories based on the different jet reconstruction techniques: (1) *merged* category with large-radius jet and a boson-tagging technique using jet substructure and (2) *resolved* category with the "standard" small-radius jets. In the 0-lepton channel, only merged category is considered. The merged category is further split into high-purity and low-purity regions based on the efficiency of boson tagging. In addition, in the case of the reconstruction of $Z \to q\bar{q}$ candidate, all categories are separated into the bottom-quark enriched subcategory (b-tagged) and the other (untagged). Thus a large-radius jet is used to reconstruct the final discriminant in merged analysis, while two separate small-radius jets are used for resolve analysis.

Dominant SM backgrounds of this analysis are W and Z bosons production in association with jets (W+jets and Z + jets, or collectively denoted as V+jets), top-quark production (both top-quark pair, $t\bar{t}$, and single top-quark), non-resonant diboson production (WW,WZ and ZZ), and multijet production. The modeling of these background processes are validated by the dedicated control region. The defined control regions are also used for statistical analysis to estimate the background. In all lepton channels and both merged and resolved categories, events are further categorized into subcategories based on the event topology consistent with VBF and ggF/DY categories, respectively.

Chapter 2

Experimental Setup

2.1 The Large Hadron Collider

The Large Hadron Collider (LHC) [53] is a proton-proton collider with a center-of-mass energy $\sqrt{s} = 13$ TeV and a design luminosity of 10^{34} cm^{-2}s^{-1}. The LHC is also able to accelerate lead ions and produce ion-ion and ion-proton collisions. The main LHC ring of a circumference of 26.7 km is located underground (between 70m and 140m) near Geneva, Switzerland. The collisions take place at four interaction points (IP) for the ALICE, ATLAS, CMS and LHCb experiments. The schematic overview of the LHC is shown in Figure 2.1a.

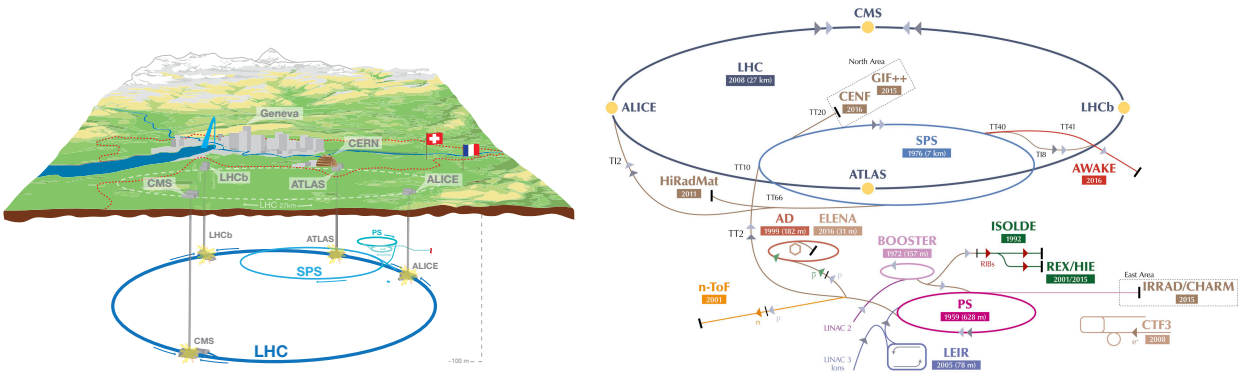

(a) (b)

Figure 2.1: (a) Overview of the LHC, including the ALICE, ATLAS, CMS and LHCb experiment [54]. (b) A schematic view of the CERN accelerator complex [55].

The LHC has two beam pipes and proton beams are circulating in opposite directions, clockwise and anti-clockwise, with an energy of 6.5 TeV. Before injecting into the LHC ring, protons are accelerated to 450 GeV by the acceleration chain which is a system of boosters: the LINAC2, Proton Synchrotron Booster (PSB), Proton Synchrotron (PS) and Super Proton Synchrotron. Figure 2.1b shows the overview of a series of accelerators.

The accelerated proton beams are directed by 1232 superconducting dipole magnets consist of niobium-titanium super-conductors which provides a magnetic field of up to 8.3 Tesla. The maximum field strength is necessary to bend protons with an energy of 7 TeV. They are operated at an extremely low temperature of 1.9 Kelvin to keep enough margin from the critical point. Furthermore, 392 quadrupole magnets are used to focus the proton beams and dedicated insertion magnets are used to focus the beams into the collision points. The proton acceleration is performed by superconducting radio frequency (RF) cavities, 8 modules per beam, operating at a frequency of 400 MHz and an accelerating gradients of 5.5 MV m^{-1} [53]. During Run 2 the LHC was running with the number of bunches per beam up to $n_b = 2544$ and the number of protons per bunch $N_b = 1.15 \times 10^{11}$ with a bunch spacing of 25 ns. The selected typical parameters for each year with standard 25 ns bunch train operation are summarized in Table 2.1.

Table 2.1: Selected LHC parameters for pp collisions at $\sqrt{s} = 13$ TeV in 2015–2018. The best accelerator performance during normal physics operation are shown. In 2017, the LHC was run in two modes: standard 25 ns bunch train operation and '8b4e' denoting a pattern of eight bunches separated by 25 ns followed by a four bunch-slot gap. The peak instantaneous luminosity of 16×10^{33} cm^{-2}s^{-1} in 2017 is part of the 8b4e period [56].

Parameter	2015	2016	2017	2018
Maximum number of colliding bunch pairs (n_b)	2232	2208	2544/1909	2544
Bunch spacing (ns)	25	25	25/8b4e	25
Typical bunch population ($10^1$1 protons)	1.1	1.1	1.1/1.2	1.1
$\beta*$ (m)	0.8	0.4	0.3	0.3-0.25
Peak luminosity (10^{33}cm^{-2}s^{-1})	5	13	16	19
Peak number of inelastic interactions/crossing ($< \mu >$)	16	41	45/60	55
Luminosity weighted mean inelastic interactions/crossing ($< \mu >$)	13	25	38	36
Total delivered integrated luminosity (fb^{-1})	4.0	38.5	50.2	63.4

Luminosity Determination

Luminosity measurements at the LHC are crucial since it directly relates to the production rate of physical processes. In ATLAS, luminosity information is provided by several detectors. The LUCID-2 (LUminosity Cerenkov Integrating Detector) [57], which is upgraded to cope with all beam conditions and luminosity ranges during Run 2, is able to provide the primary bunch-by-bunch luminosity information, both online and offline. Measurements from other detectors such as calorimeters and BCM (beam condition monitor) diamond detectors can be found in Refs. [57, 58].

The LUCID-2 consists of two simple rings of 16 PMTs (Photomultipliers) placed at approximately $z = \pm 17$ m from the interaction point, one ring per side, with the quartz window working as a Cherenkov radiator. In addition, four quartz fiber-bundles coupled to PMTs are installed 1.5 m away from the beam pipe. In order to convert the raw signals from the PMTs to a luminosity, several luminosity algorithms requiring hits information are used: BiEventORA in 2015, BiHitOR in 2016 and 2017 [56]. Since most of PMTs stopped working in 2018, a single PMT on the C-side was used for the baseline luminosity estimate.

Based on the number of hit counts, a visible interaction rate per bunch crossing μ_{vis}, which is proportional to the instantaneous luminosity, is evaluated [59]. Then, the per-bunch instantaneous luminosity can be written as:

$$\mathcal{L}_b = \frac{\mu_{\text{vis}} f_r}{\sigma_{\text{vis}}}, \tag{2.1}$$

where f_r is the LHC revolution frequency (11245 Hz for protons), and a calibration constant corresponding to the visible cross-section σ_{vis} is evaluated by vdM (*van der Meer*) scans [56, 58, 59]. In terms of beam LHC parameters, the per-bunch instanteneous luminosity can also be wrriten as:

$$\mathcal{L}_b = \frac{f_r n_1 n_2}{2\pi \sum_x \sum_y}, \tag{2.2}$$

where n_1 (n_2) is the number of protons in the beam-1 (2), and $\sum_x$ and $\sum_y$ are the convolved beam sizes in the horizontal and vertical planes. In the vdM scans, the beam separation is varied in individually horizontal and vertical direction to obtain $\sum_x$ and $\sum_y$, and to scan μ_{vis}. Combining Equations 2.1 and 2.2 gives σ_{vis} following

$$\sigma_{\text{vis}} = \mu_{\text{vis}}^{\text{max}} \frac{2\pi \sum_x \sum_y}{n_1 n_2}, \tag{2.3}$$

wehre $\mu_{\text{vis}}^{\text{max}}$ is the maximal visible rate extracted in the vdM scan. The measurements are complemented by the four-diamond BCM sensors on each side of interaction points using similar formalism. Given these parameters, the instantaneous luminosity is obtained as $\mathcal{L} = n_b \mathcal{L}_b$. The expected events number of a traget process is then calculated as $N_{\text{process}} = \sigma_{\text{process}} L$. Here L is the time-integrated luminosity of $\mathcal{L}$. Figure 2.2 shows the total integrated luminosity in Run-2.

2.2 The ATLAS Detector

The ATLAS detector [61] at the LHC is a multipurpose particle detector with an approximately 4π coverage in solid angle. It consists of an inner detector, electromagnetic and hadronic calorimeters, and a muon

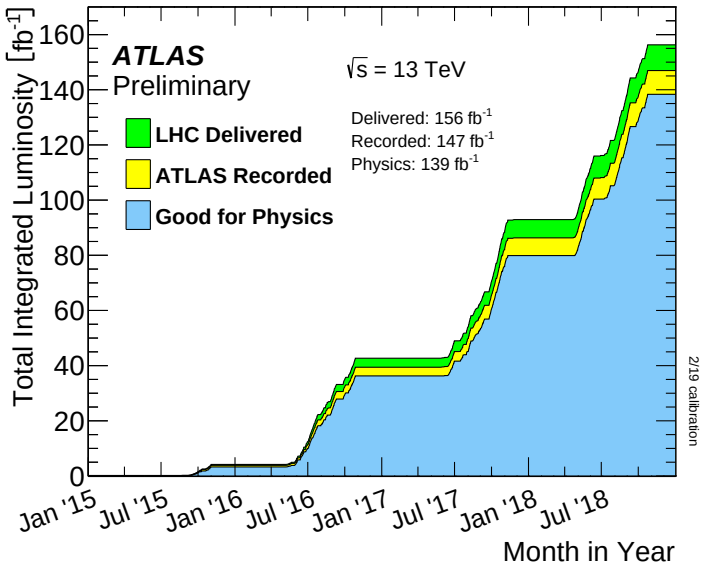

Figure 2.2: Total Integrated Luminosity and Data Quality in 2015-2018 [60].

.

spectrometer. The schematic view of the ATLAS detector is shown in Figure 2.3.

The inner detector (ID) for tracking covers the pseudorapidity range $|\eta| < 2.5$ and is immersed by a 2 T magnetic field provided by a solenoid. The inner detector is composed of silicon pixel, silicon microstrip, and transition-radiation tracking detectors. An innermost pixel layer inserted at a radius of 3.3 cm has been used since 2015.

Lead and liquid argon (LAr) electromagnetic sampling calorimeters provide electromagnetic (EM) energy measurements and the position of the electromagnetic showers with $|\eta| < 3.2$. The LAr sampling calorimeters are also used to measure hadronic showers in the endcap ($1.5 < |\eta| < 3.2$) and electromagnetic and hadronic showers in the forward regions ($3.1 < |\eta| < 4.9$). Hadronic calorimeters cover the central pseudorapidity range ($|\eta| < 1.7$). The end cap and forward regions are instrumented with LAr calorimeters for both the EM and hadronic energy measurements up to $|\eta| = 4.9$.

The muon spectrometer (MS) surrounds the calorimeters and covers the pseudorapidity range $|\eta| < 2.7$. The MS features three large air-core toroidal superconducting magnet systems with eight coils each (between 2.0 and 6.0 Tm). In the MS, Precision tracking chambers cover up to $|\eta| = 2.7$ and fast detectors for triggering cover up to $|\eta| = 2.4$.

2.2.1 Coordinate System

The ATLAS experiment adopts a right-handed coordinate system. The origin lies at the IP and the positive x-axis direction points to the center of the LHC and the positive y-axis points upwards. The x-y plane is used for transverse measurements and the z-axis points along the beamline by definition. In addition to a cartesian coordinate, polar coordinates are also used. The azimuthal angle ϕ is defined in the x-y plane and is measured from the y-axis. The polar angle θ is defined in the y-z plane and is measured from the z-axis. The pseudorapidity is defined as $\eta = -\ln\tan\frac{\theta}{2}$, which is invariant under Lorentz-transformations. The angular distance ΔR is also used and is defined as $\Delta R = \sqrt{\Delta\eta^2 + \Delta\phi^2}$.

2.2.2 Inner Detector

The ATLAS Inner Detector (ID), shown in Figure 2.4, is designed for providing position measurements of charged particles in the range $|\eta| < 2.5$. In order to provide the track measurements, the ID is immersed in a 2 T magnetic field generated by the central solenoid which has a length of 5.3 m with a diameter of 2.5 m. The ID consists of three different technologies of silicon pixel, silicon micro-strip (SCT) and straw tube transition radiation tracker (TRT) detectors. It is composed of a cylindrical barrel region arranged around the beam pipes ($|\eta| < 1.5$), and two end-caps for $1.5 < |\eta| < 2.5$. A detailed description of the inner detector can be found at [61].

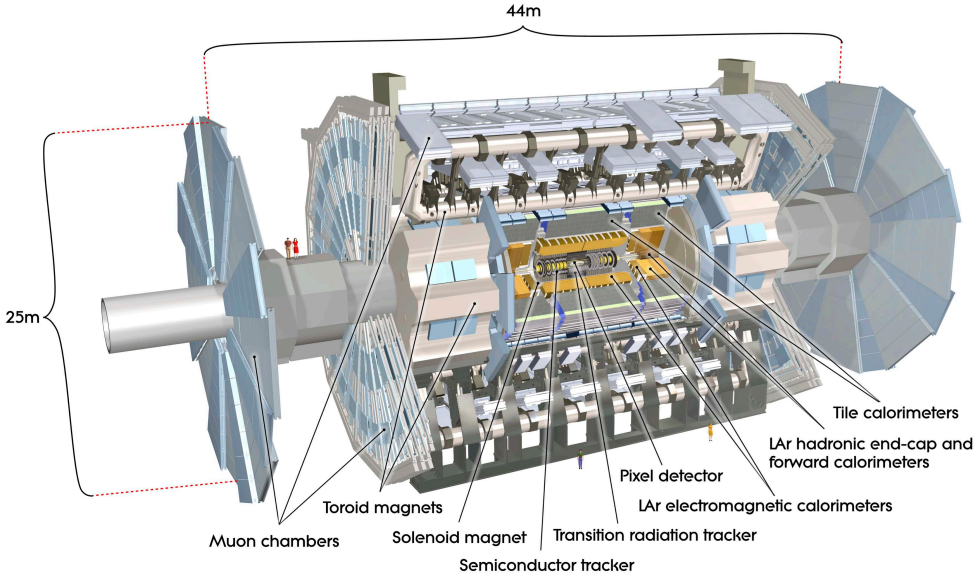

Figure 2.3: An overview of the ATLAS detector [62].

The pixel detector [63] has four-barrel layers at radii of 33, 50.5, 88.5 and 122.5 mm and three disks in each of the end-caps at $|z|$=495, 580 and 650 mm. From Run 2, the insertable B-layer (IBL) is introduced as the innermost layer [64, 65]. The typical pixel size is 50 µm $(r-\phi)\times$ 250 µm (z) for IBL and 50 µm $(r-\phi)\times$ 400 µm (z) for the outer barrel and disk layers.

The SCT [66] consists of four double strip layers at raddi of 299, 371, 443 and 514 mm, spanning $|z| <$ 746 mm, complemented by nine wheels in each of the end-caps with 854 mm $< |z| <$ 2720 mm. A typical strip of a barrel SCT sensor has a 80 µm pitch and 128 mm length running approximately along the z-(r-) direction for the barrel (end-caps). Each module consists of a double-sided sensor with a stereo angle of 40 mrad. The information from the two sides of each layer can be combined to provide a three-dimensional position measurement referred to as a space-point.

The silicon detectors are complemented by the outer volumes of the inner detectors furnished with the TRT [67]. The TRT extends track reconstruction radially up to a radius of 1082 mm. It is comprised of approximately 300 000 straw tubes and covers the pseudorapidity range of $|\eta| < 2.0$. Each straw tube only provides two-dimensional position information with a position resolution of approximately 130 µm. Starw tubes in the barrel region ($|z| <$ 712 mm) run along the z-direction providing (r, ϕ) information, while for end-caps (848 mm$<|z|<$2710 mm) they run in the radial direction providing (z, ϕ) information.

2.2.3 Calorimeter System

The ATLAS calorimeter system [68, 69] is degined for providing good measurements for electromagnetic and hadronic showers. Figure 2.5 shows the sckematic view of the ATLAS calorimeter system. The ATLAS calorimeters have a highly granular lateral and longitudinal segmentation. It covers $|\eta| < 4.9$ and is composed of the electromagnetic (EM) calorimeter and the hadronic calorimeter. The EM calorimeter can be used for precision measurement of electrons and photons, by requiring the matching between the inner detector. The hadronic calorimeter also provides the information for jet reconstruction and $E_{\mathrm{T}}^{\mathrm{miss}}$ measurements.

The EM calorimeter is a high-granularity liquid-argon sampling carolimeter (LAr) with accordion-shaped Kapton electrodes and lead absorber plates over its full coverage. The EM calorimeter is divided into one barrel (EMB; $|\eta| < 1.475$) and two end-cap (EMEC; $1.375 < |\eta| < 3.2$) components. The barrel calorimeter is separated by a small gamp (4 mm) at $z = 0$. The each end-cap calorimeter comprised two coaxial wheels. An outer wheel covers $1.375 < |\eta|, 2.5$ and an inner wheel covers the $2.5 < |\eta| < 3.2$. The radiation lengths of the EM calorimeter is $> 22X_0$ in the barrel and $> 24X_0$ in the end-caps. In the region of $|\eta| < 1.8$, a presampler detector is mounted to correct for the energy lost by electrons and photons upstream of the calorimeter. The barrel presampler covers $|\eta| < 1.52$, while the end-cap presampler covers $1.5 < |\eta| < 1.8$.

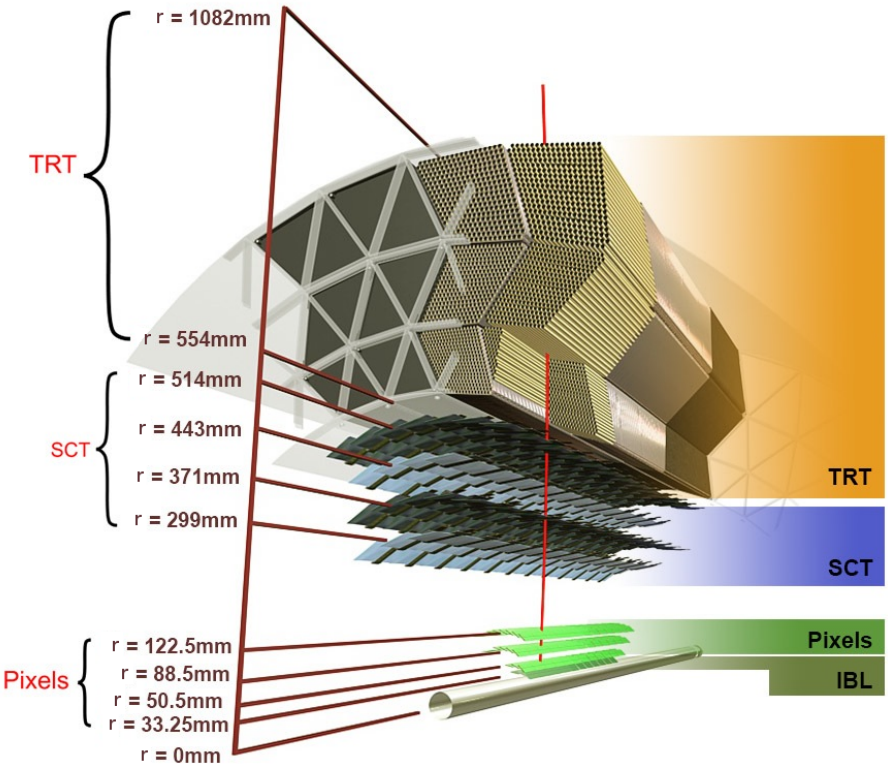

Figure 2.4: Sketch of the barrel region of the ATLAS inner detector [61].

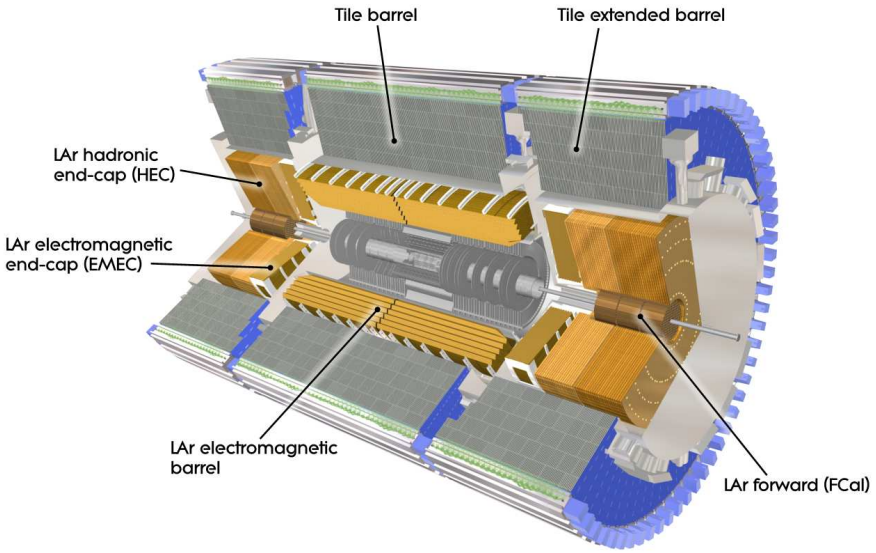

Figure 2.5: Overview of the ATLAS calorimeter system [61].

The hadronic calorimeters comprises the three distinct sections. The central section covers the barrel region ($|\eta| < 0.8$) and two extended barrel regions ($0.8 < |\eta| < 1.7$). It is a sampling calorimeter instrumented with scintillator tile/steel calorimeters and referred to as Tile calorimeter. Each barrel region is divided azimuthally into 64 modules. The two hadronic end-cap calorimeters (HEC; $1.5 < |\eta| < 3.2$) feature liquid-argon/copper calorimeter modules instrumented as an independent wheel per end-cap. The HEC is built from 32 identical wedge-shaped modules and is located directly behind the end-cap electromagnetic calorimeter with sharing the same LAr cryostats. Each wheel is divided into two segments in-depth, for a total of four layers per end-cap. The two forward calorimeters (FCAL; $3.1 < |\eta| < 4.9$) are instrumented with liquid-argon/copper and liquid-argon/tungsten modules for electromagnetic and hadronic energy measurements, respectively. The FCAL is integrated into the end-cap cryostats and consists of three modules in each end-cap. The first module is made of copper and is designed for electromagnetic measurements. On the other hand, the rest of the two modules are made of tungsten thus measure the energy of hadronic interactions.

More details of the calorimeter read-out structures, absorption characteristic, inactive material distributions, and cell signal formation can be found in Ref. [61].

2.2.4 Muon System

The ATLAS Muon Spectrometer (MS) is desgined to detect charged particle going through the calorimeters and to measure their transverse momentum with an uncertainty varying from 3% at 100 GeV to about 10% at 1 TeV. It also provides a trigger for muons with varying transverse momentum thresholds down to a few GeV. A detailed description of the muon spectrometer and its expected performance can be found at [61, 70]. The measurement of muon momentum is performed by using the track curvature in a toroidal magnetic fields. The main component of the magnetic field is always perpendicular to the muon track so that the transverse momentum resolution is approximately independent of η over the whole acceptance. The magnetic filed is given by three toroids, one is the "barrel" ($|\eta| < 1.1$) and one for each "end-cap" ($1.1 < |\eta| < 2.7$), with a filed integral between 2 and 8 Tm. The muon curvature is measured using three precision chamber stations positioned along its track. The precision measurement requires each station to detect the muon with an accuracy of 50 µm. The schematic drawing of the muon spectrometer is shown in Fig 2.6.

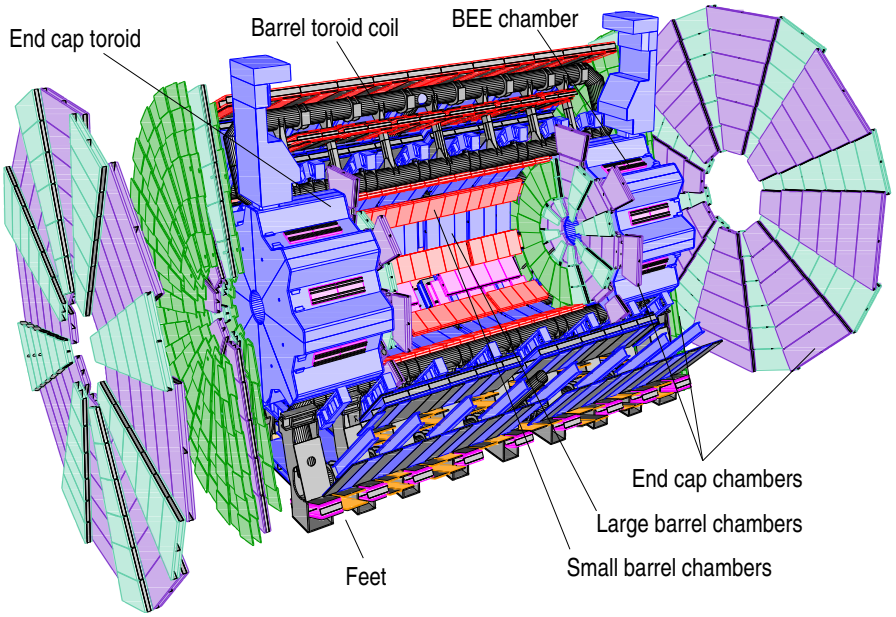

Figure 2.6: Schematic drawing of the ATLAS muon spectrometer.

.

The precision momentum measurement is performed by Monitored Drift Tube chambers (MDT's) [61] and Cathode Strip Chambers (CSC's) [61]. The MDT's cover the pseudorapidity range $|\eta| < 2.7$ (except in the innermost end-cap layer where their coverage is limited to $|\eta| < 2.0$). These chambers are comprised of three to eight layers of drift tubes with an absolute pressure of 3 bar. Each tube is 30 mm in diameter and has an anode wire of 50 µm diamter. The coordinate in the plane perpendicular to the wires, measured by the MDT is referred to as the precision or bending coordinate. The gas mixture used is 93% Ar and 7% CO_2

with a small admixture of water vapor. The total drift time is about 700 ns [71, 72] and the space resolution is 80 µm per tube, or about 35 µm per chamber.

In the end-cap inner region, for $2.0 < |\eta| < 2.7$, The CSC's are used because of their capability to cope with higher background rates and time resolution. The CSC's are multiwire proportional chambers with cathode planes. The cathode planes are segmented into strips in orthogonal directions to multiwires and the coordinate is obtained measuring the induced-charge distribution. Typical resolution obtained with this read-out shceme is about 50 µm.

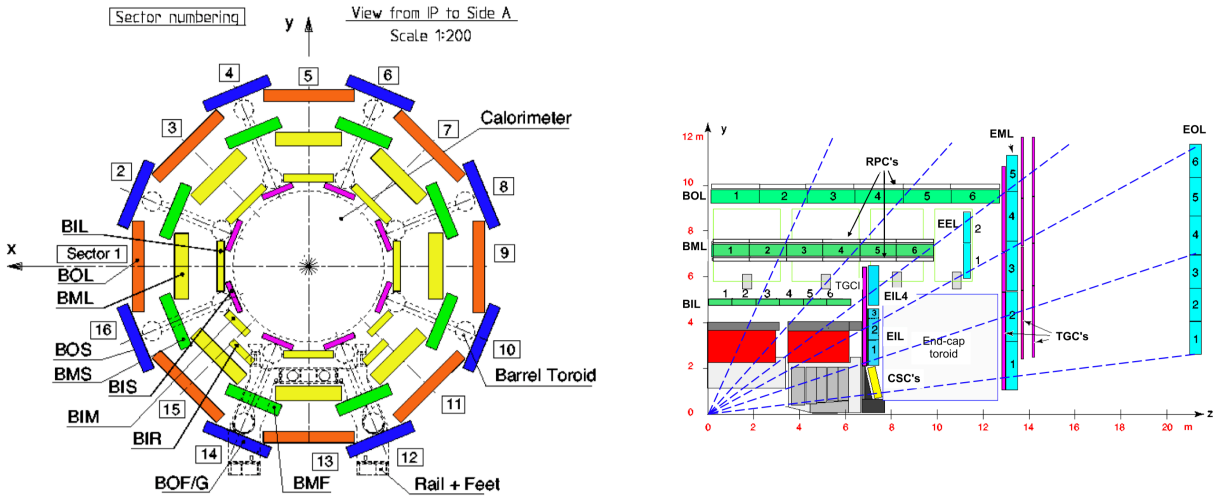

(a) (b)

Figure 2.7: (a) Cross-section of the barrel muon system perpendicular to the beam axis (non-bending plane) and (b) cross-section of the muon system in a plane containing the beam axis (bending plane) 2.7b.

The trigger system of the MS is composed of two different chamber technologies: Resistive Plate Chambers (RPC's) [61] in the barrel region and Thin Gap Chambers (TGC's) [61] in the end-cap regions. The trigger system in the barrel consists of three concentric cylindrical layers of RPC's around the beam axis. The two inner chambers provide the low-p_T trigger while the outer most layer contributes to the high-p_T trigger in combination with the inner chambers. The RPCs also provide the coordinate along the MDT wires that is not measured by the MDT chambers.

Similarly in the end-cap two TGC doublets and one triplet are installed close to the middle station and provide the low-p_T and high-p_T trigger signals. The TGC's also measure the coordinate of the muons and this coordinate is referred to as the second, or non-bending coordinate. For this purpose, TGC chambers are also installed close to the MDTs in the inner layer of the end-cap (EL). Fig 2.7a and 2.7b give cross-sections of the MS system in the planes transverse to, and containing, the beam axis.

2.2.5 Trigger and Data Acquisition

The ATLAS Trigger and Data Acquisition (TDAQ) system [73] for selecting events of interest are shown in Figure 2.8. It consists of a hardware-based first-level trigger (L1) and a software-based high-level trigger (HLT). Based on information from a subset of detectors, interesting proton-proton collisions are identified and the corresponding detector outputs are recorded to the permanent storage.

The L1 trigger searches for high transverse momentum muons, electrons, photons, jets and τ-leptons decaying into hadrons, as well as large missing and total transverse energy. The event rate is reduced from the 40 MHz bunch crossing rate to below 100 kHZ. It decides within 2.5 μs whether or not events should be kept, to satisfy the 400 reduction factor. The L1 trigger decision is made by the Central Trigger Processor (CTP) which receives inputs from the L1 calorimeter (L1Calo) and L1 muon (L1Muon) triggers sub-systems. Region-of-interest (RoI) is defined by the L1 trigger. The RoI has calorimeter clusters with high transverse energy, E_T, or muon tracks in the muon chambers.

After the L1 trigger acceptance, events are buffered in the Read-Out System (ROS) and processed by the HLT based on algorithms implemented in software. The event rate is further reduced to an average of ~ 1 kHz. The HLT utilizes the detector information including fine-granularity calorimeter information, precision measurements from the muon spectrometer and tracking information from the ID. In order to reduce the

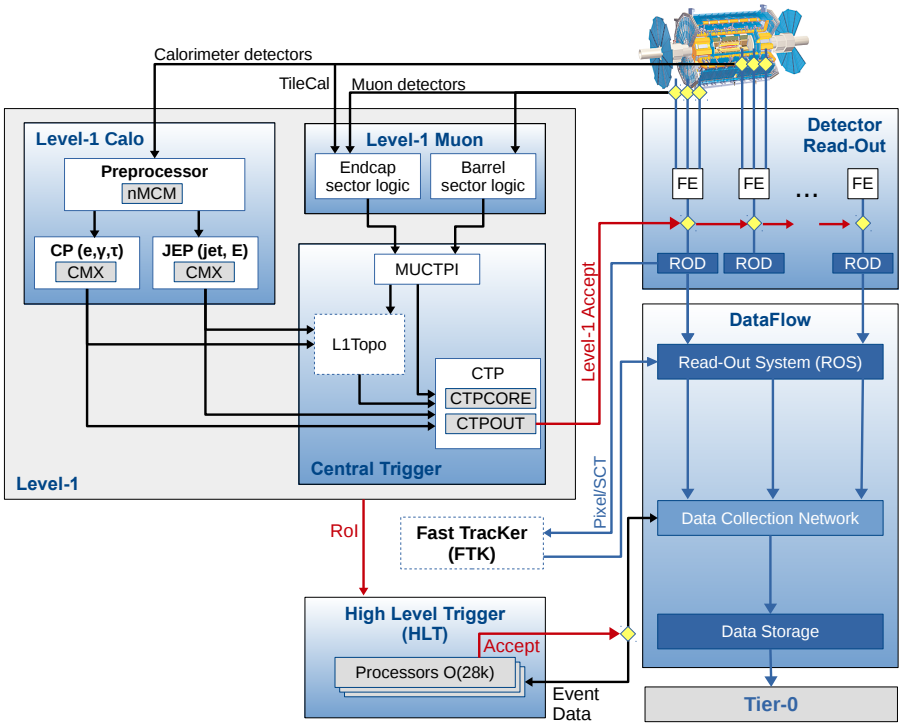

Figure 2.8: The ATLAS TDAQ system in Run 2 with emphasis on the components relevant for triggering [73]

.

time consumed by the HLT to reconstruct the event and make a decision, the selection of particle candidates by the HLT is performed at each step.

The goal of L1 and HLT trigger is to select interesting proton-proton collisions by identifying one or more particles of a given type and a given threshold of transverse energy or momentum. For example, muon triggers are meant to select events with one or more muons in the detector. The configuration of the trigger is controlled by the 'trigger menu' and the menu compositions and trigger thresholds are optimized for the LHC running conditions.

Chapter 3

Data and Monte Carlo Simulated Samples

3.1 Data Samples

This analysis is performed using the proton-proton collision data collected between years 2015 and 2018 corresponding to an integrated luminosity of 139 fb^{-1}. The uncertainty on the integrated luminosity is 1.7% [74], obtained using the LUCID-2 Cherenkov detector [57] for the primary luminosity measurements. The integrated luminosity is 36.2 fb^{-1} in 2015-16, 44.3 fb^{-1} in 2017 and 58.5 fb^{-1} in 2018, respectively.

3.2 Simulation of pp collisions

Describing and simulating the final states occuring from pp-collisions provided by the LHC is very complicated and thus is the very challenging task. In this section, a brief review of the description and the simulation of pp-collisions performed by Monte Carlo (MC) simulation is given. MC simulated events are used for the background modeling, evaluation of the signal acceptance, optimization of event selection, estimation of systematic uncertainties and the statistical analysis. The Monte Carlo simulated event generation is split into several steps as shown in Figure 3.1. All steps are performed within the ATLAS software framework ATHENA [75].

3.2.1 Factorization

Since the different energy scales of the hard interaction are involved, it is impossible to calculate the cross-section for a certain process in a pp collision directly. Making use of the factorization theorem [77], the calculation can be broken down into a high-energy part that can be described by perturbation theory and a low-energy part that is calculated by tunable models. According to the factorization theorem, the cross-section for a scattering process $pp \to n$ can be written as

$$\sigma_{pp\to n} = \sum_{i,j} \int \int_0^1 dx_i dx_j f_i(x_i, \mu_F^2) f_j(x_j, \mu_F^2) \hat{\sigma}_{ij\to n}(x_i, x_j, s, \mu_F^2), \tag{3.1}$$

where the sums run over all partonic constituents of the protons p, s is the square of the center-of-mass energy, and $\hat{\sigma}_{ij\to n}(x_i, x_j, s, \mu_F^2)$ is the partonic cross-section for the final state n from partons of type i and j. The function $f_i(x_i, \mu_F^2)$ and $f_j(x_j, \mu_F^2)$ are the parton distribution function (PDF) which describes the propability density that a parton i with a fraction x of the longitudinal momentum of the proton is found at the *factorization scale* μ_F. Since the PDFs can not be derived from the perturbation theory, they are obtained experimentally. ATLAS uses the PDFs obtained from the Les Houches Accord PDF Interface library [78].

3.2.2 The fixed-order partonic cross-section

The partonic cross-section $\hat{\sigma}_{ij\to n}(x_i, x_j, s, \mu_F^2)$ introduced in the previous section is perturbatively calculable when μ_F is reasonably large to allow for a perturbative treatment of QCD. The partonic cross-section can be expanded in powers of the strong coupling constants:

$$\hat{\sigma}_{ij\to n}(x_i, x_j, s, \mu_F^2) = \int d\Phi_n \frac{1}{2\hat{s}} |\mathcal{M}_{ij\to n}(\Phi_n; \mu_F)|^2, \tag{3.2}$$

where $\mathcal{M}_{ij\to n}$ is the matrix element for the production of the final state, Φ_n is phase space, and $\hat{s} = x_i x_j s$. The matrix element can be computed based on the QCD and EW theory, with the truncated fixed-order

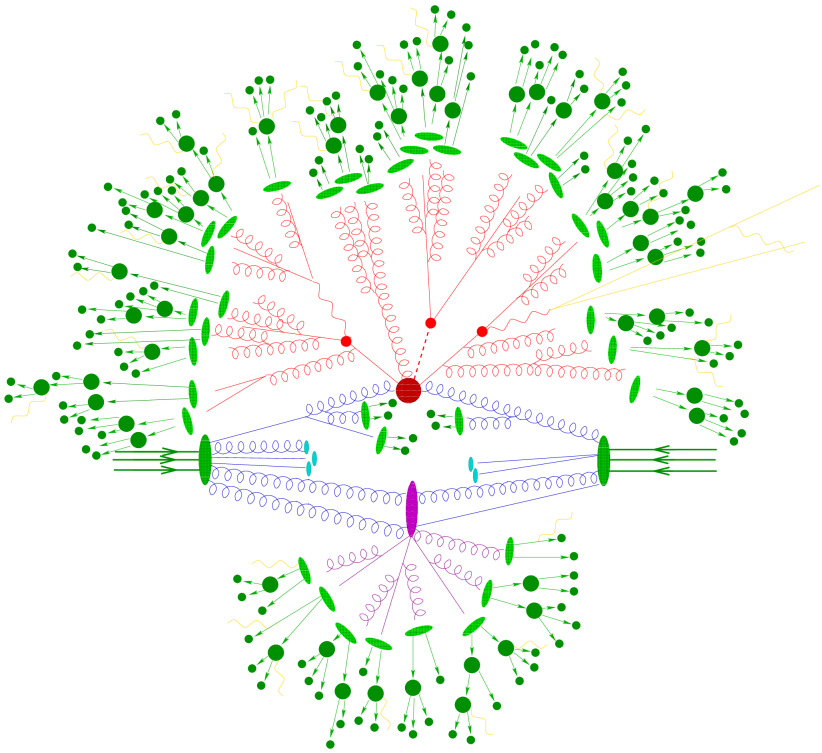

Figure 3.1: Sketch of a hadron-hadron collision simulated by a Monte-Carlo event generator [76]. The hard collision is represented by the largest red blob which is surrounded by tree-like structure describing Bremsstrahlung as simulated by parton showers. The purple blob represents a secondary hard scattering. The light green blobs represent parton-to-hadron transitions and dark green blobs indicate hadron decays, while yellow lines indicate soft proton radiation.

perturbative expansion (shown as a large red blob in Fig 3.1). While the fixed-order calculation can cover the most of the phase space, it is also significantly important to calculate the higher-order terms since this analysis searches for the phase spaces where the SM backgrounds have much smaller cross-section. For the event generator, the matrix element of each process is calculated at leading order (LO) or next-to-leading order (NLO) accuracy in perturbation theory. There are several kinds of event generators available in ATHENA, such as POWHEG [79], SHERPA [80], and AMC@NLO [81].

3.2.3 Parton showering

The hard process from the event generation is then processed via two steps, the parton showering and parton hadronization. The parton shower (PS) approximation is the approach to provide the calculations of emissions in soft and collinear regions of phase space to compensate the higher-order effects. The concept of parton showering is based on gluons splitting into quark anti-quark pairs or partons radiating gluon bremsstrahlung (red lines in Figure 3.1).

The partons showering assumes the cross-section for final states n with an additional parton radiation can be approximately factorized into the original cross-section as:

$$d\sigma_{n+1} = d\sigma_n \sum_{i \to jk} \frac{\alpha_S}{2\pi} \frac{dt}{t} dz P_{i \to jk}(z, \phi), \tag{3.3}$$

where the indices i, j are parent parton before and after the splitting, k is the emitted parton with momentum fraction z, and t is the invariant mass of the parton i. $P_{i \to jk}$ is the DGLAP splitting functions [82–84]

calculated as:

$$P_{q\to qg} = C_F \frac{1+z^2}{1-z}, \tag{3.4}$$

$$P_{q\to gq} = C_F \frac{1+(1-z)^2}{z}, \tag{3.5}$$

$$P_{g\to gg} = C_A \frac{z^4+a+(1-z)^4}{z(1-z)}, \tag{3.6}$$

$$P_{g\to q\bar{q}} = T_R(z^2+(1-z))^2. \tag{3.7}$$

The Casimir operators, $C_F = (N_c^2-1)/2N_c$ and $C_A = N_c$, depend on the number of colors and $T_R = 1/2$. As seen from the Eq.3.3, $d\sigma_{n+1}$ can diverge in the limit of soft and collinear emission (e.g. $z \to 0$). The divergences are technically avoided by introducing a cutoff below which no further parton emission is allowed. Usually, the transverse momentum of the partons is used as a cutoff and the showering is stopped once the decreasing parton energy scale is lower than a cutoff scale ~ 1 GeV.

The parton shower technique is an iterative process of parton splitting until no partons with momentum above a cutoff are produced. This recursive process is described by the probability of emitting an extra parton at each step, referred to as the Sudakov form factor [85]:

$$S_i = 1 - \exp\left(-\sum_{j,k}\int_t^T \frac{dt'}{t'}\int dz \frac{\alpha_s}{2\pi} P_{i\to jk}(z)\right), \tag{3.8}$$

where T is the maximum possible virtuality and the starting point for the shower. The initial-state radiation (ISR) is simulated similarly but needs more complicated procedure since the parent parton is coming from the non-perturbative PDFs and developed shower does not result in hard scatter. Therefore the ISRs take a backward evolution approach in which the evolution starts with the parton from the hard interaction with increasing momentum fraction and each of the resulting parton is then evolved forward. The iteration stops when a cutoff is reached. The double-counting between the fixed-order matrix element calculation and the parton showering are resolved by the matching algorithms such as CKKW [86] and MLM [87].

3.2.4 Hadronization

The resulting partons from the parton shower then conform color singlet hadrons, a process referred to as hadronization (light-green blobs in Figure 3.1). The most common model is "Lund string model" [88] which describes the interaction between the combinating partons by a string being stretched between parton pairs. Given a quark-antiquark pair, the string can be regarded as a uniform color-flux between them. As the partons move apart with increasing distance, the potential energy reaches a threshold and then the string breaks down to a new quark-antiquark pair. This process is repeated until only on-shell mesons remain.

These hadrons decay further into stable particles (dark-green blobs in Figure 3.1). The hadronization cannot be calculated due to its non-perturbative energy scale. Therefore the simulation of the hadronization relies on phenomenological models in which several free parameters are to be derived from experiments, and sets of the parameters are referred to as MC generator tunes. The EvtGen program [89] is used for properties of the bottom and charm hadron decays. "*The underlying event*", interactions and activities of the proton remnants, are also added.

3.2.5 Detector Simulation

After the generation of simulated events, the interaction of particles with the detector's material and the detector responses are simulated using the GEANT4 framwork [90]. The generated particles pass through the simulated ATLAS detector and the hits in the detector are converted to detector response during a step of digitization. The same reconstruction algorithms are used for data and simulated events, therefore the output of the simulation is identical to that of the ATLAS detector. This reconstruction method, referred to as full simulation (FULLSIM), is expensive in terms of computation, and this is a limiting factor for the production of large numbers of simulated events. To reduce the computation time, several simplified approaches have been developed at the cost of accuracy. The ATLFAST2 simulation uses FULLSIM for the inner detector and the muon system but is provided with simplified geometry and showering in the calorimeter [91].

3.2.6 Pile-up

Since multiple protons interact in each bunch crossing, *Pile-up* events need to be considered additionally for the events of interest. The rate of pile-up is represented by $R_{\text{inel}} = \mathcal{L}\sigma_{\text{inel}}$, where σ_{inel} is the inelastic cross section taken to be 80 mb for 13 TeVcollisions [92]. With this measurement, the average number of interactions per bunch crossing is defined as

$$\mu = \frac{\mathcal{L}\sigma_{\text{inel}}}{n_b f_r}. \tag{3.9}$$

Additional proton-proton collisions occurring in the same bunch-crossing as the hard process of interest are referred to as in-time pile-up. On the other hand, additional collisions occurring from other bunch crossing is called as out-of-time pile-up. The average number of interactions per bunch crossing between in 2015 and 2018 is shown in Figure 3.2. In order to account for the possible difference between Monte Carlo simulated samples

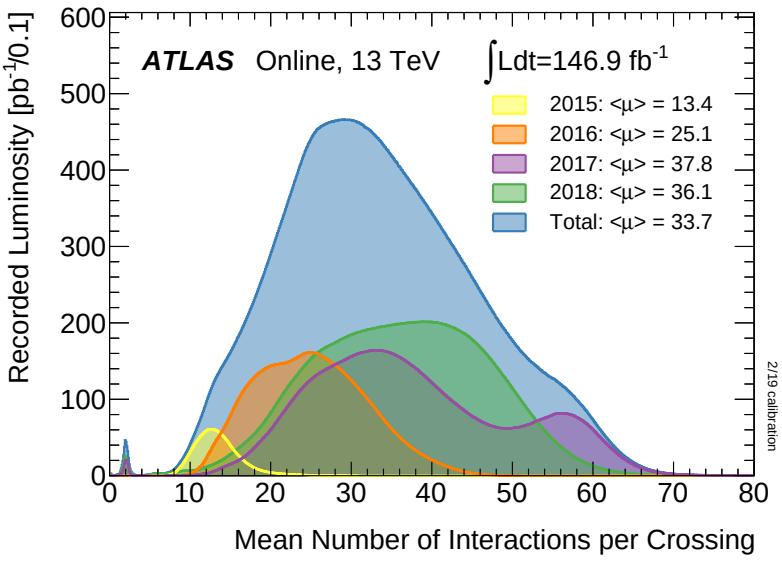

Figure 3.2: Number of Interactions per Crossing [60].

and the actual Data, the correction for pileup is applied to the simulated samples by event reweighting [93]. For the simulation of pile-up events, multiple proton-proton collisions within each bunch crossing are overlaid to each event by Pythia8 [94].

3.3 Monte Carlo Simulated Samples

3.3.1 Background samples

W/Z + jets

Events containing W or Z bosons with associated jets are simulated using the Sherpa 2.2.1 [95] generator. Matrix elements are calculated for up to 2 partons at NLO and 4 partons at LO using the Comix [96] and OpenLoops [97] matrix element generators and merged with the Sherpa parton shower [98] using the ME+PS@NLO prescription [99]. The NNPDF3.0NNLO PDF set with $\alpha_s = 0.118$ is used [100]. The W/Z + jets events are normalized to the next-to-nect-to-leading order (NNLO) cross-sections [101].

$t\bar{t}$ and single-t

The $t\bar{t}$ and single-top events are generated with the Powheg-Box [79] generator with the NNPDF3.0NLO PDF sets in the matrix element calculation. The top quarks are decayed using MadSpin [102] preserving all spin correlations, while for all processes the parton shower, fragmentation, and the underlying event are simulated using Pythia 8 with the A14 tune set [103]. The top mass, m_t, is set to 172.5 GeV. The cross-sections of $t\bar{t}$ and single-top are known to NNLO in QCD including re-summation of next-to-next-to-leading

logarithmic (NNLL) soft gluon terms [104, 105]. The parameter HDAMP to regulate the high-p_T radiation in the POWHEG is set to $1.5m_t$ for a good data/MC agreement at high p_T region [106].

Diboson

The diboson processes (WW, WZ and ZZ) are generated with SHERPA 2.2.1 [95] generator which uses the matrix element at NLO accuracy in QCD for up to one additional parton and at LO accuracy for up to three additional parton emissions. The electroweak production of diboson processes ($WWjj$, $WZjj$ and $ZZjj$) are considered in $\ell\nu qq$ channel and are neglected in $\ell\ell qq$ and $\nu\nu qq$ channel due to the extremely small contributions.

3.3.2 Signal Samples

Signal samples are produced with MADGRAPH5 (MG5) [41] event generator and the PYTHIA 8 parton shower program with NNPDF3.0NNLO PDF set and A14 tune. The RS Graviton samples are generated with $k/\bar{M}_{\text{Planck}} = 1$ and the radion samples are generated with $k\pi r_c$=35 and Λ_R=3 TeV. The HVT model A signal samples are generated with $g_H = -0.56$ and $g_F = -0.55$[1]. Model B interpretation will be performed assuming the same signal shape as the model A because the difference on the width in the model B from A is smaller than the detector resolution. Another set of HVT signal samples is generated in the model C with $g_H = 1$ and $g_F = 0$ for the generation of resonances produced via VBF. Masses of diboson resonances are varied from 300 GeV to 6 TeV for each scenario.

[1] HVT Model A is inspired by weekly coupled extensions of the SM gauge group and it predicts $g_H \sim g_F \sim -g^2$ [107].

Chapter 4

Object Reconstruction and Particle Identification

4.1 Tracks and Vertices

4.1.1 Track Reconstruction

Charged-particles leave energy-deposits when passing through the Inner Detector (ID). Combining the information of the energy-deposits clustered as *hits*, charged-particle trajectories are reconstructed and referred to as *tracks*. The reconstructed tracks give several kinds of information about charged-particle to be used in the physics analysis. There are two tracking strategies [108]; an *inside-out* track reconstruction and an *outside-in* tracking. The former is the main track reconstruction strategy targeting primary charged particles produced in the hard-scatter interaction or originating from decays of short-lived particles, while the later is the complemental procedure designed to reconstruct tracks of decays of long-lived particles or photon conversions where fewer hits are found in the silicon detector. This tracking strategy is decided based on the efficiency and acceptance difference between silicon pixel, SCT and TRT.

Inside-out track reconstruction

The inside-out strategy follows a sequence of modules. First, clusters are defined by a connected component analysis (CCA) [109] which groups pixels and strips with a charge over a given threshold. From these clusters, three-dimensional representations of the silicon detector measurements called space-point are created. In the pixel detector, each cluster provides one space-point, while the SCT needs to combine both sides of a strip layer to obtain a three-dimensional measurement. Energy deposits from multiple particles can contribute to one cluster in a dense environment, where the neighboring charged particles are separated by only a few pixels. In this case, a neural network (NN) clustering algorithm [110] is used to identify the merged clusters created by multiple charged particles. The NN clustering algorithm uses the following information as inputs: a fixed-size matrix of the charge collected in each pixel of the candidate cluster, a fixed-size vector of seven elements with the longitudinal size of the pixels in the matrix to label the long pixels, layer number and layer type (barrel or endcap), the angles of incidence ϕ and θ of the candidate charged particle with respect to the sensor surface, and η of the pixel module (only if no track candidate is available yet). The cluster judged as merged is split into multiple clusters based on the cluster positions obtained from the NN clustering algorithm.

After the space-point creation, the collection of space-point is processed for creating track seeds. Track seeds are composed of sets of three space-points, and there are three types of seed types considered: SCT-only, Pixel-only and mixed-detectors seeds, repreeinting the order of purity. One additional space-point compatible with the investigating seed is required for the improvement of the purity. With the chosen seeds, track candidates are formed by using a combinational Kalman filter [111] in which additional space-points from the remaining layers of the pixel and SCT detectors are checked if compatible with the preliminary trajectory. If more than one compatible space-point exists on the same layer, the filter creates multiple track candidates.

Resulting track candidates are then processed for the ambiguity solving. In the ambiguity solving, a track score [112] is calculated for each track candidate to describe the real trajectories of particles from the underlying physics event. The track score calculation is mainly affected by simple measures of the track quality, which includes the resolution and expected cluster multiplicities in the different subdetectors, the

number of [1]holes and the χ^2 of the track fit. Tracks with bad score or failing certain track criteria are regarded as rejected tracks and not used in further processing. If there is a cluster which is shared between multiple track candidates and not identified as merged by a neural network clustering algorithm, the ambiguity solver assigns the cluster to the track with the highest score and the cluster is removed from the remaining track candidates. The remaining track candidates are then scored again and returned to the list of track candidates in descending order.

Finally, the track extension from the silicon detector into the TRT is performed. If the track is within the TRT acceptance ($|\eta| < 2.0$), measurements in the TRT are used for the track extension and it leads to better momentum resolution.

Outside-in track reconstruction

The inside-out tracking assumes a lot of hits existing in the silicon detector. The outside-in tracking is used when the number of hits in the silicon detector is not enough to create track candidates. It starts with a segment finding in the TRT. Since the TRT consists of straw tubes, three-dimensional space-points cannot be defined. Therefore the r-ϕ plane is used in the barrel region and the z-ϕ plane is used in the end-cap region. The trajectories of charged-particles are extracted by using Hough transformation [113] and then traced back into the silicon detector for reconstructing tracks. The *outside-in* tracking does not refer to hits already used in the *inside-out* track reconstrcution.

4.1.2 Vertex Reconstruction

The position of the inelastic proton-proton collisions are identified by vertex, which is reconstructed by the iterative vertex finding algorithm [114] based on the reconstructed tracks. The vertex with the largest scalar sum of p_{T}^2 of the associated tracks is defined as the primary vertex. The vertex reconstruction consists of vertex finding and vertex fitting. First, a seed position of the first vertex is selected based on tracks which pass the following criteria:

- $p_{\mathrm{T}} > 500$ MeV; $|d_0| < 4$ mm; $\sigma(d_0) < 5$ mm; $\sigma(z_0) < 10$ mm;
- At least four hits in the SCT detector;
- At least nine silicon (SCT or pixel) hits;
- No pixel holes.

Here d_0 and z_0 represent the transverse and longitudinal impact parameter of tracks with respect to the center of the luminous region, and $\sigma(d_0)$ and $\sigma(z_0)$ correspond to the uncertainties, respectively. The track p_{T} threshold is raised from 400 MeV to 500 MeV to reduce average event size on disk during Run 2. The transverse position of the seed is fixed at the position of beam-spot and the longitudinal position is defined by using the z-coordinates of tracks. The beam-spot coordinate is determined by position distribution of vertices reconstructed by the looser definition [115]. The fitting is performed to determine the best position of the vertex. The vertex fitting utilized tracks only compatible with the seed. After the vertex position is determined, tracks that are regarded as not associated with the vertex are removed and to be used in other vertex reconstruction. This procedure is repeated until all of the tracks are assigned to vertices or no additional vertex can be found in the remaining list of tracks.

4.2 Topological cluster

4.2.1 Topo-cluster formation

Three-dimensional topological clustering of individual calorimeter cell provides the way of reconstructing signals from hadrons. The topological cell clusters, called as *topo-cluster*, have shape and location information and is established as a well-performing calorimeter signal definition for jet reconstruction. The creation of topo-cluster follows spatial signal-significance patterns generated by particle showers [116].

The cluster formation is based on the ratio of the cell signal to the average noise in this cell:

$$\zeta_{\mathrm{cell}}^{\mathrm{EM}} = \frac{E_{\mathrm{cell}}^{\mathrm{EM}}}{\sigma_{\mathrm{noise}}^{\mathrm{EM}}}, \tag{4.1}$$

[1]A hole is defined as an expected but missing hit on silicon detectors based on the particle trajectory.

where $E^{\mathrm{EM}}_{\mathrm{cell}}$ is the cell signal and $\sigma^{\mathrm{EM}}_{\mathrm{noise}}$ is the average noise in this cell. Both of them are measured on the electromagnetic (EM) scale, which is calibrated by an electron testbeam for LAr and a ^{137}Cs-based calibration system for Tile calorimeter [117, 118]. Therefore the energy deposited by electrons and photons is reconstructed correctly in the EM scale, while the signal from hadrons are not due to the non-compensating character of the ATLAS calorimeters.

Topo-clusters are formed by a sequence of seeding and collecting steps, called as a growing-volume algorithm [116]. In the seeding algorithm, the three respective signal thresholds S, N, P in terms of $\sigma^{\mathrm{EM}}_{\mathrm{noise,cell}}$ are used to control series of seeding and collection stages:

$$|E^{\mathrm{EM}}_{\mathrm{noise,cell}}| > S\sigma^{\mathrm{EM}}_{\mathrm{noise,cell}} \rightarrow \zeta^{\mathrm{EM}}_{\mathrm{noise,cell}} > S \text{ (primary seed threshold, default S = 4);} \tag{4.2}$$

$$|E^{\mathrm{EM}}_{\mathrm{noise,cell}}| > N\sigma^{\mathrm{EM}}_{\mathrm{noise,cell}} \rightarrow \zeta^{\mathrm{EM}}_{\mathrm{noise,cell}} > N \text{ (threshold for growth control, default N = 2);} \tag{4.3}$$

$$|E^{\mathrm{EM}}_{\mathrm{noise,cell}}| > P\sigma^{\mathrm{EM}}_{\mathrm{noise,cell}} \rightarrow \zeta^{\mathrm{EM}}_{\mathrm{noise,cell}} > P \text{ (principal cell filter, default P = 0).} \tag{4.4}$$

First, all cells with $\zeta^{\mathrm{EM}}_{\mathrm{cell}} > S$ are selected and forms a *proto-cluster*, as shown in Figure 4.1a. The cells neighboring a proto-cluster satisfying $\zeta^{\mathrm{EM}}_{\mathrm{cell}} > N$ and $\zeta^{\mathrm{EM}}_{\mathrm{cell}} > P$ are then merged to the proto-cluster. The cells with $\zeta^{\mathrm{EM}}_{\mathrm{cell}} > S$ and $\zeta^{\mathrm{EM}}_{\mathrm{cell}} > N$ are presented in Figure 4.1b. If a particular neighboring cell is also a seed cell, the two proto-clusters are merged. If a cell is neighboring two different proto-clusters, the two proto-clusters are merged. This procedure is iteratively repeated until the the last set of neighbouring cells satisfying $\zeta^{\mathrm{EM}}_{\mathrm{cell}} > P$, but not the one with $\zeta^{\mathrm{EM}}_{\mathrm{cell}} > N$, is collected. Cells with negative signal are also considered in the clustering procedure to cancel out positive fluctuations originating from pile-up and electronic noise.

Figure 4.1c shows the created topo-clusters. The resulting clusters are calibrated to correct for the difference of energy response between electromagnetic particles (labeled with EM) and hadrons with the local hadronic cell weighting (LCW) scheme (labeled with LCW) [116]. The calibrated clusters are then provided as input to a jet reconstruction algorithm as massless particles. More details of topo-cluster formation, including treatment of negative cells and cluster splitting, can be found at [116].

4.2.2 Topo-cluster kinematics

The created topo-clusters contain a lot of information for signal characterisation. The cluster directions $(\eta_{\mathrm{clus}}, \phi_{\mathrm{clus}})$ are calculated as,

$$\eta_{\mathrm{clus}} = \frac{\sum_{i=1}^{N_{\mathrm{cell}}} w^{\mathrm{geo}}_{\mathrm{cell,i}} \cdot |E^{\mathrm{EM}}_{\mathrm{cell,i}}| \cdot \eta_{\mathrm{cell,i}}}{\sum_{i=1}^{N_{\mathrm{cell}}} w^{\mathrm{geo}}_{\mathrm{cell,i}} \cdot |E^{\mathrm{EM}}_{\mathrm{cell,i}}|}, \tag{4.5}$$

$$\phi_{\mathrm{clus}} = \frac{\sum_{i=1}^{N_{\mathrm{cell}}} w^{\mathrm{geo}}_{\mathrm{cell,i}} \cdot |E^{\mathrm{EM}}_{\mathrm{cell,i}}| \cdot \phi_{\mathrm{cell,i}}}{\sum_{i=1}^{N_{\mathrm{cell}}} w^{\mathrm{geo}}_{\mathrm{cell,i}} \cdot |E^{\mathrm{EM}}_{\mathrm{cell,i}}|}, \tag{4.6}$$

where N_{cell} is the number of cells in the cluster, and $w^{\mathrm{geo}}_{\mathrm{cell,i}}$ are the geometrical signal weights [116]. The cluster directions are reconstructed with respect to the center of the ATLAS detector. Using the cell signals and the geometrical signal weights, the total cluster signal amplitude E^{EM}_{clus} is calculated as

$$E^{EM}_{\mathrm{clus}} = \sum_{i=1}^{N_{\mathrm{cell}}} w^{\mathrm{geo}}_{\mathrm{cell,i}} E^{EM}_{\mathrm{clus,i}}, \tag{4.7}$$

and it reflects the correct signal contribution from all cells. When using these topo-clusters as input to jet reconstruction, they are interpreted as massless pseudo-particle. The energy and momentum can be described as

$$\begin{aligned} P^{EM}_{\mathrm{clus}} =& E^{EM}_{\mathrm{clus}} \cdot (1, \sin\theta_{\mathrm{clus}} \cos\phi_{\mathrm{clus}}, \sin\theta_{\mathrm{clus}} \sin\phi_{\mathrm{clus}}, \cos\theta_{\mathrm{clus}}) \\ =& \left(E^{EM}_{\mathrm{clus}}, \vec{P}^{EM}_{\mathrm{clus}}\right). \end{aligned} \tag{4.8}$$

Here θ_{clus} is the polar angle calculated from $(\eta_{\mathrm{clus}}, \phi_{\mathrm{clus}})$.

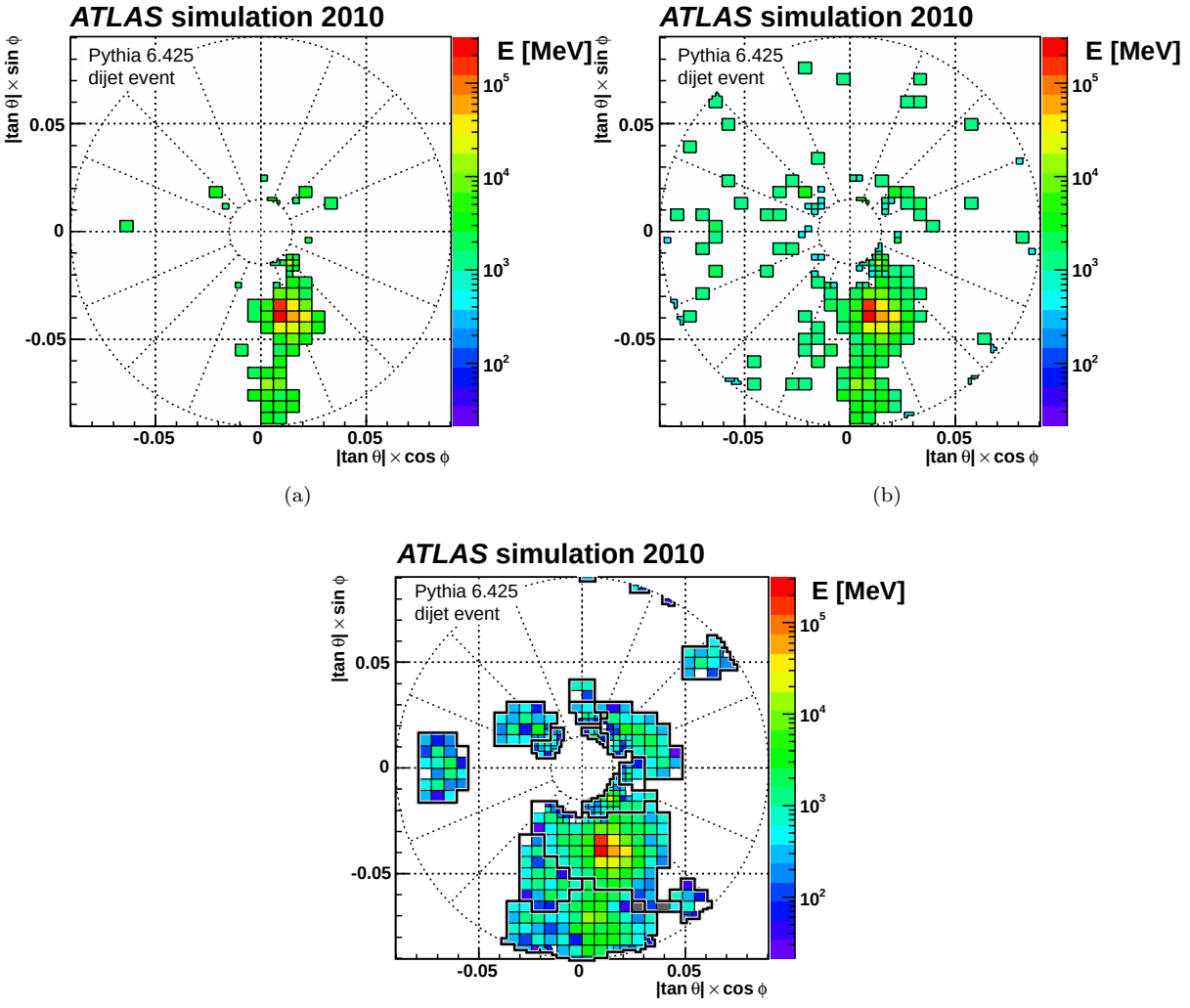

(a) (b)

(c)

Figure 4.1: Created topo-clusters in the first module (FCAL0) of the FCAL calorimeter displayed on a dimensionless grid using the polar angle θ and the azimuthal angle ϕ. Figure 4.1a and 4.1b show cells satisfying $|\mathrm{EM}| > 4$ and $|\mathrm{EM}| > 2$, respectively. All clusterd cells with the outline of topo-clusters are shown in Figure 4.1c. Clusters which do not contain a seed cell from this module are seeded in other modules. Not colored cells inside a topo-cluster correspond to a negative signal, while cells shaded grey are not part of a topo-cluster themselves [116].

4.3 Jets

4.3.1 Jets Reconstruction

Calorimeter jets are formed by performing the anti-k_T algorithm [119] with topological clusters as the input. It iteratively merges the neighboring topo-clusters based on the distance defined as

$$d_{ij} = min\left(p_{\mathrm{T},i}^{-2}, p_{\mathrm{T},j}^{-2}\right)\Delta R_{ij}^2/R^2, \tag{4.9}$$

$$d_{iB} = p_{\mathrm{T},i}^{-2}, \tag{4.10}$$

where $\Delta R_{ij} = \sqrt{\Delta\eta_{ij}^2 + \Delta\phi_{ij}^2}$. $\eta_{i(j)}$, $\phi_{i(j)}$, and $p_{\mathrm{T},i(j)}$ are respectively the pseudo-rapidity, azimuth and transverse momentum of the topo-cluster $i(j)$. R is the radius parameter of the jet to reconstruct. If $d_{ij} < d_{iB}$, a topo-cluster j is merged to a topo-cluster i and is removed from the list of remaining topo-clusters for the jet reconstruction.

In this thesis, small-R jets with $R = 0.4$ and large-R jet with $R = 1.0$ are used to reconstruct $W/Z \to qq$ candidates and the forward jets coming from VBF signal production mode. After the jet reconstruction, the trimming algorithm [120], which reconstructs k_T sub-jets with $R = 0.2$ within a jet and substructs them if their p_{T} fraction is less than 0.05, is applied to large-R jets to reduce the effect of pile-up, initial-state radiation (ISR) and the underlying event. Large-R jets built with only topological clusters are called as *LCTopo* jets. In the case of this analysis, in order to achieve more signal sensitivity at higher mass regions, clusters formed by *TCC algorithm* are used to define large-R jets (*TCC* jets). The more details of TCC jet are discussed in Chapter. 5.

Track jets

Track jet is reconstructed from charged-particle tracks reconstructed in the inner detector (ID). The same jet reconstruction procedure is applied to tracks to reconstruct track jets. In this thesis, the variable-radius (VR) track jet [121] is used to identify b-quark-induced jets. VR track jets adopt p_{T} dependent cone size defined as:

$$R_{\mathrm{eff}}(p_{\mathrm{T},i}) = \frac{\rho}{p_{\mathrm{T},i}} \tag{4.11}$$

for building track-jets with anti-kt algorithm. $\rho = 30$ GeV and upper and lower limit of cone size are set to $R_{\mathrm{max}} = 0.4$ and $R_{\mathrm{min}} = 0.02$. Collinear VR track jets are possible, however their interplay with the track-association for b-tagging is not ensured. Therefore, events are removed if they have a pair of VR track jets i,j which satisfies the following requirement,

$$\Delta R_{ij} < \min\left(R_{\mathrm{eff},i}, R_{\mathrm{eff},j}\right), \tag{4.12}$$

where the indices i, j run on all VR track jets with $p_{\mathrm{T}} > 5$ GeV and number of track > 1. The jets satisfying $p_{\mathrm{T}} > 10\,\mathrm{GeV}$ and $|\eta| < 2.5$ are considered in this analysis.

Jet substructure variable

For large-R jets, the window cut on the reconstructed jet mass is one of the strongest discriminant since jets from $W/Z \to qq$ signals have peaks around W/Z-boson masses. In addition to that, the jet substructure variable D_2 is used to separate $W/Z \to qq$ jets and background QCD jets. Figure 4.2 shows skematic view of 1-prong (background QCD) and 2-prong ($W/Z \to qq$) jets. Jets originating from $W/Z \to qq$ jet tend to have two localized energy distributions, while background QCD jets seems to have 1-prong jet substructure. From this, different energy distribution is expected and the D_2 is defined so that the jet substructure can be quantified.

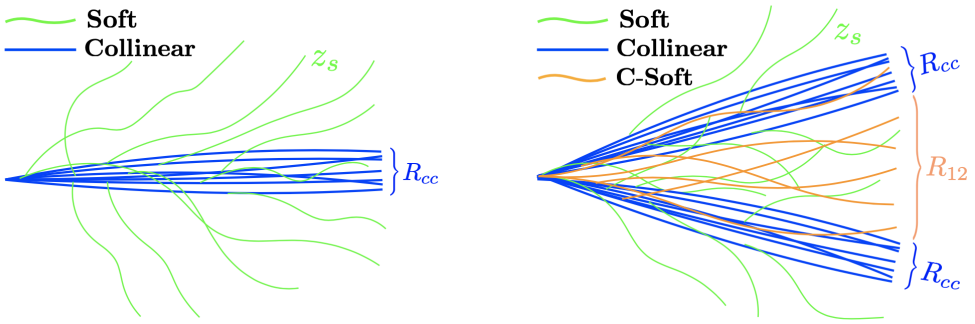

Figure 4.2: (Left) 1-prong background QCD jet, dominated by collinear (blue) and soft (green) radiation. (Right) 2-prong $W/Z \to qq$ jet resolved into two subjets, dominated by collinear (blue), soft (green), and collinear-soft (orange) radiation emitted from the two subjets [122].

The D_2 is reconstructed by the energy correlation functions based on energies and pair-wise angles of the sub-constituents [122–124]. The energy correlation functions are defined as:

$$e_2^{\beta=1} = \frac{1}{p_{\mathrm{T},J}} \sum_{ij} p_{\mathrm{T},i} p_{\mathrm{T},j} \Delta R_{ij}, \tag{4.13}$$

$$e_3^{\beta=1} = \frac{1}{p_{\mathrm{T},J}} \sum_{ijk} p_{\mathrm{T},i} p_{\mathrm{T},j} p_{\mathrm{T},k} \Delta R_{ij} \Delta R_{jk} \Delta R_{ki}. \tag{4.14}$$

Here the summation runs over the jet constituents e.g. topo-clusters for the usual small (large)-R jets, and $p_{\mathrm{T},J} = \sum_i p_{\mathrm{T},i}$. The behavior of the energy correlation function depends on soft and collinear QCD contributions. Exploring the impact of each contribution, we can see the 1- and 2-prong jets can be separated by the boundary $e_3^{\beta=1} \sim (e_2^{\beta=1})^3$ [122] as shown in Figure 4.3, and therefore the D_2 is defined as

$$D_2^{(\beta=1)} = e_3^{\beta=1} / (e_2^{\beta=1})^3. \tag{4.15}$$

The jet mass window cut and D_2 cut are applied to large-R jets to extract jets from $W/Z \to qq$ signals in this analysis.

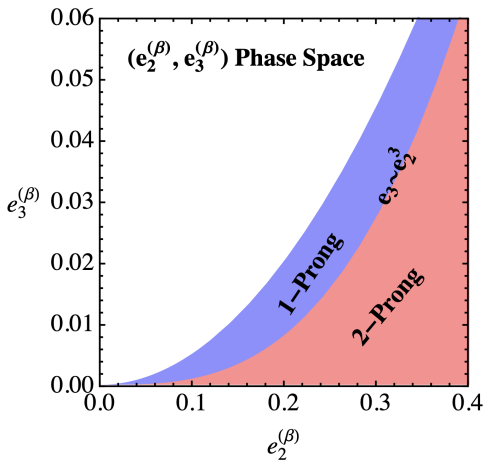

Figure 4.3: Phase space defined by the measurement of the energy correlation functions $e_2^{\beta=1}$ and $e_3^{\beta=1}$. The phase space is divided into 1- and 2-prong regions with a boundary corresponding to the curve $e_3^{\beta=1} \sim (e_2^{\beta=1})^3$ which is explored based on the power counting method [122].

4.3.2 Calibration

The jet is calibrated in several steps [125]. The effects of pile-up on jet calibration is reduced by an area-based subtraction method [126], which utilizes the average energy density in the $\eta \times \phi$ plane. The jet energy scale (JES) calibration is applied to correct the reconstructed jet energy to the particle jet energy [127]. The scale factors are derived from isolated jets in inclusive dijet events which are selected by requring back-to-back two jets passing the jet trigger. A correction in η is also applied to resolve the bias made by the energy scale calibration. Dependence of the jet energy scale on longitudinal and transverse features of the jet is corrected sequentially by the global sequential corrections [128]. Finally, the in situ corrections are applied to account for differences between data and MC in the jet p_{T} measurements, using γ/Z+jet and multijet balance [129].

Small-R jets

A series of calibration procedures are applied to small-R jets to restore the JES to that of particle jets (referred to as "*truth jets*") for compensating effects which are not fully described by topo-cluster level calibration. The JES calibration comprises of the following steps: origin correction, jet area-based pile-up correction, residual pile-up correction, absolute MC-based calibration, global sequential calibration, residual *In situ* calibration.

First, the four-momentum of jets are corrected by the origin correction so that jets point to the hard-scatter primary vertex instead of the center of the detector, without affecting the jet energy constant. The η resolution of jets is improved by this correction.

The origin correction is followed by the two pile-up corrections to address the energy contamination from both in-time and out-time pile-up: jet area-based pile-up correction, residual pile-up correction. The area-based pile-up correction [130] is applied to remove the per-event pile-up contribution to the p_{T} of each jet according to its area. This correction is based on the median p_{T} density ρ of jets in the η-ϕ plane, which is calculated by all jets reconstructed from topo-clusters using the k_T algorithm with radius parameter $R = 0.4$, and the jet area A. Since the p_{T} density, taken to be ρ/A, does not fully describe the pile-up, the corrected jet p_{T} still shows some pile-up dependence on N_{PV}, the number of reconstructed primary vertices (PV), and μ, the average number of interactions per bunch crossing. Therefore a residual pile-up correction is introduced additionally. In the second pile-up correction, the residual p_{T} dependence is measured as the difference between the reconstructed jet p_{T} and truth jet p_{T}. The residual p_{T} dependence on N_{PV} and μ is found to be reasonably linear and independent of one another. The pile-up corretion can be descirbed as:

$$p_{\mathrm{T}}^{\mathrm{corr}} = p_{\mathrm{T}}^{\mathrm{recp}} - \rho \cdot A - \alpha \cdot (N_{\mathrm{PV}} - 1) - \beta \cdot \mu, \tag{4.16}$$

where α and β denotes coefficients of linear fits for N_{PV} and μ dependency.

Next, the absolute MC-based calibration corrects the reconstructed jet four-momentum to the particle-level energy scale and accounts for biases in the jet η reconstruction. The correction is based on the inverse of the average energy response $\mathcal{R} = \langle E_{\mathrm{jet}}/E_{\mathrm{truth}} \rangle$ as a function of the reconstructed jet η_{reco} and the truth jet energy E_{truth}, and the average difference between the true η^{truth} and the origin-corrected jet η^{reco} in bins of the detector η and E_{truth}, respectively. The energy response is derived from the simulated di-jet events from PYTHIA.

After the previous jet calibrations, a remaining dependence of the JES on longitudinal and transverse features of the jet, mainly coming from fluctuations in the jet particle composition and the distribution of energy within the jet (e.g. quark- and gluon-induced jets), are observed. The resolution of JES is further improved by the global sequential calibration (GSC) [131] utilizing five observables from the calorimeter and muon spectrometer (MS), and the inner detector (ID). For each of five observable, jet four-momentum is corrected by the inverted energy response as a function of $p_{\mathrm{T}}^{\mathrm{truth}}$ and $|\eta_{\mathrm{reco}}|$, following the procedure of the absolute MC-based calibration. The dependence of the jet response on each observable is removed while keeping the overall energy scale at the EM + JES. Corrections for each observable are applied independently since no improvement was observed from including such correlations or altering the sequence of the corrections.

Finally, residual *In situ* calibration is applied to account for differences in the jet response between data and MC simulation. It consists of two calibration steps: the η-intercalibration, three other in-situ calibrations [132]. Both calibrations rely on the difference of a probe jet response against other reference objects. The η-intercalibration corrects the jet energy scale of forward jets to that of well-measured central jets using dijet events. In three other in situ calibrations, the average response of central jets is corrected by those of well-measured reference objects. Due to the limitation of statistics, it uses Z boson from Z + jets, photon from γ+jets, and multijet systems depending on a targeting jet p_{T} range for the calibration. The combined data-to-simulation ratio of the in-situ response as function of the jet p_{T} is shown in Figure 4.4. The derived factors are applied to data.

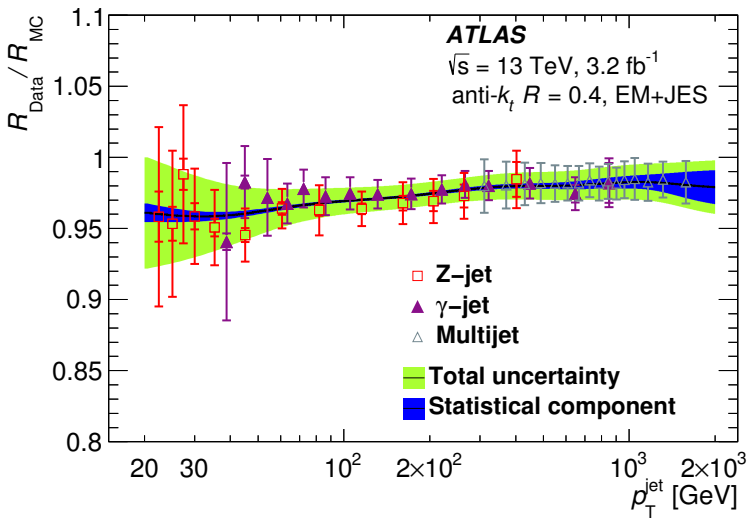

Figure 4.4: Ratio of the EM+JES jet response in data to that in the nominal MC event generator as a function of jet p_{T} for Z-jet, γ-jet, and multijet in situ calibrations [132].

Large-R jets

In the case of standard large-R jets (*LCTopo* jets), only the absolute MC-based calibration is applied to correct their average reconstructed calorimeter jet energy scale and η to those of the truth jet. Since the motivation of using large-R in this analysis is to reconstruct the jet mass accurately and precisely for high-p_{T} region, the jet mass calibration is added as a last step where the correction is derived based on the MC simulation of dijet events, as well as the jet energy correction [133]. The derived correction factor is parametrized in jet p_{T}, η, and mass, and applied according to variables of the jet..

The MC-based calibration is followed by *In situ* calibration based on the jet p_{T} balance techniques using Z boson, photon, and multijet systems depending on a targeting jet p_{T} range, as well as the case of small-R jets. *In situ* mass calibration uses the calorimeter-to-tracker response double-ratio method, referred to as R_{trk} method [129], which relies on the tracker for providing an independent measurement of the jet mass scale and its associated uncertainty. The measurement is performed after applying the in situ energy calibration since it changes the jet mass scale.

However, only R_{trk} method is applied to consider p_{T} scale uncertainty for TCC jets and *In situ* calibration is not included. Since D_2 and mass of TCC jets are used in this analysis we need to estimate D_2 and mass scale uncertainties. The evaluation of these uncertainties are discussed in Chapter. 5.

4.3.3 Pile-up Jet Tagging and Suppression

To separate hard-scatter and pile-up jets, the *Jet Vertex Tagger* (JVT) algorithm [134] which utilizes the vertex information is applied to small-R jets. The JVT is defined as output of a two-dimensional likelihood which is based on the corrected *Jet Vertex Fraction* (corrJVF) and $R_{p_{\mathrm{T}}}$. The $R_{p_{\mathrm{T}}}$ is designed to describe the charged energy fraction in the jet, and defined as:

$$R_{p_{\mathrm{T}}} = \frac{\sum_k p_{\mathrm{T}}^{\mathrm{trk_k}}(\mathrm{PV}_0)}{p_{\mathrm{T}}^{\mathrm{jet}}}, \tag{4.17}$$

where PV_0 denotes the hard-scatter vetex. The corrJVF is the modified version of JVF, which is originally defined as:

$$\mathrm{JVF} = \frac{\sum_k p_{\mathrm{T}}^{\mathrm{trk_k}}(\mathrm{PV}_0)}{\sum_l p_{\mathrm{T}}^{\mathrm{trk_l}}(\mathrm{PV}_0) + \sum p_{\mathrm{T}}(\mathrm{PV})}, \tag{4.18}$$

This variable is defined as the ratio of the scalar sum of the p_{T} of all tracks associated with PV_0 and the sum of the p_{T} of all matched tracks originating from any vertex, and used in Run1 analysis to mitigate pile-up jet contamination. The problem of the original JVF is that its discriminant power shows the pile-up dependency due to $\sum p_{\mathrm{T}}(\mathrm{PV})$ term in the denominator. To reduce this dependency, the corrJVF is defined

with $\sum p_{\mathrm{T}}(\mathrm{PV})$ devided by the total number of pile-up tracks per event $n_{\mathrm{trk}}^{\mathrm{PV}}$:

$$\mathrm{corrJVF} = \frac{\sum_k p_{\mathrm{T}}^{\mathrm{trk_k}}(\mathrm{PV}_0)}{\sum_l p_{\mathrm{T}}^{\mathrm{trk_l}}(\mathrm{PV}_0) + \sum p_{\mathrm{T}}(\mathrm{PV})/(\kappa \cdot \mathrm{n}_{\mathrm{trk}}^{\mathrm{PV}})}. \tag{4.19}$$

Here $\kappa = 0.01$ is the scaling factor determined by correlation with $\sum p_{\mathrm{T}}(\mathrm{PV})$ and $n_{\mathrm{trk}}^{\mathrm{PV}}$.

For this thesis,

- JVT > 0.59 for $p_{\mathrm{T}} < 120$ GeV and $|\eta| < 2.4$
- JVT > 0.11 for $p_{\mathrm{T}} < 120$ GeV and $2.4 < |\eta| < 2.5$

are applied to small-R jets for suppressing the pile-up jets.

4.3.4 Jet selection

Small-R jets are used to reconstruct $W/Z \to qq$ candidates resulting well separated *Signal* jets, and to select the forward jets coming from vector-boson fusion *VBF* jets. Large-R jet is used to reconstruct high-p_{T} $W/Z \to qq$ candidates. The variable-radius (VR) track jet [121] is used to identify b-quark-induced jets in the merged analysis. Selection criteria of Small-R jet, Large-R jet and VR track jet are summarized in Table 4.1–4.3.

Table 4.1: Summary of small-R jet selection and calibration

Jet reconstruction parameters		
Parameter	Value	
algorithm	anti-k$_{\mathrm{T}}$	
R-parameter	0.4	
input constituent	Topological-cluster calibrated with EM scale	
Selection requirements		
	Signal jet	VBF jet
Observable	Requirement	
p_{T}	>30 GeV	
$\lvert\eta\rvert$	<2.5	< 4.5
JVT	> 0.59 for p_{T} <120 GeV and $\lvert\eta\rvert < 2.4$ > 0.11 for p_{T} <120 GeV and $2.4 < \lvert\eta\rvert < 2.5$ (Medium working point)	

Table 4.2: Summary of large-R jet selection and calibration

Jet reconstruction parameters	
Parameter	Value
algorithm	anti-k$_T$
R-parameter	1.0
input constituent	TrackCaloCluster
Selection requirements	
Observable	Requirement
p_{T}	>200 GeV
$\lvert\eta\rvert$	<2.0
mass	> 50 GeV
SmoothedWZTagger	
Object	Working point
W/Z-boson tagger	Significance-based working point (See Section.5)

Table 4.3: Summary of VR track jet selection. No calibration is available for VR track jets.

Jet reconstruction parameters	
Parameter	Value
algorithm	anti-k$_T$
R-parameter	max(0.02, min(0.4, 30/(jet p_T [GeV])))
input constituent	ID TrackParticles
Observable	**Requirement**
p_T	>10 GeV
$\|\eta\|$	<2.5

4.3.5 Flavor tagging

Since the decay length of a b-quark reaches up to several millimetres ($c\tau \sim 450$ μm), it results in a displacement of the decay products with respect to the primary vertex. Combining the information of the displaced vertex (secondary vertex) and the displaced tracks, b-tagging algorithm can identify b-jets with a good degree of accuracy [135]. The MV2 algorithm, which consists of a boosted decision tree (BDT), is the default b-tagging algorithm. It is trained with 24 input variables obtained from several algorithms including IP3D, SV and JetFitter, discussed below.

Impact parameter-based Algorithm: IP2D, IP3D

The IP2D and IP3D algorithms [135] is based on a likelihood ratio using impact parameter information of tracks associated with the jet. IP3D relies on the transverse impact parameter d_0, its error $\sigma(d_0)$, and longitudinal impact parameter z_0, while IP2D does not use longitudinal information. Probability distribution functions (PDF) for b- and light-flavor jets are obtained from Monte Carlo simulated samples.

Secondary vertex-based Algorithm: SV

The SV algorithm [135] is designed to reconstruct the secondary vertex (SV) from tracks associated with the jet. The algorithm starts with forming two-track pairs built from tracks associated with the jet and far enough from the primary vertex. Vertices that are judged as originating from the decays of other long-lived particles such as K_s or Λ, photon conversions or hadronic interaction with material are rejected. Remaining two-track vertices are required to pass the set of qualification. Then a single secondary vertex is build from all tracks from the vertices, based on χ^2 fit.

Decay chain reconstruction: JetFitter

The JetFitter [136] algorithm exploits the topological structure of weak b- and c-hadron decays inside the jet. It assumes the primary vertex and the b- and c-hadrons lie on a common line and the line is found by a Kalman filter, as well as their position on the line with the PV approximating the b-hadron flight direction.

Multivariate Algorithm: MV2

The MV2 use input variavles obtained from several flavor tagging algorithm discussed above. The full list of input variables can be found at [135]. The MV2c10 is a discriminant which is trained with b-jets as signal and a mixture of of 90% light-flavor jet and 10% c-jets as background.

Jet flavour tagging selection

Two different jet collections are used for b-tagging. The small-R jets ("signal" jet in Table 4.1) are used in the resolved category. The VR track jets are used in the merged category. The efficiency working point showing the best sensitivity to our benchmark signals is used in each category. Jets originating from b quark are called "b-jets" regardless of tagged or not, and those selected by b-tagging algorithm are "b-tagged jets".

4.4 Leptons

4.4.1 Electrons

Reconstruction

The reconstruction of electron candidates is performed by matching localized clusters of energy deposits in the electromagnetic calorimeter and charged-particle tracks reconstructed in the inner detector (ID). Electromagnetic-energy (EM) clusters are formed by a *sliding-window* algorithm [137]. First, a fixed-size of window corresponding to 3×7 in units of $\Delta\eta \times \Delta\phi = 0.075 \times 0.175$ (5×5 in units of $\Delta\eta \times \Delta\phi = 0.125 \times 0.125$ for endcaps) is slided over the detector to search for electron cluster "seeds", which is identified as *longitudinal towers* [2] with total cluster energy within the window greater than 2.5 GeV. Given a set of the cluster "seeds", EM clusters are formed around them using a clustering algorithm [138]

The reconstructed EM clusters are then matched to tracks extrapolated from the ID to the middle EM layer, using the distance in $\eta - \phi$ plane. In order to account for energy loss of charged particle in material, a fitting procedure with an optimized *Gaussian-sum filter* (GSF) [139] is applied to reconstructed tracks which have at least four silicon hits and that are loosely matched to EM clusters. The EM cluster that is associated with the reconstructed track is considered as the electron. A schematic illustration of the path of an electron through the detector is shown in Figure 4.5.

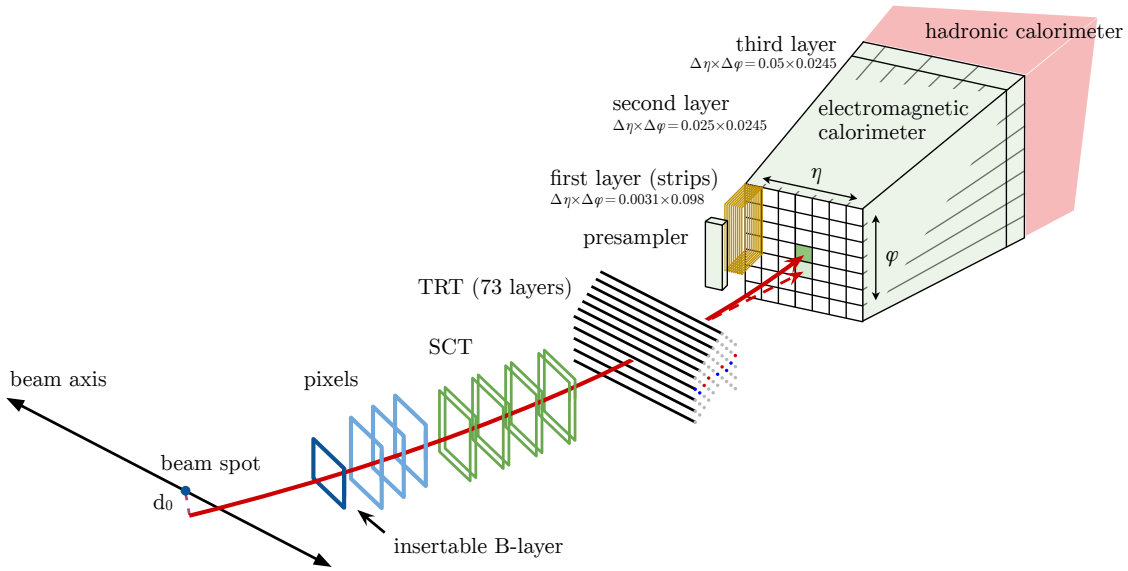

Figure 4.5: A schematic illustration of the path of an electron through the detector. The hypothetical path of an electron is shown with the red trajectory. A photon, depicted with the dashed red trajectory, is produced by the interaction of the electron with the material in the tracking system [140].

If more than a track matches the cluster, the track considered to be the primary electron track is selected, based on the distance in η and ϕ from the cluster, the number of hits in the silicon detectors, and the number of hits in the innermost silicon layer. If the selected track matches to a secondary vertex and has no pixel hits, then the object is classified as a photon.

Identification

A fraction of electron candidates originate from hadronic jets or converted photon and they are referred to as *fake*. To reject them and select prompt electrons effectively, a likelihood-based (LH) identification is applied similarly to the electron LH identification [141, 142]. The LH utilizes a set of measurements from the tracking system and the calorimeter system such as hadronic leakage, energy deposits in EM calorimeter, TRT high threshold hits and track-cluster mathcing [142]. For each electron candidate, a discriminant d_L is formed as:

$$d_L = \frac{L_S}{L_S + L_B}. \tag{4.20}$$

[2] every cell within across all EM-calorimeter layers

The electron LH, $L_{S(B)}$, is defined as

$$L_{S(B)}(\boldsymbol{x}) = \prod_{i=1}^{n} P_{S(B),i}(x_i), \tag{4.21}$$

where the $\boldsymbol{x}$ is the vector of input variables. $P_{S,i}(x_i)$ is the signal probability distribution function (PDF) for qunatity i at value x_i and $P_{B,i}(x_i)$ is the background (e.g. hadronic jets or converted photons) PDF. The PDFs of both signal and background are modeled using the simulated events of $Z \to ee$ and dijet respectively. In order to account for inaccuracies in the detector description and the modelling of the shower shapes, some corrections derived from data are applied to the input variables in the MC simulation. The discriminant of the electron LH identification, d_L, determines if an electron candidate is accepted. Based on d_L, the LH-identification operating points, referred to as *Loose*, *Medium* and *Tight*, are defined [142]. The operating points provide the vaious prompt-electron signal efficiencies and background rejection factors. For instance, the identification efficiencies for a signal (background) electron with E_T = 40 GeVare 95(0.4)%, 93(0.2)%, and 83(0.1)% for the *Loose*, *Medium*, and *Tight* operating points, respectively.

Isolation

Electron candidates ogiriginate from the prompt electrons in signal processes such as the decay of W and Z, or from background processes such as semileptonic decay of heavy quarks, hadrons misidentified as leptons and photons. Since the characteristic signature of the prompt electron is represented by a smaller activity in their surroundings, isolation from other objects would be important variable.

Two kinds of isolation variables are considered [140]. The calorimeter-based isolation, $E_T^{\text{cone0.2}}$, is defined as the energies of all topological clusters within the cone size of $\Delta R = 0.2$ around the candidate electron. The energy deposited by the electron candidate itself is substracted by removing cells in a rectangular cluster size $\Delta\eta \times \Delta\phi = 0.125 \times 0.175$ around it. The energy leakage from the electron candidate outside this fixed rectangular area and the contributions from pile-up are corrected.

The track-based isolation, $p_{\text{T}}^{\text{varcone0.2}}$, is defined as the sum of the transverse momenta of the tracks found within a cone size of $\Delta R = \min\left(10\ \text{GeV}/\text{p}_{\text{T}}\ [\text{GeV}], \text{R}_{\text{max}} = 0.2\right)$ aligned with the electron track. Tracks are required to have p_{T} >1 GeV and to satisfy loose vertex association qualification defined in Section 4.1.2. The candidate's track is excluded as well as the calorimeter-based isolation. Some requirements on the number of hits and the longitudinal impact parameter are applied to achieve better isolation performance.

As in the case of the electron identification, several operating points are set for the electron isolation [142]. In this analysis two operating points are used:

- *FCLoose*: $E_T^{\text{cone0.2}}/p_{\text{T}}^{\text{electron}} < 0.2$ and $p_{\text{T}}^{\text{varcone0.2}}/p_{\text{T}}^{\text{electron}} < 0.15$.
- *FixedCutHighPtCaloOnly*: $E_T^{\text{cone0.2}} < \max(0.015 \times p_{\text{T}}^{\text{electron}},\ 3.5\ \text{GeV})$.

The efficiencies of the various operation points have been measured by the tag-and-probe method using $Z \to \ell\ell$ candidates. Figures 4.6 shows the electron isolation efficiencies for the operation points as a function of the probe lepton p_{T} using ggF Narrow width assumption (NWA) Higgs signal with 3 TeV. *LooseTrackOnly* and *TightTrackOnly* seems to have a comparable behavior and in the low p_{T} region *FixedCutTightTrackOnly* has lower efficiency than *LooseTrackOnly* isolation point. However these operation opints are no longer supported by Isolation and Fake Forum (IFF) group of ATLAS experiment. For 3 TeV signal, the efficiencies of *FCLoose* are extremely low due to the smaller angular separation of the calo-cluster information. Therefore we decided to apply *FCLoose* isolation to only electons with $p_{\text{T}} < 100$ GeV for the sake of the high p_{T} electron efficiency. The number of background events is not increased even if we do not require any isolation cuts at $p_{\text{T}} > 100$ GeV.

Calibration

The energy calibration of electron is performed by two kinds of methods: a Monte Carlo based calibration and In-situ corrections. A Monte Carlo based calibration [143] corrects the cluster energy to the truth electron energy based on multivariate analysis (BDT). The BDT uses the following observables as input variables: uncalibrated energy, the ratio of the energies in the first two layers of the caloirmeter, the cluster barycenter in η, and the cluster barycenter inη and ϕ in the calorimeter frame.

An in-situ correction [143] is then applied to remove residual mis-modeling in the energy scale and resolution. The energy miscalibration is parametrized by the electron energies in data and simulation, with the deviation from optimal calibration in a given η region labeled i. The relative energy resolution is parametrized

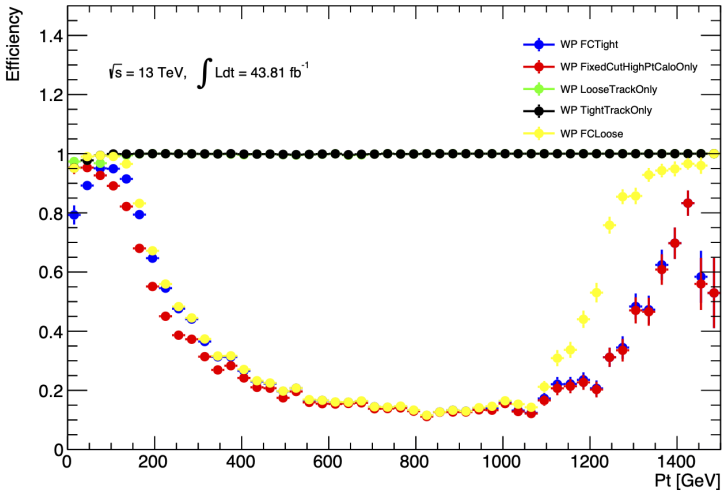

Figure 4.6: Electron isolation efficiencies for the various WPs as a function of the probe lepton pT using ggF NWA Higgs with m = 3 TeV samples.

by the sampling term related to shower fluctuations in the calorimeter and modeled by simulation, the electronic noise term measured in calibration runs.

Electron selection

Two types of electron definition [141] are used in this analysis according to the number of charged-lepton. In 2-lepton channel, *Loose* electron is used to select $Z \to e^+e^-$ candidate. In 1-lepton channel, *Tight* electron is used to select $W \to e\nu$ candidate and *Loose* electron is used to veto events with additional leptons. In 0-lepton channel, *Loose* electron is used to veto events with leptons. The looser isolation working point [142] based on the ID track variable only is preferable to keep high signal efficiency at the very high-p_{T} region, where two electron candidates are closed by each other. The definitions of the *Tight* and *Loose* electrons are summarized in Table 4.4.

Table 4.4: Summary of electron selection

Definition	*Loose*	*Tight*
Pseudorapidity range	$\lvert\eta\rvert < 2.47$	
Transverse momentum	$p_{\mathrm{T}} > 7\,\mathrm{GeV}$	> 30 GeV
Track to vertex association	$\lvert d_0(\sigma)\rvert < 5$	
	$\lvert\Delta z_0 \sin\theta\rvert < 0.5$ mm	
Identification	Loose	Tight
Isolation	FCLoose at $p_{\mathrm{T}} < 100\,\mathrm{GeV}$ and no isolation requirement at $> 100\,\mathrm{GeV}$	FixedCutHighPtCaloOnly

Efficiency correction

The efficiency of the electron reconstruction, identification, and isolation in simulated events can be different than in data. These kinds of differences are corrected by applying the scale factors derived from $Z \to ee$ and $J/\psi \to ee$ events to the simulated events. The scale factors are defined as the ratio of the efficiency in data to the efficiency in simulated event. Usually, the scale factors are functions of the electron kinematics, such as p_{T} and η [141].

4.4.2 Muons

Reconstruction

Both the inner detector (ID) and the muon spectromter (MS) provide measurements for muon reconstruction [144]. The track reconstruction algorithm in the ID is same as the one described in 4.1.1. In the MS, muon reconstruction first searches for hits inside each muon chamber. Then, muon track candidates are built by fitting hits found in each MS sub-detector. The fit starts with the segments generated in the middle layers of the detector where more hits can be expected. For the segments, criteria based on hit multiplicity and fit quality are required.

Based on the information provided by the ID and the MS, four muon types are defined in following order.

- Combined (CB) muons: the combined track is created by a global fit with tracks reconstructed in the ID and the MS. An outside-in pattern recognition in which muons are first reconstructed in the MS and then extrapolated to an ID track, is applied. An inside-out recognition is performed as a complementary approach for better reconstruction efficiency.
- Segment-tagged (ST) muons: If an extrapolation from track in the ID matches at least one local track segment in the MDT or CSC chambers, the track is identified as the muon.
- Calorimeter-tagged (CT) muons: A track in the ID is classified as a muon if it is matched to an energy deposit in the calorimeter compatible with a minimum-ionizing particle.
- Extrapolated (ME) muons: the muon trajectory is reconstructed based only on the MS track. ME muons are aimed to extend the acceptance for muon reconstruction into the region $2.5 < |\eta| < 2.7$, which is not covered by the ID.

About 90% of muons are reconstructed as CB.

Identification

Quality requirements are required to improve the purity of reconstructed muons. For CB tracks, the following variables are used:

- q/p significance: the difference between the charge-to-momentum ratios of the muons measured in the ID and MS.
- ρ': the difference between the transverse momentum measurements in the ID and MS divided by the p_{T} of the combined track.
- Reduced χ^2 of the combined track fit

Muon tracks are required to have at least one pixel hit, at least five SCT hits and fewer than three pixel or SCT holes. According to these variables, several identification working points are defined. In this thesis, the following identification working points are used.

- *Medium*: Only CB and ME tracks are used. CB tracks are required to have ≥ 3 hits in at least two MDT layers, except for tracks in the $|\eta| < 0.1$. ME tracks need to have at least three MDT/CSC layers, and are used only in $2.5 < |\eta| < 2.7$. To remove the fake muons from hadrons, a loose requirement on the compatibility between ID and MS measurements is imposed. The q/g significance is required to less than seven.
- *Loose*: All muon types are used. CT and ST muons are restricted to the $|\eta| < 0.1$ region. All *Medium* muons are included by definition.

More details of the working points and their efficiency measurements can be found in [144].

Isolation

Both calorimeter-based and track-based isolation variables are used to select muons produced from the decay of heavy particles, as well as an electron. The calorimeter-based isolation, $E_{\mathrm{T}}^{\mathrm{cone0.2}}$, is defined as the energies of all topological clusters within the cone size of $\Delta R = 0.2$ around the candidate muon. The track-based isolation, $p_{\mathrm{T}}^{\mathrm{varcone0.3}}$, is defined as the sum of the transverse momenta of the tracks found within a cone size of $\Delta R = \min\left(10\ \mathrm{GeV}/\mathrm{p_T}\ [\mathrm{GeV}], \mathrm{R_{max}} = 0.3\right)$ aligned with the muon. Tracks are required to have $p_{\mathrm{T}} >1$

GeV and to satisfy loose vertex association qualification. Contributions from pile-up and the underlying event are corrected based on the ambient energy-density technique [130].

As in the case of the electron, several operating points are also set for the muon isolation [142]. In this analysis two operating points are used:

- *FCLoose*: $E_T^{\text{cone0.2}}/p_{\text{T}}^{\mu} < 0.3$ and $p_{\text{T}}^{\text{varcone0.3}}/p_{\text{T}}^{\mu} < 0.15$.
- *FixedCutTightTrackOnly*: $p_{\text{T}}^{\text{varcone0.3}}/p_{\text{T}}^{\mu} < 0.06$.

Figures 4.7 shows the muon isolation efficiencies for the operation points as a function of the probe lepton p_{T} using ggF NWA Higgs signal with 3 TeV. In contrast to the electron isolation, the efficiency of *FCLoose* does not decrease at high p_{T} region. However, *FCLoose* isolation is applied to only muons with $p_{\text{T}} < 100$ GeV for the sake of the high p_{T} muon efficiency and the harmonization of lepton isolation between electrons and muons.

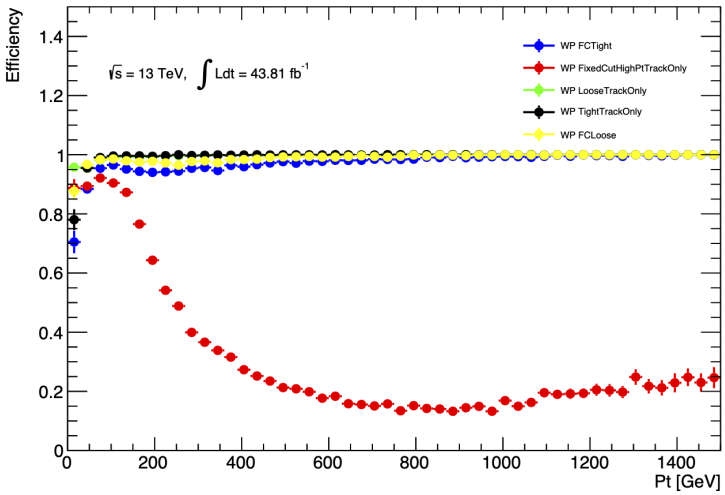

Figure 4.7: Muon isolation efficiencies for the various WPs as a function of the probe lepton pT using ggF NWA Higgs with m = 3 TeV samples.

Calibration

The muon momentum calibration is applied to correct mis-modeling coming from the imperfect understanding of the magnetic field inside the detector. Using the formula in Ref [145], the muon transverse momentum is corrected as:

$$p_{\text{T}}^{\text{Cor,Det}} = \frac{p_{\text{T}}^{\text{MC,Det}} + \sum_{n=0}^{1} s_n^{\text{Det}}(\eta,\phi)(p_{\text{T}}^{\text{MC,Det}})^n}{1 + \sum_{m=0}^{2} \Delta r_m^{\text{Det}}(\eta,\phi)(p_{\text{T}}^{\text{MC,Det}})^{m-1} g_m}, \tag{4.22}$$

where g_{m} is normally distributed random variables ranging from 0 to 1, and $p_{\text{T}}^{\text{MC,Det}}$ and $p_{\text{T}}^{\text{Cor,Det}}$ are the muon transverse momenta before and after the correction. The terms $\Delta r_m^{\text{Det}}(\eta,\phi)$ and $s_n^{\text{Det}}(\eta,\phi)$ describe the momentum resolution smearing and the scale corrections, respectively. The resolution and scale correction coefficients are obtained by a template fit on $J/\psi \to \mu\mu$ and $Z \to \mu\mu$ events. The correction is applied in η-ϕ regions. Knowledge of the magnetic field is reflected in the $s_n^{\text{Det}}(\eta,\phi)$.

Muon selection

Two types of muon definition are used in this analysis. In 2-lepton channel, *Loose* muon is used to select $Z \to \mu^+\mu^-$ candidate. In 1-lepton channel, *Tight* muon is used to select $W \to \mu\nu$ candidate, and *Loose* muon is used to veto events with additional leptons, as well as electrons. In 0-lepton channel, *Loose* muon is used to veto events with leptons, as well as electrons. Looser working points are chosen to keep high signal efficiency at the very high-p_{T} region, where two muon candidates are closed by each other. The definitions of the Tight and Loose muons are summarized in Table 4.5.

Table 4.5: Summary of muon selections

Criteria	*Loose*	*Tight*
Pseudorapidity range	$\lvert\eta\rvert < 2.5$	
Transverse momentum	$p_{\mathrm{T}} > 7$ GeV	$p_{\mathrm{T}} > 30$ GeV
d_0 Significance Cut	$\lvert d_0(\sigma)\rvert < 3$	
z_0 Cut	$\lvert z_0 \sin\theta\rvert < 0.5$ mm	
Selection Working Point	Loose	Medium
Isolation Working Point	FCLoos at $p_{\mathrm{T}} < 100$ GeV and no isolation requirement at > 100 GeV	FixedCutTightTrackOnly

Efficiency corrections

As in the case of electrons, scale factors of the efficiencies for simulated events are derived and applied similarly to the electron case. Details can be found in [144].

4.5 Missing $\mathbf{E_T}$

Production of invisible particle such as neutrinos are detected by using momentum imbalance in the transverse plane, referred to as a missing transverse momentum [146]. The missing transverse momentum consists of two components. The first is reconstructed objects such as electrons, muons, photons, and jets. The second is soft terms, which are charged-particle tracks not matched to the reconstructed objects. The missing transverse momentum components are then given by

$$E_{x(y)}^{\mathrm{miss}} = -\sum_{i\in\{\text{hard objects}\}} p_{x(y),i} - \sum_{j\in\{\text{soft terms}\}} p_{x(y),j}. \tag{4.23}$$

The set of observables constructed from E_T^{miss} is

$$\boldsymbol{E}_T^{\mathrm{miss}} = (E_x^{\mathrm{miss}}, E_y^{\mathrm{miss}}), \tag{4.24}$$

$$E_T^{\mathrm{miss}} = |\boldsymbol{E}_T^{\mathrm{miss}}| = \sqrt{(E_x^{\mathrm{miss}})^2 + (E_y^{\mathrm{miss}})^2}, \tag{4.25}$$

$$\phi^{\mathrm{miss}} = \tan^{-1}(E_y^{\mathrm{miss}}/E_x^{\mathrm{miss}}). \tag{4.26}$$

Here the multiple inclusions of the same signal in all objects are removed [146]. We can calculate the modulus and the direction in the transverse plane in terms of the azimuthal angle ϕ, via the vector $\boldsymbol{E}_T^{\mathrm{miss}}$.

The scalar sum of all transverse momenta from the objects contributing to the missing transverse momentum reconstruction is given by

$$\Sigma E_T = \sum_{i\in\{\text{hard objects}\}} p_{\mathrm{T},i} + \sum_{j\in\{\text{soft terms}\}} p_{\mathrm{T},j}. \tag{4.27}$$

This provides the information for estimating the hardness of the hard-scatter event in the transverse plane.

Chapter 5

Track-CaloClusters (TCCs)

5.1 Introduction

Jet substructure variables play a crucial role in discriminating boosted $W/Z \to qq$ bosons from non-resonant jet in W/Z + jetsbackground. In the previous analyses [147, 148], we used calorimeter-clusters as inputs of D_2 calculation, which exploits the exceptional energy resolution of the ATLAS calorimeter [116]. However, jets highly collimate in the event with much higher energy and its substructure can not be resolved because of degraded angular resolution in the calorimeter. In the simple example of a hadronically decaying vector boson $W/Z \to qq$, the distance between the two quarks get closed as the parent particle becomes more energetic, following the approximation $\Delta R \approx 2m_V/p_{\mathrm{T}}^V$[1] where ΔR is the distance between two quarks in η–ϕ plane. To provide the better jet substructure performance, the new jet input technique, referred to as Track-CaloClusters (TCCs) [149], had been developed. In the TCCs algorithm, a TCC is defined by combining the information of tracks and individual energy deposited in the calorimeter. Then the TCCs are used to reconstruct the large-R jets. By combining information from the calorimeter and tracking detectors, the precision of jet substructure techniques can be improved for a wide range of energies. As a consequence, better boson tagging performance can be achieved.

5.2 TCCs algorithm

5.2.1 Motivation

As described briefly in previous section, the fundamental problem of calorimeter-clusters is the limited angular resolution in the highly boosted large-R jet . In the range of p_{T} with greater than about 1 TeV, small numbers of calorimeter-clusters are created due to the insufficient granularity while the energy resolution is excellent. On the other hand, the tracking detector has excellent angular resolution and good reconstruction efficiency at very high energy [150], while its energy resolution degrades because of less curved tracks by magnetic field. Since tracks and calorimeter-clusters have complimentary behavior as described above, we expect to maximally exploits the strengths of individual detectors to improve jet substructure performance. This is the basic idea of TCCs and the algorithm is developed to improve the jet substructure performance in different energy regimes, reflected in their four-vector construction and energy sharing procedures. In the energy sharing of the TCCs approach, only the relative track momenta are considered to spatially redistribute the energy measured in the calorimeter. In short, the distinctive feature of the TCCs algorithm is that it uses the spatial coordinates of the tracker and the energy scale of the calorimeter.

5.2.2 Matching

Track-cluster matching criterion is defined in order to build 4-vector jet inputs (TCCs) from track and topo-cluster information. The matching procedure attempts to match every good quality track to every topo-cluster following two steps. First, the uncertainty on the track extrapolation is compared to the topo-cluster width. If the track extrapolation uncertainty is larger than the width of the topo-cluster, the track is removed from the matching procedure. Second, with the remaining tracks, a track-cluster pair is defined as matched if their angular separation satisfies $\Delta R < \sqrt{\sigma^2_{\mathrm{cluster}} + \sigma^2_{\mathrm{track}}}$ where $\sigma_{\mathrm{cluster}}$ is the topo-cluster width and σ_{track} is the track extrapolation uncertainty. Since the uncertainty on track extrapolation reduces significantly at high p_{T}, the second matching criterion becomes $\Delta R < |\sigma_{\mathrm{cluster}}|$ in high p_{T} limit. In extremely

[1] $m_V^2 \sim 2p_1 \cdot p_2 \sim p_{\mathrm{T},1}p_{\mathrm{T},2}\Delta R^2_{1,2} = z(1-z)p^2_{\mathrm{T},V}\Delta R^2_{1,2}$, where z is the fraction of the parent energy retained by the daughter quark.

high p_{T} range, particles decaying from highly boosted particle such as W boson tend to fall within a single topo-cluster. By matching tracks to this high energetic topo-cluster and defining multiple TCCs, the TCCs can resolve the hidden topo-cluster substructure originating from two regions of energy corresponding to the two quarks decaying from the vector boson. The TCC objects fall into three categories. First, tracks with the primary vertex and matched to topo-clusters are referred to as combined TCCs. Topo-clusters without matched tracks and tracks from the primary vertex not matched to cluster, are referred to as neutral and charged TCCs, respectively. While tracks from pileup vertices matched to topo-clusters are not used in building TCC objects. Figure 5.1 shows the resulting fractions of neutral, charged and combined TCCs. $W' \to WZ \to qqqq$ events with a W' mass of 1 TeV are used. The combined TCCs become the dominant

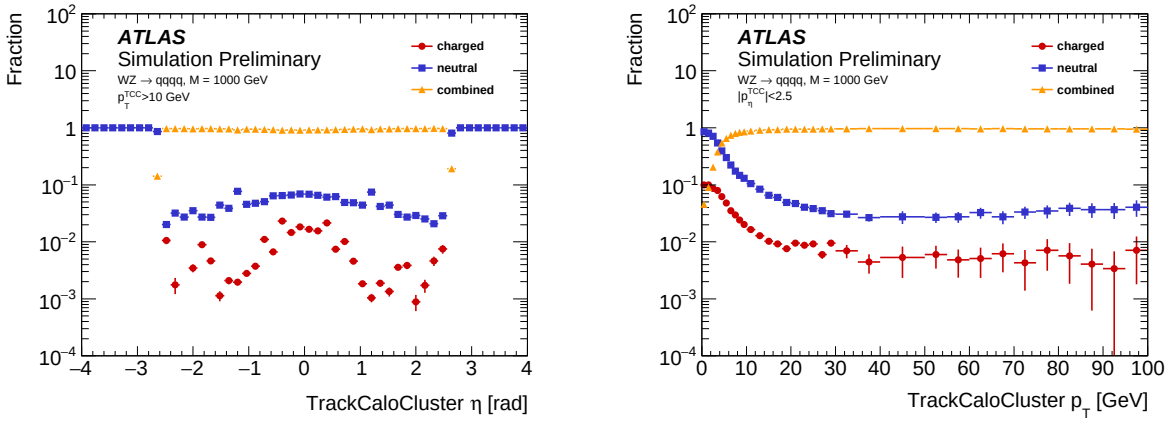

(a) (b)

Figure 5.1: The fraction of different TCCs classes as a function of (a) the TCC η and (b) the TCC p_{T} [149].

scenario at TCCs p_{T} greater than 5 GeV since highly energetic topo-clusters are likely from the hadronically decaying W/Z boson and thus close to tracks.

5.2.3 Reconstruction

After matching tracks and topo-clusters, we need to build the actual TCC 4-vectors with dedicated energy sharing algorithm. In this section some of the energy sharing examples are shown with the actual energy sharing equation. Figure 5.2 shows the schematic view of the track-cluster matching examples. When referring to the figure, ① refers to TCC object 1, c_1 refers to topo-cluster c_1 and t_1 refers to track t_1. The first case is a direct single match between a track and a topo-cluster, refered to as ①. The topo-cluster energy and the track directions are directly used to form a single TCC:

$$\mathrm{TCC}_{①} = (p_{\mathrm{T}}^{c_1}, \eta^{t_1}, \phi^{t_1}, m^{c_1} = 0). \tag{5.1}$$

In the case of topo-clusters without any matched tracks, such as ②, the topo-cluster 4-vector is directly used:

$$\mathrm{TCC}_{②} = (p_{\mathrm{T}}^{c_7}, \eta^{c_7}, \phi^{c_7}, m^{c_7} = 0). \tag{5.2}$$

It is same for tracks which does not match any topo-clusters, such as ③:

$$\mathrm{TCC}_{③} = (p_{\mathrm{T}}^{t_6}, \eta^{t_6}, \phi^{t_6}, m^{t_6} = 0). \tag{5.3}$$

In complicated cases, there is a match between multiple tracks and a single cluster, multiple topo-clusters and a single track and multiple topo-clusters with multiple tracks as in the case of ⑥ and ⑦. One track originating from a primary vertex creates the exactly one TCC object by definition and the angular coordinates are measured by the track. However, the scale coordinates must consider the energy sharing between the different matches. Two tracks matching a single topo-cluster, such as the case of ④ and ⑤, is a simple example which need energy sharing. The TCC 4-vectors are defined as:

$$\mathrm{TCC}_{④} = \left(p_{\mathrm{T}}^{c_2} \frac{p_{\mathrm{T}}^{t_2}}{p_{\mathrm{T}} \left[\mathbf{p}_{\mathrm{T}}^{t_2} + \mathbf{p}_{\mathrm{T}}^{t_3} \right]}, \eta^{t_2}, \phi^{t_2}, m^{c_2} \frac{p_{\mathrm{T}}^{t_2}}{p_{\mathrm{T}} \left[\mathbf{p}_{\mathrm{T}}^{t_2} + \mathbf{p}_{\mathrm{T}}^{t_3} \right]} = 0 \right), \tag{5.4}$$

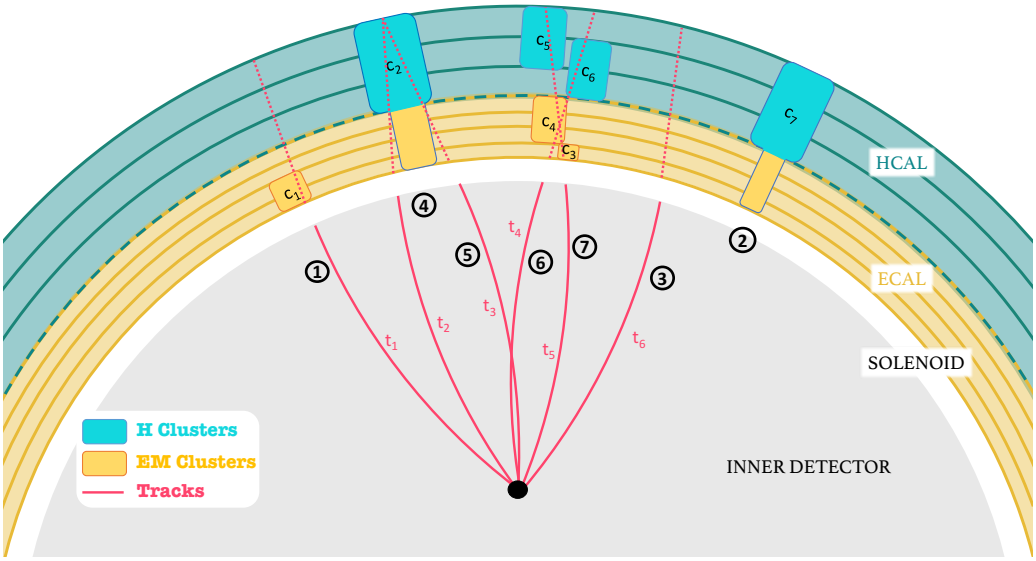

Figure 5.2: The schematic demonstrating of the TCC objects reconstruction. Details on the exact reconstruction procedure are provided in the text [149].

$$\mathrm{TCC}⑤ = \left(p_{\mathrm{T}}^{c_2} \frac{p_{\mathrm{T}}^{t_3}}{p_{\mathrm{T}}\left[\mathbf{p}_{\mathrm{T}}^{t_2} + \mathbf{p}_{\mathrm{T}}^{t_3}\right]}, \eta^{t_3}, \phi^{t_3}, m^{c_2} \frac{p_{\mathrm{T}}^{t_3}}{p_{\mathrm{T}}\left[\mathbf{p}_{\mathrm{T}}^{t_2} + \mathbf{p}_{\mathrm{T}}^{t_3}\right]} = 0 \right). \tag{5.5}$$

$\mathbf{p}^a$ is the 4-vector corresponding to a given particle a. $p_{\mathrm{T}}\left[\mathbf{p}^a + \mathbf{p}^b\right]$ means the p_{T} of the 4-vector sum of a and b.

Generally speaking, the TCC energy sharing algorithm considers the case where a seed track τ matched to a set of topo-clusters C_τ. The notation X_y represents the set of objects of type X matched to a given object y, where X is either C for topo-clusters or T for tracks. Furthermore, each topo-cluster $c \in C_\tau$ can also be matched to a set of tracks T_c. Since the energy sharing procedure needs to consider several patterns of multiple matching between track (s) and topo-cluster (s), we need to introduce three general concepts of p_{T} fractions. First, the energy scale of the TCC object resulting from the seed track τ must be contributed by each matched cluster $c \in C_\tau$, weighted by the p_{T} fraction out of the all matched clusters. The fraction f_τ^c is defined as

$$f_\tau^c = \frac{p_{\mathrm{T}}^c}{p_{\mathrm{T}}\left[\sum_{k \in C_\tau} \mathbf{p}^k\right]}. \tag{5.6}$$

Second, each cluster $c \in C_\tau$ can also contribute to other TCC objects such as the case of ④, ⑤, ⑥ and ⑦, so its contribution to the TCC object should be also weighted by the p_{T} fraction of the seed track τ compared to all other tracks matched to the cluster c. The fraction $\mathcal{F}_{c,t}^\tau$ is

$$\mathcal{F}_{c,t}^\tau = \frac{p_{\mathrm{T}}^\tau}{p_{\mathrm{T}}\left[\sum_{t \in T_c} \mathbf{p}^t f_t^c\right]}. \tag{5.7}$$

Notice that the p_{T} fraction f_t^c is applied to those tracks $t \in T_c$ to account for the weighted contribution of tracks t matched to multiple clusters, and this is the third p_{T} fraction concept. In calculating the third fraction f_t^c, tracks from any vertex are considered, while the seed track τ must be originating from the primary vertex.

Applying these definitions to the actual building of TCC object built from the seed track τ, the final 4-vector becomes

$$\mathbf{M}_\tau = \sum_{c\in C_\tau} \mathbf{p}^c f_\tau^c \mathcal{F}_{c,t}^\tau = \sum_{c\in C_\tau} \mathbf{p}^c \frac{p_{\mathrm{T}}^c}{p_{\mathrm{T}}\left[\sum_{k\in C_\tau}\mathbf{p}^k\right]} \frac{p_{\mathrm{T}}^\tau}{p_{\mathrm{T}}\left[\sum_{t\in T_c}\mathbf{p}^t \frac{p_{\mathrm{T}}^c}{p_{\mathrm{T}}\left[\sum_{k\in C_t}\mathbf{p}^k\right]}\right]} \tag{5.8}$$

Using the 4-vector $\mathbf{M}_\tau$ definced as above, the final TCC 4-vector is

$$\mathrm{TCC}_\tau = (p_{\mathrm{T}}[\mathbf{M}_\tau], \eta^\tau, \phi^\tau, m[\mathbf{M}_\tau]). \tag{5.9}$$

The p_{T} and mass of the TCC 4-vector is defined by the 4-vector sum $\mathbf{M}_\tau$, taking into account of the energy sharing between multiple tracks and clusters. The mass is zero when only one topo-cluster is matched to the seed track, and non-zero if at least two topo-clusters are matched to the seed track. This formula handles all matching cases including examples shown in this section.

5.3 Jet reconstruction and performance

5.3.1 Jet reconstruction

Large-R jets are built from anti-k_t algorithm [119] with a distance parameter $R = 1.0$. Different sets of TCC objects can be used as the jet inputs to the large-R jet reconstruction. We consider two selections of TCC inputs: all-TCCs and only combined-TCCs, where all TCCs include both neutral and charged TCCs in addition to combined TCCs. All-TCCs is used in this analysis based on the performance studies of mass and D_2 resolution, as discussed in Section 4.3.1.

A comparison of three types of large-R jets built from TCCs is presented in Figure 5.3. Each type of the TCC jets is matched to the corresponding truth jet and is used at the uncalibrated scale for this study. The jet inputs are compared using the jet mass response, $\mathcal{R}_m^r = m_{\text{TCC jet}}/m_{\text{matched truth jet}}$. Comparing distributions of the untrimmed and trimmed TCC jets built from all TCCs, the trimming algorithm [151] is found to be able to improve the jet mass response significantly. On the other hand, jets built from combined TCCs shows good mass response without trimming.

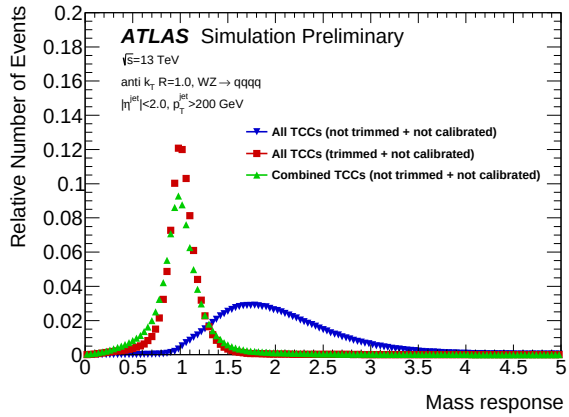

Figure 5.3: A comparison of the mass response, $\mathcal{R}_m^r$, for jets built with all TCCs, all TCCs after trimming and only combined TCCs.[149].

The p_{T}[2]pseudo response, comparing p_{T} of TCC jets with topo-cluster jets, is shown in Figure 5.4a. The reference topo-cluster jet is trimmed and not calibrated. Since all types of TCC jets are at the same calibration scheme to topo-cluster jet, the distribution is to be peaked around 1. For the small shift to smaller p_{T}, it comes from the removal of pileup topo-clusters matching tracks from pileup primary vertices. Comparing trimmed all TCCs and not trimmed combined TCCs shows the pileup contribution is well controlled and topo-clusters coming from the hard scattering are retained by the TCC algorithm.

[2]Pseudo-response where the reference jet is a different reconstructed jet definition. This is useful when comparing TCC jets against the standard topo-cluster jet definition.

Figure 5.4b shows the η residual distribution for the three jet definitions. Topo-cluster jet shows a better η residual than TCC jets due to the well-known centroid of the high energy topo-clusters. However, the aim of TCC jets is improving the jet substructure and the impact of a bit larger η uncertainties is negligible in this analysis.

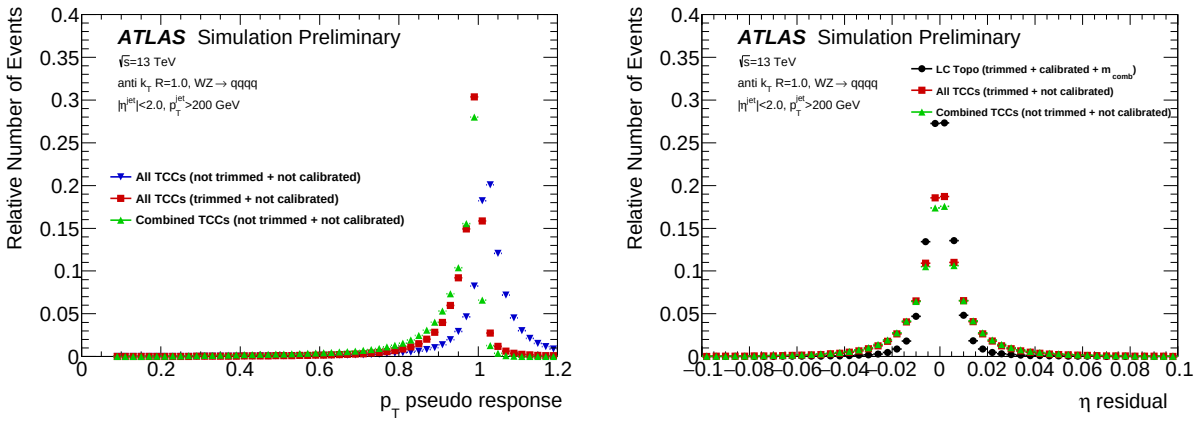

(a) (b)

Figure 5.4: The (a) TCC jet p_{T} pseudo-response with respect to trimmed topo-cluster jets and (b) η residual for both topo-cluster and TCC jet [149].

The distributions of three kinds of jet inputs in η-ϕ plane are shown in Figure 5.5. TCC jets (Figure 5.5b and 5.5c) show an additional k_t subjet of size $R_{\mathrm{sub}} = 0.2$ denoted by grey region within each of the two large-R jets demarcated by a blue circle. The total number of jet inputs to jet reconstruction is significantly suppressed by the combined TCCs.

5.3.2 Jet substructure performance

The jet substructure variables, jet mass, and D_2, are used in the boson tagging to extract two quarks from $W/Z \to qq$. A comparison of the mass response for LCTopo jets built from topo-clusters only, all-TCCs, and combined-TCCs is shown in Figure 5.6. Figure 5.6a is for 700 GeV $< p_{\mathrm{T}} <$ 800 GeV, and Figure 5.6b is for 2.1 TeV $< p_{\mathrm{T}} <$ 2.5 TeV. At high p_{T} as seen in Figure 5.6b, the peak of the all-TCCs and combined-TCCs jets are larger than one, however, this is because they are not calibrated and not a problem. Therefore, the performance of these jets is seen to be similar.

A comparison of D_2 residual, $\mathcal{R}^d_{D_2}$ for jets built from different jet inputs is shown for 700 GeV $< p_{\mathrm{T}} <$ 800 GeV in Figure 5.7a and for 2.1 TeV $< p_{\mathrm{T}} <$ 2.5 TeV in Figure 5.7b. Better D_2 residual distribution is observed for both all-TCCs and combined-TCCs jets. In addition, the TCC jets remain centered around zero while topo-clusters jets shift towards larger D_2. However, the combined-TCCs jet has a long tail, indicating the missing of relevant energy contributions from track-cluster matches. The distribution of Topo-cluster jets changes dramatically when changing the p_{T} by an order of magnitude.

Figure 5.8 shows the comparison of mass and D_2 resolutions of jets built from topo-clusters, all-TCCs and combined-TCCs as a function of jet p_{T}. A resolution metric is defined using the Inter-Quantile Range (IQR) of the distribution width. $\mathcal{Q}_x$ is the x% of quantile boundary. For instance, $\mathcal{Q}_{50}$ means the median. To account for the resolution of the response and the residual distribution, two kinds of IQR definitions are used:

$$\mathrm{IQR}^r = \frac{1}{2}\frac{\mathcal{Q}_{84}(\mathcal{R}^r) - \mathcal{Q}_{16}(\mathcal{R}^r)}{\mathcal{Q}_{50}(\mathcal{R}^r)}, \tag{5.10}$$

$$\mathrm{IQR}^d = \frac{1}{2}\left[\mathcal{Q}_{75}(\mathcal{R}^d) - \mathcal{Q}_{25}(\mathcal{R}^d)\right] \tag{5.11}$$

These definitions correspond to half of a 68% window for the mass resolution, and half of 50% window for the D_2 resolution. The difference of the definitions come from the distribution to use: the response $\mathcal{R}^r$ or the residual $\mathcal{R}^d$. The resolution shown in Figure 5.8 is presented by using IQR^r. For $p_{\mathrm{T}}^{\mathrm{truth}} > 2$ TeV, the mass resolution of all-TCCs jets outperforms the topo-cluster jet, but shows the sligtly worse resolution for most of the $p_{\mathrm{T}}^{\mathrm{truth}}$ range below that. All-TCCs jets are seen to be superior to the topo-cluster jets over the entire

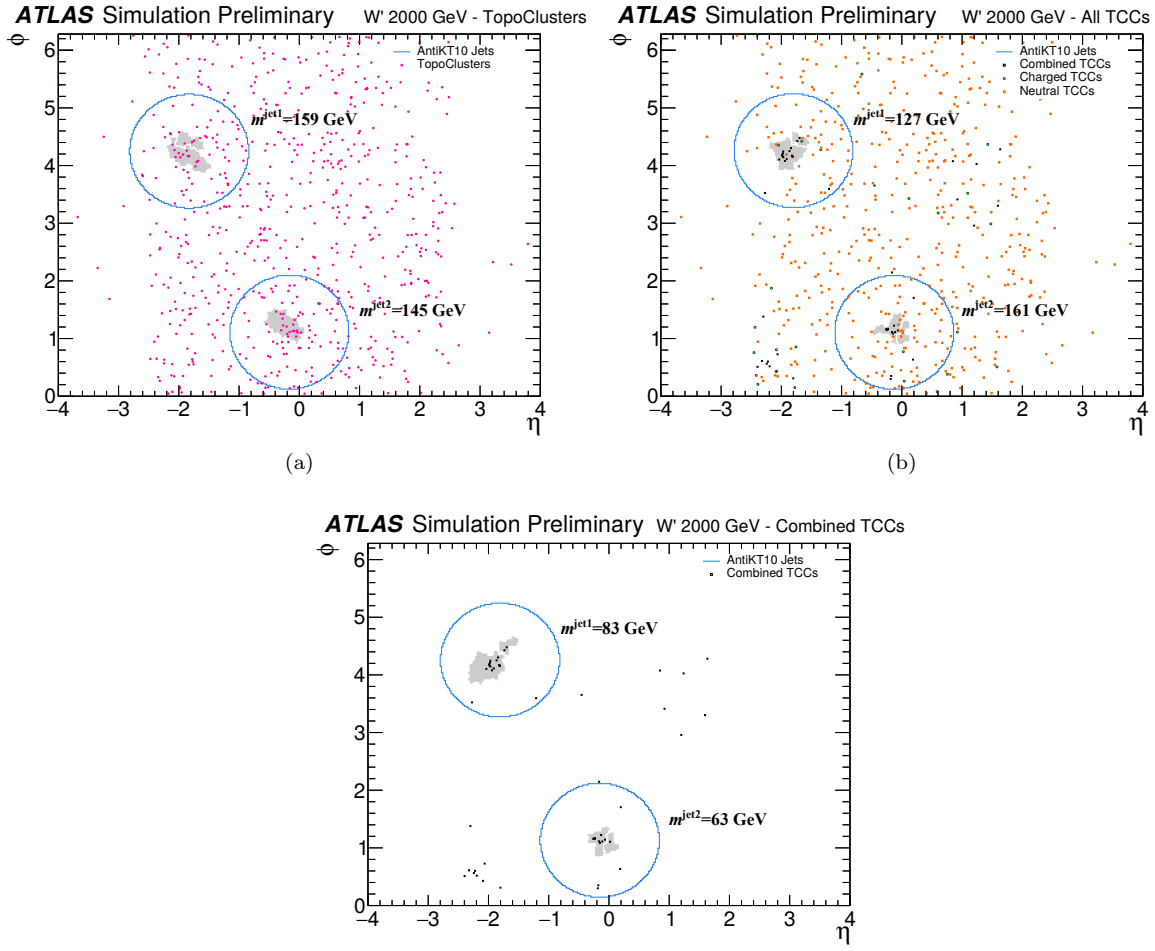

Figure 5.5: The distributions of jet inputs for (a) topo-clusters, (b) all TCCs and (c) only combined TCCs in η-ϕ plane. [149].

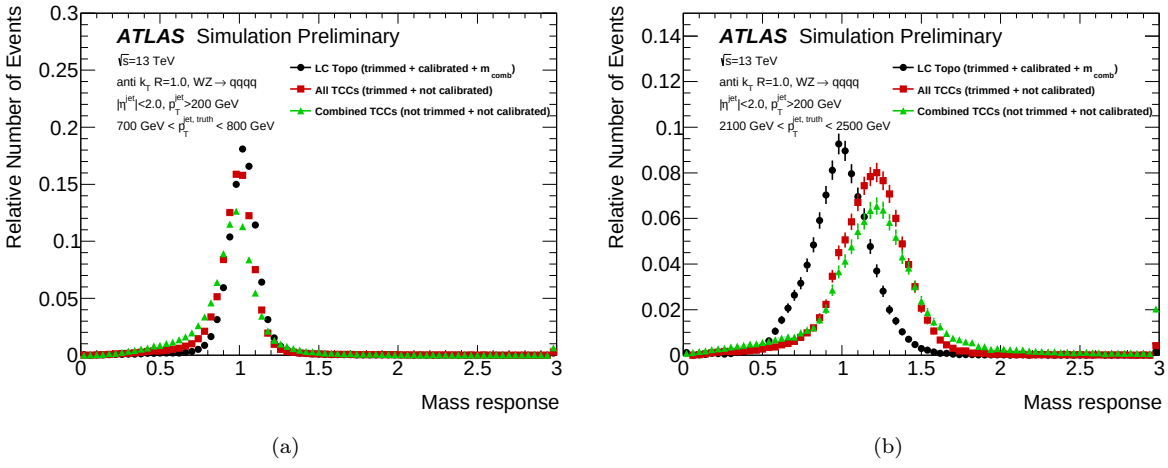

Figure 5.6: A comparison of the mass response for jets built from topo-clusters (black circles), all-TCCs (red squares) and combined-TCCs (green triangles) for 700 GeV $< p_{\mathrm{T}} <$ 800 GeV in Figure reffig:MassResponse1 and for 2.1 TeV $< p_{\mathrm{T}} <$ 2.5 TeV in Figure 5.6b. [149]

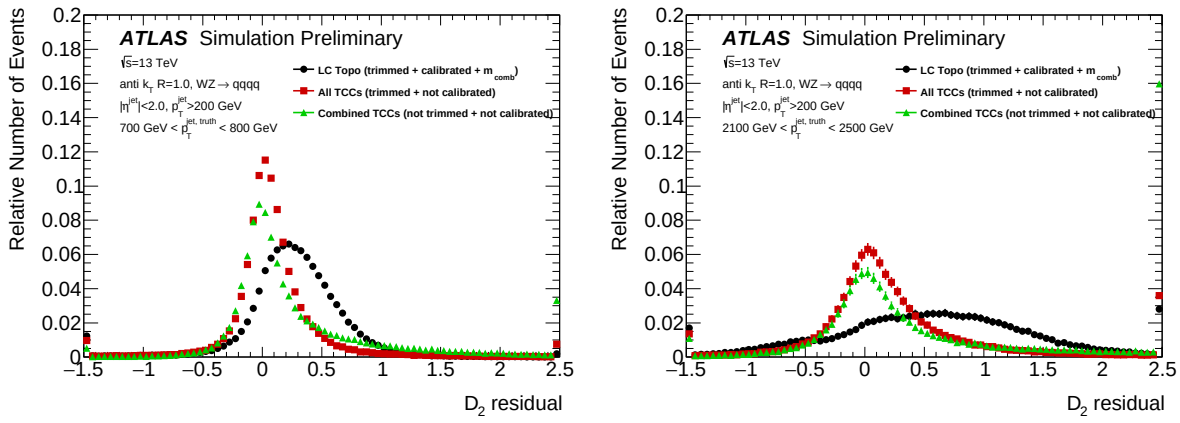

(a) (b)

Figure 5.7: A comparison of the D_2 residual for jets built from topo-clusters (black circles), all-TCCs (red squares) and combined-TCCs (green triangles). [149]

$p_{\mathrm{T}}^{\mathrm{truth}}$ ranges. Although the mass and D_2 resolutions of all types of jets degrade with increasing $p_{\mathrm{T}}^{\mathrm{truth}}$, the degradation of D_2 of all-TCCs jets are highly suppressed. According to the performance studies discussed above, we descided to use All TCCs as default jet inputs.

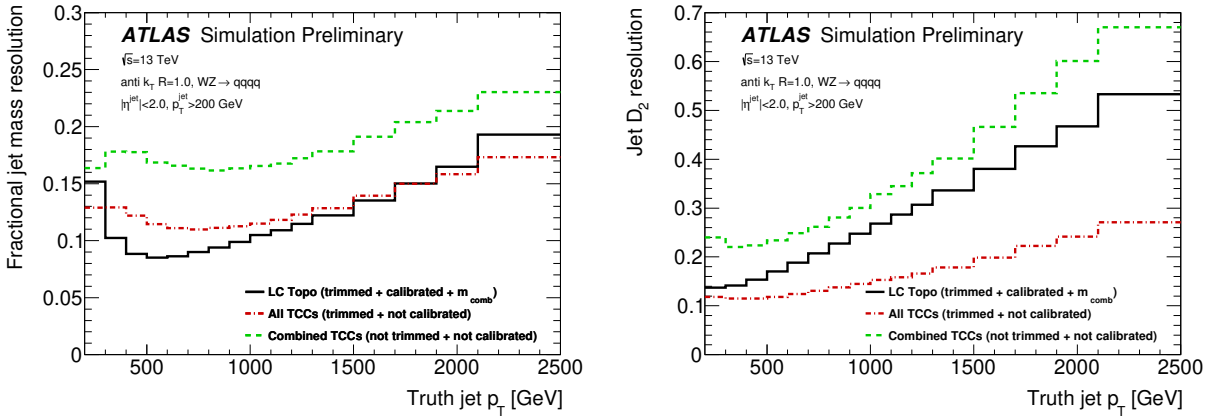

(a) (b)

Figure 5.8: A comparison of the fractional jet mass (a) and D_2 (b) resolution for topo-cluster jets (solid black lines), jets built using all-TCC objects (dash-dotted red lines) and jets built using only combined-TCC objects (dashed green lines), as a function of truth-jet p_{T}. The TCC definitions are seen to outperform at high p_{T}, particularly for D_2 [149].

5.4 Boson Tagger Optimization

Designed to extract the jet substructure originating from two quarks from $W/Z \to qq$, the boson tagger performance is also sensitive to the source of background. For example, jets in $W/Z + jets$ background are dominated by single quark-induced jets, while the jets in QCD multi-jet are dominated by gluon-induced jets, In our analysis, $W/Z + jets$ background is the dominant background. On the other hand, the other analysis such as $VV \to JJ$ [152] suffers from QCD multi-jet background. Therefore we need to optimize the boson tagger depending on the dominant background in each analysis. In this section, the effect of the quark/gluon fraction in the background on the optimal working point of the W/Z tagger is discussed first. Then, the boson tagger optimized for the VV semi-leptonic analysis is described in detail.

Effect of quark/gluon fraction

Figure 5.9 shows D_2 distributions of both quark- and gluon-induced jets, devided by low- and high-p_{T} range.A The shape difference is observed especially in lower p_{T} region, and it might lead to the different optimized D_2 thresholds for boson tagger.

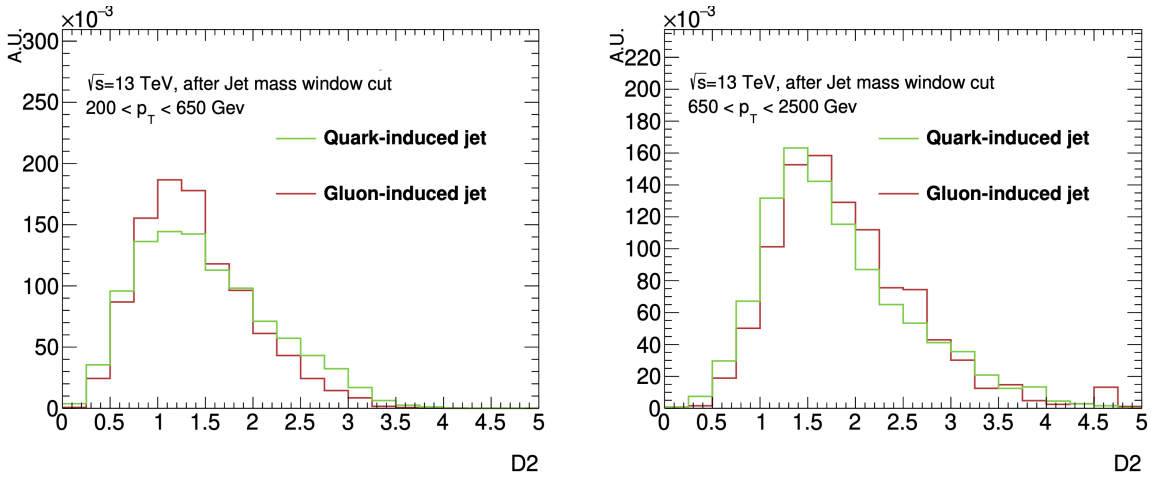

(a) (b)

Figure 5.9: D_2 distribution of quark- and gluon-induced jets derived from Z+jets, separated by $200 < p_T < 650$ (a) and $650 < p_T < 2500$ (b). In low p_{T} region (b), quark-induced jets have a tail in higher D_2 and causing the difference from gluon-induced jets. The difference is getting small in high p_{T} region (b) due to boost of jets

In order to estimate the impact of D_2 difference, the quark/gluon fraction in the Z+jets background is varied in the range of 0% to 100% (overall normalization is not changed) and the optimal D_2 threshold to $G \to ZZ \to llqq$ signal is checked as a function of that, as shown in Figure 5.10. A fixed jet mass window cut (70 GeV$< m_J <$110 GeV) is applied in this study. The quark/gluon fraction significantly affects the optimal D_2 threshold at low-p_{T} region. Looser cut on D_2 is preferred if the quark-jet fraction is closed to one. On the other hand, the dependency of the optimal threshold on the quark/gluon fraction becomes to be small at high-p_{T} region, since both quark- and gluon-jets have a similar D_2 distributions at that region as shown in Figure 5.9b. Due to this quark/gluon fraction dependency, we need to use the W/Z boson tagger optimized for VV semileptonic analysis, where W/Z+jets with quark-induced jets are the dominant backgrounds.

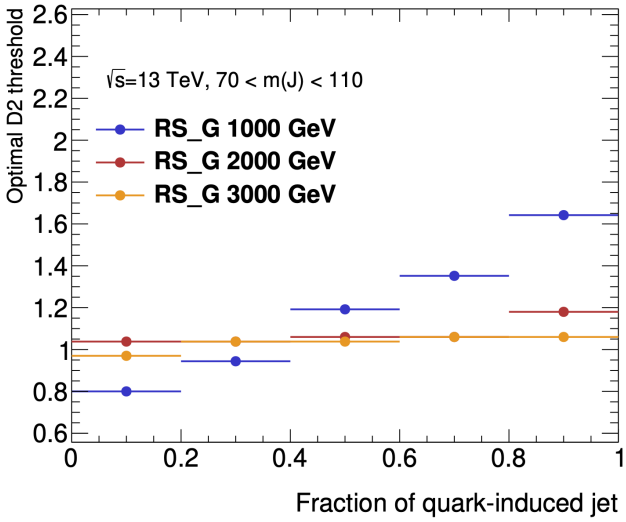

Figure 5.10: Optimal D_2 thresholds as a function of quark-induced jet fraction. Jet mass window cut assuming naive boson tagger is applied. A quark fraction dependency observed at low mass signal, but not at high mass signal as expected.

Optimization

A two-dimensional optimization of the jet mass and D_2 is performed at $p_T > 200$ GeV. A jet mass window and D_2 thresholds are scanned simultaneously in each p_{T} bin for each $W' \to WZ$ and $W' \to WW$ signal, respectively. Then, the ones showing the highest sensitivity to the signals is selected, as shown by dots in Figure 5.11. The definition of the significance is

$$Z = \sqrt{2\left(n \ln\left[\frac{n(b+\sigma^2)}{b^2+n\sigma^2}\right] - \frac{b^2}{\sigma^2}\ln\left[1+\frac{\sigma^2(n-b)}{b(b+\sigma^2)}\right]\right)}, \tag{5.12}$$

which is based on the asymptotic formula for the distribution of profile likelihood test statistics. Here s and b are the number of signal and background events ($n = s + b$), and σ is the statistical uncertainty of background MC events (to avoid extreme selection in the region of lack of MC statistics). F Figure 5.11 shows the optimized thresholds on D_2 and jet mass as a function of p_{T}. The solid lines show the fit results. Figure 5.12 shows the efficiency of the optimized W/Z taggers to W- and Z-induced jets as a function of p_{T}. The taggers are optimized to achieve about 40-50% efficiency at the lowest-p_{T}, region, about 60 % at the intermediate p_{T}, range and about 70% at the highest-p_{T}, region.

Signal efficiency and background rejection compared with the previous working point with topo-cluster jet are shown in Figure 5.13. TCC jet tagger achieved higher signal efficiency while keeping better or similar background rejection to topo-cluster jet tagger at highest-p_{T}, region.

5.5 Boson Tagging Efficiency SF

In this analysis, p_{T}, mass and D_2 of the TCC jet are used in the event selection for better signal sensitivity and we need to estimate the scale factors (SFs) which describe the difference of data and MC simulation and the systematic uncertainties of them. The TCC jet p_{T} is equivalent to the LCTopo jet p_{T} in the first approximation. Therefore the R_{trk} method [153], in which the possible mis-modeling is estimated by comparing the TCC jet p_{T} and the associated track jet p_{T}, can be used in the estimation of the jet p_{T} scale uncertainty. However, it is not the case for D_2 and mass scale uncertainty, because these variables highly depend on the tracks information due to the TCCs algorithm [149]. To take into account D_2 and mass scale uncertainty as well as p_{T}, boson tagging efficiency (fraction) scale factors are estimated in a data sample enriched in semi-leptonic $t\bar{t}$ events for signal and W/Z+jets for a background. Since the boson tagging utilizes D_2 and mass window cut, their uncertainties should be included in boson tagging scale factor uncertainty.

In our analysis the events with a large-R jet are categorized into four specific regions according to both D_2 and jet mass cut results of the boson tagger. All of the defined regions are to be used as inputs of statistical analysis and the boson tagging SFs must be estimated for each of these regions including events mitigation between them. The detailed definitions of signal region and background control region are discussed in 6.9. We consider the three kinds of SFs: boson tagging SFs for W-boson, top-quark and single q/g background. The estimated SFs for W-boson is also used for Z-tagger since the boson tag efficiency is similar and the SFs for both W- and Z-tagger should be same.

5.5.1 Signal Efficiency

Event selection

For the boson tagging efficiency SF of large-R jets originating from W-boson and top-quark, a sample of data enriched in semi-leptonic $t\bar{t}$ is used. The inclusive sample of events is further split into two exclusive subsamples, enriched in W-boson jets and top-quark jets by using the angular distance between a b-tagged jet and the large-R jet. Only the muon channel is used for the sake of purity of the target process. The selection for the semi-leptonic $t\bar{t}$ event is performed in a similar manner to Ref. [154]. Both data and MC simulated events are required to pass an single muon trigger. The event selection is split into two steps: Leptonic top selection, large-R jet from W/top candidate selection.

- Leptonic top selection
  - Require one muon candidate with $p_{\mathrm{T}} > 30$ GeV and $|\eta| < 2.5$ satisfying the *Medium* identification criteria defined in Ref.[144].
  - Events containing additional muons with $p_{\mathrm{T}} > 25$ GeV are rejected.

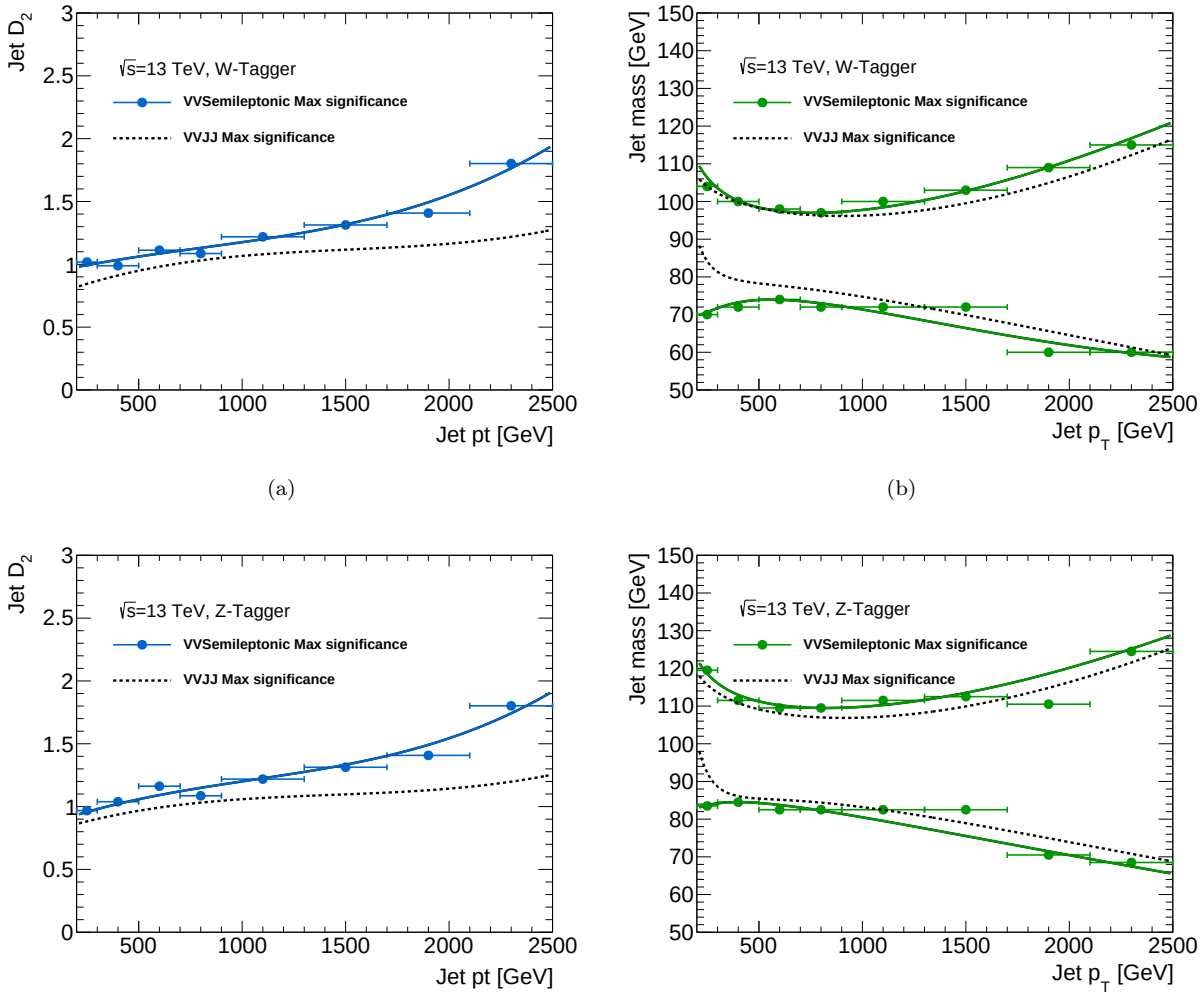

(a) (b)

(c) (d)

Figure 5.11: The upper cut on (a) D_2 and (b) jet mass window cut i.e. the upper and lower boundary of the mass of the W-tagger as a function of jet p_{T}. Corresponding values for Z-tagger are shown in (c) and (d). The optimal cut values for maximum significance are shown as solid markers and the fitted function as solid lines. Working points from $VV \to JJ$ is also shown as dashed lines as a reference.

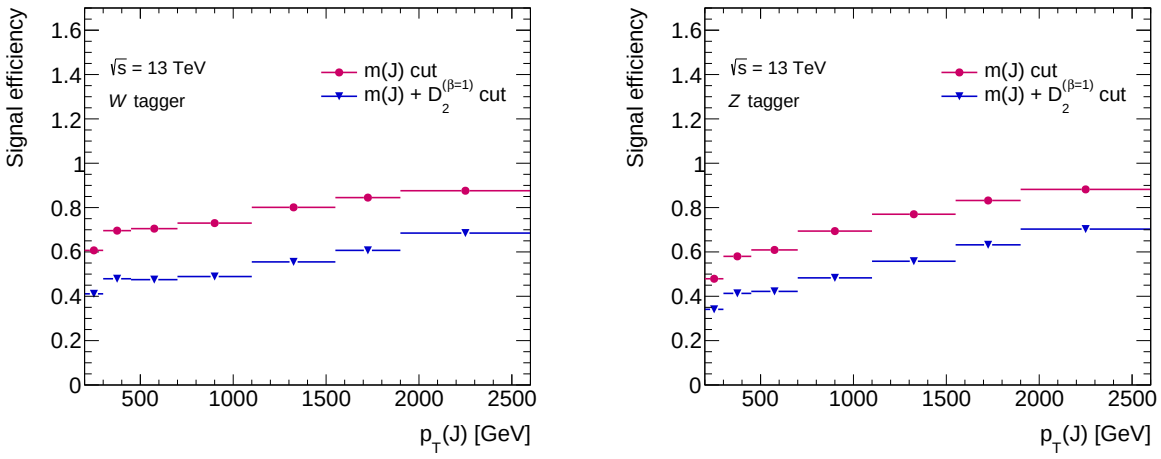

(a) (b)

Figure 5.12: Efficiencies of the m_J and $D_2^{(\beta=1)}$ requirements as functions of the large-R jet p_{T} for the $V \to J$ tagging for (a) the W boson and (b) the Z boson.

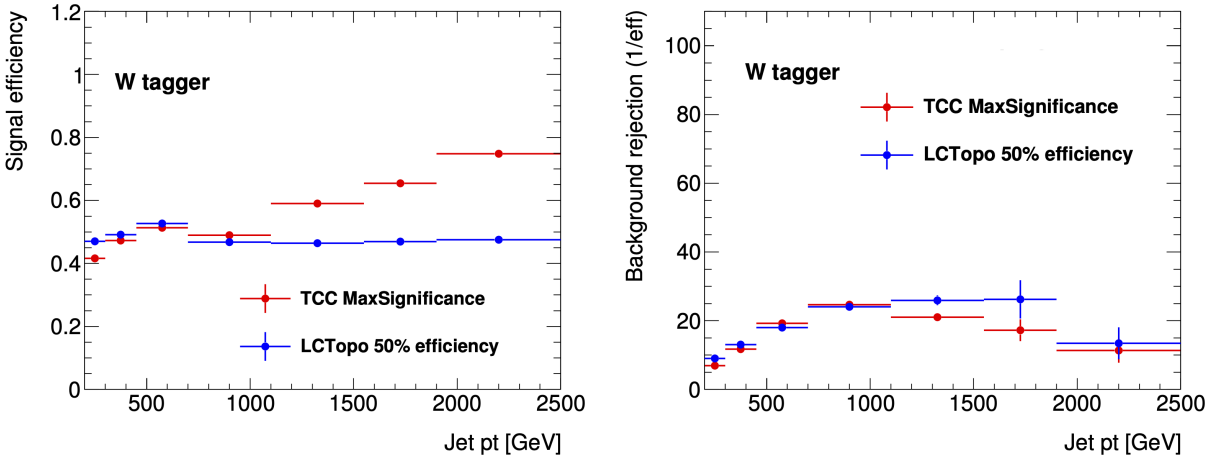

(a) (b)

Figure 5.13: (a) Signal efficiency and (b) background rejection comparison between TCC jet tagger and LCTopo jet tagger. Red points show the result of the TCC boson tagger optimized for the VV semi-leptonic analysis. Blue points correspond to the boson tagger with LCTopo jet, optimized to keep 50% signal efficiency over the full range of the jet p_{T}.

- At least one topo-cluster based small-R jet (preselected by $p_{\mathrm{T}} > 20$ GeV, $|\eta| < 2.5$ and the *loose* quality criteria defined in Ref.[155]) is required to have $p_{\mathrm{T}} > 25$ GeV and $\Delta R(\text{muon, jet}) < 1.5$ to ensure the topology is consistent with a $t\bar{t}$ event.
- The missing transeverse momentum is required to be greater than 20 GeV .
- The scaler sum of $E_{\mathrm{T}}^{\mathrm{miss}}$ and the transverse mass of the leptonically decaying W boson candidate must satisfy $E_{\mathrm{T}}^{\mathrm{miss}} + m_{\mathrm{T}}^{W} > 60$ GeV.

- Large-R jet from W/top candidate selection
  - The higest-p_{T} large-R jet with a radius parameter of 1.0 with $p_{\mathrm{T}} > 200$ GeV and $|\eta| < 2.0$ is used to study the boson tagging efficiency SF.
  - The large-R jet is required to be well-separated from the semileptonic top-quark decay by requring $\Delta R > 1.5$ between the large-R jet and the small-R jet close to muon.
  - The angular separation between the muon and the large-R jet is requird to be $\Delta\phi > 2.3$.

After the event selection, the sample is divided into two subsamples for the efficiency measurement of W-boson and inclusive top-quark jets. The b-tagged fixed-cone track-jet with a radius parameter of 0.2 is used to separate them. The sample satisfying ΔR(b-tagged jet, large-R jet) <1.0 is categorized into "top-quark selection", otherwise "W-boson selection". The large-R jet mass distributions of events after W-boson jets and top-quark jets selection are shown in Figure 5.14.

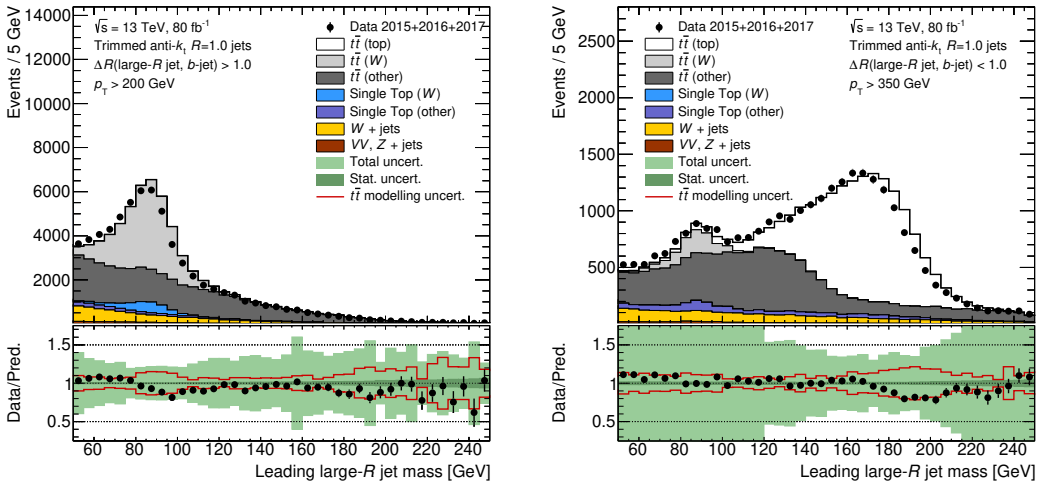

(a) (b)

Figure 5.14: A comparison of the observed data and predicted MC distribution of the leading p_{T} large-R jet (TCC jet) in the event for the (a) W boson and (b) top quark selections in a sample enriched in lepton-plus-jets $t\bar{t}$ events.

Truth labeling

In order to estimate the SF for the target processes such as W boson and top quark, the selected large-R jet must be identified from which processes does the jet come. The *truth* label of the large-R is obtained by the MC generator information including truth jet mass and number of b-hadrons associated with the jet. Based on that, large-R jets are labeled as "W", "top", and "other".

Signal efficiencies measurements

The four regions including both signal and control regions are defined by the boson tagger results based on the D_2 and mass window cut. Events passing both mass and D_2 cuts are selected in the high-purity (HP) SR. Events passing mass window cut but failing D_2 cut are used in the low-purity (LP) SR. Events passing D_2 cut but failing mass window cut are selected in the HPCR. Events failing both mass and D_2 cuts are used in the LPCR. Therefore we need to estimate the boson tagging efficiency SFs for each of these regions, respectively. In order to convolute the effect of D_2 and mass scale uncertainty to the boson tagging efficiency

SF, the event migration between the four regions needs to be considered. For this reason, we estimate each of these efficiency SFs simultaneously.

The number of signal-like events in data which would be categorized into one of these regions is obtained from a simultaneous chi-square template fit of "signal" and "background" templates. The "signal"/"background" labeling is performed based on the truth labels defined above. In W boson (top quark) selection, the signal template is composed of events with "W (top)" large-R jets from $t\bar{t}$ and single-top processes. In both selections, events other than signal templates are merged as the background template to increase the fit stability. Therefore, we have different components of signal and background templates according to types of the boson tagging SF to estimate.

For the SF for W boson, the signal template is composed of W-boson from $t\bar{t}$ and single top processes, while top quark from both $t\bar{t}$ and single top processes comprise the signal template in top quark efficiency measurement. In each of efficiency measurements, MC simulated processes without processes described above are regarded as background and they compose the merged background template. The normalization of each template is allowed to float freely in the fit. The fit is performed using distributions of the leading large-R jet mass to make better signal and background separation. The total normalization of the background component is allowed to float and is extracted in the fit. The floating parameters to be decided in the fit are listed in Table 5.1.

Table 5.1: A list of normalization factors to be decided in fit.

Name	
μ^1_{signal}	Normalization factor of signal (W/Top) in D_2 failed & Mass failed region (LPCR)
μ^2_{signal}	Normalization factor of signal (W/Top) in D_2 passed & Mass failed region (HPCR)
μ^3_{signal}	Normalization factor of signal (W/Top) in D_2 failed & Mass passed region (LPSR)
μ^4_{signal}	Normalization factor of signal (W/Top) in D_2 passed & Mass passed region (HPSR)
μ_{bkg}	Normalization factor of background (common in all regions)

The signal efficiency (fraction) for each region in data can be extracted as

$$\epsilon_{\text{data}} = \frac{N^{\text{region}}_{\text{fitted signal}}}{N^{\text{all regions}}_{\text{fitted signal}}}, \tag{5.13}$$

where $N^{\text{region}}_{\text{fitted signal}}$ means the number of fitted signal events in one of each cateogry (HPSR, LPSR, HPCR, LPCR), and $N^{\text{all region}}_{\text{fitted signal}}$ means the number of fitted signal events in all regions. These values are compared to the signal efficiencies evaluated in MC simulation,

$$\epsilon_{\text{MC}} = \frac{N^{\text{region}}_{\text{signal}}}{N^{\text{all regions}}_{\text{signal}}}. \tag{5.14}$$

The efficiencies are obtained in both data and simulations as a function of the large-R jet p_{T}. The post-fit large-R jet mass distributions are shown in Figure 5.15 for W-bosons and 5.16 for inclusive top-quarks. The discrepancy between data and fitted MC events are observed. This comes from the shift of the TCC jet mass. Since the TCC jet is not calibrated, this effect is expected.

The boson tagging efficiency SF, the ratio of signal efficiencies in the data to signal efficiencies in the MC simulation, is shown in Figures 5.17 for W-bosons and 5.18 for inclusive top-quarks. The dominant uncertainties come from $t\bar{t}$ modeling. For W boson selection, the mass failed region (a) and (b) have large uncertainty due to the small fraction of W boson jets. Since these large-R jets with large systematic uncertainty are sub-dominant, its impact on our analysis would be small. On the other hand, in the top-quark selection, the mass passed region (c) and (d) show relatively large fluctuations since most of the top-quark jets fail the mass window cut. For the jet p_{T} larger than the range of the plot, the values of the highest bin is used with additional high-p_{T} extraction uncertainty, which is evaluated by comparing different generators.

The derived SFs are applied to the MC simulated events according to the jet labelling and the boson tagging result.

5.5.2 Background Rejection

The similar measurement to W-boson and top-quark jet need to be performed for the background jet (e.g. W/Z+jets). The behavior of the background jet for the boson tagger is studied in two sets of events to cover

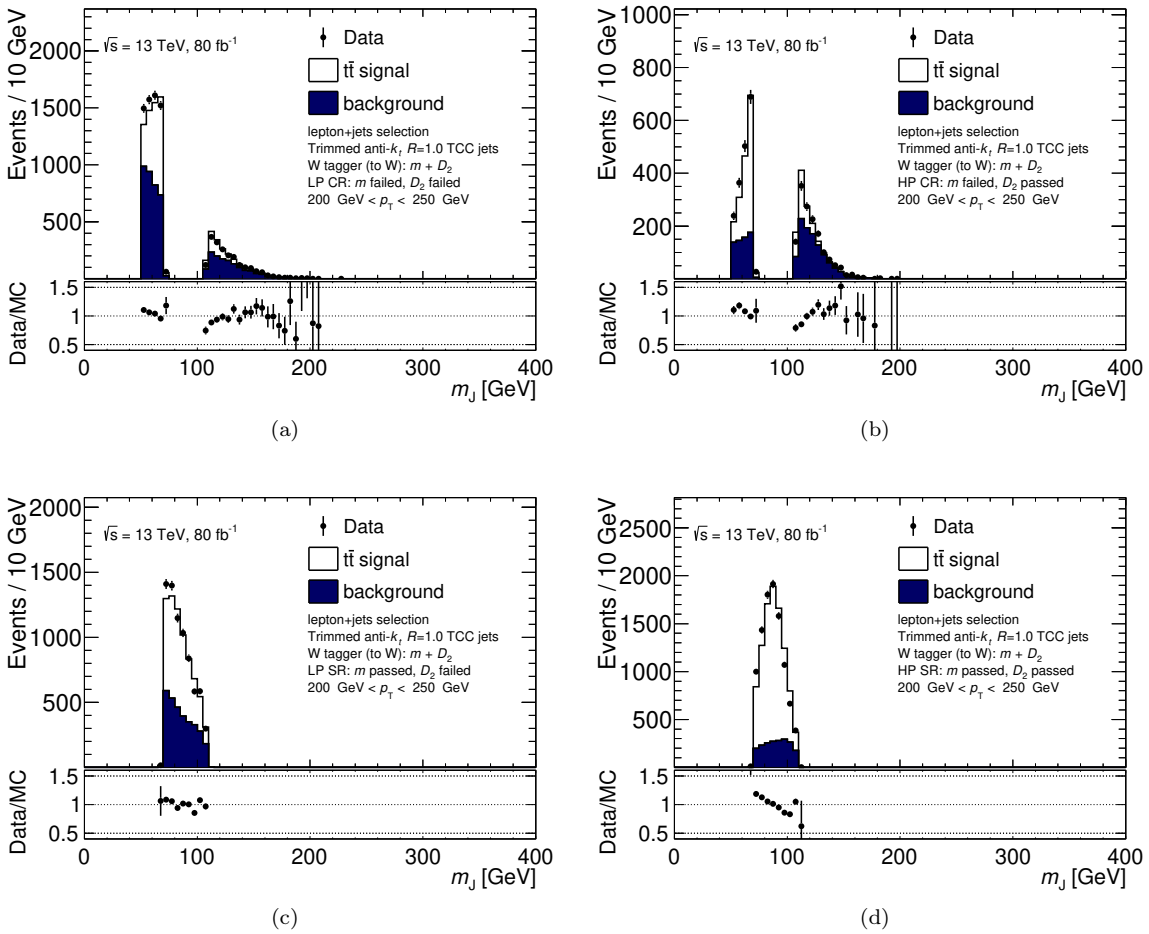

Figure 5.15: The post-fit distribution of the large-R jet mass in (a) D_2 failed, mass failed, (b) D_2 passed, mass failed, (c) D_2 failed, mass passed and (d) D_2 passed, mass passed for W-boson selection.

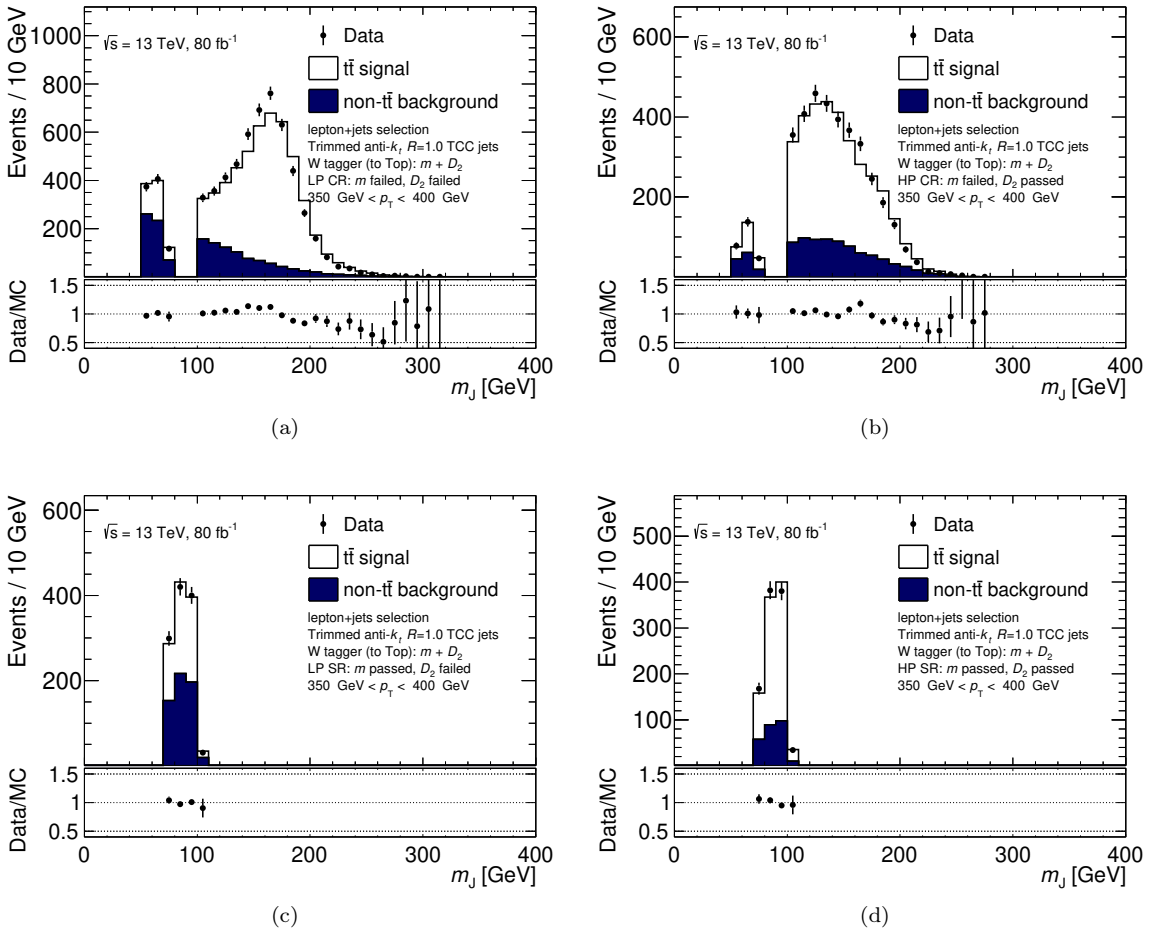

Figure 5.16: The post-fit distribution of the large-R jet mass in (a) D_2 failed, mass failed, (b) D_2 passed, mass failed, (c) D_2 failed, mass passed and (d) D_2 passed, mass passed for top-quark selection.

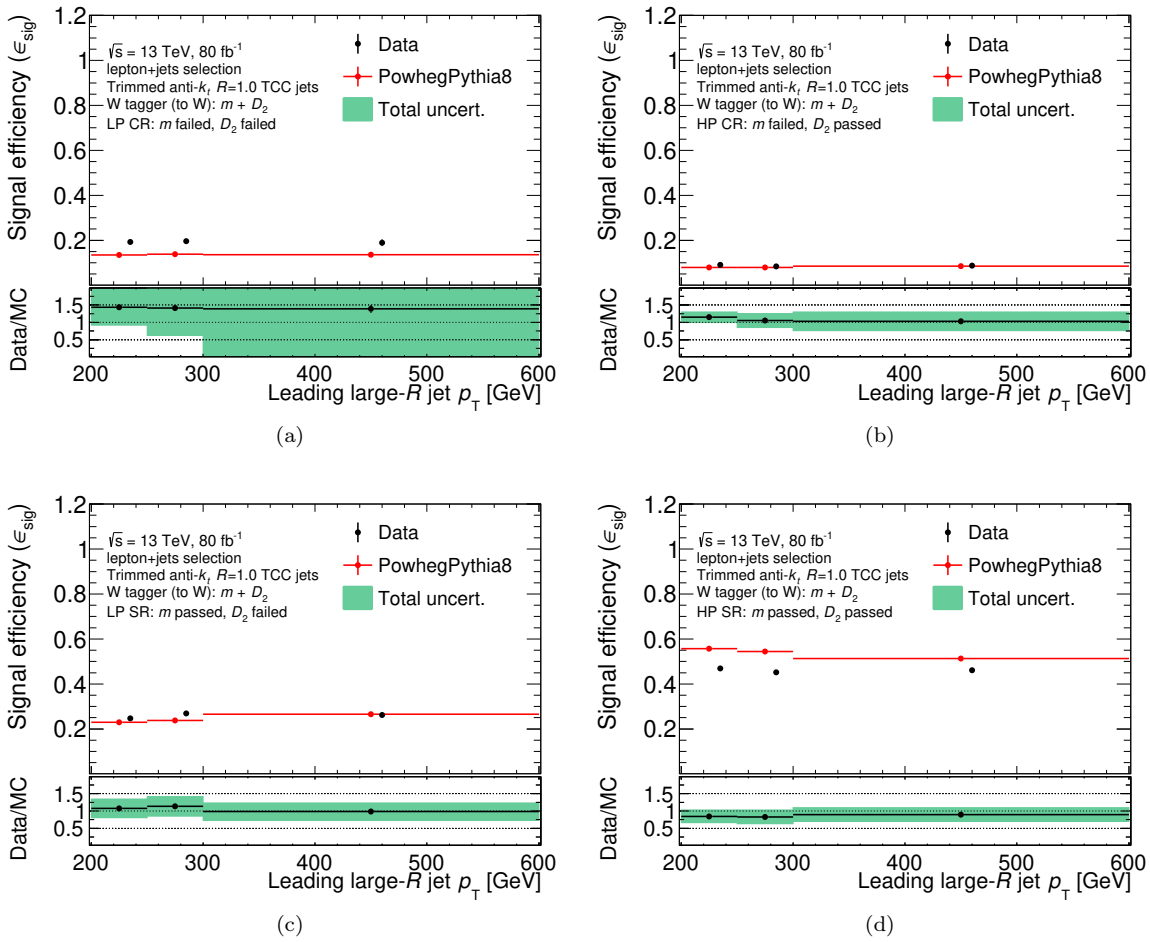

Figure 5.17: The signal efficiency on W-boson jet for the boson tagger as a function of the large-R jet p_{T} in (a) D_2 failed, mass failed, (b) D_2 passed, mass failed, (c) D_2 failed, mass passed and (d) D_2 passed, mass passed. In the bottom panel, the boson tagging efficiency SF are shown.

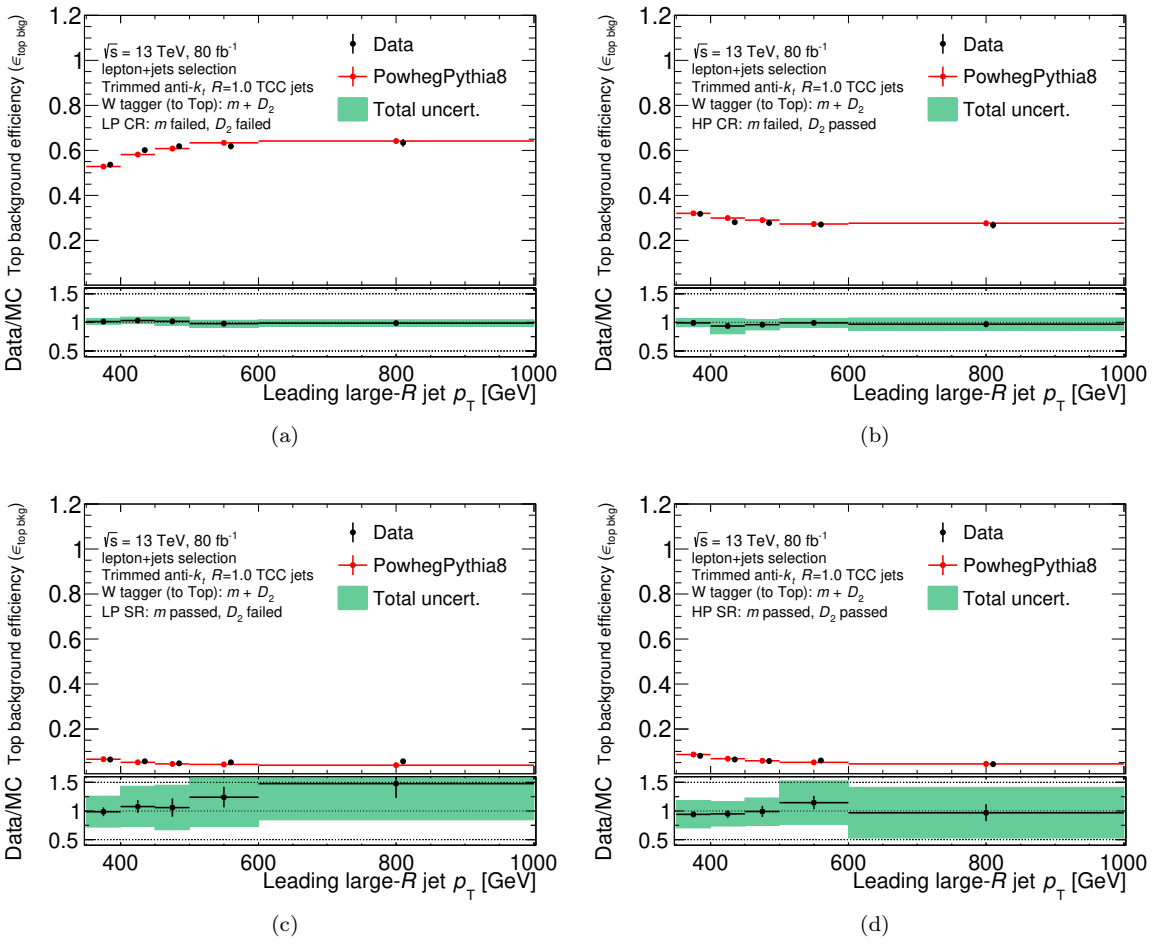

Figure 5.18: The signal efficiency on top-quark jet for the boson tagger as a function of the large-R jet p_{T} in (a) D_2 failed, mass failed, (b) D_2 passed, mass failed, (c) D_2 failed, mass passed and (d) D_2 passed, mass passed. In the bottom panel, the boson tagging efficiency SF are shown.

a broad kinematic range. For large-R jets with p_{T} from 450 GeV to 3000 GeV, multi-jet events are used to study a mixture of light-quark and gluon jets. For p_{T} from 200 GeV to 300 GeV, the γ+jet sample is used to study quark jets. Using these sample provides a means to probe the behavior of quark- and gluon-enriched regions of phase space separately. As in the case of the study of W-boson and top-quark jets, the background rejection is quantified in both data and MC simulation.

Event selection

The multi-jet events are selected by a single-jet trigger based on a single large-R jet with an online requirement of $E_{\mathrm{T}} > 360$ GeV during 2015 data taking and 420 GeV from 2016 to 2017. Then at least one large-R jet is required to have $p_{\mathrm{T}} > 450$ GeV. For γ+jet selection, events are selected with a single-photon trigger which requires *loose* quality photon with $E_{\mathrm{T}} > 120$ GeV in 2015 and 140 GeV in 2016 to 2017. The photon candidates are required to be within $|\eta| < 2.5$ and satisfy both the identification and the isolation criteria of the *tight* working points defined in Ref [156]. Furthremore, large-R jets are required to have $p_{\mathrm{T}} > 200$ GeV, $|\eta| < 2.0$ and $\Delta\phi(\mathrm{jet}, \gamma) > \frac{\pi}{2}$. Then events with at least one photon with $E_{\mathrm{T}} > 150$ GeV are selected to ensure that the trigger efficiency reaches plateau.

The normalization of selected multi-jet and γ+jet event is derived from data after the selection discussed above. First the contributions from hadronically decaying W-boson and top-quarks are subtracted from data. Then, the remaining simulated samples are normalized to the background-subtracted data.

Background rejection measurements

The background rejection $1/\epsilon_{\mathrm{bkg}}$ is measured for the boson tagger. This measurement is performed in both the multi-jet and γ+jet topologies as a function of the large-R jet p_{T}. Because of the purity of the target processes, the approach in this measurement is simpler than the signal efficiencies measurements. Using the signal-substracted data, the normalization of the multi-jet and γ+jet samples is performed and the background efficiency is calculated directly for the four regions. The derived SFs are applied to the MC simulated events coming from $W/Z + jets$ processes.

5.5.3 Systematic uncertainty

Various systematic uncertainty sources, such as MC generator differences, cross-section uncertainty, jet momentum and resolution uncertainties are propagated to the efficiency measurement. The propagation of systematic uncertainty is performed by repeating the fit procedure with templates varied by each systematic uncertainty. The difference of measured SF between the nominal and the varied templates is regarded as the corresponding SF uncertainty. Estimated SF uncertainties are combined by quadrature-sum with pruning systematic source with the uncertainty less than 5% of the total uncertainty. Large-R jet p_{T} scale, $t\bar{t}$ modeling, b-tagging SF uncertainty, and high-p_{T} extrapolation uncertainties are considered at the end of prunning. The correlation between the four regions is considered by definition. For background measurement uncertainty, γ+jets is used in 500 $<$ GeV, multi-jet result is used in 500 $>$ GeV due to the limitation of statistics. In the high-p_{T} region, the highest bin of each measurement is used with additional uncertainty derived from Herwig/Sherpa showering modeling and detector variations. Possible difference between W- and Z- tagger is also considered by taking the difference of signal efficiency.

Chapter 6

Event Selection

The event selection of the main analysis for heavy $WW/WZ/ZZ$ resonances in semi-leptonic final states is presented in this chapter. The event selection has been optimized to maximize signal sensitivities. As described in Section 6.2 and 6.3, a set of preselection including event cleaning and trigger requirements is applied first. At the beginning of the main selection, the leptonic decaying boson candidate V_ℓ is selected according to the number of charged-leptons and events are categorized into three channels: 0-lepton ($V_\ell = Z$, $Z \to \nu\nu$), 1-lepton ($V_\ell = W$, $W \to l\nu$), 2-lepton ($V_\ell = Z$, $Z \to ll$). For each channel, a VBF and ggF/DY categorization is applied as described in Section 6.4. Then a hadronically decaying vector boson candidate V_h is selected in each event. First the merged $V \to J$ identification is tried and if it fails the resolved $V \to jj$ identification is applied, as described in Section 6.5. Several signal regions (SRs) are defined to enhance signal sensitivities in all mass ranges. $V_\ell W$ and $V_\ell Z$ selections are independently analyzed by using different mass window cut for W and Z, however these selections have large overlap. Illustration of the selection flow and signal regions are summarized in Figure 6.1.

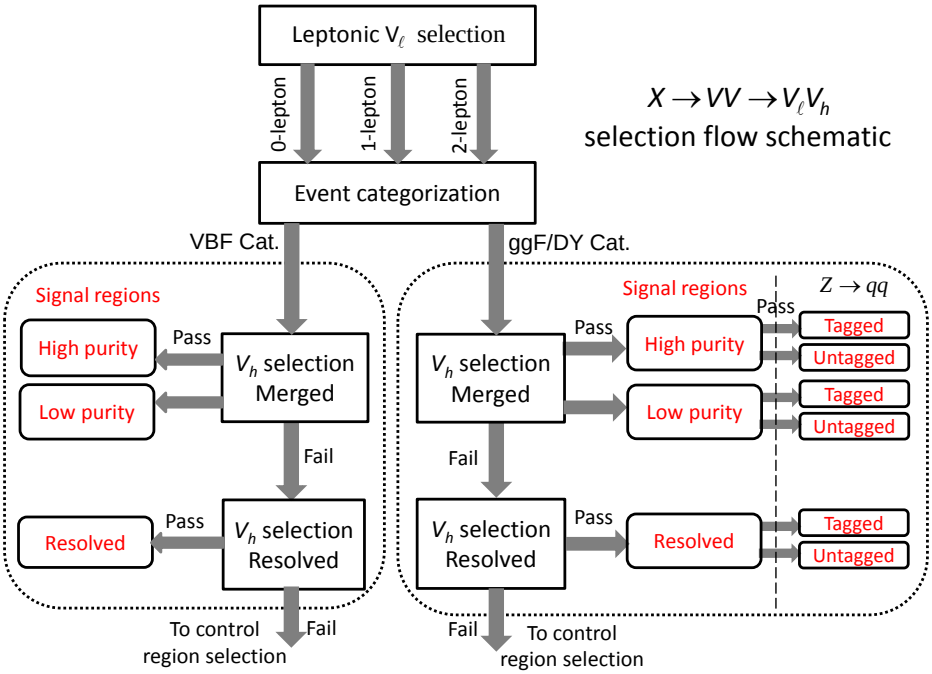

Figure 6.1: Illustration of the selection flow and signal regions of the $X \to VV$ search. The VBF category is targeted for VBF production whereas the ggF/DY category is for the rest. Three signal regions (high purity, low purity and resolved) are selected for each category based on the $V \to qq$ reconstruction. The 0-lepton channel does not consider resolved selection. For final states with hadronic decaying Z bosons, the three signal regions in the ggF/DY category are each further split into tagged and untagged according to the b-tagging information of jets from $Z \to qq$ decays.

6.1 Strategy to the SR orthogonalization

In VBF and ggF/DY categories of 0-, 1- and 2-lepton channels, events are checked if they pass each of both SRs and CRs selection. When an event fails a given selection, it is tested on the next selection according to the following order. Evens failing all of the selection are discarded and not used in the analysis. The order of selection is as follows:

- VBF categories
  - Merged high-purity signal region(s)
  - Merged low-purity signal region(s)
  - Resolved signal region(s)
  - Merged high-purity control region(s)
  - Merged low-purity control region(s)
  - Resolved control region(s)
- ggF/DY categories
  - Merged high-purity signal region(s)
  - Merged low-purity signal region(s)
  - Resolved signal region(s)
  - Merged high-purity control region(s)
  - Merged low-purity control region(s)
  - Resolved control region(s)

The order of event selection is most important in the transition region from $500 \leq m_X \leq 800$ GeV, where the hadronically decaying W/Z boson is reconstructed as both two small-R jets and one large-R jet. By switching the order of "Merged" and "Resolved" category, about 5% of events go to "Resolved" from "Merged". The prioritization was studied and this "merged-then-resolved" scheme is found to maximize the sensitivity since the most of two small-R jets are getting overlapped and a large-R jet can observe the hadronic decay more precisely in the intermediate-mass region.

6.2 Event Cleaning

To maintain the good data quality, the following event-level requirements are applied to the collected data. Events not listed in GRL (Good Run List) files, which contain the list of luminosity blocks approved for the ATLAS analysis, are discarded. Events affected by the recovery of SCT's single event upset (SEU)-induced bit flips [157] are also rejected. To remove the effect of the coherent noise burst over a large region of Liquid argon calorimeter [158], events within a time window of a burst are not used since energy measurements are corrupted in these events. Furthermore, corrupted data due to the non-optimal algorithm of Tile for rejecting problematic events are also discarded. Events are required to have a primary vertex with at least two associated tracks as defined in Section 4.1.2. The additional veto is applied to 2015 to 2016 data to suppress the events with calorimeter saturation problems [159].

6.3 Trigger requirements

The data was collected by the unprescaled single-lepton or $E_{\mathrm{T}}^{\mathrm{miss}}$ triggers with the lowest thresholds, according to number of charged lepton in each channel. 0-lepton channel uses $E_{\mathrm{T}}^{\mathrm{miss}}$ trigger which is available from $E_{\mathrm{T}}^{\mathrm{miss}} = 150$ GeV. Since $E_{\mathrm{T}}^{\mathrm{miss}}$ trigger efficiency reaches to the plateau at $E_{\mathrm{T}}^{\mathrm{miss}} \sim 250$ GeV, 0-lepton channel does not cover the region of $m_{VV} < 500$ GeV. In 1-lepton channel the single lepton or $E_{\mathrm{T}}^{\mathrm{miss}}$ triggers are used. The single electron triggers need to be satisfied in the electron sub-channel. The single muon triggers are required in the events with W-boson p_{T} reconstructed by muon and $E_{\mathrm{T}}^{\mathrm{miss}}$, $p_{\mathrm{T},\mu\nu}$, below 150 GeV and the $E_{\mathrm{T}}^{\mathrm{miss}}$ triggers are required in the events with $p_{\mathrm{T},\ell\nu}$ above 150 GeV in muon sub-channel to recover inefficiency of muon trigger due to the lack of detector coverage. In 2-lepton channel, single-electron or single-muon triggers are used. In all sub-channels, trigger efficiencies with regard to signal region are greater than 90% in the range of mass above 300 GeV. At the lowest target mass points, $m_{VV} = 300$ GeV, the trigger efficiencies are

about 70% in $\mu\nu qq$, 85% in $e\nu qq$, and greater than 90% in $llqq$ channel, respectively. Trigger efficiency scale factors are applied to the simulated events to compensate for the possible data/MC difference on the lepton trigger efficiency. For $E_{\mathrm{T}}^{\mathrm{miss}}$ trigger, scale factors are applied to take into account the data/MC difference in the range of between 150 GeV and 250 GeV. The trigger efficiency SF is not applied above 250 GeV because the efficiency is $\sim$ 100%. The total integrated luminosity is 139 fb^{-1}and this corresponds to about 95% of recorded luminosity as shown in Figure 2.2.

6.4 Categorization of production processes

The event selection for VBF and ggF/DY categorization is applied at the beginning of the analysis since ideally the VBF process results in two additional reconstructed jets, referred to as VBF-tag jets. These jets are typically well separated in pseudorapidity and have large dijet invariant mass.

In this analysis, a Recurrent Neural Network (RNN) [160] is adopted to classify the VBF and ggF/DY event topologies. The RNN uses four-momentum kinetic variables (p_T, η, ϕ, E) of up to two small-R jets in decreasing order of p_{T} as the RNN's input parameter. Figure 6.2 shows the leading jet kinematics. The kinematics for the sub-leading jet (Jet2) are similar to the leading jet. The VBF-jet topology is quite clear and we expect to have VBF jets in the forward region of the detector with higher energy with respect to the usual extra jets we have in the other physics processes.

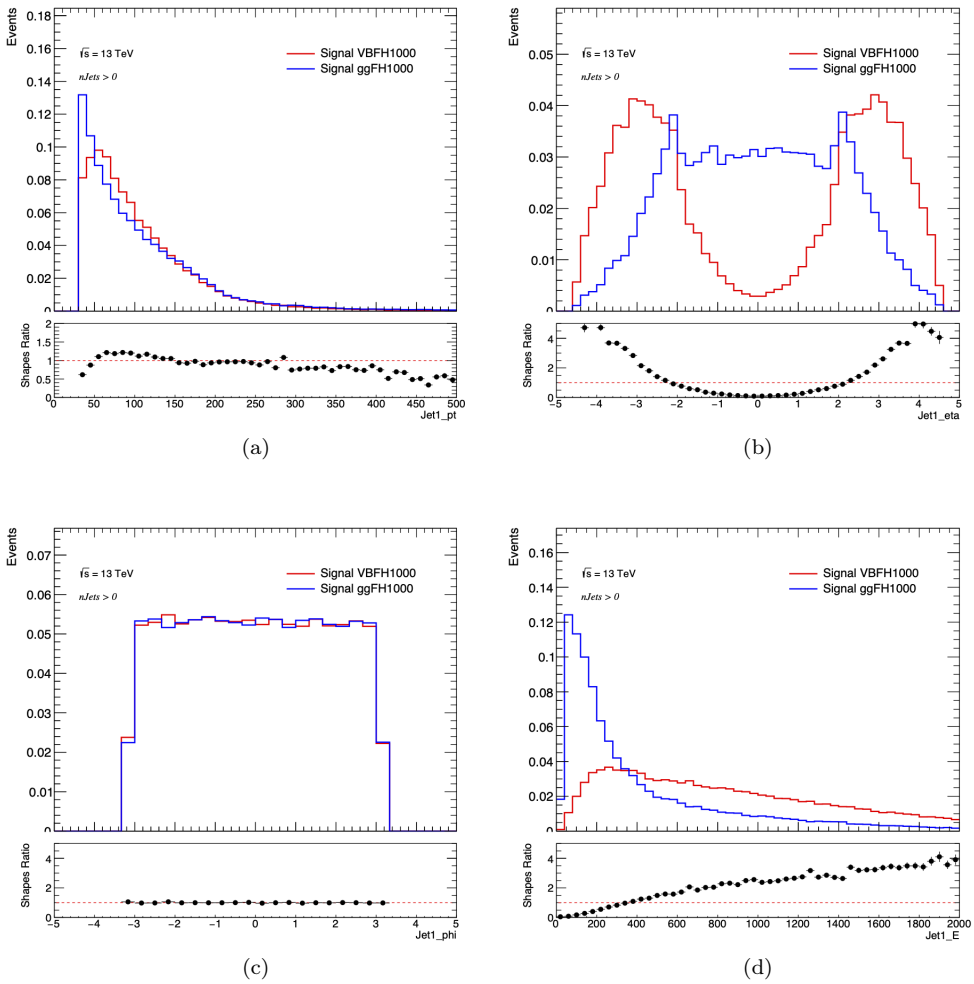

(a) (b)

(c) (d)

Figure 6.2: 4-momentum of the Jet1 used as RNN input for VBF (red) and ggF (blue) a scalar signal in 2-lepton channel.

To avoid overlapping with $V \to qq$ candidate jets, small-R jets with an angular separation of $\Delta R < 1$ with the leading large-R jet are removed from the VBF candidates jets. If large-R jets do not exist in the event,

a pair of small-R jets with its invariant mass closest to $W(Z)$ mass is removed. Events with no small-R jets left are automatically classified as ggF/DY events. The efficiency for VBF events is significantly improved by the RNN, while keeping contamination from ggF/DY low.

The training of RNN is performed to separate VBF and ggF/DY signal events. Though the RNN score distributions depend on the assumed model of a heavy resonance and its mass, these small differences are overshadowed by the large differences between the VBF and ggF/DY processes. Since the kinematics of VBF candidate jets are independent from the number of charge leptons, the RNN trained with the 1 TeV scalar resonance in the $X \to ZZ \to \ell\ell qq$ decay is applied to the three leptonic channels, the three resonance models and for all resonance masses. Based on signal sensitivity studies, events with RNN score > 0.8 are selected as the VBF category, and remaining events are categorized as the ggF/DY category. Figure 6.3 (a) compares the RNN score of simulated events of various signal models considered in this search. Figure 6.3 (b) shows the fraction of simulated signal events passing the RNN score requirement for different signal models.

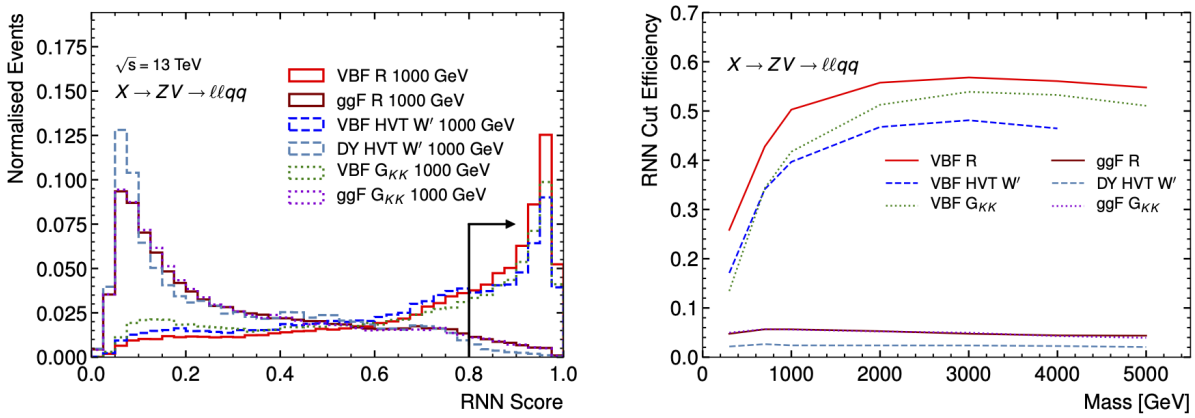

(a) (b)

Figure 6.3: (a) RNN score distributions for the signal models considered for this search; (b) The fraction of signal events passing the requirement on the RNN score.

Comparison of distributions of input variables for the RNN between data and MC are shown in Fig 6.4. The modeling of RNN scores between data and MC are shown in Fig 6.5. In general, the input variables and output scores are reasonably well modeled.

6.5 Reconstruction and identification of the $V \to qq$ decay

Two quarks from a hadronicaly decaying boson result in two energy deposits and the distance between them depend on their momentum. Therefore the $V \to qq$ decay can be either reconstructed from two resolved small-R jets ($V \to jj$) or one merged large-R jet ($V \to J$).

6.5.1 $W/Z \to J$ candidates (merged category)

Merged category is dedicated to high resonance masses, i.e. $m_{VV} > 500$ GeV. When the resonance mass gets higher, the hadronic W/Z boson is highly boosted so that the resulting two quarks can often be reconstructed as a large-R jet. This merged category requires at least one large-R jet, with the assumption that the one with the highest-p_T is assumed to be from $V \to q\bar{q}$ decay. Finally, the selected large-R jet is asked to be tagged as W/Z boson, based on the boson tagger discussed in Section 5.4.

Events are divided into four categories (HPSR, LPSR, HPCR and LPCR) based on the results of mass and D_2 cuts of the boson tagger, as described in Section 5.5.1. The detailed description of HPCR and LPCR can be also found in Section 6.8. Figure. 6.6 shows large-R jet mass and D_2 distributions before the boson tagging in 0-lepton channel. Comparing HVT W' 1.6 TeV signal (red line) and MC backgrounds indicates these variables have strong separation power.

Directions of two quarks tend to be perpendicular to a longitudinally-polarized W/Z boson, while to be horizontal in a transversely-polarized W/Z boson. This causes a higher D_2 variable for a transversely-polarized W/Z boson. Since the W/Z-boson tagger is optimized using longitudinally-polarized W/Z bosons,

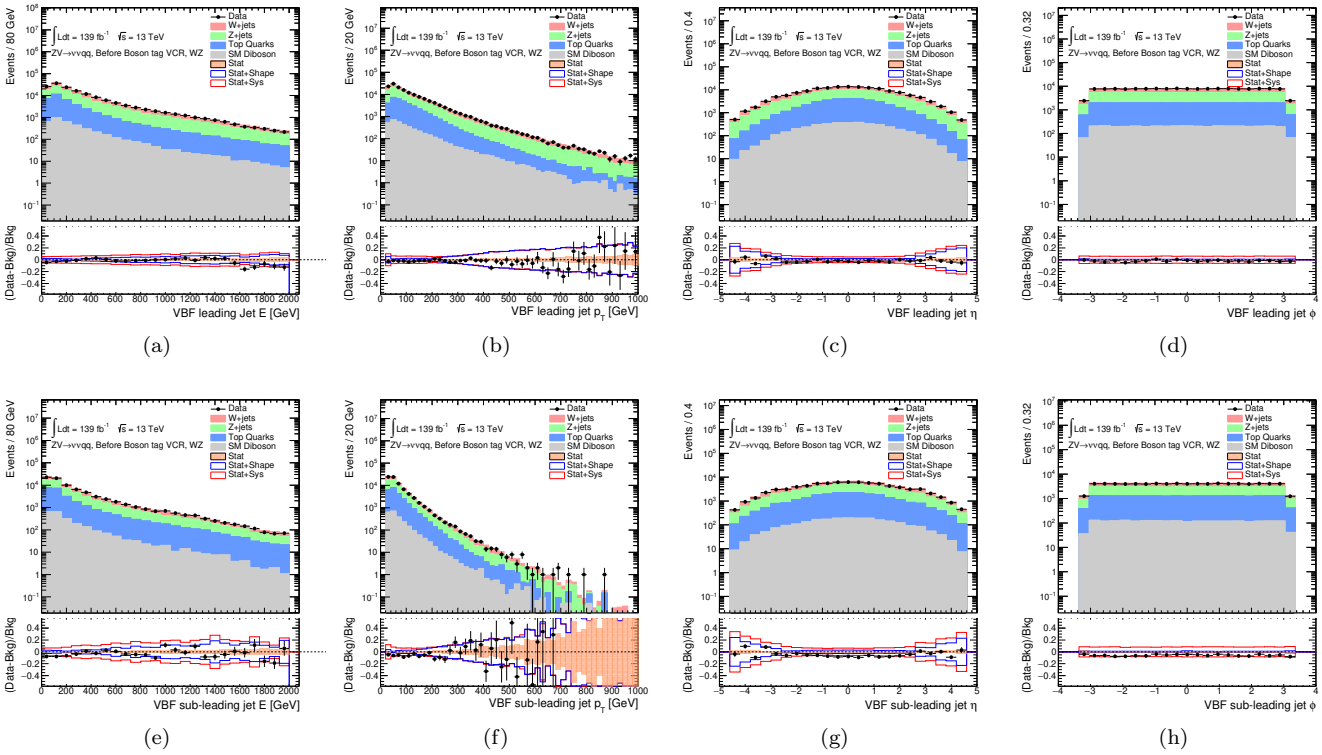

Figure 6.4: Comparison of distributions of input variables for the RNN between data and MC. (Top) Leading jet. (Bottom) Sub-leading jet.

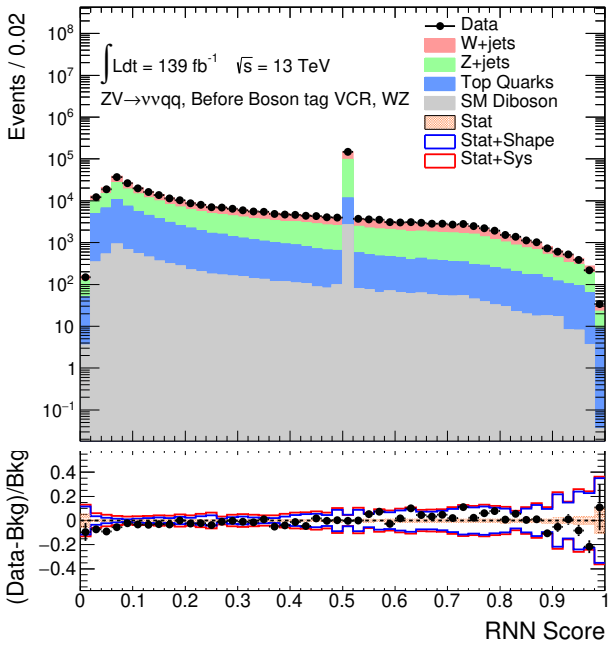

Figure 6.5: Comparison of distribution of RNN score between data and MC. The peak around score=0.5 corresponds to events with no small-R jets, which are categorized into ggF/DY category.

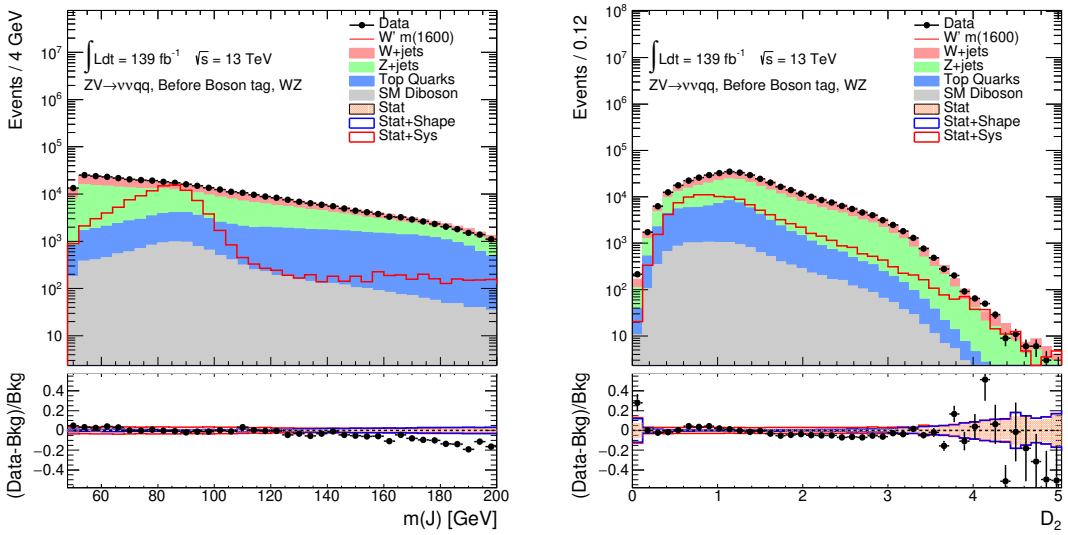

(a) (b)

Figure 6.6: Large-R jet (a) mass and (b) D_2 distributions before boson tagging in 0-lepton channel.

the tagger may not be sufficient for transversely-polarized W/Z bosons. To keep our analysis model-independent as much as possible, LPSR with higher D_2 is used in addition. This LPSR also contributes to the sensitivity of longitudinally-polarized signals.

In $Z \to q\bar{q}$ selection, events are further divided into *tagged* and *untagged* categories as well as resolved category. Since the b-tagging can not be applied to large-R jets directly, two leading VR track jets ghost-associated to the large-R jet are used. If both of VR track jets are b-tagged, events are used in *tagged* sub-category. Otherwise, events are selected in *untagged* sub-category. The efficinecy of double b-tagging on $Z \to bb$ signal is ∼10% while ∼1% on the background.

6.5.2 $W/Z \to jj$ candidates (resolved category)

Resolved category is important for the resonance mass below about 1 TeV. This category is applied in 1- and 2-lepton channels. 0-lepton channel does not use resolved category due to $E_{\mathrm{T}}^{\mathrm{miss}} > 250$ GeV cut. In this category, events are required to contain at least two *signal* jets with $|\eta| < 2.5$.

$Z \to q\bar{q}$ candidates

$Z \to b\bar{b}$ makes up 21% of $Z \to q\bar{q}$ signal events, while events with 2 b-jets are rare in the $W/Z + jets$ process that forms the dominant background. In order to exploit this feature, events are further split into *tagged* category with two b-tagged jets and *untagged* category with less than two b-tagged jets. In *tagger* cateogry, two b-tagged *signal* jets in events are used to reconstruct the hadronic Z. *untagged* cateogry uses the two jets with the highest-p_T, regardless of their b-tagged status.

$W \to q\bar{q}$ candidates

No enhancement of b-tagged jets is expected in $W \to q\bar{q}$ decay, thus no b-tagging selection is applied and that two signal jets with the highest-p_T are selected. If both selected jets are b-tagged, the event is discarded. The VBF category also does not adopt b-tagging selection since there is no significant sensitivity improvement expected due to the statistical limitation.

Kinematic cuts

After selecting $V \to q\bar{q}$ candidates, the leading jet of the two is required to have $p_T > 60$ GeV and the subleading jet is required to have $p_{\mathrm{T}} > 45(30)$ GeV in the 1-lepton (2-lepton) channel. Tighter cut on the subleading jet is preferred in 1-lepton channel for further multijet background rejection. Finally the dijet mass $m(jj)$ is used to maximize the sensitivity. The selected two jets are required to satisfy $78(68) < m(jj) < 105(98)$ GeV for the consistency with the hadronically decaying $Z(W)$ boson. Events failing the dijet mass

window cut are used in the control regions discussed in 6.8. The analysis for $W \to q\bar{q}$ and $Z \to q\bar{q}$ channels are performed separately.

6.6 Event selections of individual leptonic channels

As described in Section 6.5, the selection of hadronic decaying V boson is common to all three channels. On the other hand, the selection of leptonic decaying V boson is specific to individual leptonic channels and described below.

6.6.1 0-lepton: $ZV \to \nu\nu qq$

As described in 6.5.2, 0-lepton channel employs only merged category due to its high $E_{\mathrm{T}}^{\mathrm{miss}}$ threshold. A $\nu\nu$ pair from a Z boson decay is chosen by requiring no *Loose* lepton and $E_{\mathrm{T}}^{\mathrm{miss}} > 250$ GeV. To reduce QCD multijet and non-collision backgrounds, events are required to satisfy $p_{\mathrm{T}}^{\mathrm{miss}} > 50$ GeV, $\min(\Delta\phi(E_{\mathrm{T}}^{\mathrm{miss}}, j)) > 0.4$ and $\Delta\phi(E_{\mathrm{T}}^{\mathrm{miss}}, p_{\mathrm{T}}^{\mathrm{miss}}) < 1.0$, where $p_{\mathrm{T}}^{\mathrm{miss}}$ is the track-based missing momentum, $\min(\Delta\phi(E_{\mathrm{T}}^{\mathrm{miss}}, j))$ is the minimum azimuthal angle difference between $E_{\mathrm{T}}^{\mathrm{miss}}$ and small-R jets, and $\Delta\phi(E_{\mathrm{T}}^{\mathrm{miss}}, p_{\mathrm{T}}^{\mathrm{miss}})$ is the azimuthalangle difference between $E_{\mathrm{T}}^{\mathrm{miss}}$ and $p_{\mathrm{T}}^{\mathrm{miss}}$.

Figure 6.7 shows that the QCD multijet backgrounds are highly suppressed by these selections. Only statistical uncertainty is included in the plots. The large discrepancy between the observed data and the simulated events are coming from multijet and non-collision backgrounds. Before the anti-QCD cuts (top figures), most of multijet and non-collision backgrounds dominated at the lowest $p_{\mathrm{T}}^{\mathrm{miss}}$ region. The background rejection is achieved by the cut on $p_{\mathrm{T}}^{\mathrm{miss}}$ and $\min(\Delta\phi(E_{\mathrm{T}}^{\mathrm{miss}}, j))$ (top-bottom: g-i). Small non-collision background is found at high-$\Delta\phi(E_{\mathrm{T}}^{\mathrm{miss}}, p_{\mathrm{T}}^{\mathrm{miss}})$ region. The cut on it and large-R jet mass cut $m(J) > 50$ GeV can reduce the remaining non-collision background more (bottom: j-l). The fraction of the multijet and non-collision backgrounds is negligibly small after the anti-QCD cuts. The event selection of 0-lepton channle is summarized in Table 6.1. Validation region (VR) is defined in Section 6.8.

Reconstruction of m_{ZV}

For the final discriminant, we use the transverse mass m_T reconstructed by $E_{\mathrm{T}}^{\mathrm{miss}}$ and the large-R jet,

$$m_{\mathrm{T}} = \sqrt{(E_{\mathrm{T}}^{J} + E_{\mathrm{T}}^{\mathrm{miss}})^2 - (\vec{p}_{\mathrm{T}}^{J} + \vec{E}_{\mathrm{T}}^{\mathrm{miss}})^2}, \tag{6.1}$$

where E_{T}^{J} and $\vec{p}_{\mathrm{T}}^{J}$ are the transverse energy and momentum of the large-R jet.

Table 6.1: A summary of signal region event selection. These regions are split into VBF and ggF(DY) categories as described in Section 6.4.

Selection	SR		VR	
	HP	LP	HP	LP
Number of Loose leptons	0			
$E_{\mathrm{T}}^{\mathrm{miss}}$	> 250 GeV			
$p_{\mathrm{T}}^{\mathrm{miss}}$	> 50 GeV			
$\min(\Delta\Phi(E_{\mathrm{T}}^{\mathrm{miss}}$,small-$R$ jets))	> 0.4			
$\Delta\Phi(E_{\mathrm{T}}^{\mathrm{miss}}, p_{\mathrm{T}}^{\mathrm{miss}})$	< 1			
Number of large-R jets	≥ 1 large-R jets			
D_2 cut	pass	fail	pass	fail
W/Z mass window cut	pass	pass	$m_J > 50$ GeV, fail mass window cut	
Numb. of associated VR track jets b-tagged	For $Z \to J$: ≤ 1 ($= 2$) for untagged (tagged) category			

The cutflow for HVT signal yields without cross-section normalization are summarized in Table 6.8.

6.6.2 1-lepton: $WV \to \ell\nu qq$

1-leton channel requires events containing a $W \to \ell\nu$ candidate. The identification requires exactly one *Tight* lepton. To suppress the multijet background, $E_{\mathrm{T}}^{\mathrm{miss}} > 100$ (60) GeV and $p_{\mathrm{T},\ell\nu} > 200$ (75) GeV are applied in merged (resolved) category.

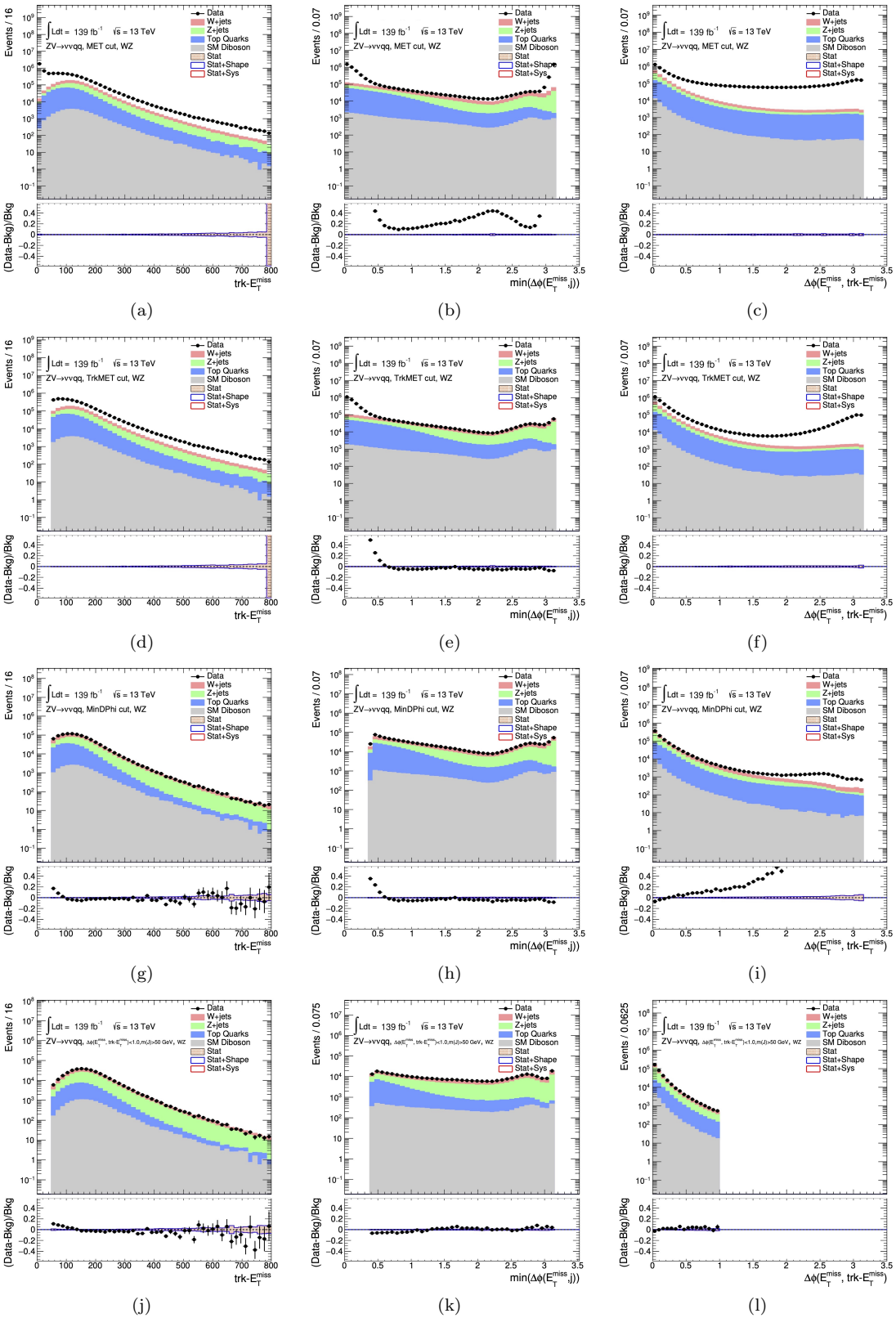

Figure 6.7: Observed and expected distributions of the three variables used to reject QCD background. These are $p_{\mathrm{T}}^{\mathrm{miss}}$ (left), $\min(\Delta\phi(E_{\mathrm{T}}^{\mathrm{miss}}, j))$ (middle), and $\Delta\phi(E_{\mathrm{T}}^{\mathrm{miss}}, p_{\mathrm{T}}^{\mathrm{miss}})$ (right) following the selections from top to bottom.

Table 6.2: Cutflow for HVTWZ DY (VBF) signals with 600 GeV and 2000GeV in 0-lepton.

Signal	ggF/DY				VBF			
	600 GeV		2000 GeV		600 GeV		2000 GeV	
Selection								
Generated	90000		45000		150000		150000	
Preselection	77151		44233		102215		136545	
Trigger	76822		44232		100212		136410	
$E_{\mathrm{T}}^{\mathrm{miss}} > 250$ GeV	48258		44158		41483		130434	
$p_{\mathrm{T}}^{\mathrm{miss}} > 50$ GeV	46817		43995		39876		128904	
min$\Delta\Phi(E_{\mathrm{T}}^{\mathrm{miss}}$,small-$R$ jets) >0.4 GeV	43520		39742		33205		100156	
$\Delta\Phi(E_{\mathrm{T}}^{\mathrm{miss}}, p_{\mathrm{T}}^{\mathrm{miss}}) < 1.0$	43443		37873		32624		99784	
RNN categorization	ggF/DY	VBF	ggF/DY	VBF	ggF/DY	VBF	ggF/DY	VBF
Number of large-R jets ≥ 1	35921	330	37075	439	17889	5531	60425	38063
Merged HP CR	2436	22	3205	41	1129	297	5467	3564
Merged LP CR	4575	34	4700	55	2111	606	7638	4704
Merged HP SR	16401	169	17913	218	5758	2595	23473	16758
Merged LP SR	6982	50	8337	102	2534	1066	12394	8479

Reconstruction of m_{WV}

1-lepton channel uses the WV system mass m_{WV}, reconstructed by lepton, neutrino and the hadronically decaying boson candidate. The neutrino momentum in z-direction, p_z, is obtained by assuming that the mass of the lepton and neutrino system is the PDG value of W boson mass [18]. This constraint leads to a quadratic equation and p_z is taken as either the real component of the complex solutions or the one with the smaller absolute value of the two real solutions.

In the resolved category, the $W(Z)$ mass constraint is imposed on the dijet system in the $W(Z) \to q\bar{q}$ channel. The kinetic variables of the corrected dijet system are

$$p_{\mathrm{T},jj}^{\mathrm{corr}} = p_{\mathrm{T},jj} \times \frac{m_{W(Z)}}{m_{jj}}, \tag{6.2}$$

$$m_{jj}^{\mathrm{corr}} = m_{W(Z)}, \tag{6.3}$$

where m_{jj} and $m_{W(Z)}$ are the reconstructed invariant mass of the hadronically decaying W/Z boson and the W/Z boson mass value taken by PDG (Particle Data Group) [18], respectively. The m_{WV} is reconstructed by using these corrected variables and the resolution is improved by 20% for signal samples with negligible shape distortion of background samples. Figure 6.8 shows the comparison between before and after the correction in 1- and 2-lpeton channels. Since the signal sensitivity improvement is not found in the merged category

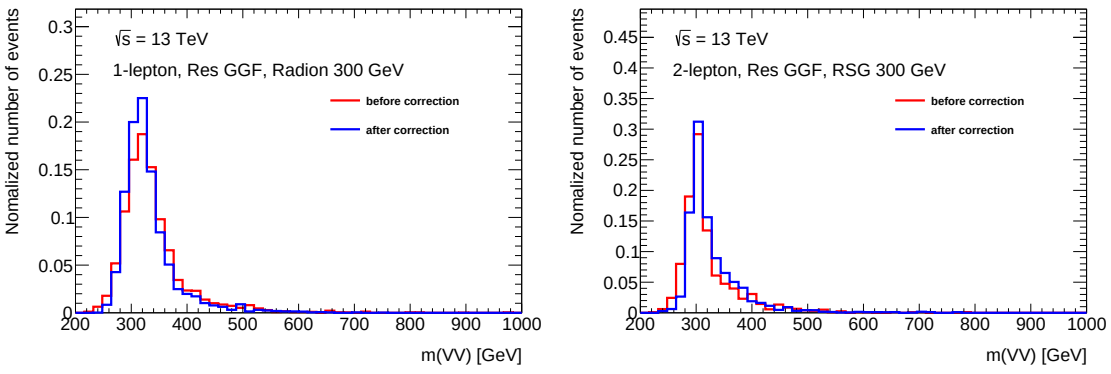

(a) (b)

Figure 6.8: Comparison of the reconstructed invariant m_{VV} between before and after the dijet mass correction in (a) 1-lepton and (b) 2-lepton.

due to the trimming algorithms as defined in Section 4.3.1, we do not constrain the large-R jet mass.

Table 6.3: Summary of selection criteria used to define the signal region (SR), W+jets control region (W CR) and $t\bar{t}$ control region ($t\bar{t}$ CR) for merged 1-lepton channel.

Selection		SR		W CR (WR)		$t\bar{t}$ CR (TR1)	
		HP	LP	HP	LP	HP	LP
$W \to l\nu$	Num of Tight leptons	1					
	Num of Loose leptons	0					
	E_{T}^{miss}	> 100 GeV					
	$p_{\mathrm{T},\ell\nu}$	> 200 GeV					
$W/Z \to J$	Num of large-R jets	≥ 1					
	D_2 cut	pass	fail	pass	fail	pass	fail
	W/Z mass window cut	pass	pass	fail	fail	pass	pass
	Numb. of associated VR track jets b-tagged	For $Z \to J$: ≤ 1 ($= 2$) for untagged (tagged) category					
Topology cut	$\min(\mathrm{p_{T,\ell\nu}}, \mathrm{p_{T,J}})/\mathrm{m_{WV}}$	$> 0.35(0.25)$ for DY/ggF (VBF) category					
Top-quark veto	Num of b-tagged jets outside of large-R jet	0				≥ 1	
Pass VBF selection		no (yes) for DY/ggF (VBF) category					

Merged category

In the merged category, the relative boson p_{T} cut is introduced:

- $\min(\mathrm{p_{T,\ell\nu}}, \mathrm{p_{T,J}})/\mathrm{m_{WV}} > 0.35$ (0.25)

for DY(VBF) category. The optimal threshold does not depend on signal mass point and signal models (spin-0,-1 and -2). Figure 6.9 shows the relative boson p_{T} distributions of signal and background in merged category.

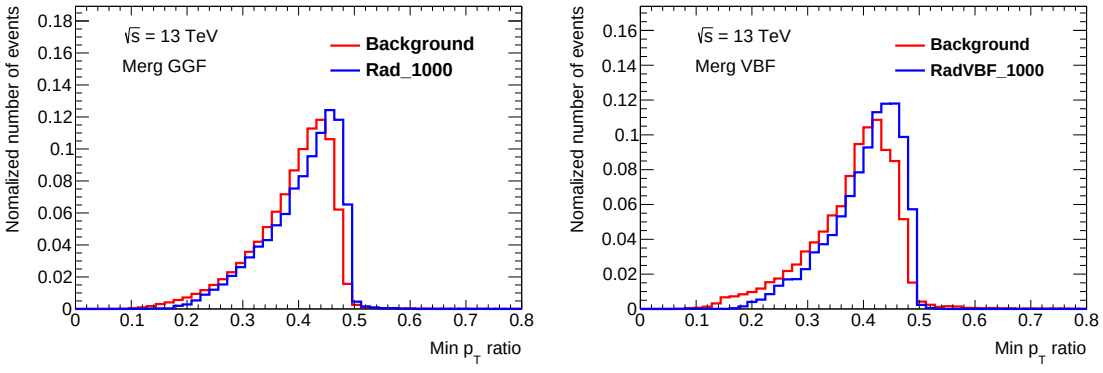

(a) (b)

Figure 6.9: Comparison of distributions for relative boson p_{T} between 1 TeV Radion signal and background in (a) $\ell\nu qq$ merged ggF and (b) $\ell\nu qq$ merged VBF categories.

In order to suppress $t\bar{t}$ background, the event is removed if there is at least one b-tagged jet with ΔR(b-tagged jet, large-R jet) > 1.0. About 70% of the remaining $t\bar{t}$ backgrounds are removed by this cut. Event selection for the merged category is summarized in Table 6.3.

Resolved category

Events failing the merged category are analyzed in the resolved category. The following topological cuts are applied to enhance the event of which two high-p_{T} bosons are back-to-back in the x-y plane:

- $\Delta\phi(l, E_{\mathrm{T}}^{\mathrm{miss}}) < 1.5$
- $\Delta\phi(j1, j2) < 1.5$
- $\Delta\phi(l, j1(2)) > 1.$

Table 6.4: The list of selection cuts in the resolved analysis for the WW and WZ signal regions (SR), W + jets control region (WR) and $t\bar{t}$ control region (TR). More details of the object definitions can be found in Section 4.

cuts		SR	W CR (WR)	$t\bar{t}$ CR (TR1)
$W \to l\nu$	Number of Tight leptons	1		
	Number of Loose leptons	0		
	$E_{\mathrm{T}}^{\mathrm{miss}}$	> 60 GeV		
	$p_{\mathrm{T},\ell\nu}$	> 75 GeV		
$W/Z \to jj$	Number of small-R jets	≥ 2		
	Leading jet p_{T}	> 60 GeV		
	Subleading jet p_{T}	> 45 GeV		
	$Z \to q\bar{q}$ $W \to q\bar{q}$	$78. < m_{jj} < 105.$Gev $68. < m_{jj} < 98.$Gev	$50. < m_{jj} < 68.$ GeV or $105. < m_{jj} < 150.$ GeV	$50 < m_{jj} < 150$Gev
	Num. of b-tagged jets	For $Z \to jj$: ≤ 1 ($= 2$) for untagged (tagged) category		
Topology cuts	$\Delta\phi(j, l)$	> 1.0		
	$\Delta\phi(j, E_{\mathrm{T}}^{\mathrm{miss}})$	> 1.0		
	$\Delta\phi(j, j)$	< 1.5		
	$\Delta\phi(l, E_{\mathrm{T}}^{\mathrm{miss}})$	< 1.5		
	$\min(p_{\mathrm{T},\ell\nu}, p_{\mathrm{T},jj})/m_{WV}$	$> 0.35(0.25)$ for DY/ggF (VBF) category		
Top veto	Number of additional b-tagged jets	0		≥ 1
Pass VBF selection		no (yes) for DY/ggF (VBF) category		

- $\Delta\phi(j1(2), E_{\mathrm{T}}^{\mathrm{miss}} > 1.0$
- $\mathrm{min}(\mathrm{p_{T,\ell\nu}}, \mathrm{p_{T,jj}})/\mathrm{m_{WV}} > 0.35(0.25)$ for DY/ggF(VBF) category

As in the merged category, the relative boson p_{T} cut is applied:

- $\mathrm{min}(\mathrm{p_{T,\ell\nu}}, \mathrm{p_{T,jj}})/\mathrm{m_{WV}} > 0.35$ (0.25).

Finally, the event with additional b-tagged jets not associated to the W/Z in the event is rejected to suppress $t\bar{t}$ background as well as the merged category. Event selection for the merged category is summarized in Table 6.4. The cutflow for HVT signal yields without cross-section normalization are summarized in Table 6.5. Only the merged category is shown since 1-lepton channel has better sensitivity in higher mass range where the most of events are categorized into the merged cateogry.

Table 6.5: Cutflow for HVTWZ DY (VBF) signals with 600 GeV and 2000GeV in 1-lepton Merged category.

Signal	ggF/DY				VBF			
	600 GeV		2000 GeV		600 GeV		2000 GeV	
Selection								
Generated	90000		80000		150000		150000	
Preselection	47818		40133		73136		90316	
Only 1 lepton	45751		38666		70240		86434	
RNN categorization	ggF/DY	VBF	ggF/DY	VBF	ggF/DY	VBF	ggF/DY	VBF
≥ 1 large-R jet	30368	295	37484	457	24307	9042	45930	32704
$E_{\mathrm{T}}^{\mathrm{miss}} > 100$GeV	21045	205	35238	422	15349	5173	41653	29621
$p_{\mathrm{T},\ell\nu} > 200$GeV	20390	196	34105	407	13574	4320	40809	29027
p_{T} ratio	19288	196	29324	395	10469	4308	18355	23126
LP Untagged TCR	88	1	361	3	99	29	215	254
LP Tagged TCR	11		71		11		48	
LP Untagged WCR	714	3	2196	36	496	213	1135	1804
LP Tagged WCR	131		459		49		255	
LP Untagged SR	2199	25	4660	76	972	528	2959	4365
LP Tagged SR	371		668		134		442	
HP Untagged TCR	201	2	961	9	215	91	597	578
HP Tagged TCR	22		177		32		73	
HP Untagged WCR	463	8	1840	30	1041	112	1041	1678
HP Tagged WCR	80		377		242		242	
HP Untagged SR	6306	76	11166	181	7088	1673	7088	9969
HP Tagged SR	991		1874		1096		1096	

6.6.3 2-lepton: $ZV \to \ell\ell qq$

The $Z \to ll$ candidates are selected by requiring two isolated same-flavor leptons (electrons or muons) satisfying *Loose* criteria defined in Section 4.4.1 and 4.4.2. The lepton p_T threshold is optimized to achieve better signal sensitivity. Both leading and sub-leading leptons are required to have $p_T > 30$ GeV. The optimized lepton p_T cut also makes a better fake leptons reduction compared to the previous round of analysis [148].

For muon pairs, opposite charges are required. Electron pairs are not required to have opposite charges since electrons are more susceptible to charge mis-identification due to the conversions of photons from bremsstrahlung. The reconstructed dilepton invariant mass is then required to be consistent with the Z boson mass. Fixed mass window cut is applied to electrons while $p_{T,ll}$ dependent mass window cut is applied to muons:

$$83 \text{ GeV} < m_{ee} < 99 \text{ GeV}, \tag{6.4}$$

$$(85.6 - 0.0117 p_{\mathrm{T},\mu\mu}) \text{ GeV} < m_{\mu\mu} < (94.0 + 0.0185 p_{\mathrm{T},\mu\mu}) \text{ GeV}, \tag{6.5}$$

which was optimized from the 2015+16 analysis [148]. The signal efficiencies for the $Z \to \ell\ell$ boson mass window cut are shown in Figure 6.10.

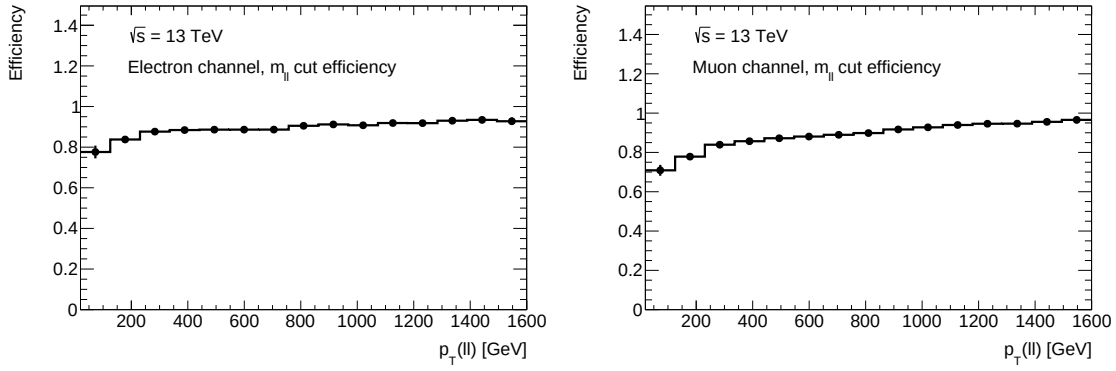

(a) (b)

Figure 6.10: The dilepton mass window cut efficiencies for signal in (a) electron and (b) muon channesl.

Reconstruction of m_{ZV}

The m_{ZV} is reconstructed by the selected two leptons and the hadronically decaying boson candidate (A large-R jet or two small-R jets). The dijet mass is corrected by imposing W/Z mass constraint as with 1-lepton channel. Furthermore, the Z-mass constraint is also imposed on the dimuon system by the same equation,

$$p_{T,\mu\mu}^{\mathrm{corr}} = p_{T,\mu\mu} \times \frac{m_Z}{m_{\mu\mu}}, \tag{6.6}$$

$$m_{\mu\mu}^{\mathrm{corr}} = m_Z. \tag{6.7}$$

This correction compensates the poor muon momentum resolution at the very high-p_T region and improves the m_{ZV} resolution significantly. Since the electron p_{T} is measured by the EM calorimeter, this constraint is not applied in the electrons pair because of the better momentum resolution at high-p_T region.

Merged category

In the marged category, events are required to have at least one large-R jet. Events are further required to satisfy

- $\min(\mathrm{p_{T,ll}}, \mathrm{p_{T,J}})/\mathrm{m_{ZV}} > 0.35(0.25)$

in DY/ggF(VBF) category as well as 1-lepton channel. Summary of the $llqq$ event selections in the merged category is found in Table 6.6.

Table 6.6: Event selection summary for merged analysis in 2-lepton channel.

Selection		SR		Z CR (ZR)		$t\bar{t}$ CR (TR2)	
		HP	LP	HP	LP	HP	LP
$Z \to \ell\ell$	Number of Loose leptons	2					
	Same flavor	yes				no	
	Subleading lepton p_T	$> 30\,\text{GeV}$					
	dilepton invariant mass	$83 < m_{ee} < 99\text{Gev}$ $-0.01170p_{T,ll} + 85.63 < m_{\mu\mu} < 0.01850p_{T,ll} + 94.00\text{GeV}$				$76 < m_{e\mu} < 106\,\text{GeV}$	
	Opposite sign	For $\mu\mu$ channel only				–	
$W/Z \to J$	Num of large-R jets	≥ 1					
	D_2 cut	pass	fail	pass	fail	pass	fail
	W/Z mass window cut	pass	pass	fail	fail	pass	pass
	Numb. of associated VR track jets b-tagged	For $Z \to J$: ≤ 1 $(= 2)$ for untagged (tagged) category					
Topology cut	$\min(p_{T,ll}, p_{T,J})/m_{WV}$	$> 0.35(0.25)$ for the DY/ggF (VBF) category					
Pass VBF selection		no (yes) for the DY/ggF (VBF) category					

Resolved category

The $ZV \to lljj$ candidates are selected from the events rejected in the merged category. Two small-R 'signal' jets are required to have a dijet invariant mass which is consistent with a $V \to q\bar{q}$ decay. The relative boson p_T cut is also applied,

- $\min(\text{P}_{\text{T,ll}}, \text{p}_{\text{T,jj}})/\text{m}_{\text{ZV}} > 0.35$

in both ggF/DY(VBF) category. The definitions of SR and CRs for 2-lepton channel in the resolved category are summarized in Table 6.7.

Table 6.7: Event selection summary for resolved analysis in 2-lepton channel.

Selection		SR	Z CR (ZR)	$t\bar{t}$ CR (TR2)
$Z \to \ell\ell$	Number of Loose leptons	2		
	Same flavor	yes		no
	Subleading lepton p_T	$> 30\,\text{GeV}$		
	dilepton invariant mass	$83 < m_{ee} < 99\text{GeV}$ $-0.01170p_{T,ll} + 85.63 < m_{\mu\mu} < 0.01850p_{T,ll} + 94.00\text{GeV}$		$76 < m_{e\mu} < 106\,\text{GeV}$
	Opposite sign	For $\mu\mu$ channel only		–
$W/Z \to jj$	Num of signal small-R jets	2		
	Leading jet p_T	$> 60\,\text{GeV}$		
	Subleading jet p_T	$> 30\,\text{GeV}$		
	$Z \to q\bar{q}$ $W \to q\bar{q}$	$78. < m_{jj} < 105.\text{GeV}$ $68. < m_{jj} < 98.\text{GeV}$	$50. < m_{jj} < 68.\,GeV$ or $105. < m_{jj} < 150.\,\text{GeV}$	$50 < m_{jj} < 150\text{GeV}$
	Num. of b-tagged jets	For $Z \to jj$: ≤ 1 $(= 2)$ for untagged (tagged) category		
Topology cut	$\min(p_{T,ll}, p_{T,J})/m_{WV}$	$> 0.35(0.25)$ for the DY/ggF (VBF) category		
Pass VBF selection		no (yes) for DY/ggF (VBF) category		

The cutflow for HVT signal yields without cross-section normalization are summarized in Table **??**. Only the resolved category is shown since 2-lepton channel has better sensitivity in lower mass range where the most of events are categorized into the resolved cateogry. For 2 TeV signal, number of events in Resolved SR/ZCR are significantly small since most of events are categorized as Merged.

6.7 Signal efficiencies and mass resolutions

Signal selection efficiencies depend on the signal model, the production process, and the mass of heavy resonances. Figures 6.11, 6.12 and 6.13 show the acceptance times efficiency ($A \times \epsilon$) of the signal events from MC simulations as a function of the resonance mass for (a) ggF/DY and (b) VBF production, combining all SRs of both ggF/DY and VBF categories of both resolved and merged analyses. The $A \times \epsilon$ curves are mostly determined by the merged analyses and the resolved analyses contribute only at the low mass region, up to approximately 1 TeV.

Large differences in $A \times \epsilon$ for different resonances are the results of the different spins. The spin-0 radions are produced with isotropic angular distributions for both ggF and VBF production, while the spin-1

Table 6.8: Cutflow for HVTWZ DY (VBF) signals with 600 GeV and 2000GeV in 2-lepton Resolved category.

Signal	ggF/DY				VBF			
	600 GeV		2000 GeV		600 GeV		2000 GeV	
Selection								
Generated	89000		75000		150000		150000	
Preselection	44008		42628		70068		78682	
Lepton p_{T}	38384		40651		56960		74744	
m_{ll}	31830		35463		48580		65501	
Same flavor	31753		35322		48562		65459	
RNN categorization	ggF/DY	VBF	ggF/DY	VBF	ggF/DY	VBF	ggF/DY	VBF
Two signal jets	28862	350	18384	194	37462	12405	26870	12121
Leading jet p_{T}	28742	343	18383	194	36704	12141	26776	12082
p_{T} ratio	21135	302	13162	175	7347	7396	3788	5629
Resolved CR	760	27	45	1	319	559	19	55
Resolved SR	5823	86	15	1	1758	2683	18	132

HVT resonances and spin-2 RS gravitons are produced more centrally (more forward) for ggF/DY (VBF) production. These different angular distributions lead to different efficiencies of the p_{T} ratio requirement. Moreover, the angular requirements between jets and $E_{\mathrm{T}}^{\mathrm{miss}}$ in the 0-lepton channel are more efficient for DY production of HVT resonances than for ggF production of radion and graviton due to the difference in the color factors between the initial-state quarks and gluons.

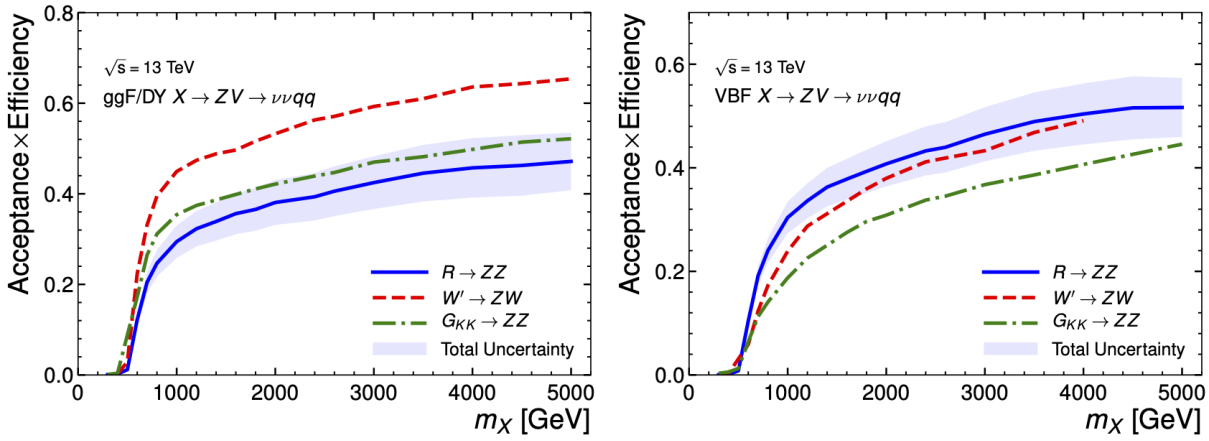

Figure 6.11: Selection acceptance times efficiency for the $X \to ZV \to \nu\nu qq$ signal events from MC simulations as a function of the resonance mass for (a) ggF/DY and (b) VBF production, combining HP and LP signal regions.The light blue band represents the total statistical and systematic uncertainties for the radion model, and the total uncertainties are similar for the other signal models.

6.8 Control region definitions

The control regions (CRs) are defined in order to estimate the dominant backgrounds in this analysis: Z+jets , W + jets and $t\bar{t}$. The CRs are used in the fit in addition to SRs to give a constraint to the normalization of each background process. The CRs for each background are defined in which the background becomes most dominant e.g. Z + jets for 2-lepton and W + jets and $t\bar{t}$ for 1-lepton. The sckematic view of SR/CR relation is shown in Figure 6.14. The dedicated CRs are used commonly for all of 0-, 1- and 2-lepton channels. However, the independent CRs for resolved/merged, b-tagged/untagged, HP/LP, and VBF/ggF categories are employed to take into account for possible mis-modeling of the background modeling caused by each event selection. In addition, the possible mis-modeling between the number of charged-lepton is considered as a systematic uncertainty as discussed in Section 8.2.

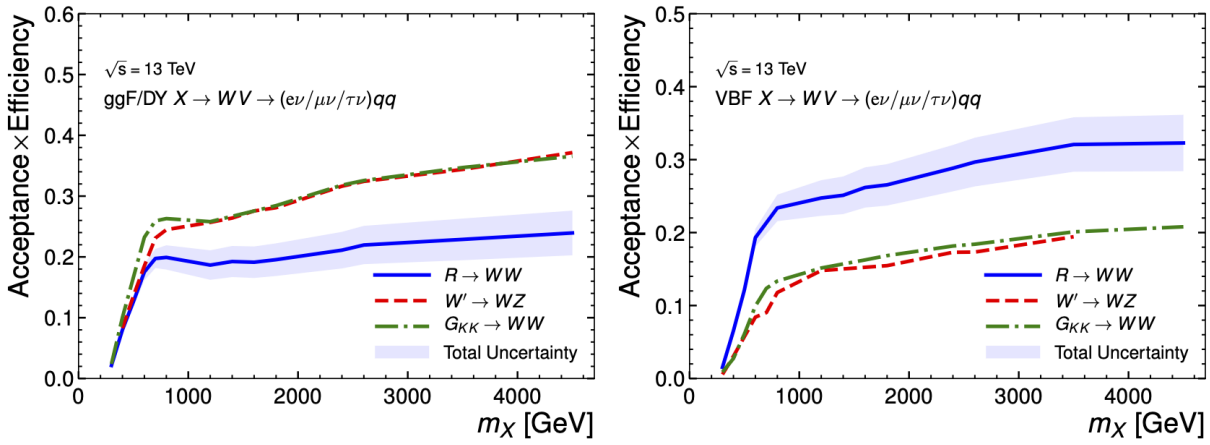

Figure 6.12: Selection acceptance times efficiency for the $X \to WV \to (e\nu/\mu\nu/\tau\nu)qq$ signal events from MC simulations as a function of the resonance mass for (a) ggF/DY and (b) VBF production, combining all SRs of both ggF/DY and VBF categories of both resolved and merged analyses. Signal contributions from $W \to \tau\nu$ decays are included in the efficiency calculation. The light blue band represents the total statistical and systematic uncertainties for the radion model, and the total uncertainties are similar for the other signal models. The "bump" structure around 800 GeV is due to the falling off of the resolved analysis.

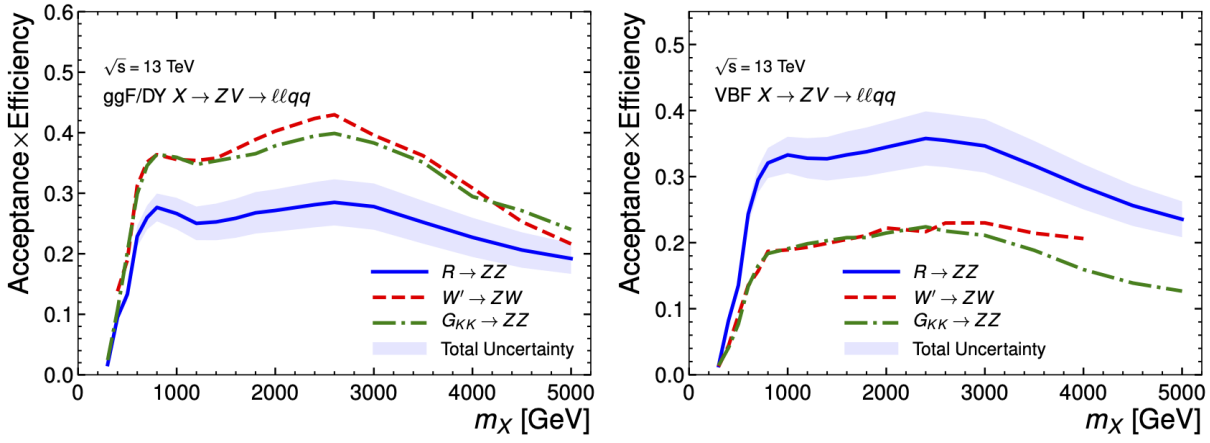

Figure 6.13: Selection acceptance times efficiency for the $X \to ZV \to \ell\ell qq$ signal events from MC simulations as a function of the resonance mass for (a) ggF/DY and (b) VBF production, combining all SRs of both ggF/DY and VBF categories of both resolved and merged analyses.The light blue band represents the total statistical and systematic uncertainties for the radion model, and the total uncertainties are similar for the other signal models. The decreases in efficiencies for resonance masses above approximately 2.5 TeV are due to the merging of electrons from the highly boosted $Z \to ee$ decays. The "bump" structure around 800 GeV is due to the falling off of the resolved analysis.

W + jets CR (WCR) and Z + jets CR (ZCR)

W+jets background is the main background in 1-lepton channel, while 0- and 2-lepton channels are dominated by Z + jets background. The mass sideband of the hadronically decaying $W(Z)$ boson candidate is used as the W + jets CR (WR) and Z + jets CR (ZCR) in 1- and 2-lepton channels, respectively. Events passing the mass window cut are used as SRs as described in 6.6.1, 6.6.2 and 6.6.3. In the merged category, the mass sideband is defined using the mass window cut of the W/Z boson tagger, while the resolved category requires 50 GeV $< m_{jj} <$ 62 GeV or 105 GeV $< m_{jj} <$ 150 GeV in order to avoid possible migration of signal events due to poor m_{jj} resolution.

$t\bar{t}$ CR (TCR)

$t\bar{t}$ background is the sub-dominant background in 1- and 0-lepton channels. Especially, the fraction of $t\bar{t}$ background is increased in b-tagged regions. The TCRs are defined in 1-lepton channel by requiring at least one additional b-tagged jet in each region.

$\nu\nu qq$ sideband validation region(VR)

The mass sideband region in 0-lepton channel is used as the validation region (VR). The VR is used to validate the background estimation derived from 1-/2-lepton CRs by checking data and MC consistency in 0-lepton channel. The possible different phase spaces between 0- and 1/2-lepton channels are also studied in this region. Therefore the VRs are not used in the final results.

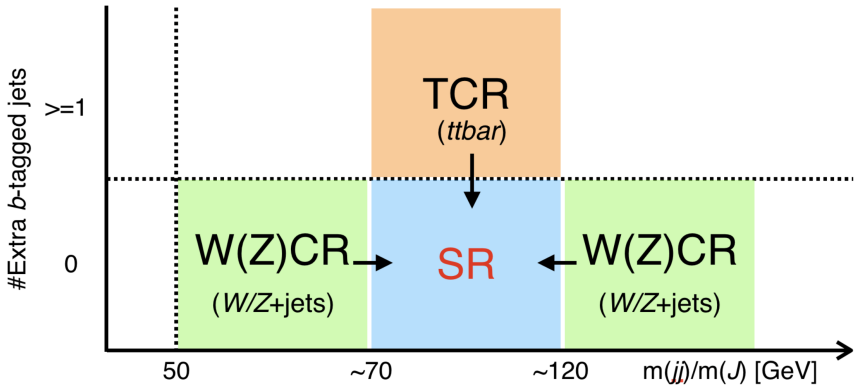

Figure 6.14: The sckematic view of SR and CR.

6.9 Summary of Signal and Control Regions

Finally, there are 10 SRs in the 0-lepton channel, 15 SRs each in the 1-lepton and 2-lepton channel with a total of 40 SRs. These SRs are not exclusive since overlapping mass windows are used to select hadronic decays of the W and Z bosons. Counting in terms of the diboson final states of resonance decays, there are 6 SRs for WW, 15 for ZZ and 19 for WZ. SRs in each diboson final state are orthogonal. Table 6.9 shows the breakdowns in each leptonic channel for different diboson final states.

Table 6.9: Numbers of signal regions in each leptonic channel and of control regions for different diboson final states.

VV final state	Signal regions						Control regions		
	VBF category			ggF/DY category			$W+\text{jets}$	$Z+\text{jets}$	$t\bar{t}$
	0-lep.	1-lep.	2-lep.	0-lep.	1-lep.	2-lep.			
WW	0	3	0	0	3	0	6	–	6
ZZ	2	0	3	4	0	6	–	9	–
WZ	2	3	3	2	6	3	9	6	9

Chapter 7

Background Estimations

The dominant background processes depend on the required number of charged-lepton and the signal regions. The background compositions for each lepton channel in all SRs are shown in Figure 7.1. The main background processes are W+jets, $t\bar{t}$ and non-resonant diboson in 1-lepton channel. In 2-lepton channel, Z+jets and non-resonant diboson are the major backgrounds ($t\bar{t}$ is also the source of the background in the tagged SRs). In 0-lepton channel, the main background processes are Z+jets, W+jets, $t\bar{t}$ and non-resonant diboson. These backgrounds are modeled by the MC simulation first, and the normalizations are evaluated

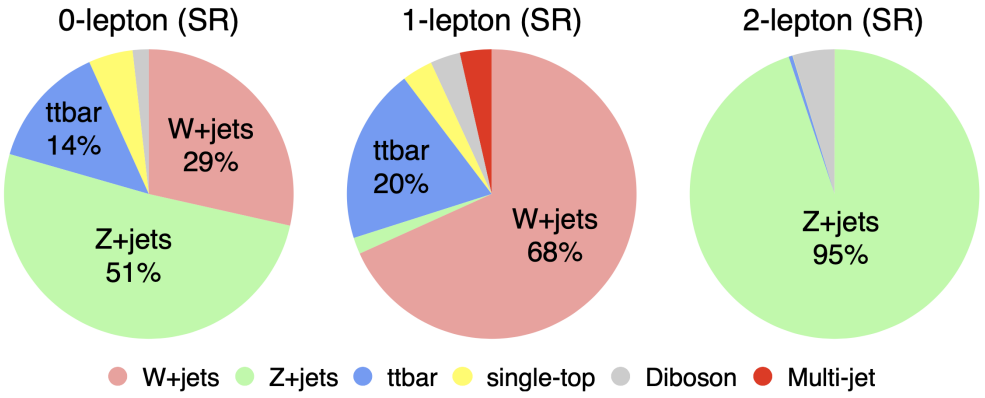

Figure 7.1: Background compositions for each lepton channel in all SRs.

by various control regions (CRs) defined in Section 6.8. In 1-lepton channel there are non-negligible multi-jet contributions due to a jet misidentified as lepton. A dedicated data-driven method is used to estimate the contribution from multi-jet background, as described in Section 7.4.

In this section, distributions of final discriminant i.e. the invariant mass of diboson resonances, comparing data and MC simulated sample are shown in the CRs. The CRs are also used to control the normalization of the corresponding backgrounds in the global profiled likelihood fit (Section 9) and all plots shown here are before the profiled likelihood fit (prefit). Since the MC simulation is not perfect in SRs/CRs, some difference between data and MC is expected in the prefit distributions. The uncertainty band includes both statistical uncertainties and systematic uncertainties which are described in details in Section 8.

7.1 Z + jets

ZCRs are defined as the mass sideband of hadronically decaying $W(Z)$ boson candidate and are used to control normalizations of Z + jets background in signal regions of all three channels (See Section 6.8). The comparison of distributions of final discriminant (invariant mass of the WZ system) between data and MC in different ZCRs for WZ analysis are shown in Figure 7.2. Besides, Figure 7.3 shows data and MC comparison of the final discriminant (invariant mass of the ZZ system) in different ZCRs. The ZZ analysis has more CRs than the WZ analysis due to b-tagging categorization for extracting $Z \to bb$. Overall, reasonable agreement with MC predictions is observed in all regions.

As shown in Figure 7.3a–7.3c, in merged b-tagged categories, the overall normalization of the MC sample is about 20% lower than data, while it is about 5% higher than data in untagged categories in Figure 7.3b–7.3d. The observation can be explained by the modeling of the fraction of Z+heavy-flavor jets, where the fraction of Z+hevay-flacor jets in Sherpa MC can be about 20% lower than the observed data [161]. In order to

handle different normalization between b-tagged and untagged categories, we use the separate normalization factors for $Z+$jets in the final fit. The resolved category shows the similar feature (Figure 7.3g–7.3h). In the tagged region the normalization differs by about 20%, while the good agreement is observed in the untagged regions.

As seen from Figure 7.2a and 7.2b, the background normalization is differenet between HP and LP (LP shows the higher background prediction). In order to handle different normalization between HP and LP categories, we use the separate normalization factors for $Z+$jets as well as $W+$jets and $t\bar{t}$ in the final fit.

In VBF categories, the MC simulated events overestimate the data by 5 (20%) for the resolved (merged) channels. In order to absorb the possible mismodeling on the RNN score distribution, we use the different normalization factors for $Z+$jets in VBF categories. Finally, nomalization factor for $Z+$jets are listed in Table.7.1.

Table 7.1: Summary of normalization factors for Z+jets.

Nuisance Parameter	Sample	Category	Notes
`SigXsecOverSM`	Signal	All regions	
`norm_Zmerged_HP_ggF_tagged`	Z+jets	ggF HP merged tagged	$X \to Z(\to qq)V$ only
`norm_Zmerged_LP_ggF_tagged`	Z+jets	ggF LP merged tagged	"
`norm_Zmerged_HP_ggF_untagged`	Z+jets	ggF HP merged untagged	"
`norm_Zmerged_LP_ggF_untagged`	Z+jets	ggF LP merged untagged	"
`norm_Zmerged_HP_ggF`	Z+jets	ggF HP merged	$X \to W(\to qq)V$ only
`norm_Zmerged_LP_ggF`	Z+jets	ggF LP merged	"
`norm_Zmerged_HP_VBF`	Z+jets	VBF HP merged	
`norm_Zmerged_LP_VBF`	Z+jets	VBF LP merged	
`norm_Zresolved_ggF_tagged`	Z+jets	ggF resolved tagged	$X \to Z(\to qq)V$ only
`norm_Zresolved_ggF_untagged`	Z+jets	ggF resolved untagged	"
`norm_Zresolved_ggF`	Z+jets	ggF resolved	$X \to W(\to qq)V$ only
`norm_Zresolved_VBF`	Z+jets	VBF reolsved	

7.2 $W+$jets

WCRs are defined as the mass sideband of hadronically decaying $W(Z)$ boson candidate and are used to constrain normalizations of $W+$jets background in signal regions of all three channels (See Section 6.8). The selection for the $W+$jets background control region in the $\ell\nu qq$ channel is summarized in Section 6.6.2. Comparison of distributions of the final discriminant (invariant mass of the WZ system) between data and MC in different WCRs are shown in Figure 7.4. In addition, Figure 7.5 shows data and MC comparison of the final discriminant (invariant mass of the WW system) in different WCRs. In 1-lepton analysis, the WZ analysis has more CRs than the WW analysis due to b-tagging categorization for extracting $Z \to bb$.

In general, the reasonable agreement with MC predictions is observed. As shown in Figure 7.4a, 7.4c and 7.4g in the tagged region, WCRs are enriched by $t\bar{t}$ contribution, especially in the lower-mass region of less than 1 TeV. The plots imply the different normalization factors for tagged and untagged categories and those for ggF and VBF categories as well as ZCRs. As with Z+jets normalizations, we use separate normalization factors for them in the final fit. Nomalization factor for W+jets are listed in Table 7.2.

7.3 ttbar

TCRs are defined by requiring an additional b-tagged jet for each SRs in 1-lepton channel and used to constrain normalizations of $t\bar{t}$ background in signal regions of all three channels (See Section 6.8). The selection for the $t\bar{t}$ background control region in the $\ell\nu qq$ channel is summarized in Table 6.3 and 6.4. Comparison of distributions of the final discriminant (invariant mass of the WZ system) between data and MC in different TCRs are shown in Figure 7.6. In addition, Figure 7.7 shows data and MC comparison of the final discriminant (invariant mass of the WW system) in different TCRs.

In general good agreement between data and MC is observed. In the resolved category, about 5% overestimation is found in ggF region, while VBF regions show very good agreement. In the merged category, about 10% (20%) overestimation is also found in ggF (VBF) category. No significant difference is observed between tagged and untagged regions, in both resolved and merged categories.

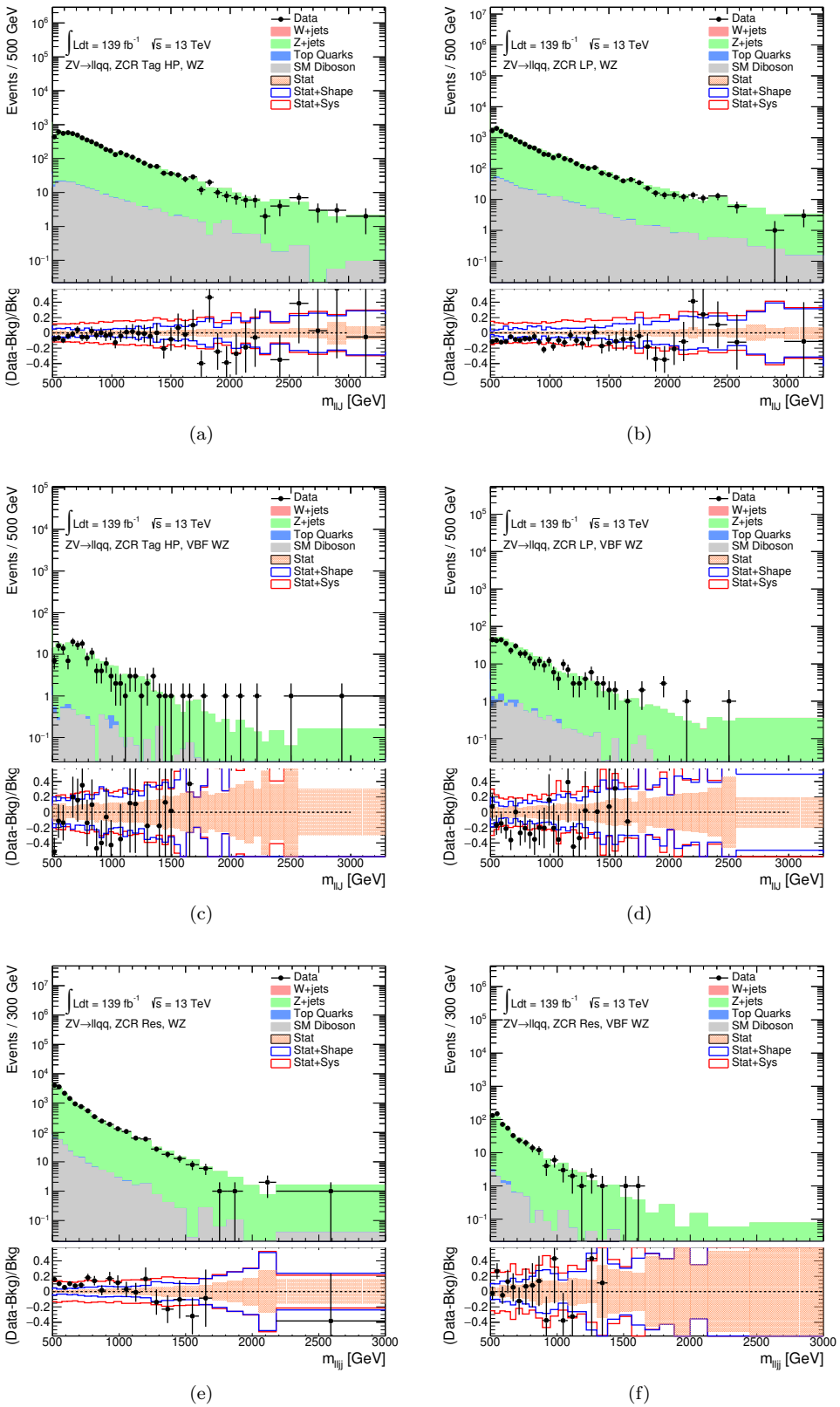

Figure 7.2: Observed and expected distributions of transverse mass of the leptons and jets from the WZ resonance decay in (a) ggF merged HP ZCR, (b) ggF merged LP ZCR, (c) VBF merged HP ZCR, (d) VBF merged LP ZCR, (d) ggF resolved ZCR and (e) VBF resolved ZCR.

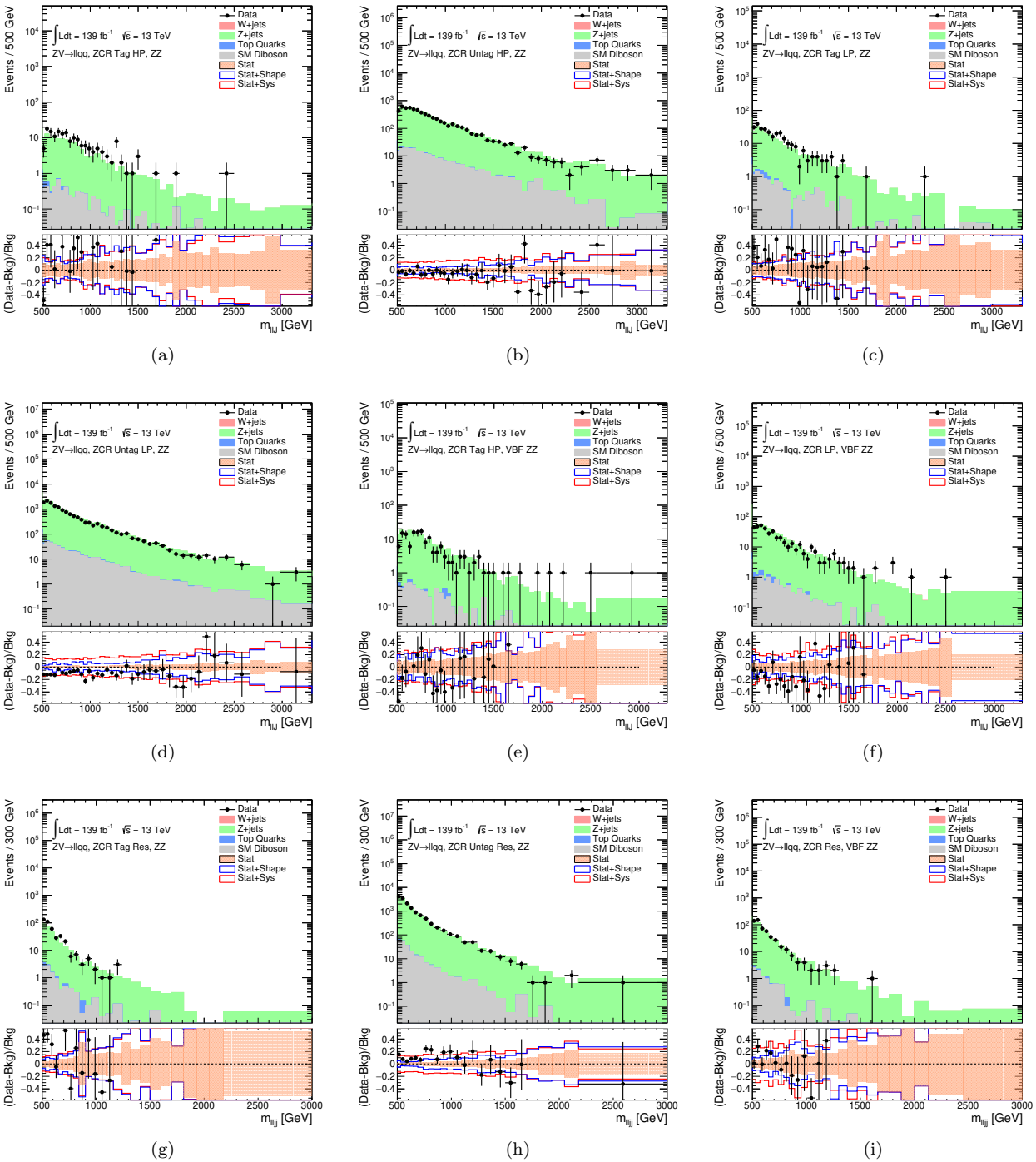

Figure 7.3: Observed and expected distributions of invariant mass of the leptons and jets from the ZZ resonance decay in (a) ggF merged HP tagged ZCR, (b) ggF merged HP untagged ZCR, (c) ggF merged LP tagged ZCR, (d) ggF merged LP untagged ZCR, (e) VBF merged HP ZCR, (f) VBF merged LP ZCR, (g) ggF resolved tagged ZCR, (h) ggF resolved untagged ZCR and (i) VBF resolved ZCR.

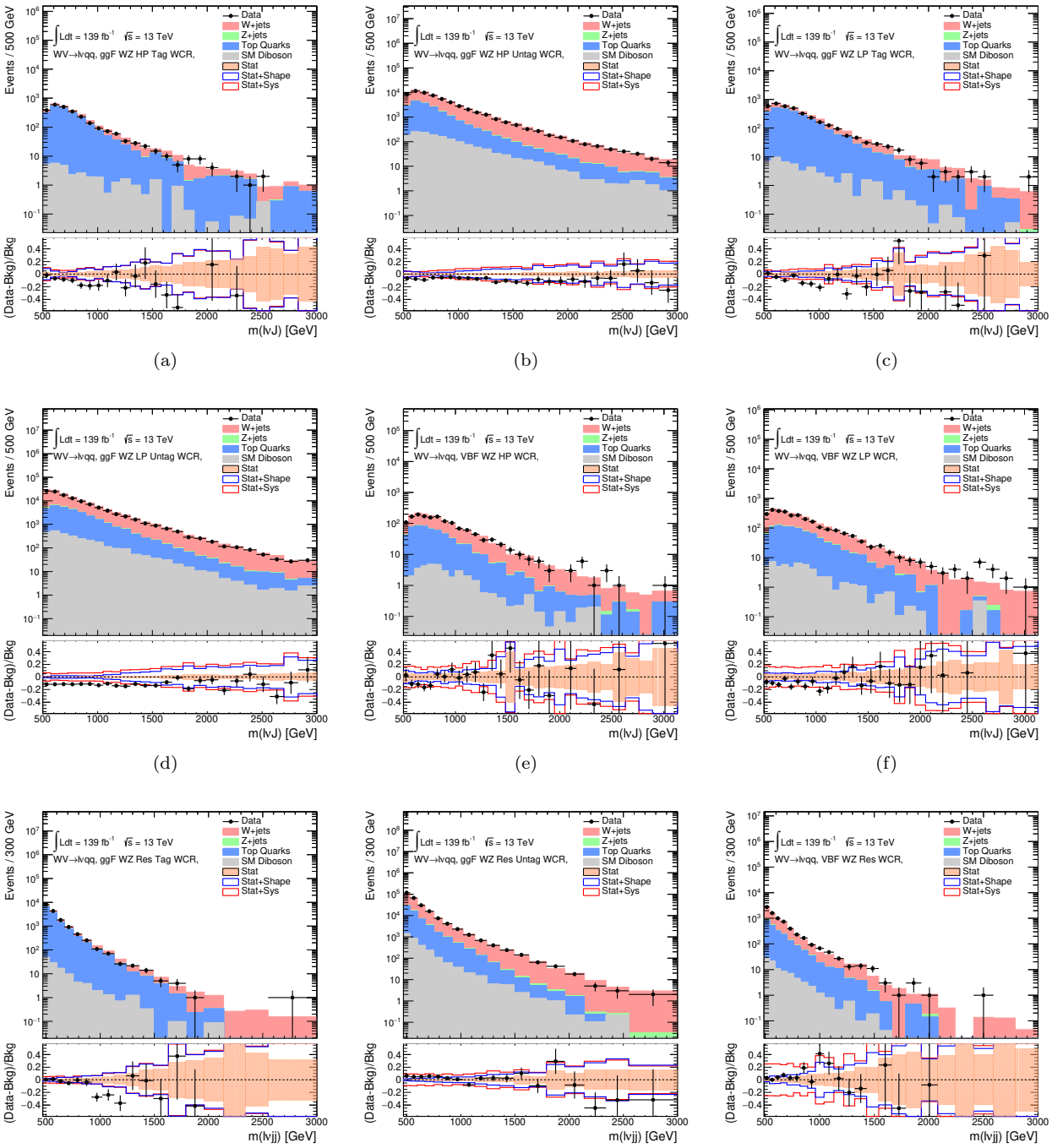

Figure 7.4: Observed and expected distributions of invariant mass of $l\nu qq$ from the WZ resonance decay in (a) ggF merged HP tagged WCR, (b) ggF merged HP untagged WCR, (c) ggF merged LP tagged WCR, (d) ggF merged LP untagged WCR, (e) VBF merged HP WCR, (f) VBF merged LP WCR, (g) ggF resolved tagged WCR, (h) ggF resolved untagged WCR and (i) VBF resolved WCR

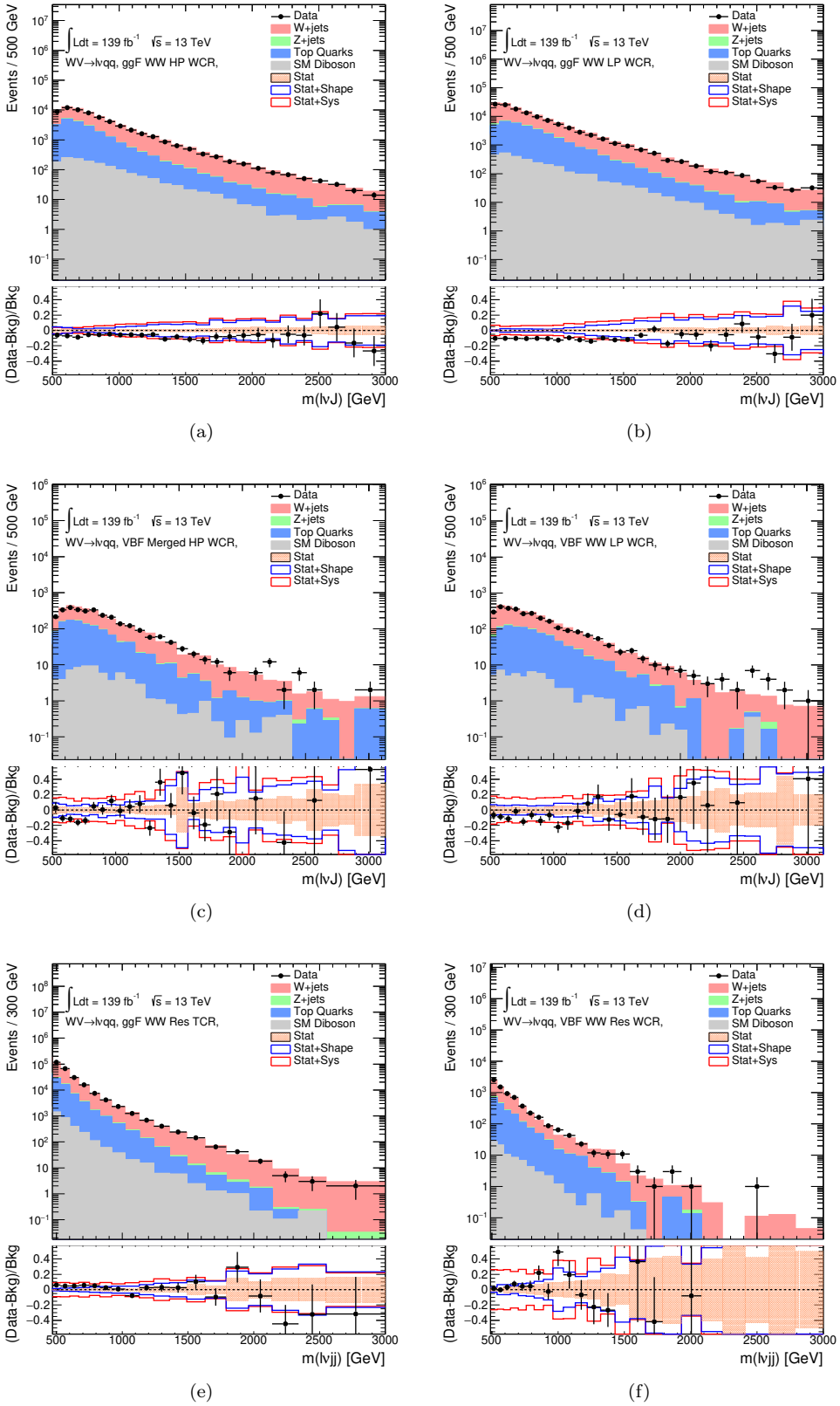

Figure 7.5: Observed and expected distributions of invariant mass of $l\nu qq$ from the WW resonance decay (a) ggF merged HP WCR, (b) ggF merged LP WCR, (c) VBF merged HP WCR, (d) VBF merged LP WCR, (d) ggF resolved WCR and (e) VBF resolved WCR.

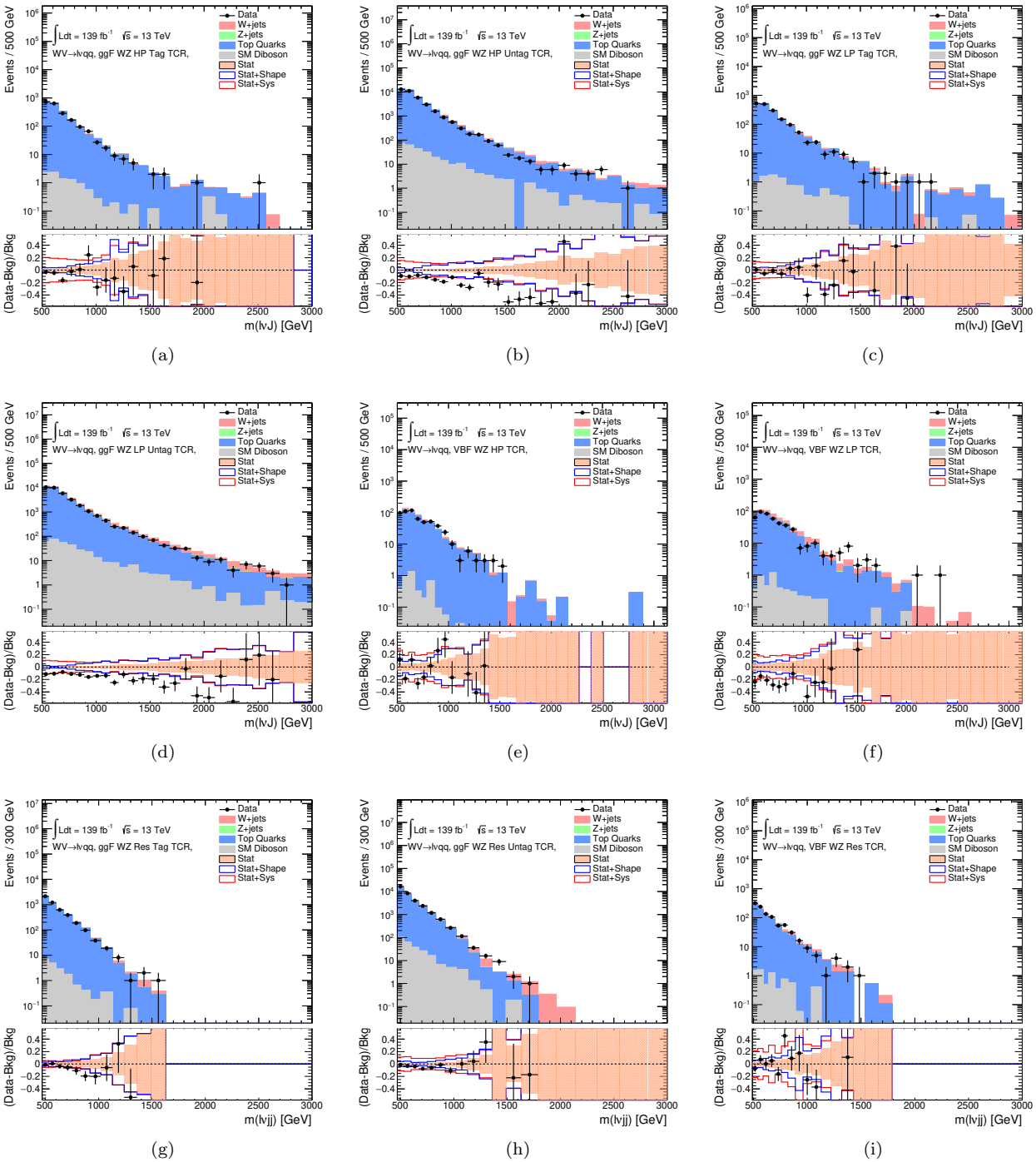

Figure 7.6: Observed and expected distributions of invariant mass of $l\nu qq$ from the WZ resonance decay in (a) ggF merged HP tagged TCR, (b) ggF merged HP untagged TCR, (c) ggF merged LP tagged TCR, (d) ggF merged LP untagged TCR, (e) VBF merged HP TCR, (f) VBF merged LP TCR, (g) ggF resolved tagged TCR, (h) ggF resolved untagged TCR and (i) VBF resolved TCR

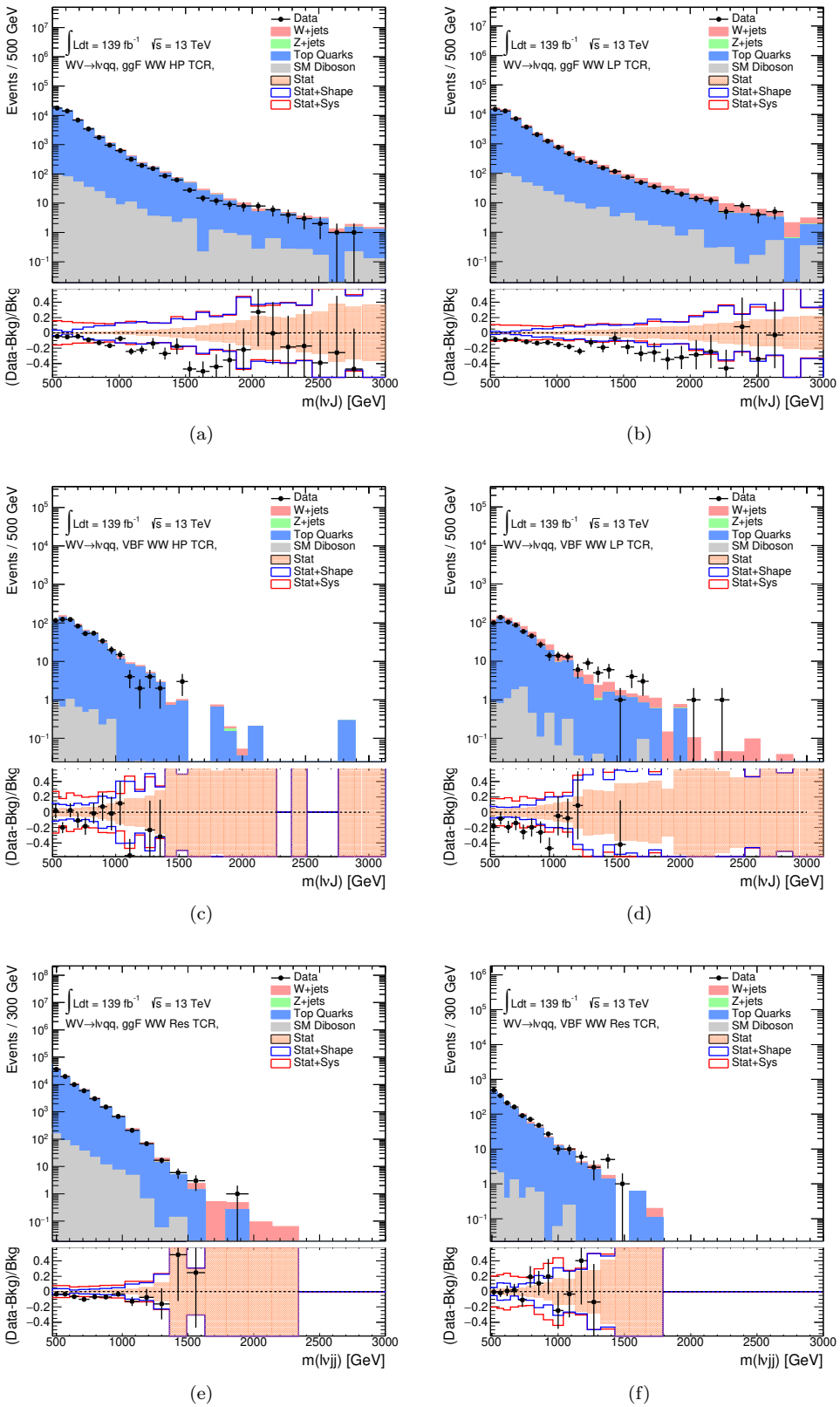

Figure 7.7: Observed and expected distributions of invariant mass of $l\nu qq$ from the WW resonance decay in (a) ggF merged HP TCR, (b) ggF merged LP TCR, (c) VBF merged HP TCR, (d) VBF merged LP TCR, (d) ggF resolved TCR and (e) VBF resolved TCR.

Table 7.2: Summary of normalization factors for W+jets.

Nuisance Parameter	Sample	Category	Notes
SigXsecOverSM	Signal	All regions	
norm_Wmerged_HP_ggF_tagged	W+jets	ggF HP merged tagged	$X \to Z(\to qq)V$ only
norm_Wmerged_LP_ggF_tagged	W+jets	ggF LP merged tagged	"
norm_Wmerged_HP_ggF_untagged	W+jets	ggF HP merged untagged	"
norm_Wmerged_LP_ggF_untagged	W+jets	ggF LP merged untagged	"
norm_Wmerged_HP_ggF	W+jets	ggF HP merged	$X \to W(\to qq)V$ only
norm_Wmerged_LP_ggF	W+jets	ggF LP merged	"
norm_Wmerged_HP_VBF	W+jets	VBF HP merged	
norm_Wmerged_LP_VBF	W+jets	VBF LP merged	
norm_Wresolved_ggF_tagged	W+jets	ggF resolved tagged	$X \to Z(\to qq)V$ only
norm_Wresolved_ggF_untagged	W+jets	ggF resolved untagged	"
norm_Wresolved_ggF	W+jets	ggF resolved	$X \to W(\to qq)V$ only
norm_Wresolved_VBF	W+jets	VBF resolved	

Table 7.3: Summary of normalization factors for $t\bar{t}$.

Nuisance Parameter	Sample	Category	Notes
SigXsecOverSM	Signal	All regions	
norm_TTbarmerged_HP_ggF_tagged	$t\bar{t}$	ggF HP merged tagged	$X \to Z(\to qq)V$ only
norm_TTbarmerged_LP_ggF_tagged	$t\bar{t}$	ggF LP merged tagged	"
norm_TTbarmerged_HP_ggF_untagged	$t\bar{t}$	ggF HP merged untagged	"
norm_TTbarmerged_LP_ggF_untagged	$t\bar{t}$	ggF LP merged untagged	"
norm_TTbarmerged_HP_ggF	$t\bar{t}$	ggF HP merged	$X \to W(\to qq)V$ only
norm_TTbarmerged_LP_ggF	$t\bar{t}$	ggF LP merged	"
norm_TTbarmerged_HP_VBF	$t\bar{t}$	VBF HP merged	"
norm_TTbarmerged_LP_VBF	$t\bar{t}$	VBF LP merged	"
norm_TTbarresolved_ggF_tagged	$t\bar{t}$	ggF resolved tagged	$X \to Z(\to qq)V$ only
norm_TTbarresolved_ggF_untagged	$t\bar{t}$	ggF resolved untagged	"
norm_TTbarresolved_ggF	$t\bar{t}$	ggF resolved	$X \to W(\to qq)V$ only
norm_TTbarresolved_VBF	$t\bar{t}$	VBF resolved	

7.4 Multi-jet Background

The backgrounds containing the real lepton from W/Z decay ($t\bar{t}$, W/Z + jets, diboson, single-t) are modeled with the MC simulated events. The multi-jet background contributes via two different sources: fake leptons[1] or semileptonic decay of heavy flavor jet. The rate of fake leptons is about 10^{-3} to 10^{-4} while the cross-section of multi-jet background is significantly larger than that of W/Z+jets. Therefore we need to estimate the non-negligible contribution from multi-jet background. However, the same approach is not applicable for multi-jet background. Since multi-jet backgrounds are poorly modeled in the simulation, a data-driven template method is used to estimate the multi-jet background in the 1-lepton channel. The contribution of multi-jet background is negligible in the 0- (as discussed in Section 6.6.1) and 2- (becuase of requiring 2 charged-leptons from Z boson) lepton channels.

Multi-jet template extraction

The *template* shape of the multi-jet background is extracted from data using multi-jet-enriched control regions (MJCRs) which are defined by requiring the same event selections to the SR/WCRs in 1-lepton resolved category but the different lepton ID and isolation. The MJCRs is used to extract the MJ template that is used for SR/WCRs. The requirements of the *inverted* leptons to define MJCR are summarized in Table 7.4.

For the electron channel in which the misidentified electron comes from hadron-jet fake and heavy-flavor decay, events with one electron failing *Tight* but passing *Medium* identification operation points (see Section 4.4.1) are used.

[1] This contribution could be from particles mistaken as electrons originating from jets

	Criterion	signal lepton	inverted lepton
Electron	ID	Tight	Medium !Tight
	Calo Isolation	FixedCutHighPtCaloOnly	FixedCutHighPtCaloOnly
Muon	ID	Medium	Medium
	Track Isolation	FixedCutTightTrackOnly	!FixedCutTightTrackOnly $p_{\mathrm{T}}^{\mathrm{varcone0.3}}/p_{\mathrm{T}} < 0.07^{*}$
	*Only applied to events with $p_{\mathrm{T},\ell\nu} < 150$ GeV		

Table 7.4: Definitions of "*inverted*" leptons used in multi-jet control region

For the muon channel in which the misidentified muon mainly comes from the heavy-flavor decay, the MJCR is required to have muon passing a relaxed, but failing the tight isolation requirement. As described in Section 6.3, two different triggers are used in the muon channel. For events with transverse momentum of $W \to \mu\nu$ greater than 150 GeV, $E_{\mathrm{T}}^{\mathrm{miss}}$ trigger is used, while events with W-boson p_{T} of less than 150 GeV are recorded by single muon trigger. The isolation requirements in the muon trigger result in the different multi-jet shape templates between the two samples. Therefore, the muon channel is divided into two sub-channels for multi-jet estimation.

Pre MJ template fit

The multi-jet contribution is estimated by using the template shapes extracted from data in a multi-jet enriched control region. First, the MJ template is obtained by subtracting the contribution from other background processes in the MJCRs, based on MC predictions. Systematic variations of the MC predictions are later applied as a source of systematic uncertainty.

Second, the normalization factors for both the multi-jet and the electroweak components are obtained by a fit ("pre-MJ-fit") on the $E_{\mathrm{T}}^{\mathrm{miss}}$ distribution in the WCRs. Templates for the multi-jet contributions are estimated separately depending on the lepton flavor (e or μ). In the fit, the multi-jet component is left free to float. The normalization of the other backgrounds are constrained to reasonable ranges according to their expected normalization within the statistical uncertainties. Z+jets and diboson are fixed in the fit since their contributions are small. W+jets and top quark are combined as one component in the fit because of their similarity of shapes. Both electron and muon channels are used in the pre-MJ-fit. The normalization scale factors are shared by the same background components in the fit, while the electron and muon MJCR templates have separate scale factors.

Third, the obtained scale factors for MJCR are applied to the corresponding templates and the scaled MJCR templates are used in the analysis, with uncertainties obtained from the pre-MJ-fit.

In principle, for each final WCR and SR used in the 1-lepton analysis, a corresponding MJ template should be derived. Due to tight cuts, some MJ regions suffer from low statistic. By comparing the MJ shapes between VBF and ggF region, it is found that the shapes of MJ template are consistent within the statistical uncertainty. Therefore the MJ templates are obtained using ggF+VBF combined regions.

Extraction of multi-jet background normalizations

The extracted normalization factor is applied to MJVR templates in WCRs, for various kinematic variables, such as $E_{\mathrm{T}}^{\mathrm{miss}}$, W transverse mass, lepton p_{T}, and the invariant mass, as shown in Figure 7.8. The multi-jet contribution in muon channel with $p_{\mathrm{T},\ell\nu} > 150$ GeV is consistent with zero, hence neglected in the final fit. In general, good consistency between data and background estimation is observed. The yields and extracted normalization factors are summarized in Table 7.5.

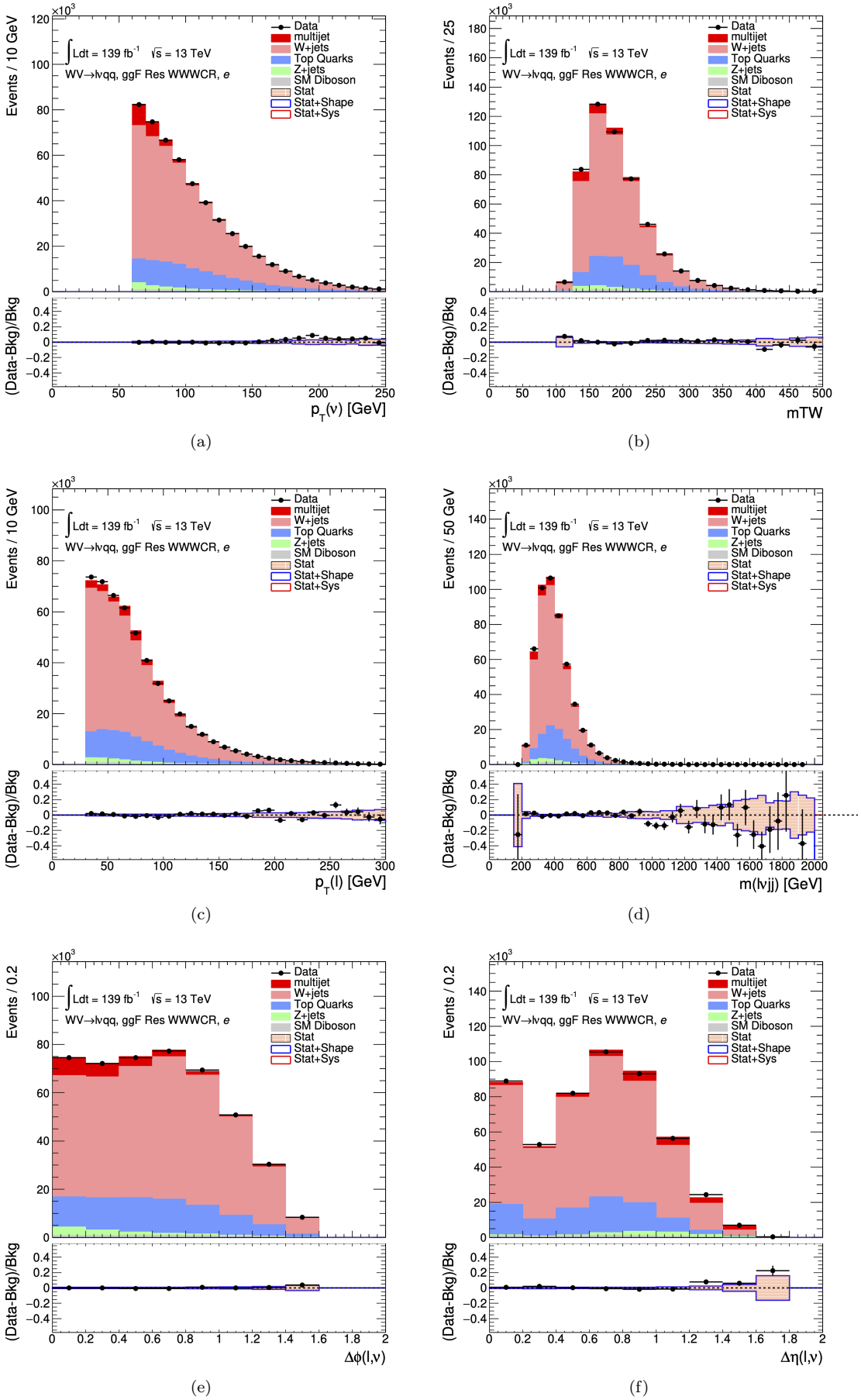

Figure 7.8: Observed and expected distributions of (a) $E_{\mathrm{T}}^{\mathrm{miss}}$, (b) $p_{\mathrm{T},\ell\nu}$, (c) p_{T}^{ℓ}, (d) transverse mass of the leptons and jets from the WZ resonance decay, (e) $\Delta\phi$ between a lepton and $E_{\mathrm{T}}^{\mathrm{miss}}$ and (f) $\Delta\eta$ between a lepton and $E_{\mathrm{T}}^{\mathrm{miss}}$ with estimated multi-jet

Table 7.5: The fit is done in various WCRs, in order to obtain the corresponding scale factors for MJ templates: ggF resolved WCR for the $WW \to lvqq$ selection, ggF resolved untagged WCR for the $WZ \to lvqq$ selection, ggF resolved tagged WCR for the $WZ \to lvqq$ selection, VBF resolved WCR for the $WW \to lvqq$ selection, and VBF resolved WCR for the $WZ \to lvqq$ selection. Post-fit event yields for electroweak processes and MJ contributions are shown. The "SF" column shows the corresponding normalization scale factors for electroweak processes from the fit.

Sample	Yield	SF
ggF Resolved WW WCR		
Top quarks & W+jets	645040 ± 1972	1.00
Z+jets & SM Dibosons	24075	fixed
Multi-jet (electron)	24156 ± 1225	3.97
Multi-jet (muon)	35528 ± 924	9.02
ggF Resolved WZ Untag WCR		
Top quarks & W+jets	644690 ± 1981	1.00
Z+jets & SM Dibosons	24076	fixed
Multi-jet (electron)	24367 ± 1233	3.87
Multi-jet (muon)	35529 ± 921	8.75
ggF Resolved WZ Tag WCR		
Top quarks & W+jets	71237 ± 688	1.03
Z+jets & SM Dibosons	519	fixed
Multi-jet (electron)	596 ± 449	0.09
Multi-jet (muon)	1197 ± 222	0.29
VBF Resolved WW WCR		
Top quarks & W+jets	19032 ± 364	0.93
Z+jets & SM Dibosons	1092	fixed
Multi-jet (electron)	1426 ± 214	0.24
Multi-jet (muon)	1281 ± 157	0.31
VBF Resolved WZ WCR		
Top quarks & W+jets	21342 ± 392	0.94
Z+jets & SM Dibosons	1112	fixed
Multi-jet (electron)	1414 ± 230	0.23
Multi-jet (muon)	1281 ± 157	0.31

Chapter 8

Systematic Uncertainty

Systematic uncertainties impact sensitivities for target signal models through their effects on background estimations, signal selection efficiencies, and the distributions of mass discriminants. The sources of these uncertainties are classified into mainly two groups: (a) Experimental uncertainties related to the detector and reconstruction performance and (b) Theoretical uncertainties associated with the MC modeling of both background and signal processes. In this section the source and the size of uncertainties are discussed.

8.1 Experimental Uncertainties

Luminosity

The uncertainty on the integrated luminosity for the 2015+2016 dataset is 2.1%, 2.4% for the 2017 dataset, and 2.0% for the 2018 data. The uncertainty for the combined run-2 dataset (2015-2018) is 1.7% [74]. The combined uncertainty is applied to all simulated samples including both backgrounds and signal samples.

Pileup reweighting

The uncertainty associated with the pileup reweighting is included by considering a variation in the pileup reweighting of MC. It covers the uncertainty on the ratio between the predicted and measured inelastic cross-section in the fiducial volume defined by $M_X > 13\,\text{GeV}$ where M_X is the mass of the non-diffractive hadronic system [162].

Trigger

Systematic uncertainties on the efficiency of the electron or muon triggers are evaluated with the tag and probe method using $Z \to ll$ events in data and simulation [144, 163]. It is applied to the MC simulated samples. The $E_{\text{T}}^{\text{miss}}$ trigger uncertainty arises from the estimation on scale factor which contains two contributions: statistics and the efficiency discrepancy between MC samples ($t\bar{t}$ and W + jets) [164]. Small corrections are applied to the simulation to better model the performance seen in data. These corrections have associated uncertainties on the order of 1% and uncertainties on the lepton triggers efficiencies are found to be negligible.

Muons/Electrons reconstruction and identification

The systematic uncertainties related to electrons and muons are estimated based on the difference between data and simulation [141, 144]. Identification and reconstruction efficiencies are measured with the tag and probe method using $Z \to ll$ events in data and simulation. Scale factor and its uncertainty of lepton isolation efficiency are derived by tag and probe method as well. Energy and momentum scales are measured with Z mass distribution shape. These uncertainties are considered in the analysis but their impacts are very small. Uncertainties on the lepton energy (or momentum) scale and resolution, especially for muon momentum resolution (3%), are also taken into account.

Small-R Jet Energy Scale and Resolution Uncertainty

The jet energy scale and resolution of the small-R jets are measured in situ by calculating the response between MC and data in various bins of kinematic phase space [165]. There are roughly 100 kinds of well-defined systematic uncertainty sources. This thesis uses simplified groups of the uncertainty sources, which are grouped into about 20 categories considering each correlation. For jets with $|\eta| < 2.5$, the total relative uncertainty on the jet energy scale varies in the range 1-4% for $p_{\text{T}} > 20$ GeV. The jet energy resolution

uncertainty ranges from 10-20% for jets with $p_{\mathrm{T}} \sim 20$ GeV to less than 5% for jets with $p_{\mathrm{T}} > 200$ GeV. They also affect the merged regime because they are included in the calculation of the missing transverse energy.

Large-R Jet Energy Scale and Resolution Uncertainty

The large-R jet energy scale uncertainties are considered as one of the dominant uncertainties in this analysis. The p_{T} of the large-R jet can be approximated to be equivalent with calorimeter-jet p_{T}, since the track measurements enter the calculation of TCC jet p_{T} as only "p_{T} ratio". The uncertainty on the p_{T} scale of the large-R jet is evaluated by comparing the ratio of the large-R jet p_{T} to track-jet p_{T} using dijet data and simulation, which is called as R_{trk} method [129, 153]. The precision on the relative jet energy scale is 1–2% for $200\,\mathrm{GeV} < p_T < 2\,\mathrm{TeV}$, while that on the mass scale is 2–10%. The jet energy resolution uncertainty is estimated to be approximately 2%. In addition to this "*Baseline*" uncertainty, the uncertainties on track measurements ("*Tracking*"), the difference between Pythia and Sherpa dijet simulations ("*Modelling*") and statistical uncertainty of dijet data ("*TotalStat*") are considered. In order to take into account the possible difference between TCC and calorimeter-jet p_{T}, the difference between TCC jet and calorimeter-jet p_{T} in dijet data and simulation is additionally considered as "*Closure*" uncertainty. As a p_{T} resolution uncertainty, jet p_{T} is smeared by Gaussian with 2% width.

W/Z-tagging efficiency SF Uncertainty

For the evaluation of mass and $D_2^{(\beta=1)}$ scale uncertainties, the efficiency of W/Z-tagging based on cuts on jet mass and $D_2^{(\beta=1)}$ is estimated in data using the control sample and corrected by comparing it with simulation, as described in Sec. 5.5. The efficiency of W/Z-induced jet signal is estimated by $t\bar{t}$ control sample, while the efficiency on single-q/g background is estimated by the dijet sample. The effects of experimental and theoretical uncertainties on the efficiency SF is studied. By taking the double ratio (ratio of efficiencies between data and simulation), the uncertainties which are not related to jet mass and $D_2^{(\beta=1)}$ scale/resolution are canceled out. The efficiency SF and uncertainties on it are estimated in each of (1) pass mass and pass $D_2^{(\beta=1)}$ (HP SR), (2) pass mass and fail $D_2^{(\beta=1)}$ (LP SR), (3) fail mass and pass $D_2^{(\beta=1)}$ (HP CR) and (4) fail mass and fail $D_2^{(\beta=1)}$ (LP CR) regions, which are used to define SR and CR in our analysis (Sec. 6.5.1), and correlation between four regions are correctly taken into account. The measurement is extrapolated to higher-p_{T} region with additional uncertainties estimated from simulations. The efficiency for background large-R jets from light-quarks or gluons is estimated using dijet and γ+jets samples.

B-tagging systematics

The systematic uncertainties on the efficiencies for tagging b-jets and for mis-tagging light-flavor jets are considered. They are evaluated as uncertainties on the scaling factor to take account for possible disagreement of the b-tag efficiency between data and MC. Scale factors and corresponding systematic uncertainties are divided into several components like b-, c- and light-flavor-induced jets, based on several measurements [166]. The total uncertainties are 1–10%, 15–50%, and 50–100% for b-jets, c-jets, and light-flavour jets respectively.

Missing transverse energy

The missing transverse energy is calculated using physics objects, such as muons, electrons, taus, photons, and jets. Therefore, all of the systematic errors on these objects, e.g. the jet energy scale, are propagated to $E_{\mathrm{T}}^{\mathrm{miss}}$ uncertainty. In addition, there is an uncertainty called the "Soft Term", from the unassociated tracks. The resolution and scale of this soft term are varied within their errors to evaluate their contribution to the total uncertainty [167].

Track missing transverse energy

As discussed in Section 6.6.1, a very loose cut on $p_{\mathrm{T}}^{\mathrm{miss}}$ is applied for the event cleaning in 0-lepton channel. The impact of possible mismodeling of $p_{\mathrm{T}}^{\mathrm{miss}}$ on the total background yield is estimated by varying the $p_{\mathrm{T}}^{\mathrm{miss}}$ value by $\pm 2\%$ and found to be negligible.

8.2 Theoretical Uncertainties

Several theoretical uncertainties are considered to take into account the possible mis-modeling of the normalizations of diboson and single top-quark backgrounds, the shapes of the mass discriminant distributions of background processes, and the signal acceptances. They are estimated by comparing the choices of event generators, PDFs, parton shower models, underlying event tunes, etc. For the dominant backgrounds such as W + jets, Z + jets and $t\bar{t}$, only uncertainties on the shapes of discriminant variables matter since their normalizations are controlled by the dedicated CRs.

Uncertainties in the modeling of $t\bar{t}$

For $t\bar{t}$, an uncertainty on the shape of discriminants used in the fit are derived comparing the default POWHEG [79]+PYTHIA8 [94] sample with the distribution obtained using aMC@NLO [81]+PYTHIA8 as an alternative sample. The normalizations of the alternative samples after the event selections are scaled to the nominal sample and the difference between alternative generators is regarded as the shape uncertainty on the distribution of final discriminant. The shape difference is found to be approximately 4% in merge signal regions, doubling the value in the resolved analysis. Additional systematic uncertainties are also evaluated by comparing the nominal sample showered with PYTHIA8 [94] to one showered with HERWIG [168], and are found to be between 2 and 5%.

W/Z+jets modeling uncertainty

W/Z+jets modeling uncertainty is also considered as well as $t\bar{t}$ modeling uncertainty by comparing the nominal SHERPA samples with samples produced using MADGRAPH5. The resummation scale and the CKKW matching scale in the nominal samples are also varied. In addition, a matrix element and parton shower variations are considered by comparing the nominal SHERPA samples with MADGRAPH+PYTHIA samples.

The evaluated shape differences are stored as weights in the m_{VV} spectrum and evaluated for each of the individual signal/control regions during the final fit. To reduce the effects of statistics, noticeably in the tails of distributions, all signal and control regions among the resolved/merged and ggF/VBF categories are merged in the calculation of the shape uncertainties.

The shape systematic uncertainty is typically smaller than 10%, with the SHERPA-MADGRAPH comparison reaching 25% in the merged ggF WZ untagged signal regions for the $\ell\nu qq$ channel. The comparison of recontructed m_{VV} distributions between SHERPA and MADGRAPH W/Z+jets samples are shown in Figure 8.1.

Uncertainties on the modeling of single-t, diboson

Estimations of background contributions from diboson and single-t rely on MC prediction since it is not possible to define a dedicated control region to control its modeling. For diboson process, the cross-section uncertainty is estimated to be 10% [95, 169], using SHERPA samples. Furthermore, renormalization and factorization scale and PDF variations contribute to the uncertainty on the diboson normalization with an impact of 6%. A contribution from electroweak production is also evaluated with MADGRAPH+PYTHIA8 for the diboson normalization. A conservative uncertainty of 50% is considered and the impact on the ggF/DY analysis is negligible. Single-t process is a minor component in our analysis. For the cross-section of single t process, conservative 20% uncertainty is considered.

Uncertainty on modeling multi-jet background

As described in Sec. 7.4, the multi-jet (MJ) background template is obtained from dedicated control regions with reverted electron identification or muon isolation requirement. The shape uncertainty of the multijet background is estimated according to the following uncertainties. The normalization of the background processes could affect the extracted MJ template shape. This systematic uncertainty is evaluated by varying the normalization factors for $t\bar{t}$ and W+jets processes, and the resulting difference in MJ template shape is taken as the systematic uncertainty. They are found to be a few percent to up to 15%.

Extrapolation uncertainty on background normalization in the 0-lepton channel

In the 0-lepton channel, it is not possible to define pure control regions for W+jets, Z+jets and $t\bar{t}$. The normalization factors for these backgrounds are obtained from the 1-lepton (for W+jets and $t\bar{t}$) and 2-lepton

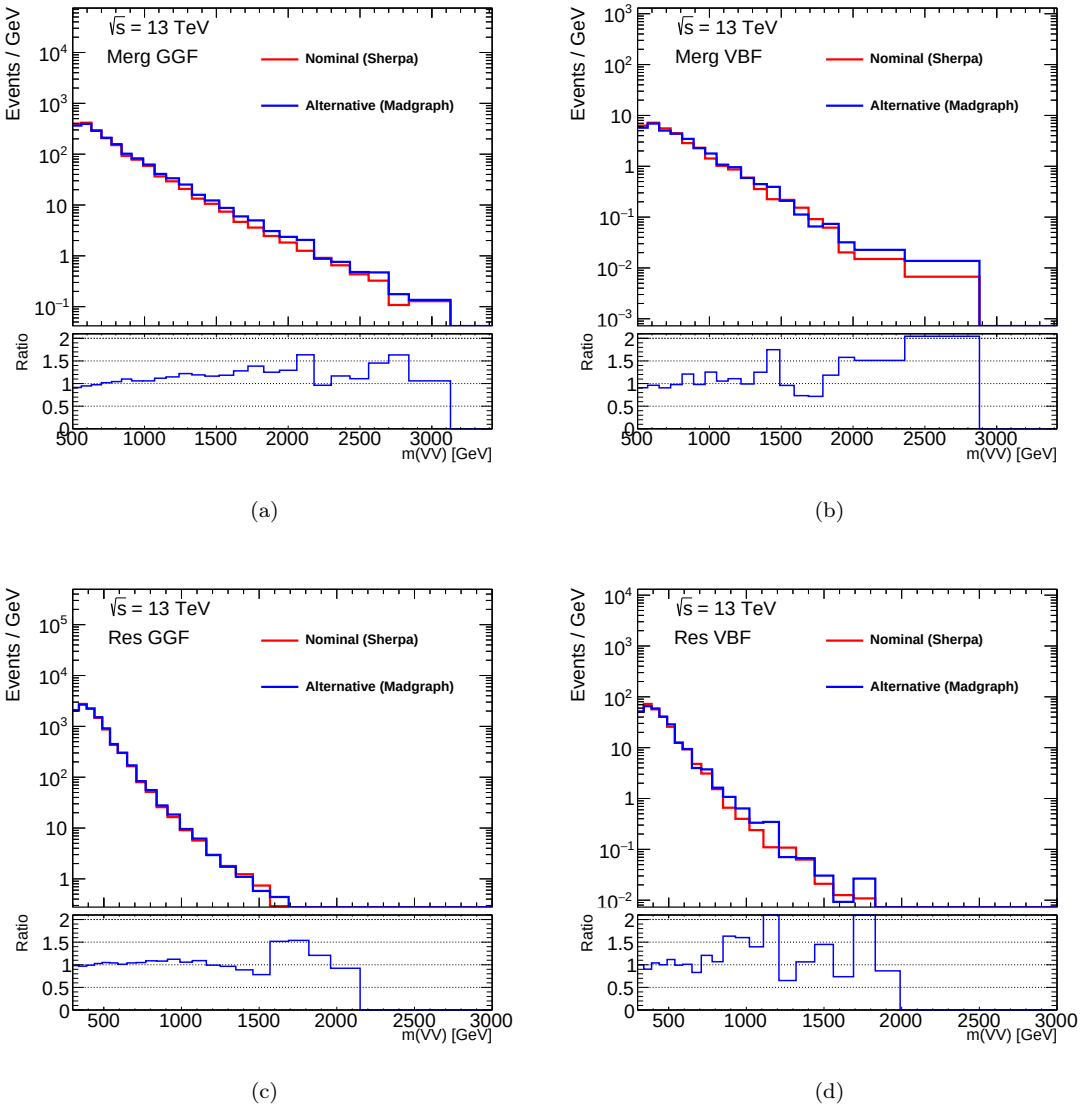

(a) (b)

(c) (d)

Figure 8.1: The comparison of recontructed m_{VV} distributions between nominal and alternative $V + jets$ samples in (a) Merged ggF, (b) Merged VBF, (c) Resolved ggF, and (d) Resolved VBF categories.

(for Z+jets) channels, and extrapolated to the 0-lepton channel. Such extrapolations can introduce additional systematic uncertainties due to different phase space in the different lepton channels. As an illustration, the normalization for W+jets in 0-lepton channel can be written as:

$$N_{\text{bkg,0-lep}} = N_{\text{bkg,0-lep,MC}} \cdot \mu_{\text{bkg,1-lep}} \tag{8.1}$$

$$= N_{\text{bkg,0-lep,MC}} \cdot \frac{N_{\text{bkg,1-lepWCR,data}}}{N_{\text{bkg,1-lepWCR,MC}}} \tag{8.2}$$

$$= N_{\text{bkg,1-lepWCR,data}} \cdot \frac{N_{\text{bkg,0-lep,MC}}}{N_{\text{bkg,1-lepWCR,MC}}} \tag{8.3}$$

$$\tag{8.4}$$

The factor $N_{\text{bkg,0-lep,MC}}/N_{\text{bkg,1-lepWCR,MC}}$ could be model dependent, given the large phase space difference among different channels. Therefore, it is necessary to study associated uncertainties due to such cross channel extrapolation.

This effect can be studied by comparing the ratio of event yields for alternative sample to that for nominal sample in each $W(Z)$+jets and $t\bar{t}$ prediction between 0 and 1(2) lepton channel. We define a double ratio as:

$$R = \frac{N^{0-\text{lep}}_{\text{Alternative MC}}/N^{1-\text{lep (2-lep)}}_{\text{Alternative MC}}}{N^{0-\text{lep}}_{\text{Nominal MC}}/N^{1-\text{lep (2-lep)}}_{\text{Nominal MC}}}. \tag{8.5}$$

and this double ratio R is studied for W+jets, Z+jets and $t\bar{t}$, in each signal region. The extrapolation uncertainty is evaluated by the double ratio, defined as the absolute value of $R-1$.

Z+jets background yield ratio between 0- and 2-lepton channel

The extrapolation uncertainties for Z+jets are estimated by comparing the nominal Sherpa samples and alternative MadGraph samples, as summarized in Table 8.1 for ggF and VBF categories, respectively. Non-negligible extrapolation uncertainty for Z+jets should be considered, especially for ggF categories.

Table 8.1: Summary of evaluated ratio and extrapolation uncertainties for $Z+$jets

$Z+$jets ggF	HPSR	HPCR	LPSR	LPCR
Sherpa ratio	0.317	0.23	0.284	0.267
Madgraph ratio	0.358	0.261	0.329	0.31
Extrapolation uncertainty [%]	12.9	13.5	15.8	16.1
$Z+$jets VBF	HPSR	HPCR	LPSR	LPCR
Sherpa ratio	0.565	0.414	0.546	0.477
Madgraph ratio	0.537	0.371	0.532	0.454
Extrapolation uncertainty [%]	5.0	10.4	2.6	4.8

W+jets background yield ratio between 0- and 1-lepton channel

The extrapolation uncertainties for W+jets are studied by comparing the nominal Sherpa samples and alternative MadGraph samples, as summarized in Table 8.2 for ggF and VBF categories, respectively.

$t\bar{t}$ background yield ratio between 0- and 1-lepton channel

The extrapolation uncertainties for $t\bar{t}$ are studied by comparing the nominal Powheg+Pythia8 samples and alternative aMC@NLO samples, as summarized in Table 8.3, for ggF and VBF categories, respectively.

Table 8.2: Summary of evaluated ratio and extrapolation uncertainties for W + jets

W + jets ggF	HPSR	HPCR	LPSR	LPCR
Sherpa ratio	0.397	0.458	0.576	0.435
Madgraph ratio	0.374	0.377	0.511	0.371
Extrapolation uncertainty [%]	5.8	17.7	11.3	14.7
W + jets VBF	HPSR	HPCR	LPSR	LPCR
Sherpa ratio	0.355	0.362	0.429	0.361
Madgraph ratio	0.3502	0.3022	0.4246	0.2852
Extrapolation uncertainty [%]	1.4	16.5	1.0	30.0

Table 8.3: Summary of evaluated ratio and extrapolation uncertainties for $t\bar{t}$

W + jets ggF	HPSR	HPCR	LPSR	LPCR
Sherpa ratio	0.551	0.697	0.727	0.857
Madgraph ratio	0.467	0.53	0.616	0.688
Extrapolation uncertainty [%]	15.2	24.0	15.3	19.7
W + jets VBF	HPSR	HPCR	LPSR	LPCR
Sherpa ratio	0.34	0.403	0.386	0.49
Madgraph ratio	0.419	0.366	0.501	0.522
Extrapolation uncertainty [%]	23.2	9.2	29.8	6.5

Signal Uncertainties

For possible mis-modeling of signal generators, uncertainties on signal acceptances are estimated for the choice of the parton distribution function, the modeling of the initial- and final-state radiations. The PDF uncertainties are studied by taking the acceptance difference due to internal PDF error sets and the difference between the choice of PDF sets. The uncertainty from ISR/FSR modeling is estimated by varying parameters in the tunes used and applied to the HVT, the RS Graviton and Radion models. These uncertainties, calculated in several resonant mass points, are retrieved for each model, production and decay and considered as conservative. Those uncertainties on the signal acceptance are included in the fit. The PDF uncertainties were evaluated to be under 5% for all models. ISR/FSR uncertainties ranges from 2% in the HVT model merged regime to about 11% in the VBFHVT model in resolved regime.

Chapter 9

Statistical Interpretation

For the extraction of background normalizations and the signal strength of the hypothetical signal processes, the search utilizes the statistical treatment using a combined profile likelihood fit to binned discriminants in all categories and regions simultaneously. The binning of the discriminant for each region is determined based on the signal mass resolution, as described in Section 9.4. In the likelihood function definition, the signal strength is assigned as the parameter of interest (POI) and the systematic uncertainties and the background normalization factors are assigned as nuisance parameters (NPs). The nuisance parameters are either free to float, or constrained using Gaussian terms. Constructed likelihood function is then used to calculate the p-value for the discussion of discovery and signal exclusion.

9.1 Likelihood function definition

A binned likelihood function is defined as the product of Poisson probability terms,

$$\mathcal{L}(\mu,\vec{\theta}) = \prod_{c}\prod_{i} \text{Pois}\left(n_{c_i}^{\text{obs}}|\mu\cdot n_{c_i}^{\text{sig}}(\vec{\theta}) + n_{c_i}^{\text{bkg}}(\vec{\theta})\right)\prod_{k} f_k(\theta_k'|\theta_k), \tag{9.1}$$

where a signal strength parameter μ multiplies the expected signal yield for a given benchmark set of parameters $n_{c_i}^{\text{sig}}$ in each histogram bin i of the discriminant from channel c, and $n_{c_i}^{\text{bkg}}$ represents the background content for bin i from channel c.

The effect of the systematic uncertainties on the signal and background predictions is introduced by a set of nuisance parameters (NP) $\vec{\theta}$. The NPs affect the mean value of Poisson probability terms by shifting $n_{c_i}^{\text{sig}}$ and $n_{c_i}^{\text{bkg}}$ with the constraints from the asigned prior distribution. The term $f_k(\theta_k'|\theta_k)$ represents the set of constraints on $\vec{\theta}$ from auxiliary measurements θ_k', which include systematics normalization and shape uncertainties in the signal and background models, and include the statistical uncertainties of the simulated bin content. Each of NPs is parametrized by Gaussian or log-normal priors. The latter one, the log-normal prior, is used for normalization uncertainties in order to keep a positive likelihood. Therefore the expected numbers of signal and background events in each bin are regarded as functions of θ. For a normally distributed θ, the rates in each category are log-normally distributed. MC statistical uncertainty is parametrized by Poisson distribution.

The likelihood function, $\mathcal{L}(\mu,\vec{\theta})$, is therefore a function of μ and $\vec{\theta}$. The nominal fit of the likelihood function 9.1 is performed in terms of μ and $\vec{\theta}$ by maximizing the likelihood function with respect to all parameters. The maximized function is referred to as the maximized log-likelihood value, MLL. Maximizing the likelihood with floating μ corresponds to signal+background fit, and fixing $\mu = 0$ corresponds to background only fit.

9.2 Hypothesis Testing

To test a hypothesized value of μ the profile likelihood ratio

$$\lambda(\mu) = \frac{\mathcal{L}(\mu,\hat{\hat{\theta}}_{\mu})}{\mathcal{L}(\hat{\mu},\hat{\theta})}, \tag{9.2}$$

is considered, where $\hat{\mu}$ and $\hat{\theta}$ are the parameters that maximise the likelihood and $\hat{\hat{\theta}}_{\mu}$ are the nuisance parameter values that maximise the likelihood for a given μ. The test statistic q_{μ} is then constructed

according to the profile likelihood ratio:

$$q_\mu = -2\ln\lambda(\mu), \tag{9.3}$$

This test statistic is used to measure the compatibility of the background-only model with the observed data and to extract upper limits derived with the CL_s method [170, 171]. The limit set on μ is then translated into a limit on the signal cross-section times branching ratio, using the theoretical cross-section and branching ratio for the given signal model.

9.2.1 Discovery of a positive signal

The defined test statistic with $\mu = 0$:

$$q_0 = \begin{cases} -2\ln\lambda(0) & (\hat{\mu} \geq 0) \\ 0 & (\hat{\mu} < 0) \end{cases} \tag{9.4}$$

is used to discuss the discovery of a new signal. We don't consider the case $\hat{\mu} < 0$ as evidence against the background-only hypothesis, since our signal models do not lead to a decrease in the data and the data is expected to contain the signal event. This type of upward fluctuation of the data is dealt with the NPs in this analysis.

The p_0-value is calculated as

$$p_0 = \int_{q_0^{\rm obs}}^{\infty} f(q_0|0)dq_0, \tag{9.5}$$

where $q_0^{\rm obs}$ is the value of q_0 observed with data, and $f(q_0|0)$ denotes the pdf of the statistics q_0 under assumption of the background-only hypothesis ($\mu = 0$). If p_0 is below the certain value, the background-only hypothesis is rejected. Conventionally, a significant excess is declared if the p_0-value is greater than 3σ, and a discovery is declared when the p_0-value reaches 5σ.

9.2.2 Signal exclusion and Upper limit

If the methodology of the previous section can not reject the background-only hypothesis, the test statistic q_μ is then used to exclude a given signal model and to establish an upper limit on the signal strength μ. We redefine

$$q_\mu = \begin{cases} -2\ln\lambda(\mu) & (\hat{\mu} \leq \mu) \\ 0 & (\hat{\mu} > \mu) \end{cases}. \tag{9.6}$$

Here the test statistic is set to $q_\mu = 0$ for $\hat{\mu} > \mu$ since it is not a part of the rejection region of the test. The higher value of q_μ represents more incompatibility between the data and the hypothesized value of μ. As in the case of discovery, the p-value is defined as

$$p_\mu = \int_{q_\mu^{\rm obs}}^{\infty} f(q_\mu|\mu')dq_\mu, \tag{9.7}$$

where $q_\mu^{\rm obs}$ is the value of q_μ observed with data, and $f(q_\mu|\mu')$ is the pdf of q_μ under the assumption of the hypothesis μ'. The confidence level (CL) for signal plus background hypothesis ($\mu = 1$) is defined as

$$CL_{s+b} = \int_{q_\mu^{\rm obs}}^{\infty} f(q_\mu|1)dq_\mu, \tag{9.8}$$

If the value of CL_{s+b} is below $1-\alpha$, we can conclude the value of μ is said to be excluded at α CL. However, this definition is sometimes too aggressive to exclude a signal model properly, especially for signal models with small sensitivity. To avoid the wrong excluding, the different CL,

$$CL_s = \frac{CL_{s+b}}{CL_b} \tag{9.9}$$

is introduced, where

$$CL_b = \int_{-\infty}^{q_\mu^{\rm obs}} f(q_\mu|0)dq_\mu. \tag{9.10}$$

The greater CL_b means more compatibility between the data and the background-only hypothesis ($\mu = 0$). Since CL_b is always less than 1, CL_s is always larger than CL_{s+b}. It allows the exclusion results to be more conservative and to be protected from background fluctuations by considering compatibility between the data and background-only hypothesis. Upper limits on the signal strength at confidence level α are obtained by scanning the value of μ for which CL_s is equal to $1 - \alpha$.

9.2.3 Asymptotic Formulas

According to the Wald's theorem [172], the test statistic can be approximated as:

$$q_\mu = -2\ln\lambda(\mu) = \frac{(\mu - \hat{\mu})^2}{\sigma^2} + \mathcal{O}(1/\sqrt{N}). \tag{9.11}$$

Here N represents the data sample size, and $\hat{\mu}$ follows a Gaussian distribution with a mean μ' and standard deviation σ. The standard deviation σ of $\hat{\mu}$ is estimated by the Asimov data set [170] corresponding to a strength μ' which gives $\hat{\mu} = \mu'$. When the data sample size N is significantly large so that the $\mathcal{O}(1/\sqrt{N})$ term can be neglected, one finds the test statistic is written as:

$$-2\ln\lambda_{\rm A}(\mu) \sim \frac{(\mu - \mu')^2}{\sigma^2} = \Lambda. \tag{9.12}$$

Therefore, with the Asimov data set, the distribution of $f(q_\mu|\mu')$ can be characterized by the noncentrality parameter Λ. The deviation σ is obtained as

$$\sigma^2 = \frac{(\mu - \mu')^2}{q_{\mu,{\rm A}}}, \tag{9.13}$$

where $q_{\mu,{\rm A}} = -2\ln\lambda_{\rm A}(\mu)$.

Using the validity of the asymptotic approximation discussed above, the p-value of the hypothesized μ can be decribed in a simple way. For instance, in upper limit calculation the test statistic can be written as:

$$q_\mu = \begin{cases} \frac{(\mu-\hat{\mu})^2}{\sigma^2} & \hat{\mu} < \mu \\ 0 & \hat{\mu} > \mu \end{cases}. \tag{9.14}$$

Following the discussion of Ref. [170] based on Equation (9.14), the simple expression of the p-value for the hypothesized μ is obtained:

$$p_\mu = 1 - \Phi(\sqrt{q_\mu}), \tag{9.15}$$

where Φ is the cumulative distribution function for the Gaussian distribution. Thanks to this approximation, we can estimate the p-value by only one fit.

9.3 Fit inputs

The analysis uses many kinds of fit inputs which are arranged as the product of channel, category, regime and region for a binned likelihood function 9.1. The channel refers to the analysis with different numbers of leptons in the final states (0-lepton, 1-lepton and 2-lepton). The category refers to the selection for VBF or ggF signal. The regime refers to the merged and resolved jet analysis objects used in selection and the region refers to signal (SR) and control regions (CR) which normally consist of subregions of different properties. The merged regimes of both SR and CR are further split into high-purity (HP) and low-purity (LP) subregions based on the result of the boosted boson tagging. For $Z \to qq$ selection in the ggF category (SRWZ in 1-lepton channel and SRZZ in 0- and 2-lepton channels), signal and control regions in both merged and resolved regimes are further split into untagged (0 or 1 b-tagged jet) and tagged subregions (exactly 2 b-tagged jets) according to the number of b-tagged jets. For 0-lepton channel, only merged regime is considered

(see Section 6.6.1). For each of the final regions, the input to the likelihood is the invariant mass (for 1-lepton and 2-lepton channels) or transverse mass (for the 0-lepton channel) distribution of the VV system.

In the fit of Equation 9.1, resonance signal, W+jets, Z+jets, $t\bar{t}$, single-top, diboson and multijet processes are considered. The detailed description of these processes can be found at Section 3.3.1 and 7. Since whether or not applying $Z \to bb$ tagging depends on the target signal model and the lepton channels, two different fit configurations are used:

- $ZZ + WW$, to probe for heavy spin-0 and spin-2 gravitons;
- ZW, to probe for heavy charged spin-1 vectors ($W'^{\pm}$);

The complete list of regions used in each fit model are shown in Tables 9.1–9.2.

Regions			Spin-0 and Spin-2 fit model ($X \to ZZ/WW$)					
			Merged HP		Merged LP		Resolved	
			Tagged	Untagged	Tagged	Untagged	Tagged	Untagged
0-lepton	ggF	SR	✓	✓	✓	✓	–	
	VBF	SR	✓		✓		–	
1-lepton	ggF	SR	✓		✓		✓	
		WCR	One bin		One bin		One bin	
		TopCR	One bin		One bin		One bin	
	VBF	SR	✓		✓		✓	
		WCR	One bin		One bin		One bin	
		TopCR	One bin		One bin		One bin	
2-lepton	ggF	SR	✓	✓	✓	✓	✓	✓
		ZCR	One bin	One bin	One bin	One bin	One bin	One bin
	VBF	SR	✓		✓		✓	
		ZCR	One bin		One bin		One bin	

Table 9.1: Summary of the regions entering the likelihood of the fit models to search for heavy resonances decaying to ZZ and WW in semileptonic final states. "✓" indicates that the shape of the final discriminant is taken into account in the fit. "One bin" implies that a single bin without any shape information is used in the corresponding fit region and "–" means that the region is not present in the fit.

Regions			Spin-1 fit model ($X \to ZW$)					
			Merged HP		Merged LP		Resolved	
			Tagged	Untagged	Tagged	Untagged	Tagged	Untagged
0-lepton	ggF	SR	✓		✓		–	
	VBF	SR	✓		✓		–	
1-lepton	ggF	SR	✓	✓	✓	✓	✓	✓
		WCR	One bin	One bin	One bin	One bin	One bin	One bin
		TopCR	One bin	One bin	One bin	One bin	One bin	One bin
	VBF	SR	✓		✓		✓	
		WCR	One bin		One bin		One bin	
		TopCR	One bin		One bin		One bin	
2-lepton	ggF	SR	✓		✓		✓	
		ZCR	One bin		One bin		One bin	
	VBF	SR	✓		✓		✓	
		ZCR	One bin		One bin		One bin	

Table 9.2: Summary of the regions entering the likelihood of the fit models to search for heavy resonances decaying to ZW in semileptonic final states. "✓" indicates that the shape of the final discriminant is taken into account in the fit. "One bin" implies that a single bin without any shape information is used in the corresponding fit region and "–" means that the region is not present in the fit.

9.4 Signal Resolution

The appropriate binning of VV invariant mass distribution is determined based on the expected signal mass resolution. The MC simulated HVT signal is used to estimate the mass resolution for each mass point separately in for ggF and VBF production and merged and resolved regions. The mass distribution is fit with dedicated functions. The one and two lepton channels use a Gaussian function, $f(m) = A\exp(\frac{(m-m_0)^2}{2\sigma^2})$, where σ is taken as the resolution. In the zero lepton channel, a Landau function is used to fit the transverse mass distribution. The estimated scale parameter is used as an estimate of the resolution. Figure 9.1 shows some examples of these fits.

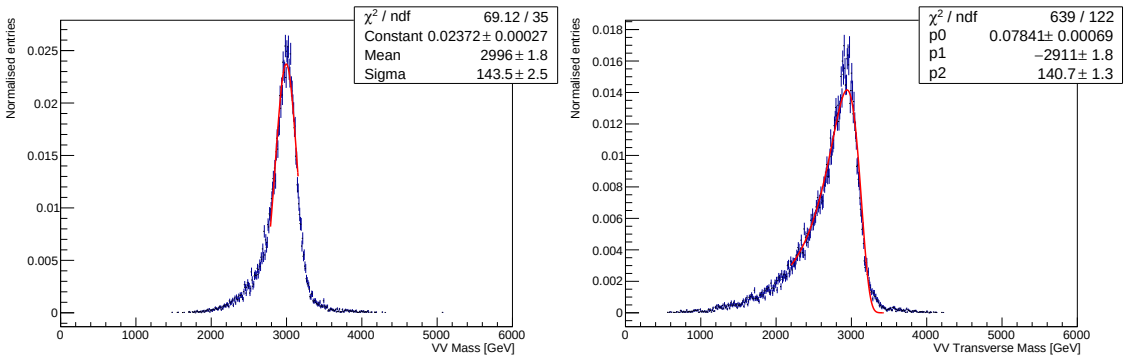

(a) (b)

Figure 9.1: Examples of the invariant VV mass fit with a Gaussian function (1- and 2- lepton) and transverse mass fit with a Landa function (0-lepton). (a); ggF merged region, mass = 3 TeV in 1-lepton (b) ggF merged region , mass = 3 TeV in 0-lepton.

The width of each mass peak is then plotted as a function of the resonance mass and fit with a straight line. Some examples of the fit results are shown in Figure 9.2. With the parameterized resolution, the bin edges are chosen such that the bins are larger than the mass resolution. In addition, it requires that the number of background events in the bin is non-zero, and that the relative statistical uncertainty on the number of background events in the bin is less than 10%.

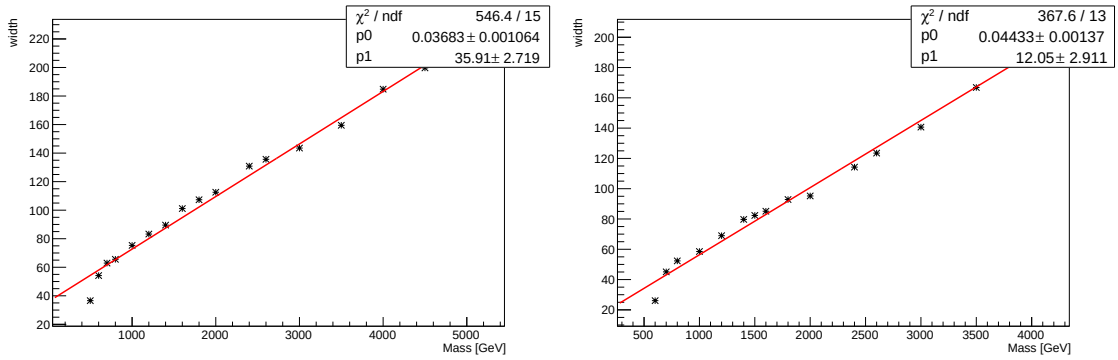

(a) (b)

Figure 9.2: The HVT signal mass resolution as a function of mass fit with a straight line in (a) ggF merged 1-lepton and (b) ggF merged 0-lepton channel.

9.5 Nuisance parameters: normalization and systematic uncertainties

In addition to background processes, all the systematic uncertainties denoted in Section 8 also enter the profile likelihood fit as nuisance parameters (NPs). Two different types of nuisance parameters are used:

floating parameters and parameters with priors. In general, a prior probability distribution is assigned to the systematic uncertainties. On the other hand, for the most significant backgrounds, the floating parameter is assigned to the normalization since the analysis is designed to constrain them by the dedicated control regions. The normalization factores for the background contributions are discussed and summarized in Section 7. Furthermore, there are several extra nuisance parameters which correspond to the uncertainties on the acceptance or normalization of signal or a certain background component, as discussed in Section 8.2.

The statistical uncertainties for the total background MC samples in each bin are taken into account in the profile likelihood as an extra nuisance parameter. This is performed by using a light weight version of the Barlow-Beeston method [173] as implemented in HistFactory [174]. The additional nuisance parameters for the statistical uncertainty is completely uncorrelated across bins. For the sake of fit stability, bins with the relative statistical uncertainty less than 1% are ignored in the fit.

9.5.1 Smoothing and Symmterization of Systematic Uncertainties

When estimating systematic uncertainties, there is the possibility to have unsmooth distribution with unphysically large fluctuations due to low MC statistics. This may lead to artificial problems in the fit. In order to remove such issues, a smoothing procedure composing the following steps is applied to all systematic variation distribution in all regions.

- Rebin distributions with relative integral statistical error $> 5\%$ into a single bin.
- In all of local extrema, the smallest one is identified as a fluctuation and iteratively merged with the neighboring bin until only four local extrema remain.
- Rebin distributions until $< 5\%$ statistical uncertainty remain in each bin.

The up/down variations are sometimes in the same directions with respect to the nominal distribution. In this case, a symmetrization procedure is performed. For up/down systematic variations, if there are more than 3 bins in the same direction with respect to nominal, the variation is averaged by replacing the variation bin content by $b_{\pm}^{new} = b_{nom} \pm \frac{|b_+ - b_-|}{2}$, where b_{nom} is the nominal bin content, and b_+/b_- are the original up/down variation bin content. For variations in a region, if the integral of the difference of the up/down variation is twice that of the other up/down variation, the same procedure is applied to the variation.

9.5.2 Pruning of the Systematic Uncertainties

This analysis consider several kinds of the systemtic uncertainties. However, some of them have a negligible effect on the final result. In addition, low MC statistics can cause large fluctuations on systematic templates, which lead to artificial variations in the fit. To remove such effects, a *Prunning* procedure is applied to remove uncertainties with negligible effects on the results. Pruning is performed as follows:

- Neglect the normalization uncertainty for a given sample in a region if either of the following is true:
  - the variation is less than 1%;
  - both up and down variations have the same sign.
- Neglect the shape uncertainty for a given sample in a given region if the following is true:
  - not one single bin has a deviation over 1% after the overall normalization is removed;
  - if only the up or the down variation is non-zero and passed the previous pruning steps.

The list of pruned uncertainties is regularly checked to ensure that this is behaving as expected.

9.5.3 Pull and Impact of nuisance parameters

In order to investiage how far a nuisance parameter θ needs to be varied from its expected value θ_0 while finding MLL, the "*Pull*" is defined as

$$\text{Pull}(\theta) = \frac{\hat{\theta} - \theta_0}{\sigma_\theta}. \tag{9.16}$$

When the pull average is zero with a standard deviation close to 1, we can say the corresponding NP is fine. If this is not the case, further investigation is required. The expected value of a nuisance parameter and

its assumed standard deviation will be based on an auxiliary measurement or MC studies as discussed in Section 8.

The impact of a nuisance parameter on signal sensitivities are studied by evaluating the variation of POI (parameter of interest) when fixing a nuisance parameter shifted from its expected value by $\pm$ one standard deviation and keeping other parameters being float. The impact helps to investigate how much our parameter of interest varies when the nuisance parameter is changed.

Chapter 10

Results

This section presents the results of the search for new heavy diboson resonances decaying into semi-leptonic final states, which are obtained from the combined fit of all three lepton channels with the fit configuration described in Sec. 9. Background only fit (see Section 9.2) results for two different selections are shown: $X \to WZ$ with $WZ \to \ell\ell qq, \ell\nu qq, \nu\nu qq$ and $X \to WW/ZZ$ with $WW \to \ell\nu qq$ and $ZZ \to \ell\ell qq, \nu\nu qq$. In general, no significant deviations from the post-fit SM predictions are observed. Then the interpretation results for several benchmark BSM signal models are discussed.

10.1 Search for $X \to WW/ZZ$ signal

WW/ZZ background-only fit results are summarized in this section. All regions of the WW/ZZ analysis of three lepton channels are included in the fit. Background estimation is derived from a simultaneous fit in both signal and control regions. All experimental and statistical uncertainties are included. Results of the search for WZ analysis can be found in Appendix A since most of the regions are largely overlapped with WW/ZZ analysis.

10.1.1 Post-fit distributions

Event yields in each signal/control region are summarized in Figure 10.1. Good agreement between observed data and post-fit predictions is observed in both control regions and signal regions. The final discriminant variable in the signal regions are shown in Figures 10.2-10.4. No significant deviations from the post-fit predictions are indicated. Table 10.1 shows the post-fit estimated background event yields from different sources in all WW/ZZ SRs compared with the number of the observed events in data.

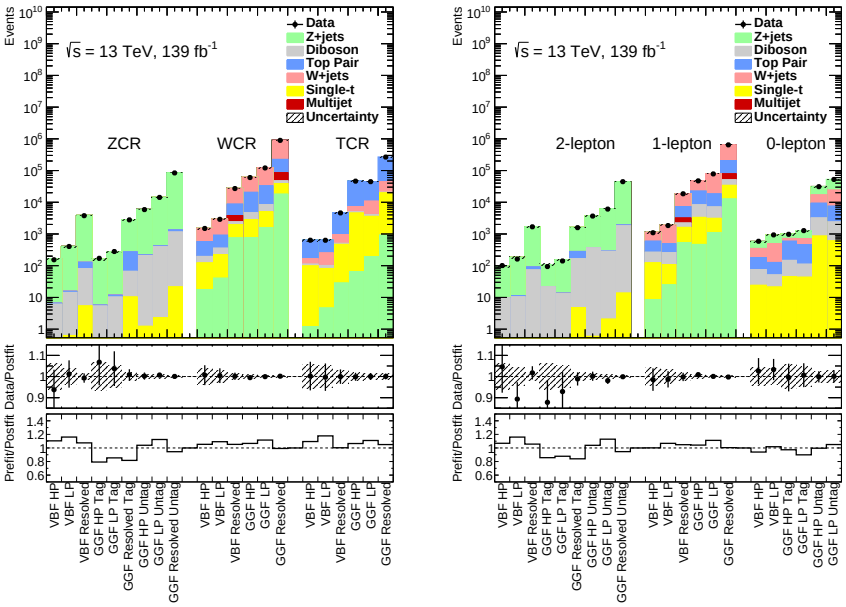

Figure 10.1: Postfit distributions in all (left) control regions and (right) signal regions of the WW/ZZ analysis.

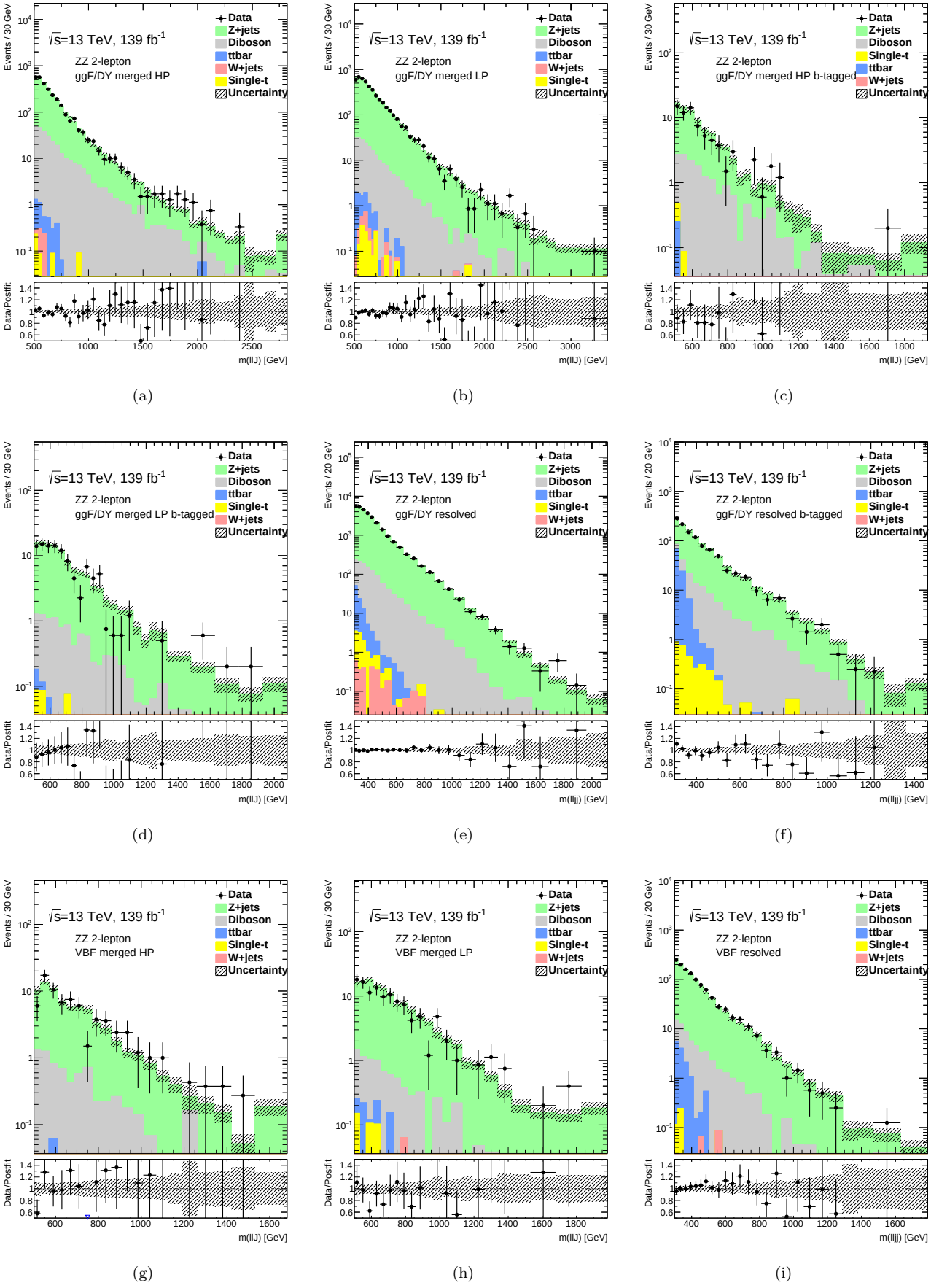

Figure 10.2: Postfit distributions of the invariant mass in the *llqq* (a) GGF merged HP ZZ Tag SR (b) GGF merged HP ZZ Untag SR (c) GGF merged LP ZZ Tag SR (d) GGF merged LP ZZ Untag SR (e) GGF resolved ZZ Tag SR (f) GGF resolved ZZ Untag SR (g) VBF merged HP ZZ SR (h) VBF merged LP ZZ SR (i) VBF resolved ZZ SR.

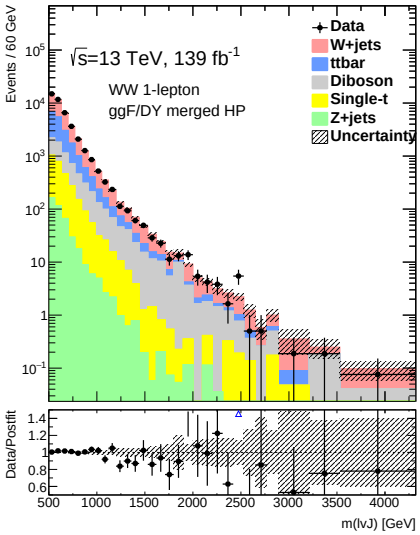

(a)

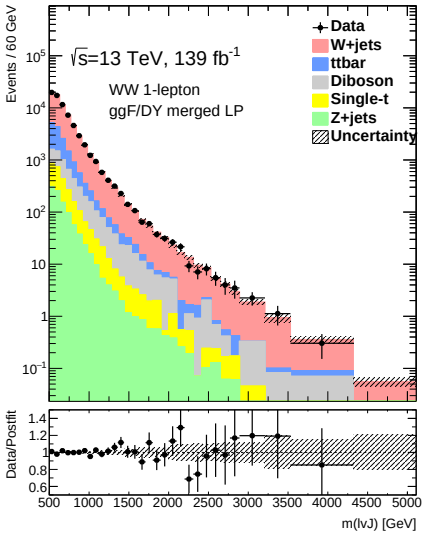

(b)

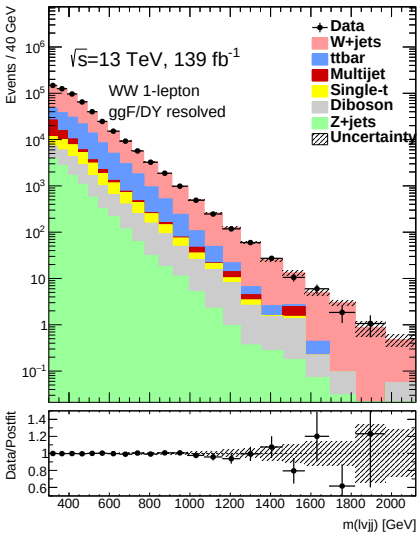

(c)

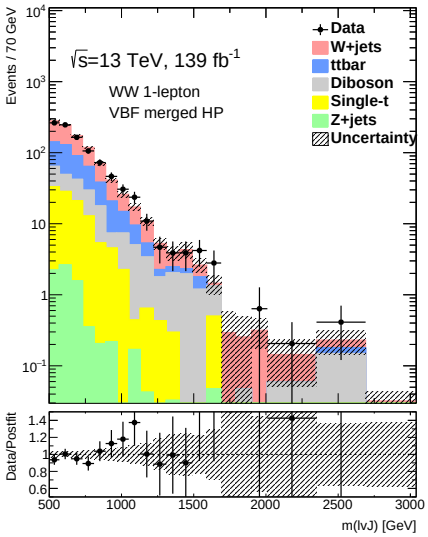

(d)

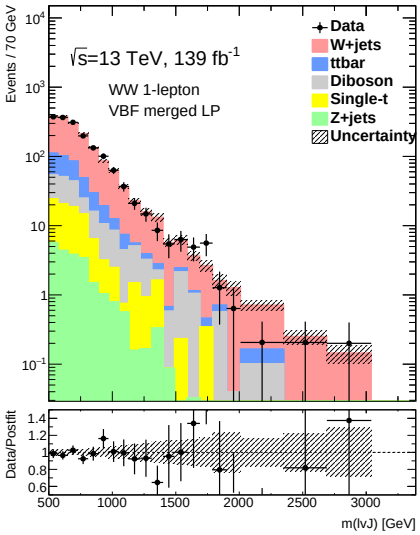

(e)

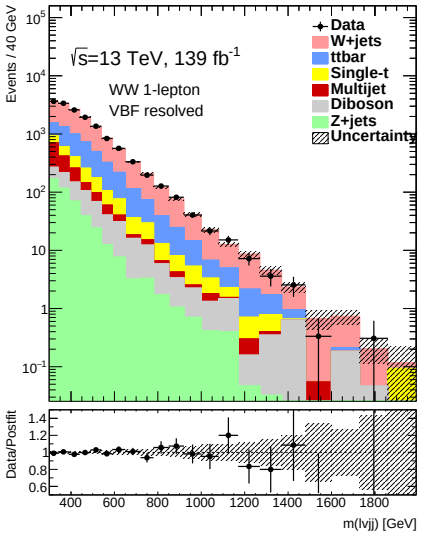

(f)

Figure 10.3: Postfit distributions of the invariant mass in the $l\nu qq$ (a) GGF merged HP WW SR (b) GGF merged LP WW SR (c) GGF resolved LP WW SR (d) VBF merged HP WW SR (e) VBF merged LP WW SR (f) VBF resolved LP WW SR.

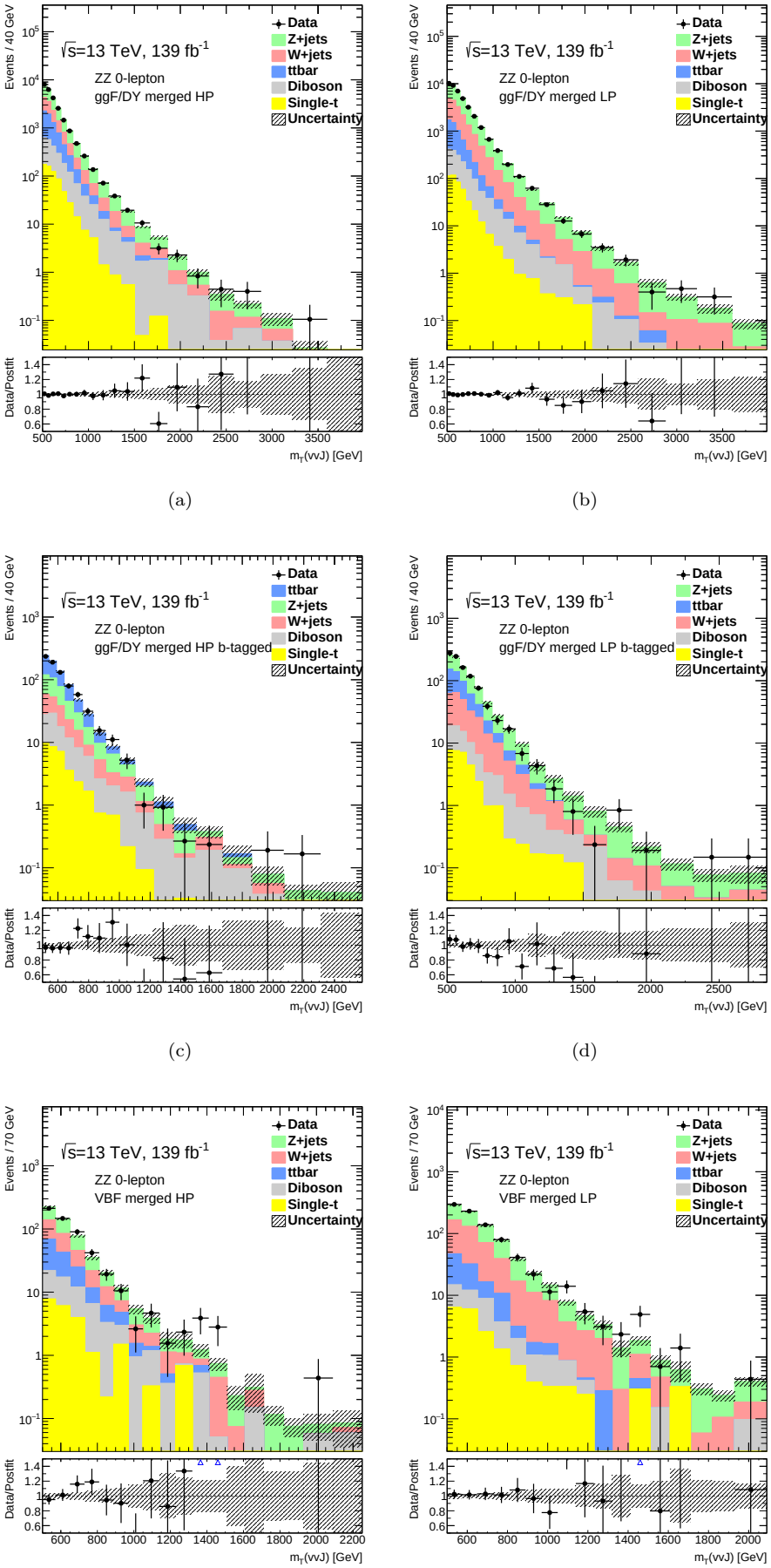

Figure 10.4: Postfit distributions of the transverse mass in the $\nu\nu qq$ (a) GGF merged HP ZZ Tag SR (b) GGF merged HP ZZ Untag SR (c) GGF merged LP ZZ Tag SR (d) GGF merged LP ZZ Untag SR (e) VBF merged HP ZZ SR (f) VBF merged LP ZZ SR.

Table 10.1: The expected background events with breakdowns from individual sources in 6 WW and 15 ZZ SRs compared with the data. The backgrounds are estimated from a background-only simultaneous fit to all WW and ZZ SRs and their corresponding CRs.

Channel	$V \to qq$ recon.	Signal regions		Background estimates							Data
				$W+$jets	$Z+$jets	$t\bar{t}$	Diboson	Single-t	Multijet	Total	
0-lepton (ZZ)				VBF category							
	Merged	HP		168 ± 18	228 ± 18	103 ± 24	51.7 ± 13	23.9 ± 5.3	-	575 ± 38	589
		LP		369 ± 33	411 ± 24	75 ± 18.6	29.5 ± 5	21.1 ± 5.2	-	906 ± 46	936
				ggF/DY category							
	Merged	HP	Tag	134 ± 18	266 ± 61	436 ± 50	101 ± 13	45 ± 9	-	982 ± 82	978
			Untag	7669 ± 635	14276 ± 757	6009 ± 461	2317 ± 273	844 ± 151	-	31116 ± 1134	31074
		LP	Tag	261 ± 34	556 ± 64	341 ± 39	67.4 ± 9.2	42.7 ± 8.5	-	1269 ± 83	1277
			Untag	16450 ± 1353	5023 ± 387	28517 ± 1442	1771 ± 218	596 ± 107	-	52358 ± 2030	52396
1-lepton (WW)				VBF category							
	Merged	HP		529 ± 35	8.3 ± 0.58	320 ± 26	141 ± 41	113 ± 24	-	1112 ± 64	1096
		LP		1384 ± 56	24.5 ± 1.2	225 ± 21	151 ± 46	83.3 ± 18.7	-	1871 ± 77	1846
	Resolved			11365 ± 271	526 ± 11	4061 ± 160	582 ± 338	1074 ± 232	958 ± 144	18586 ± 539	18530
				ggF/DY category							
	Merged	HP		24819 ± 213	463 ± 6	13885 ± 282	4917 ± 345	2831 ± 501	-	46914 ± 703	47330
		LP		60269 ± 309	1096 ± 9	11048 ± 197	3951 ± 296	1972 ± 351	-	78335 ± 587	78380
	Resolved			443515 ± 2444	12479 ± 43	126009 ± 1935	16787 ± 1451	21186 ± 3691	27124 ± 2321	647100 ± 5655	645610
2-lepton (ZZ)				VBF category							
	Merged	HP		0	86.8 ± 6.04	0.08 ± 0.01	9.65 ± 1.89	0	-	96.5 ± 6.3	101
		LP		0.13 ± 0.01	170 ± 8	0.84 ± 0.08	9.9 ± 2.01	0.43 ± 0.09	-	181 ± 8	162
	Resolved			0.27 ± 0.01	1566 ± 34	17 ± 0.8	72.5 ± 13.6	0.49 ± 0.38	-	1656 ± 34	1685
				ggF/DY category							
	Merged	HP	Tag	0.01 ± 0.00	85.3 ± 6.2	0.28 ± 0.03	21.1 ± 2.5	0.34 ± 0.06	-	107 ± 7	94
			Untag	0.77 ± 0.01	3299 ± 43	4.27 ± 0.1	361 ± 35	0.58 ± 0.13	-	3667 ± 56	3671
		LP	Tag	0.01 ± 0.00	138 ± 8	0.31 ± 0.03	12.8 ± 1.5	0.3 ± 0.06	-	152 ± 8	141
			Untag	2.34 ± 0.02	5923 ± 52	10.2 ± 0.2	279 ± 28	2.03 ± 0.39	-	6216 ± 59	6095
	Resolved	Tag		0	1323 ± 28	114 ± 11	160 ± 14	4.72 ± 1	-	1602 ± 33	1583
		Untag		4.68 ± 0.03	42747 ± 174	111 ± 2	1775 ± 133	13.4 ± 2.6	-	44651 ± 219	44604

10.2 Test of background-only hypothesis

Since no significant deviation is observed in the background only post-fit distributions, p_0-value is calculated for each signal model with all three lepton channels combined, as shown in Figure 10.5. p_0-value is calculated for ggF and VBF Radion with all three lepton channels combined in $X \to WW/ZZ$, as shown in Figure 10.5a–10.5b. Results for HVT W' in $X \to WZ$ analysis are shown in Figure 10.5c and 10.5d. No significant excesses with respect to the background only hypothesis have been observed. The largest excess is found to be less than 3σ of local significance around 1.5 TeV in VBF signal produced. This corresponds to the slight excess observed in Figure A.3 (g) and Figure A.4 (c). Similar plots for Graviton are also shown in Figure 10.5e–10.5f. No significant excesses with respect to the background only hypothesis have been observed.

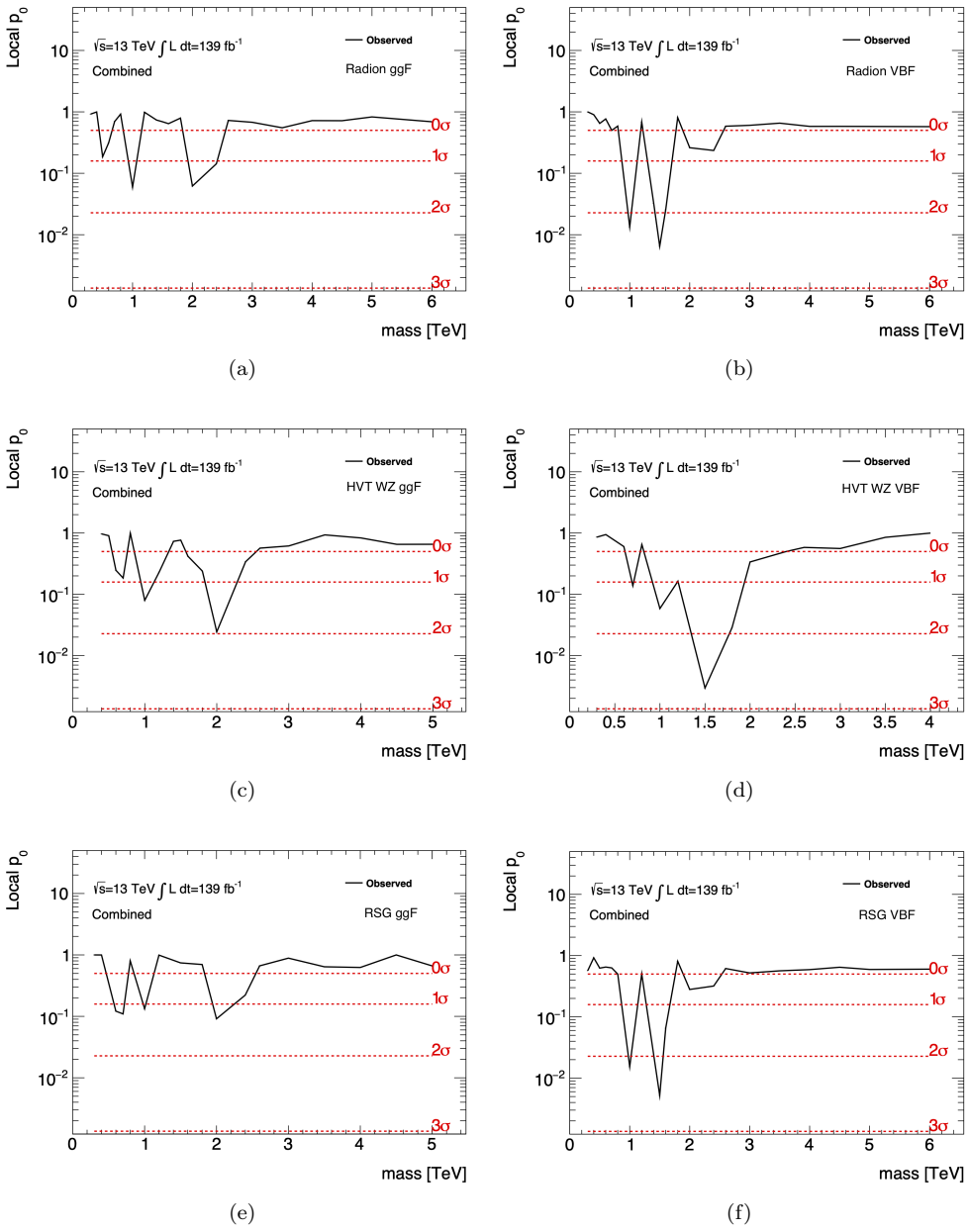

Figure 10.5: Scan of p_0 as a function of the resonance mass of (a) ggF Radion, (b) VBF Radion, (c) DY HVT W', (d) VBF HVT W', (e) ggF Graviton and (f) VBF Graviton with three lepton channels combined.

10.3 Interpretations

Since there are no significant deviations from background-only hypothesis, 95% CL upper limits on the cross-section times branching ratio are set on several signal models: Spin-0 Radion, Spin-1 HVT and Spin-2 Bulk RS Graviton.

10.3.1 Results for spin-0 Radion models

95% CL upper limits on $\sigma(pp \to X) \times \mathrm{BR}(X \to VV)$ are set for spin-0 Radions. Both ggF and VBF production modes are considered. Figure 10.6 shows exclusion limits on $\sigma(pp \to X) \times \mathrm{BR}(X \to VV)$ for ggF and VBF Radion with all three lepton channels combined. Comparison of exclusion limits from the combined fit and each lepton channel is also shown. At the highest-mass region of greater than 3 TeV the sensitivity equally comes from $\ell\nu qq$ and $\nu\nu qq$ channels, while $\ell\ell qq$ channel contributes to it at lower-mass region. $m < 3.45$ TeV for spin-0 Radion via ggF production is excluded at 95% CL.

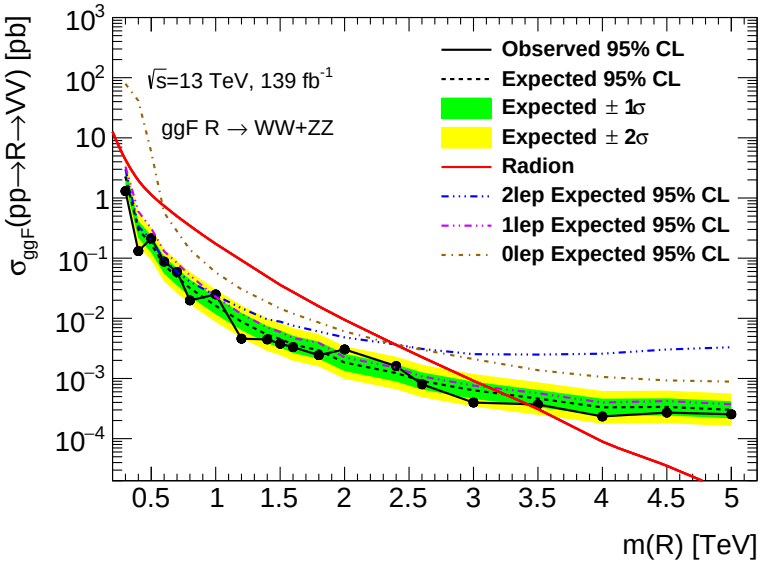

(a)

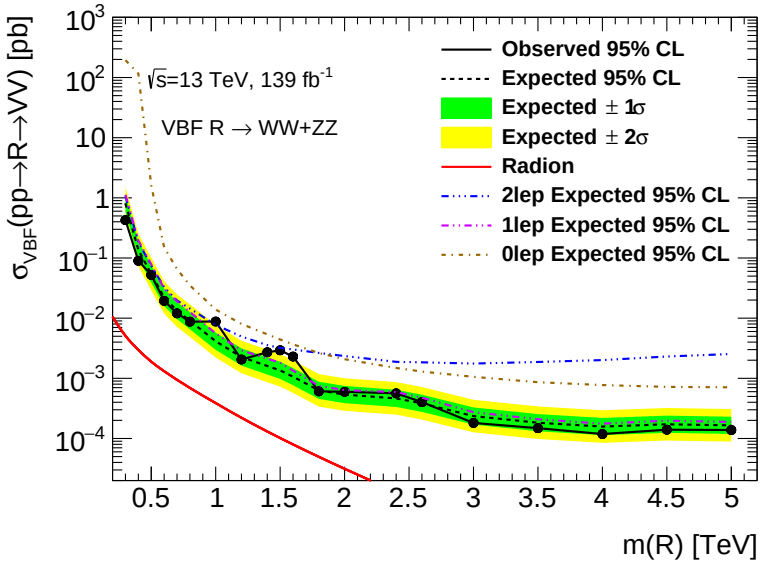

(b)

Figure 10.6: 95% CL upper limit on cross section times branching ratio of Radions produced via (a) ggF and (b) VBF decaying to WW/ZZ pair, with all three lepton channels combined.

10.3.2 Results for spin-1 HVT models

95% CL upper limits on $\sigma(pp \to X) \times \mathrm{BR}(X \to WZ)$ are set for spin-1 HVT W'. Both Drell-Yan and VBF production modes are considered.

Figure 10.7 shows exclusion limits on $\sigma(pp \to X) \times \mathrm{BR}(X \to WZ)$ for DY and VBF HVT W' with all three lepton channels combined. Comparison of exclusion limits from the combined fit and each lepton channel is also shown. At the highest-mass region of greater than 3 TeV the sensitivity equally comes from $\ell\nu qq$ and $\nu\nu qq$ channels, while $\ell\ell qq$ channel contributes to it at lower-mass region. For the phenomenological heavy-vector-triplet benchmark Model A (B) with coupling constant $g_V = 1$ (3) , $m(W') < 4.08$ (4.36) TeV for spin-1 vector triplet produced via DY mode is excluded at 95% CL.

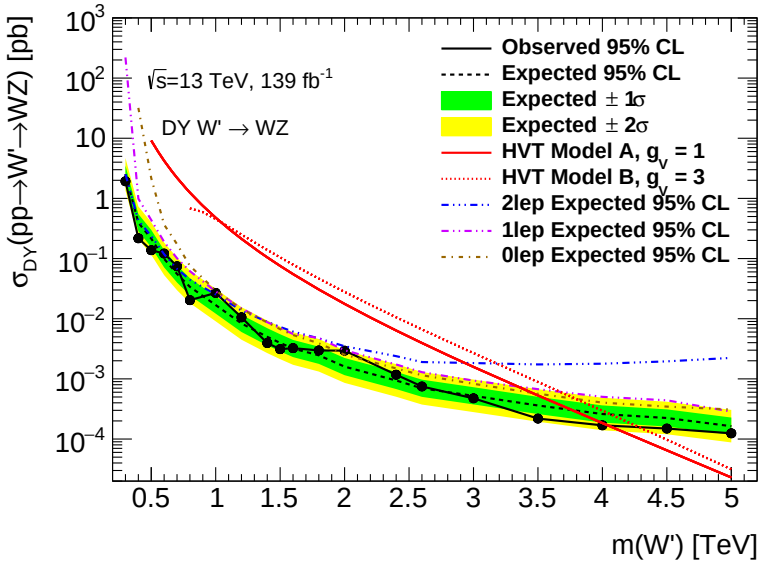

(a)

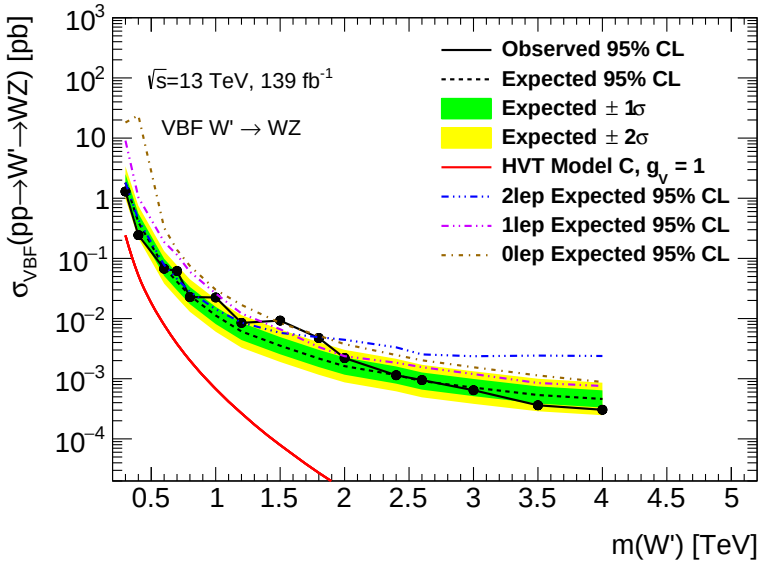

(b)

Figure 10.7: 95% CL upper limit on cross section times branching ratio of HVT W' produced via (a) DY and (b) VBF decaying to WZ pair, with all three lepton channels combined.

Constraints on the coupling strengths to both quarks and bosons (g_q, g_H) have been studied in the context of HVT models, as shown in Figure 10.8. As with Figure 1.10, the limits are not valid in the shaded region since resonance would have a width greater than 5% of their mass and the area outside each curve is excluded for each mass point. The constraints become weak when the couplings for both g_H and g_f decrease since

the resonance couplings to VV and VH decreases as the g_H coupling approaches zero, and production of the resonance tends to zero as the g_f couplings approach zero.

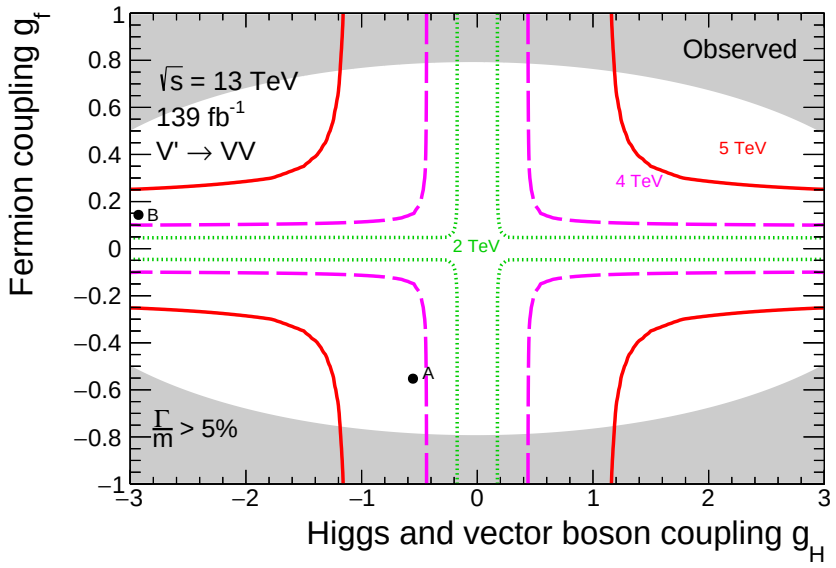

(a)

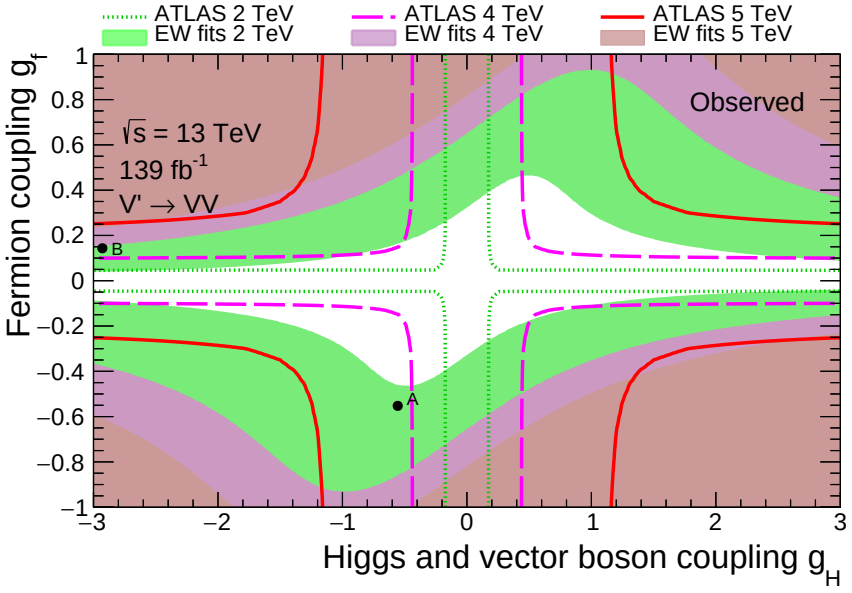

(b)

Figure 10.8: Observed 95% CL exclusion contours in the HVT parameter space $\{g_H, g_f\}$ for resonances of mass 2, 4 and 5 TeV for the combination of (a) VV channel, and (b) VV channel with the filled regions which show the constraints from precision EW measurements. The dot A, B in the plots indicate Model A and Model B, respectively.

10.3.3 Results for spin-2 Graviton models

95% CL upper limits on $\sigma(pp \to X) \times \mathrm{BR}(X \to VV)$ are set for spin-2 Graviton. Both ggF and VBF production modes are considered.

Figure 10.9 shows exclusion limits on $\sigma(pp \to X) \times \mathrm{BR}(X \to VV)$ for ggF and VBF Graviton with all three lepton channels combined. Comparison of exclusion limits from the combined fit and each lepton channel is also shown. At the highest-mass region of greater than 3 TeV the sensitivity equally comes from $\ell\nu qq$ and $\nu\nu qq$ channels, while $\ell\ell qq$ channel contributes to it at lower-mass region. For the bulk Randall-Sundrum model with $k/\bar{M}_{\mathrm{Pl}} = 1$, $m(\mathrm{GKK}) < 2.0(0.84)$ TeV for a spin-2 Kaluza-Klein graviton produced via ggF (VBF) is excluded at 95% CL.

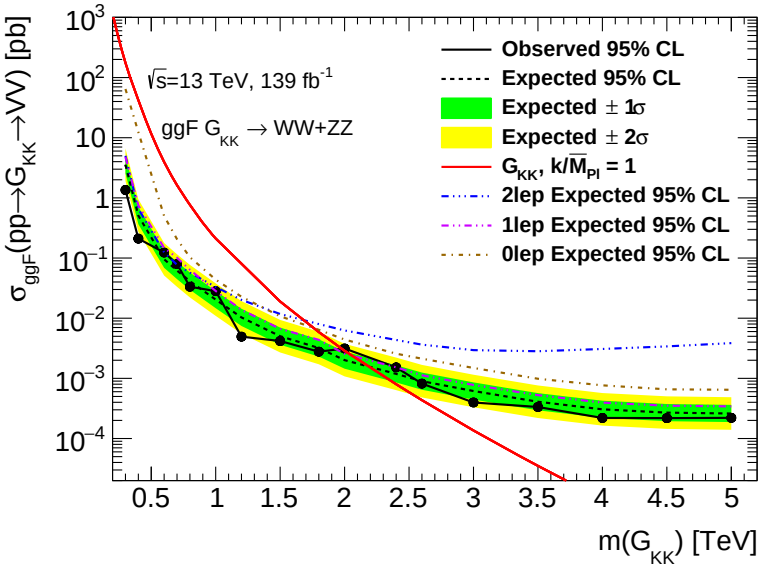

(a)

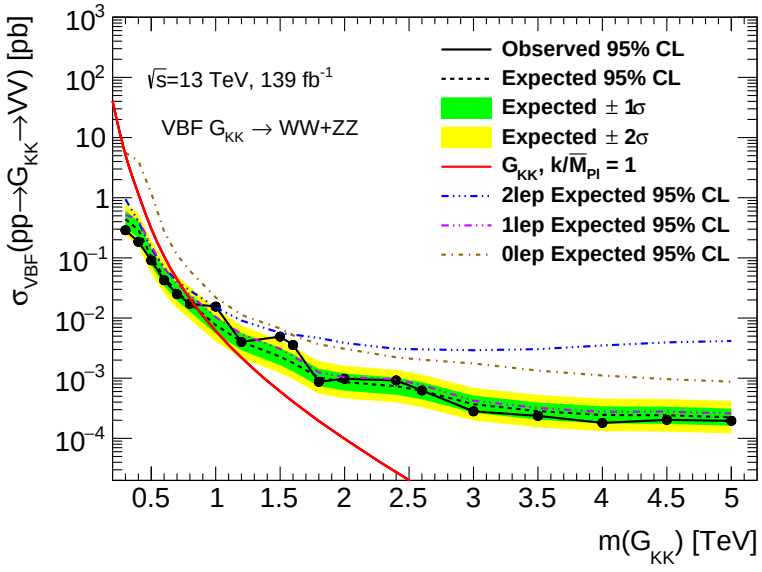

(b)

Figure 10.9: 95% CL upper limit on cross section times branching ratio of Graviton produced via (a) ggF and (b) VBF decaying to WW/ZZ pair, with all three lepton channels combined.

10.4 Impact of systematic uncertainties

The effects of systematic uncertainties are studied for hypothesized signals using the signal-strength parameter μ. The relative uncertainties in the best-fit μ value from the leading sources of systematic uncertainty are shown in Table 10.2 for ggF and VBF Radion signal with $m(X) = 600$ GeV and 2 TeV, respectively. The tables for spin-1/2 signals can be found in Appendix C. The uncertainties with the largest impact on the sensitivity of the searches are from the size of the MC samples, floating background normalizations, measurements of small-R and large-R jets, and background modeling. The effects of systematic uncertainties for the other searches are similar to those shown for the ggF Graviton search.

Table 10.2: Ranking of the nuisance parameter impact on the best-fit μ value on ggF Radion with $m(X) = 600$ GeV and $\sigma(pp \to X) \times \mathrm{BR}(X \to VV) = 0.01$ pb, ggF Radion with $m(X) = 2000$ GeV and $\sigma(pp \to X) \times \mathrm{BR}(X \to VV) = 0.002$ pb, VBF Radion with $m(X) = 600$ GeV and $\sigma(pp \to X) \times \mathrm{BR}(X \to VV) = 0.01$ pb and VBF Radion with $m(X) = 2$ TeV and $\sigma(pp \to X) \times \mathrm{BR}(X \to VV) = 0.002$ pb, corresponding to approximately the expected median upper limits at these two mass values.

ggF Radion			
600 GeV		2000 GeV	
Source	$\Delta\mu$	Source	$\Delta\mu \times 10^{-3}$
V+jets Generator difference	0.0294	V+jets Generator difference	1.001
MC statistical uncertainty	0.0219	MC statistical uncertainty	0.340
Z+jets cross-section normalization	0.0147	Boson tag SF b-tag effieicny	0.180
Small-R jet JER	0.0095	Large-R jet p_{T} scale	0.158
VV RF Scale	0.0090	Boson tag SF ttbar Modeling	0.141
Small-R jet b-tag efficiency SF	0.0086	Boson tag SF Gamma+jet	0.138
Large-R jet JER	0.0072	VV RF Scale	0.104
Boson tag SF ttbar Modeling	0.0061	VR track jet b-tag efficiency SF	0.085
VV cross-section normalization	0.0057	Boson tag SF Dijet	0.082
ttbar cross-section	0.0044 normalization	Boson tag SF other	0.071

VBF Radion			
600 GeV		2000 GeV	
Source	$\Delta\mu$	Source	$\Delta\mu \times 10^{-3}$
MC statistical uncertainty	0.0167	Large-R jet p_{T} scale	0.253
Small-R jet JER	0.0059	V+jets Generator difference	0.123
Large-R jet p_{T} scale	0.0051	Boson tag SF b-tag efficiency SF	0.113
V+jets Generator difference	0.0047	MC statistical uncertainty	0.108
Z+jets cross-section normalization	0.0041	Boson tag SF ttbar Modeling	0.076
VV EW contribution	0.0035	Boson tag SF other	0.051
W+jets cross-section	0.0025	Small-R jet JER	0.031
Boson tag SF ttbar Modeling	0.0022	ttbar PH7	0.021
Boson tag SF b-tag efficiency SF	0.0021	Boson tag SF Gamma+jet	0.020
MET	0.0013	VR track jet b-tag efficiency SF	0.019

Chapter 11

Conclusion

Although the discovery of the Higgs boson represents a major milestone in the understanding of electroweak symmetry breaking, it is also known that the SM is not the ultimate theory due to underlying problems such as Dark Matter and Hierarchy problem. Several kinds of BSMs are proposed in order to solve them. The BSMs predict a TeV-scale new particle which can decay into a pair of vector bosons. We have several decay modes for the diboson resonance: $VV \to \ell\ell\ell\ell$, $\ell\ell\ell\nu$, $\ell\nu\ell\nu$, $\ell\ell\nu\nu$, $\nu\nu qq$, $\ell\nu qq$, $\ell\ell qq$, and $qqqq$. Since these final states can be reconstructed and explored by the ATLAS experiments, it is one of the biggest motivations to search for the new heavy diboson resonances at the LHC.

The full-leptonic channels like $lll\nu$ have better sensitivity in low m_{VV} region, while the full-hadronic channel ($qqqq$) shows the compatible sensitivity with $\ell\nu qq$ and $\nu\nu qq$ channels in high m_{VV} region. However, both full-leptonic and full-hadronic channels can only probe the lower or higher m_{VV} region. On the other hand, the semi-leptonic channels can probe the broader range of m_{VV} by combining each channel: $\nu\nu qq$, $\ell\nu qq$ and $\ell\ell qq$, and therefore it could be the good probe for exploring new physics. In addition, most of the resonance mass produced via VBF is not excluded, and VBF production can be searched by only the semi-leptonic analysis. In ggF production mode, the higher mass region is still not excluded for most of benchmark signal models. Therefore sensitivity improvements for higher mass region are significantly important. Since the semi-leptonic analysis could be a significant indicator of new physics, the analysis improvement for higher mass region and VBF signal is surely helpful.

To achieve the analysis improvement, the author introduce several new ideas such as TCC (Section 5), variable-radius (VR) track-jet b-tagging for the boosted $Z \to bb$ reconstruction (Section 6.5.1), machine-learning (ML) based ggF(DY)/VBF categorization (Section 6.4). The author contributed in the ATLAS collaboration to all of the developments, in particular the optimization of boson tagging criteria and the calibration of TCC jets. By introducing the TCC jets, the signal sensitivity is improved by $\sim 30\%$ in high mass region (3–5 TeV).

This thesis presents searches for new heavy diboson resonances, using pp collision data collected with the ATLAS detector at a center-of-mass energy of $\sqrt{s} = 13\,\text{TeV}$ in years 2015-18 corresponding to an integrated luminosity of $139\,\text{fb}^{-1}$. The semi-leptonic final states of the heavy diboson resonances are used, where one of the boson pair decays leptonically and the other decays hadronically. The invariant-mass (for 1-lepton and 2-lepton channels) and transverse mass (for the 0-lepton channel) reconstructed by the final-state boson candidates are used as a final discriminant, and an excess against the estimated SM background is explored.

The observed data is consistent with the SM background expectation and no significant excess is found in all regions. 95% CL upper limits on the production cross-section times branching ratio, $\sigma \times \text{BR}\ (X \to VV)$, as a function of the new resonance mass are set for various new physics models. For spin-0 Radion via ggF production, $m_{VV} < 3.45$ TeV is excluded at 95% CL. For the phenomenological heavy-vector-triplet benchmark Model A (B) with coupling constant $g_V = 1$ (3) , $m_{VV} < 4.08$ (4.36) TeV for spin-1 vector triplet produced via DY mode is excluded at 95% CL. For the bulk Randall-Sundrum model with $k/\bar{M}_{\text{Pl}} = 1$, $m_{VV} < 2.0$ (0.84) TeV for a spin-2 Kaluza-Klein graviton produced via ggF (VBF) is excluded at 95% CL.

The mild excess is observed around 1.5 TeV for signals produced via VBF with p_0-value less than 3σ, as shown in Figure 10.6b, 10.7b and 10.9b. This excess is already reported in 36.1 fb^{-1} results corresponding to Figure 1.5d, 1.7b and 1.7d and still observed in 139 fb^{-1} results. Since 1.5 TeV signal via VBF production mode can be explored by only the semi-leptonic analysis, further improvement is not expected by combining other channels with full Run 2 dataset. To confirm if the excess is real or not, more data in the LHC Run 3 and further improvement of analysis is needed.

Appendix A

Search for $X \to WZ$ signal

WZ background-only fit results are summarized in this section. All regions of the WZ analysis of three lepton channles are included in the fit. Fit values of the nuisance parameters are derived from a fit in both signal and control regions. All experimental and statistical uncertainties are included.

Since single-bin control regions are used in the fit, event yields in signal/control region are summarized in Figure A.1. Good agreement between observed data and post-fit predictions is observed in both control regions and signal regions. The final discriminant variable in the signal regions are shown in Figures A.2-A.4. No significant deviations from the post-fit predictions are indicated. Table A.1 shows the post-fit estimated background event yields from different sources in all WZ SRs compared with the number of the observed events in data.

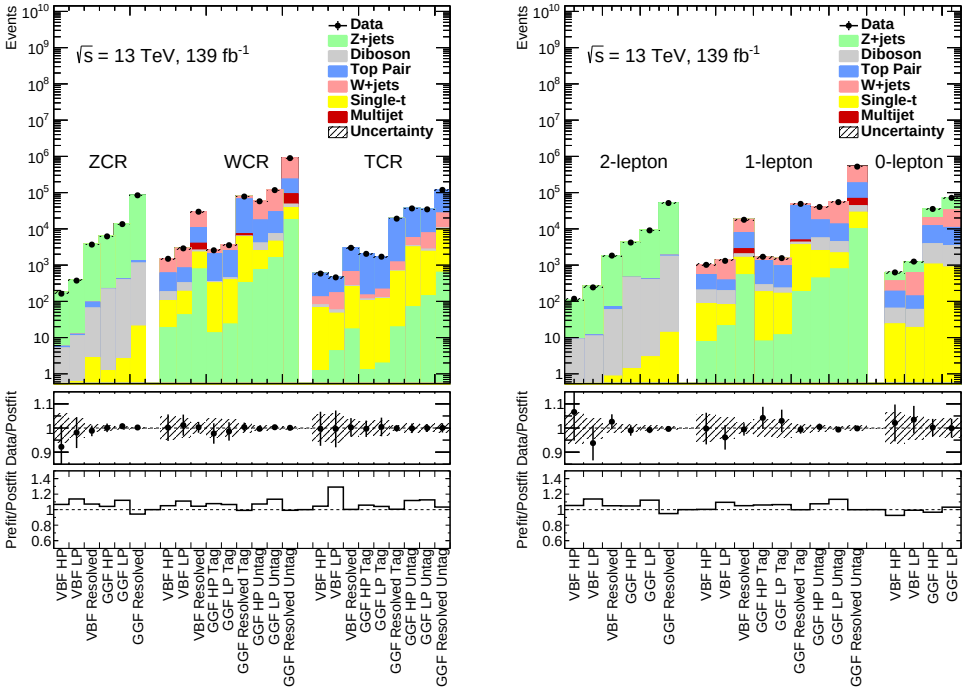

Figure A.1: Postfit distributions in all (left) control regions and (right) signal regions of the WZ analysis

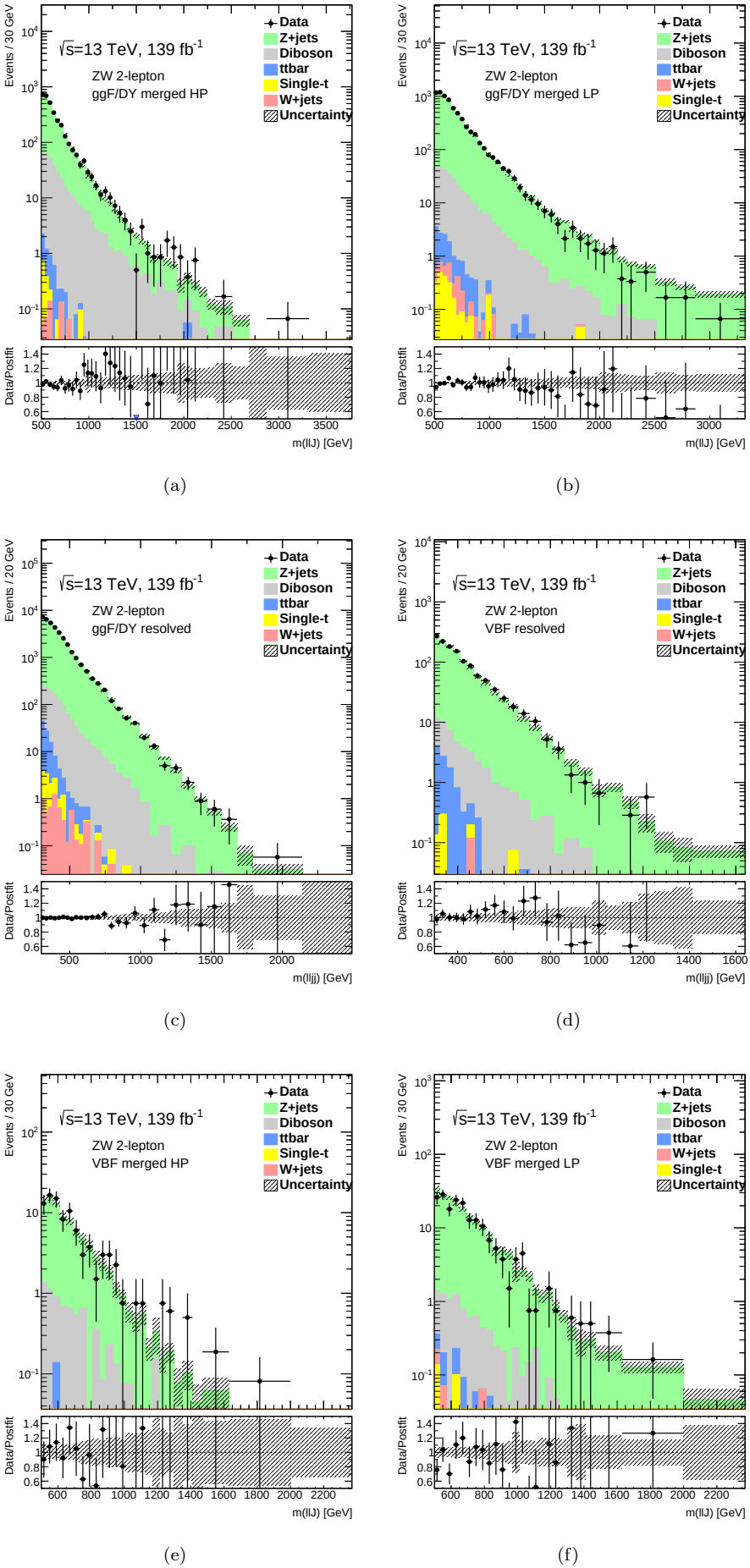

Figure A.2: Postfit distributions in the *llqq* (a) GGF merged HP WZ SR (b) GGF merged LP WZ SR (c) GGF resolved WZ SR (d) VBF merged HP WZ SR (e) VBF merged LP WZ SR (f) VBF resolved WZ SR.

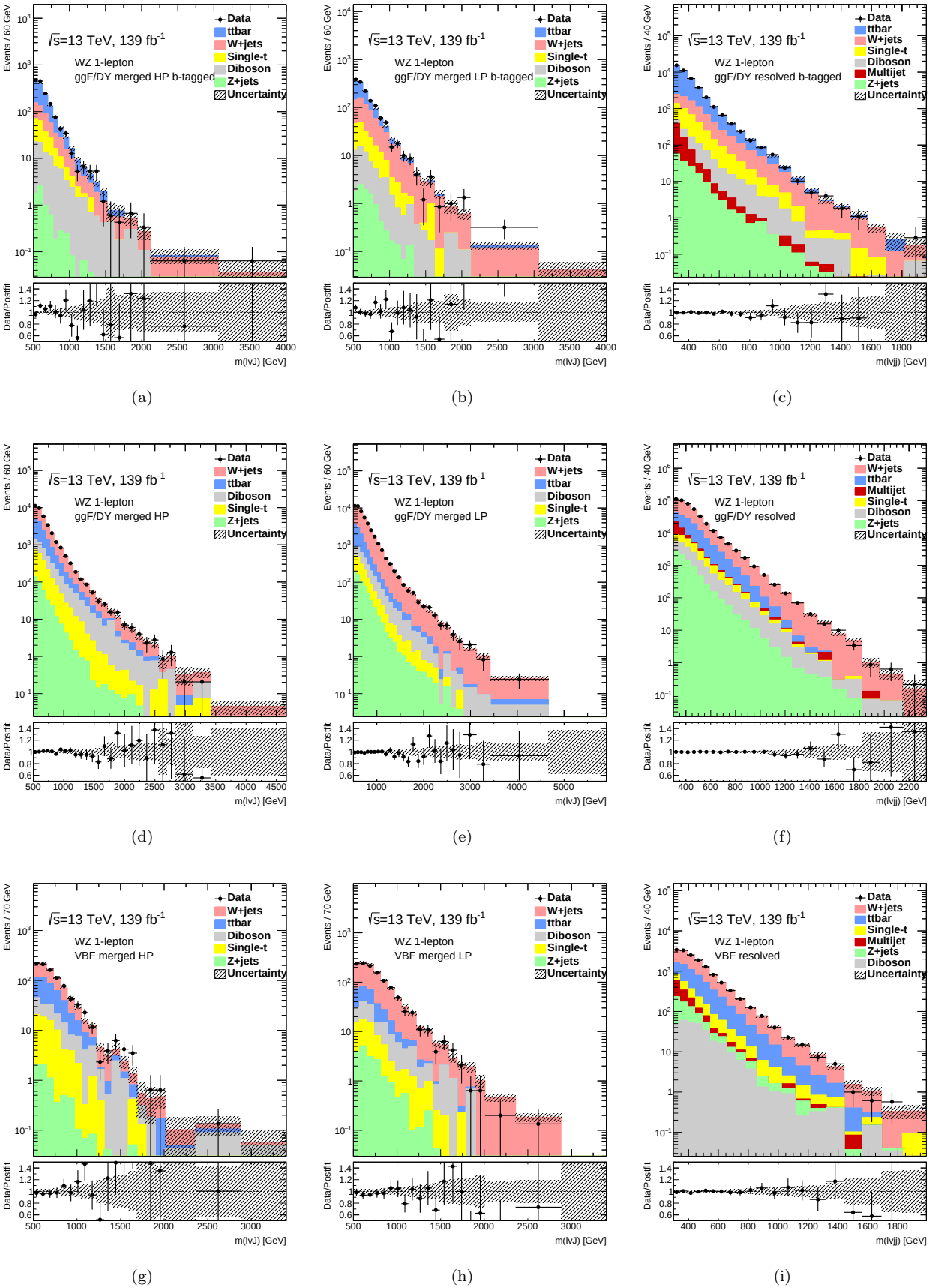

Figure A.3: Postfit distributions in the $\ell\nu qq$ (a) merged HP WZ VBF SR and (b) Merged LP WZ VBF SR (c) Resolved WZ VBF SR. Fit is performed using data from all WZ regions.

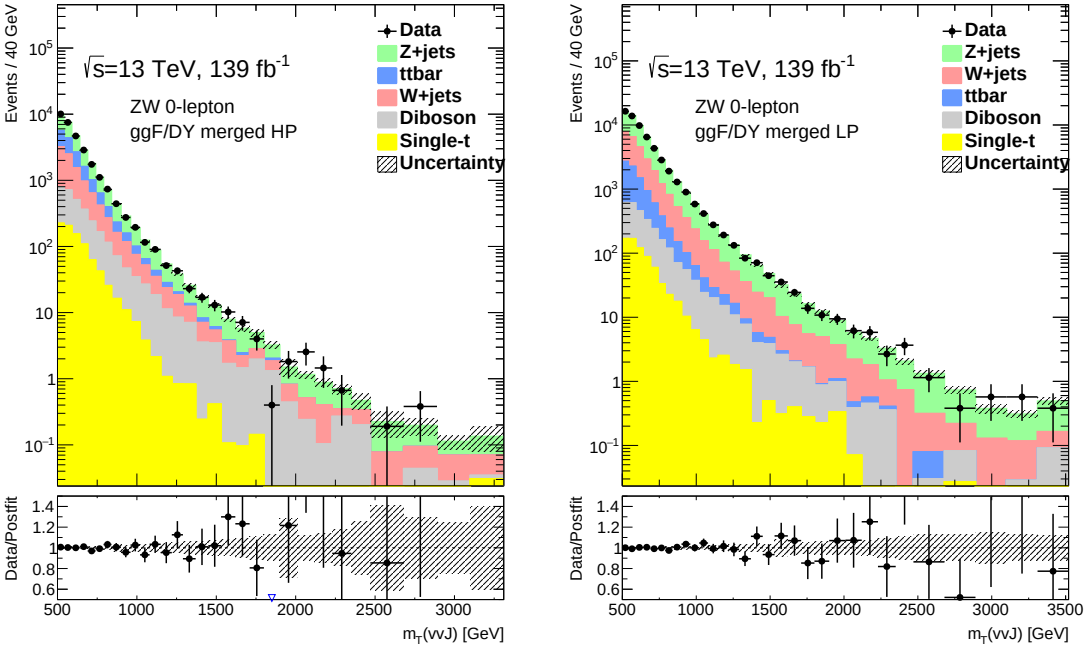

(a)

(b)

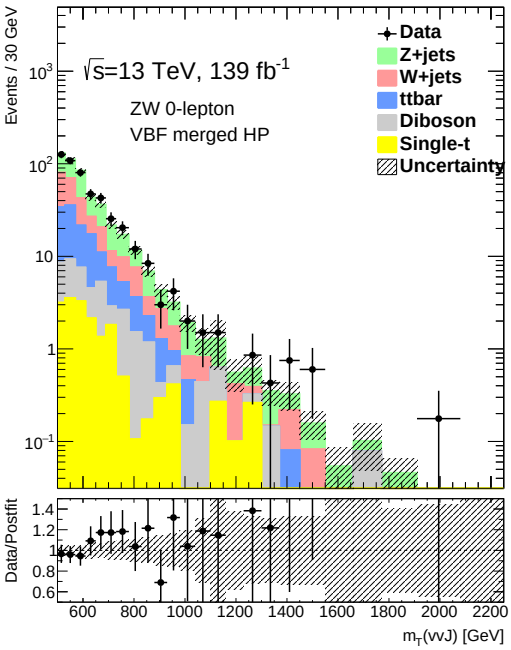

(c)

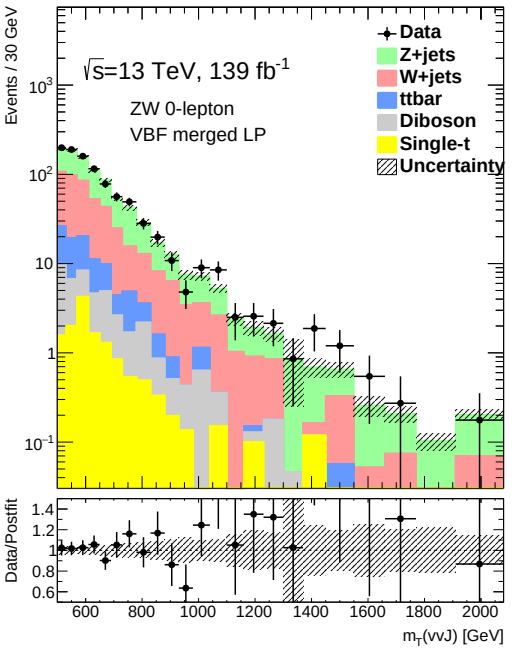

(d)

Figure A.4: Postfit distributions in the $\nu\nu qq$(a) merged HP WZ VBF SR, (b) merged LP WZ VBF SR. Fit is performed using data from all WZ regions.

Table A.1: The numbers of observed data events in the 19 WZ SRs are compared with the expected background events with breakdowns from individual sources. The backgrounds are estimated from a background-only simultaneous fit to all WZ SRs and their corresponding CRs. The uncertainties on the estimated backgrounds combine statistical and systematic contributions.

Channel	$V \to qq$ recon.	Signal regions		Background estimates							Data
				W + jets	Z + jets	$t\bar{t}$	Diboson	Single-t	Multijet	Total	
0-lepton						VBF category					
	Merged	HP		175 ± 19	255 ± 19	123 ± 26	40 ± 10	23.3 ± 5.1	-	616 ± 39	629
		LP		475 ± 42	598 ± 33	78.2 ± 18.1	40.2 ± 8.7	18.7 ± 4.5	-	1210 ± 57	1252
						ggF/DY category					
	Merged	HP		8103 ± 681	15323 ± 814	8111 ± 521	2768 ± 333	1041 ± 160	-	35345 ± 1239	35426
		LP		21933 ± 1832	39265 ± 1956	7336 ± 473	2562 ± 300	862 ± 131	-	71959 ± 2743	71892
1-lepton						VBF category					
	Merged	HP		482 ± 34	7.7 ± 0.5	339 ± 25	114 ± 38	78.3 ± 16.9	-	1020 ± 59	1018
		LP		988 ± 44	20.8 ± 0.9	186 ± 18	112 ± 38	58.6 ± 12.8	-	1365 ± 62	1313
	Resolved			10196 ± 247	529 ± 1 1	4973 ± 206	383 ± 151	1076 ± 235	773 ± 126	17929.3 ± 444	17826
						ggF/DY category					
	Merged	HP	Tag	331 ± 40	7.8 ± 0.8	1020 ± 32	100 ± 11	172 ± 29	-	1630 ± 60	1699
			Untag	22788 ± 186	428 ± 5	11721 ± 194	2998 ± 264	2066 ± 317	-	40020 ± 492	40193
		LP	Tag	577 ± 43	11.6 ± 1.2	709 ± 26	63.8 ± 7.6	152 ± 25	-	1514 ± 56	1559
			Untag	41819 ± 222	765 ± 6	8919 ± 128	2238 ± 202	1353 ± 207	-	55095 ± 386	54735
	Resolved	Tag		6217 ± 440	183 ± 19	38206 ± 391	616 ± 57	3403 ± 540	600 ± 128	49226 ± 811	48919
		Untag		341725 ± 2068	9961 ± 33	112923 ± 1974	14378 ± 1187	18202 ± 2716	25513 ± 2078	522702 ± 4613	521813
2-lepton						VBF category					
	Merged	HP		0	101 ± 7	0.22 ± 0.02	8.92 ± 1.92	0	-	110 ± 7	118
		LP		0.31 ± 0.02	247 ± 11	0.76 ± 0.07	10.6 ± 2	0.27 ± 0.06	-	259 ± 11	243
	Resolved			0.19 ± 0.01	1714 ± 32	12.7 ± 0.6	56.8 ± 9.6	0.84 ± 0.3	-	1784 ± 33	1831
						ggF/DY category					
	Merged	HP		0.73 ± 0.01	3788 ± 49	5.16 ± 0.1	445 ± 43	1.38 ± 0.23	-	4240 ± 66	4197
		LP		2.98 ± 0.02	8751 ± 71	13.6 ± 0.2	388 ± 37	2.89 ± 0.51	-	9159 ± 80	9088
	Resolved			8.57 ± 0.06	50005 ± 184	116 ± 2	1705 ± 133	13.7 ± 2.2	-	51848 ± 227	51655

Appendix B

Yields Table, Pulls and Correlation

B.1 Background only Fit results for the $X \to WZ$ search

Fit values of the nuisance parameters are derived from a fit in both signal and control regions. All experimental and statistical uncertainties are included.

Yields in Signal and Control Region

A table of all the final value of all floating normalization factors can be found in Tables B.1.

Region	Normalization
W+jets GGF Merg HP Tag	0.92 ± 0.114
W+jets GGF Merg HP Untag	0.95 ± 0.00753
W+jets GGF Merg LP Tag	0.915 ± 0.0694
W+jets GGF Merg LP Untag	0.879 ± 0.00462
W+jets GGF Res Tag	1.21 ± 0.0859
W+jets GGF Res Untag	1.01 ± 0.0061
Z+jets GGF Merg HP	0.962 ± 0.0118
Z+jets GGF Merg LP	0.893 ± 0.00698
Z+jets GGF Res	1.06 ± 0.0035
$t\bar{t}$ GGF Merg HP Tag	0.955 ± 0.0272
$t\bar{t}$ GGF Merg HP Untag	0.896 ± 0.0147
$t\bar{t}$ GGF Merg LP Tag	0.976 ± 0.0329
$t\bar{t}$ GGF Merg LP Untag	0.896 ± 0.0128
$t\bar{t}$ GGF Res Tag	1.0 ± 0.0102
$t\bar{t}$ GGF Res Untag	0.968 ± 0.0169
W+jets VBF Merg HP	0.911 ± 0.0618
W+jets VBF Merg LP	0.915 ± 0.0398
W+jets VBF Res	0.945 ± 0.0211
Z+jets VBF Merg HP	0.942 ± 0.0593
Z+jets VBF Merg LP	0.879 ± 0.0366
Z+jets VBF Res	0.936 ± 0.0166
$t\bar{t}$ VBF Merg HP	0.931 ± 0.0665
$t\bar{t}$ VBF Merg LP	0.693 ± 0.0643
$t\bar{t}$ VBF Res	0.991 ± 0.0404

Table B.1: Fitted values of background normalization factors in the WZ region.

Postfit event yields are summarized in Tab B.2-B.4 for each lepton channel after the combined WZ fit.

Nuisance parameter pulls and constraints

The pull distribution from the fits in all WZ regions using data are shown in Figures B.1.

WZ GGF Untagged WCR	Merged HP	Merged LP	Resolved
Electron Multi-jet	-	-	15105.22 ± 2292.09
Muon Multi-jet	-	-	28493.93 ± 2747.40
Diboson	1499.85 ± 145.64	2737.54 ± 267.69	8959.86 ± 695.06
Single-top	1740.58 ± 267.21	2878.57 ± 446.35	20290.50 ± 3073.01
$t\bar{t}$	13177.71 ± 216.77	21848.33 ± 311.89	140473.53 ± 2452.46
W+jets	40723.97 ± 322.79	87872.35 ± 462.38	663555.44 ± 4011.61
Z+jets	744.42 ± 9.15	1585.50 ± 12.40	17739.60 ± 58.48
Total	57886.54 ± 493.84	116922.29 ± 762.96	894618.12 ± 6696.22
Data	57699.00	117306.00	895362.00

WZ GGF Tagged WCR	Merged HP	Merged LP	Resolved
Electron Multi-jet	-	-	384.46 ± 57.11
Muon Multi-jet	-	-	614.17 ± 190.78
Diboson	30.16 ± 4.51	47.54 ± 6.60	259.72 ± 26.65
Single-top	303.33 ± 49.13	364.84 ± 60.45	5625.30 ± 897.67
$t\bar{t}$	1685.72 ± 47.98	2048.23 ± 68.96	58454.48 ± 597.34
W+jets	592.30 ± 73.26	1113.22 ± 84.40	11997.53 ± 850.07
Z+jets	13.19 ± 1.34	23.05 ± 2.33	324.69 ± 32.84
Total	2624.69 ± 100.53	3596.87 ± 124.83	77660.34 ± 1388.05
Data	2565.00	3546.00	77973.00

WZ VBF WCR	Merged HP	Merged LP	Resolved
Electron Multi-jet	-	-	866.19 ± 132.61
Muon Multi-jet	-	-	522.95 ± 167.75
Diboson	76.75 ± 26.52	133.06 ± 45.66	305.03 ± 116.92
Single-top	85.02 ± 18.46	143.61 ± 31.79	1463.68 ± 320.99
$t\bar{t}$	415.10 ± 30.54	497.00 ± 46.62	6661.92 ± 271.84
W+jets	897.58 ± 57.07	2047.84 ± 84.41	19084.95 ± 425.96
Z+jets	18.42 ± 1.20	41.62 ± 1.82	761.86 ± 13.55
Total	1492.86 ± 72.35	2863.12 ± 111.35	29666.56 ± 646.49
Data	1495.00	2898.00	29755.00

Table B.2: Postfit yield in the $\ell\nu qq$ WZ WCR in the (top) GGF Untag, (middle) GGF Tag, and (bottom) VBF regions from a simultaneous fit in all WZ regions

WZ GGF Untagged TCR	Merged HP	Merged LP	Resolved
Diboson	285.05 ± 26.82	342.87 ± 33.14	639.95 ± 62.83
Single-top	3033.37 ± 462.34	2216.99 ± 336.29	9432.03 ± 1507.44
$t\bar{t}$	31095.54 ± 511.51	26994.93 ± 385.36	92100.61 ± 1607.94
W+jets	2240.10 ± 17.76	4885.96 ± 25.71	16065.98 ± 97.13
Z+jets	69.27 ± 0.85	140.09 ± 1.10	620.64 ± 2.05
Total	36723.33 ± 690.24	34580.84 ± 513.18	118859.20 ± 2207.09
Data	36677.00	34573.00	118928.00

WZ GGF Tagged TCR	Merged HP	Merged LP	Resolved
Diboson	9.62 ± 1.07	8.73 ± 1.07	34.24 ± 4.82
Single-top	102.51 ± 17.98	115.15 ± 19.73	643.72 ± 118.29
$t\bar{t}$	1907.09 ± 49.78	1488.68 ± 46.25	17972.40 ± 183.66
W+jets	32.85 ± 4.16	86.02 ± 6.86	493.37 ± 34.96
Z+jets	1.27 ± 0.13	1.93 ± 0.20	19.14 ± 1.94
Total	2053.34 ± 53.10	1700.51 ± 50.76	19162.86 ± 221.29
Data	2047.00	1708.00	19143.00

WZ VBF TCR	Merged HP	Merged LP	Resolved
Diboson	12.26 ± 4.44	10.48 ± 3.83	15.80 ± 6.44
Single-top	64.76 ± 14.27	41.71 ± 9.21	236.26 ± 56.86
$t\bar{t}$	456.43 ± 30.06	292.72 ± 25.47	2345.71 ± 82.77
W+jets	51.16 ± 3.84	111.50 ± 5.75	378.31 ± 11.82
Z+jets	1.21 ± 0.08	4.24 ± 0.20	16.78 ± 0.40
Total	585.81 ± 33.79	460.65 ± 27.95	2992.86 ± 101.31
Data	584.00	459.00	3001.00

Table B.3: Postfit yield in the $\ell\nu qq$ WZ TCR in the (top) GGF Untag, (middle) GGF Tag and (bottom) VBF regions from a simultaneous fit in all WZ regions

WZ GGF ZCR	Merged HP	Merged LP	Resolved
Diboson	212.73 ± 21.22	383.79 ± 37.93	1095.52 ± 84.04
Single-top	1.20 ± 0.25	2.58 ± 0.48	20.25 ± 3.36
$t\bar{t}$	7.67 ± 0.13	20.41 ± 0.29	181.37 ± 3.17
W+jets	1.53 ± 0.01	7.79 ± 0.04	10.43 ± 0.06
Z+jets	5982.12 ± 73.54	13013.78 ± 101.77	82819.46 ± 273.03
Total	6205.25 ± 76.54	13428.35 ± 108.61	84127.03 ± 285.71
Data	6210.00	13531.00	84316.00

WZ VBF ZCR	Merged HP	Merged LP	Resolved
Diboson	5.08 ± 1.05	10.41 ± 2.08	61.41 ± 10.05
Single-top	0.00 ± 0.00	0.59 ± 0.12	2.75 ± 0.80
$t\bar{t}$	0.57 ± 0.04	1.09 ± 0.10	28.92 ± 1.23
W+jets	0.02 ± 0.00	0.20 ± 0.01	0.32 ± 0.01
Z+jets	171.13 ± 10.56	368.89 ± 15.12	3635.61 ± 55.51
Total	176.80 ± 10.62	381.18 ± 15.27	3729.02 ± 56.44
Data	163.00	374.00	3685.00

Table B.4: Postfit yield in the $\ell\ell qq$ WZ CR in the (top) GGF and (bottom) VBF regions from a simultaneous fit in all WZ regions

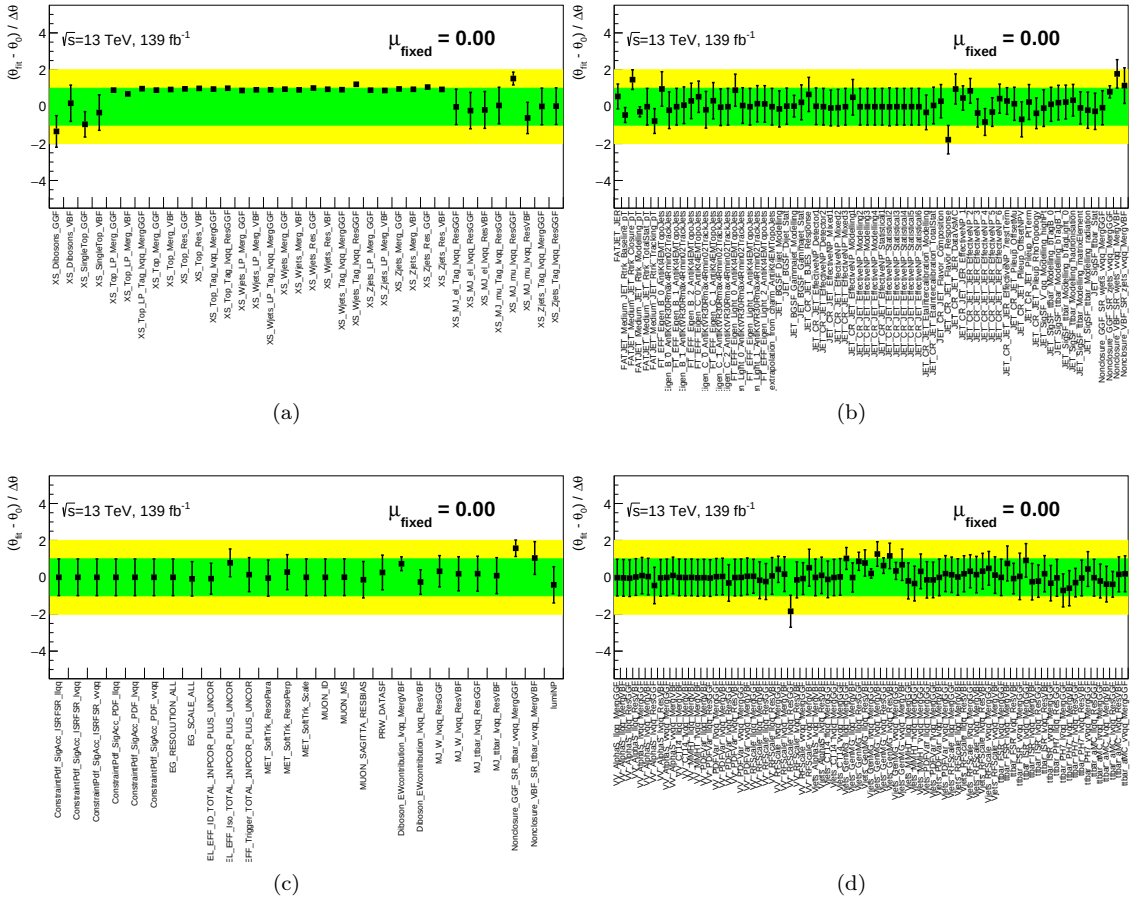

Figure B.1: Pull distributions for the nuisance parameters (a) Jet relevant NPs (b) Other experimantal NPs (c) Theory NPs (d) XS NPs.

Correlation matrices

The correlation matrix from the fits in all regions using data is shown in Figures B.2. Only nuisance paramters with more than a cross-correlation 0.25 positive or negative correlation are shown. Visible off-diagonally correlations come from normalization, which are expected to be anti-correlated, and the large-R jet experimental systematics, which are expect to be constrained.

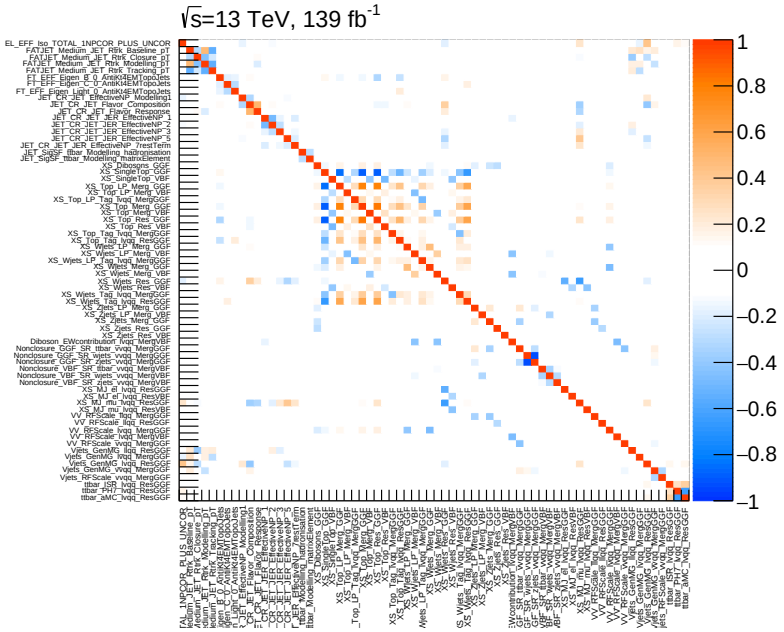

Figure B.2: Correlation matrix for the nuisance parameters for the final WZ GGF+VBF, HP+LP+Res,Tag+Untag, 0+1+2-lepton fit using data.

A summary of exclusion limits for HVT W' can be found in Tables **??-??**.

Table B.5: A summary of exclusion limits for HVT W' from WZ fit.

M[GeV]	Observed [pb]	Expected [pb]	$\pm1\sigma$ [pb]	$\pm2\sigma$ [pb]
400	2.17E-01	3.93E-01	1.54E−01 1.10E−01	3.40E−01 1.82E−01
500	1.37E-01	2.14E-01	8.40E−02 5.99E−02	1.86E−01 9.94E−02
600	1.21E-01	9.88E-02	3.87E−02 2.76E−02	8.55E−02 4.58E−02
700	7.44E-02	5.55E-02	2.17E−02 1.55E−02	4.80E−02 2.57E−02
800	2.03E-02	3.39E-02	1.33E−02 9.46E−03	2.93E−02 1.57E−02
1000	2.68E-02	1.69E-02	6.60E−03 4.71E−03	1.46E−02 7.81E−03
1200	1.05E-02	8.34E-03	3.27E−03 2.33E−03	7.22E−03 3.86E−03
1400	3.94E-03	5.00E-03	1.96E−03 1.40E−03	4.33E−03 2.31E−03
1500	3.12E-03	3.96E-03	1.55E−03 1.11E−03	3.43E−03 1.84E−03
1600	3.24E-03	3.19E-03	1.25E−03 8.92E−04	2.76E−03 1.48E−03
1800	2.97E-03	2.46E-03	9.65E−04 6.89E−04	2.13E−03 1.14E−03
2000	2.94E-03	1.60E-03	6.26E−04 4.47E−04	1.38E−03 7.40E−04
2400	1.17E-03	9.40E-04	3.68E−04 2.63E−04	8.14E−04 4.35E−04
2600	7.48E-04	6.97E-04	2.73E−04 1.95E−04	6.03E−04 3.23E−04
3000	4.75E-04	5.22E-04	2.04E−04 1.46E−04	4.52E−04 2.42E−04
3500	2.19E-04	3.61E-04	1.41E−04 1.01E−04	3.13E−04 1.67E−04
4000	1.69E-04	2.60E-04	1.02E−04 7.27E−05	2.25E−04 1.21E−04
4500	1.49E-04	2.24E-04	8.76E−05 6.25E−05	1.94E−04 1.04E−04
5000	1.24E-04	1.63E-04	6.40E−05 4.57E−05	1.41E−04 7.57E−05

Table B.6: A summary of exclusion limits for HVT VBF W' from WZ fit.

M[GeV]	Observed [pb]	Expected [pb]	$\pm1\sigma$ [pb]	$\pm2\sigma$ [pb]
300	1.29E+00	1.80E+00	7.04E−01 5.03E−01	1.56E+00 8.33E−01
400	2.43E-01	3.98E-01	1.56E−01 1.11E−01	3.45E−01 1.85E−01
600	6.71E-02	7.06E-02	2.76E−02 1.97E−02	6.11E−02 3.27E−02
700	6.11E-02	4.08E-02	1.60E−02 1.14E−02	3.53E−02 1.89E−02
800	2.26E-02	2.40E-02	9.40E−03 6.70E−03	2.08E−02 1.11E−02
1000	2.22E-02	1.12E-02	4.40E−03 3.14E−03	9.72E−03 5.20E−03
1200	8.43E-03	6.09E-03	2.39E−03 1.70E−03	5.27E−03 2.82E−03
1500	9.18E-03	3.53E-03	1.38E−03 9.86E−04	3.05E−03 1.63E−03
1800	4.71E-03	2.16E-03	8.46E−04 6.04E−04	1.87E−03 1.00E−03
2000	2.19E-03	1.61E-03	6.32E−04 4.51E−04	1.40E−03 7.48E−04
2400	1.14E-03	1.15E-03	4.49E−04 3.20E−04	9.92E−04 5.31E−04
2600	9.47E-04	9.11E-04	3.57E−04 2.55E−04	7.89E−04 4.22E−04
3000	6.42E-04	7.10E-04	2.78E−04 1.99E−04	6.15E−04 3.29E−04
3500	3.61E-04	5.34E-04	2.09E−04 1.49E−04	4.63E−04 2.48E−04
4000	3.04E-04	4.59E-04	1.80E−04 1.28E−04	3.98E−04 2.13E−04

B.2 Background only Fit results for the $X \to WW/ZZ$ search

Fit values of the nuisance parameters are derived from a fit in both signal and control regions. All experimental and statistical uncertainties are included. S

Yields in Signal and Control Region

A table of all the final value of all floating normalization factors can be found in Tables B.7.

Region	Normalization
W+jets GGF Merg HP	0.934 ± 0.00788
W+jets GGF Merg LP	0.886 ± 0.00455
W+jets GGF Res	1.02 ± 0.00562
Z+jets GGF Merg HP	0.963 ± 0.0118
Z+jets GGF Merg LP	0.889 ± 0.00714
Z+jets GGF Res	1.06 ± 0.00361
$t\bar{t}$ GGF Merg HP	0.942 ± 0.019
$t\bar{t}$ GGF Merg LP	0.908 ± 0.00162
$t\bar{t}$ GGF Res	0.949 ± 0.0146
W+jets VBF Merg HP	0.934 ± 0.0599
W+jets VBF Merg LP	0.905 ± 0.0369
W+jets VBF Res	0.929 ± 0.0195
Z+jets VBF Merg HP	0.909 ± 0.0605
Z+jets VBF Merg LP	0.85 ± 0.0378
Z+jets VBF Res	0.928 ± 0.017
$t\bar{t}$ VBF Merg HP	0.847 ± 0.0644
$t\bar{t}$ VBF Merg LP	0.767 ± 0.0675
$t\bar{t}$ VBF Res	0.973 ± 0.0361

Table B.7: Fitted values of background normalization factors in the $WWZZ$ region.

Postfit event yields are summarized in Tab **??**-B.10 for each lepton channel after the combined $WWZZ$ fit.

Nuisance parameter pulls and constraints

The pull distribution from the fits in all WW/ZZ regions using data are shown in Figures B.3.

Correlation matrices

The correlation matrix from the fits in all regions using data is shown in Figures B.4. Only nuisance paramters with more than a cross-correlation 0.25 positive or negative correlation are shown. Visible off-diagonally correlations come from normalization, which are expected to be anti-correlated, and the large-R jet experimental systematics, which are expect to be constrained.

A summary of exclusion limits for spin-0/2 signals can be found in Tables B.11-B.14.

WW GGF WCR	Merged HP	Merged LP	Resolved
Electron Multi-jet	-	-	16462.82 ± 2306.77
Muon Multi-jet	-	-	20745.21 ± 2618.33
Diboson	1849.20 ± 166.53	3433.12 ± 307.53	8587.28 ± 718.49
Single-top	2048.82 ± 368.16	3382.40 ± 605.16	20442.62 ± 3712.72
$t\bar{t}$	15627.72 ± 315.41	24159.79 ± 430.27	137818.89 ± 2115.56
W+jets	40300.21 ± 338.28	88368.52 ± 451.96	672246.81 ± 3706.95
Z+jets	753.24 ± 9.24	1576.65 ± 12.67	17694.56 ± 60.25
Total	60579.19 ± 614.23	120920.48 ± 922.15	893998.19 ± 6685.66
Data	60264.00	120852.00	895362.00

WW VBF WCR	Merged HP	Merged LP	Resolved
Signal	-	-	-
Electron Multi-jet	-	-	886.59 ± 136.47
Muon Multi-jet	-	-	474.05 ± 144.25
Diboson	73.37 ± 23.62	129.05 ± 41.54	426.21 ± 250.72
Single-top	103.42 ± 22.29	183.64 ± 40.16	1215.74 ± 268.92
$t\bar{t}$	378.80 ± 29.86	547.21 ± 49.06	4843.50 ± 182.68
W+jets	912.11 ± 54.35	1986.92 ± 77.44	18499.61 ± 382.88
Z+jets	17.53 ± 1.21	39.61 ± 1.84	741.49 ± 13.57
Total	1485.23 ± 70.01	2886.44 ± 108.38	27087.18 ± 595.62
Data	1495.00	2898.00	27120.00

Table B.8: Postfit yield in the $\ell\nu qq$ $WWZZ$ WCR in the (top) GGF and (bottom) VBF regions from a simultaneous fit in all $WWZZ$ regions

WW GGF TCR	Merged HP	Merged LP	Resolved
Diboson	422.35 ± 35.88	529.79 ± 47.47	964.98 ± 106.50
Single-top	4434.82 ± 783.34	3353.14 ± 593.35	18516.60 ± 3469.99
$t\bar{t}$	39218.39 ± 791.54	33963.82 ± 604.88	222535.00 ± 3415.98
W+jets	2267.26 ± 19.03	6583.81 ± 33.67	23433.17 ± 129.22
Z+jets	64.17 ± 0.79	190.45 ± 1.53	904.09 ± 3.08
Total	46407.01 ± 1114.37	44621.01 ± 849.32	266353.84 ± 4872.14
Data	46354.00	44629.00	266443.00

WW VBF TCR	Merged HP	Merged LP	Resolved
Diboson	13.64 ± 4.72	19.83 ± 7.36	35.48 ± 22.03
Single-top	95.84 ± 20.22	76.64 ± 16.41	439.20 ± 102.19
$t\bar{t}$	470.27 ± 34.04	386.81 ± 32.43	3665.64 ± 127.45
W+jets	53.57 ± 3.76	147.99 ± 7.11	448.53 ± 11.37
Z+jets	1.19 ± 0.08	4.56 ± 0.22	27.94 ± 0.61
Total	634.50 ± 40.05	635.84 ± 37.76	4616.79 ± 165.23
Data	636.00	634.00	4615.00

Table B.9: Postfit yield in the $\ell\nu qq$ $WWZZ$ TCR in the (top) GGF and (bottom) VBF regions from a simultaneous fit in all $WWZZ$ regions

ZZ GGF Untagged ZCR	Merged HP	Merged LP	Resolved
Diboson	206.58 ± 21.18	392.37 ± 39.55	1119.49 ± 83.85
Single-top	1.21 ± 0.28	2.25 ± 0.48	21.11 ± 4.04
$t\bar{t}$	7.43 ± 0.15	19.29 ± 0.34	181.46 ± 2.79
W+jets	1.51 ± 0.01	8.25 ± 0.04	10.86 ± 0.06
Z+jets	5647.09 ± 69.24	13715.71 ± 110.25	82747.66 ± 281.74
Total	5863.83 ± 72.41	14137.85 ± 117.13	84080.58 ± 294.00
Data	5876.00	14236.00	84128.00

ZZ GGF Tagged ZCR	Merged HP	Merged LP	Resolved
Diboson	5.17 ± 0.69	9.94 ± 1.24	55.55 ± 6.54
Single-top	0.12 ± 0.02	0.19 ± 0.03	10.18 ± 2.71
$t\bar{t}$	0.37 ± 0.04	1.48 ± 0.15	203.02 ± 20.08
W+jets	0.04 ± 0.00	0.32 ± 0.03	0.14 ± 0.01
Z+jets	154.35 ± 10.74	257.94 ± 13.74	2495.09 ± 50.08
Total	160.05 ± 10.77	269.87 ± 13.80	2763.98 ± 54.42
Data	171.00	280.00	2788.00

ZZ VBF ZCR	Merged HP	Merged LP	Resolved
Diboson	6.03 ± 1.25	13.60 ± 2.65	74.72 ± 13.10
Single-top	0.00 ± 0.00	0.63 ± 0.12	5.34 ± 1.47
$t\bar{t}$	0.48 ± 0.04	1.23 ± 0.11	47.00 ± 1.85
W+jets	0.03 ± 0.00	0.19 ± 0.01	0.26 ± 0.01
Z+jets	157.60 ± 10.34	383.59 ± 16.59	3677.06 ± 57.53
Total	164.13 ± 10.41	399.23 ± 16.80	3804.38 ± 59.05
Data	154.00	404.00	3777.00

Table B.10: Postfit yield in the $\ell\ell qq$ $WWZZ$ ZCR in the (top) GGF Untagged, (middle) GGF Tagged and (bottom) VBF regions from a simultaneous fit in all $WWZZ$ regions

M[GeV]	Observed [pb]	Expected [pb]	$\pm1\sigma$ [pb]	$\pm2\sigma$ [pb]
300	2.48E+00	2.07E+00	9.73E−01 6.94E−01	2.15E+00 1.15E+00
400	2.90E-01	1.30E-01	1.14E−01 8.11E−02	2.51E−01 1.34E−01
500	1.67E-01	2.09E-01	6.55E−02 4.67E−02	1.45E−01 7.74E−02
600	7.55E-02	8.60E-02	2.96E−02 2.11E−02	6.54E−02 3.50E−02
700	5.58E-02	4.83E-02	2.18E−02 1.56E−02	4.83E−02 2.58E−02
800	3.17E-02	1.97E-02	1.24E−02 8.85E−03	2.74E−02 1.47E−02
1000	2.02E-02	3.11E-02	7.89E−03 5.63E−03	1.74E−02 9.34E−03
1200	8.81E-03	4.58E-03	3.45E−03 2.46E−03	7.62E−03 4.08E−03
1400	5.33E-03	4.45E-03	2.09E−03 1.49E−03	4.61E−03 2.47E−03
1500	4.54E-03	3.78E-03	1.78E−03 1.27E−03	3.93E−03 2.10E−03
1600	3.68E-03	3.31E-03	1.44E−03 1.03E−03	3.18E−03 1.70E−03
1800	2.94E-03	2.44E-03	1.15E−03 8.21E−04	2.54E−03 1.36E−03
2000	1.79E-03	3.01E-03	7.02E−04 5.01E−04	1.55E−03 8.30E−04
2400	1.23E-03	1.60E-03	4.82E−04 3.44E−04	1.06E−03 5.70E−04
2600	9.06E-04	7.99E-04	3.55E−04 2.53E−04	7.84E−04 4.20E−04
3000	5.91E-04	3.77E-04	2.31E−04 1.65E−04	5.11E−04 2.74E−04
3500	4.63E-04	3.68E-04	1.81E−04 1.29E−04	4.01E−04 2.15E−04
4000	3.23E-04	2.31E-04	1.26E−04 9.01E−05	2.79E−04 1.49E−04
4500	3.38E-04	2.71E-04	1.32E−04 9.43E−05	2.92E−04 1.56E−04
5000	2.90E-04	2.47E-04	1.13E−04 8.09E−05	2.51E−04 1.34E−04

Table B.11: A summary of exclusion limits for Radion from WW/ZZ fit.

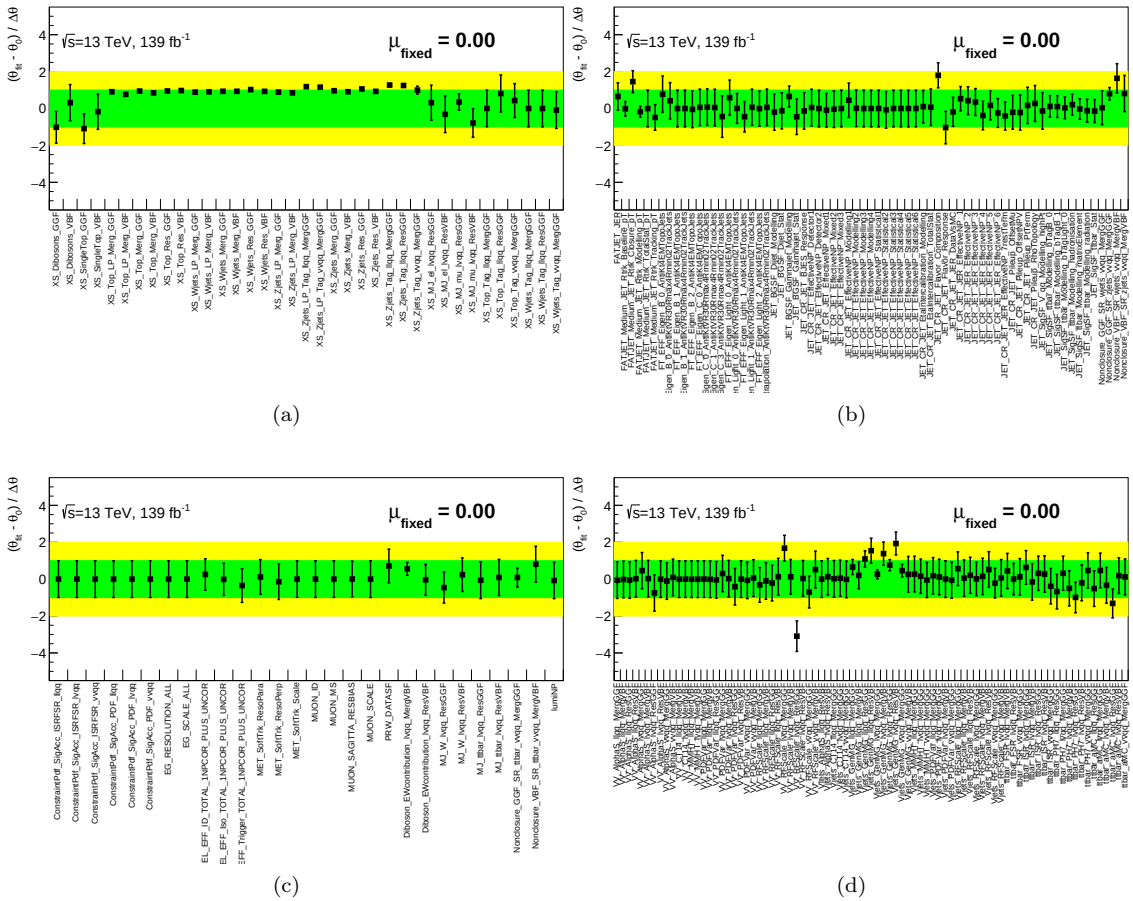

Figure B.3: Pull distributions for the nuisance parameters (a) Jet relevant NPs (b) Other experimantal NPs (c) Theory NPs (d) XS NPs.

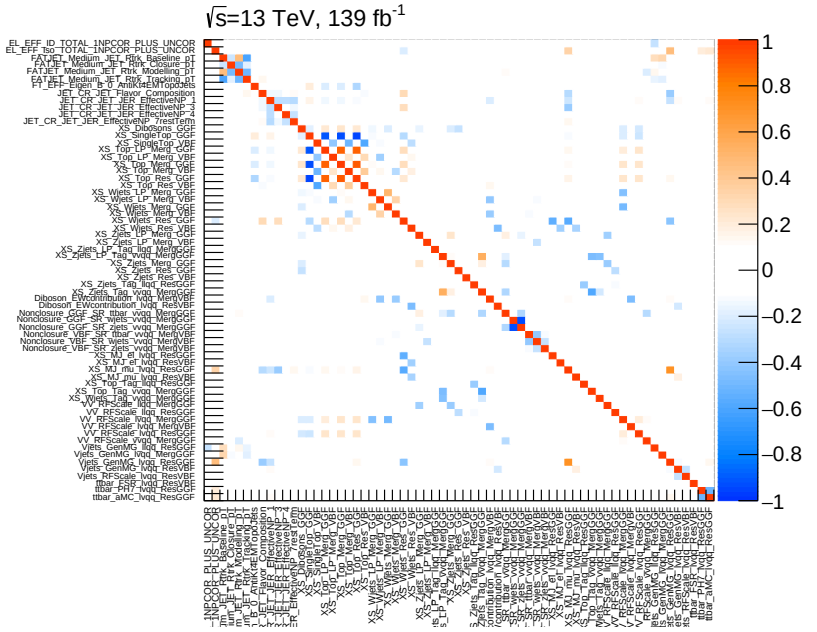

Figure B.4: Correlation matrix for the nuisance parameters for the final WW/ZZ GGF+VBF, HP+LP+Res,Tag+Untag, 0+1+2-lepton fit using data.

M[GeV]	Observed [pb]	Expected [pb]	$\pm1\sigma$ [pb]	$\pm2\sigma$ [pb]
300	8.37E-01	4.59E-01	3.28E−01 2.34E−01	7.25E−01 3.88E−01
400	1.35E-01	9.21E-02	5.27E−02 3.76E−02	1.17E−01 6.23E−02
500	5.22E-02	4.92E-02	2.04E−02 1.46E−02	4.52E−02 2.42E−02
600	2.15E-02	1.97E-02	8.42E−03 6.01E−03	1.86E−02 9.96E−03
700	1.34E-02	1.26E-02	5.24E−03 3.74E−03	1.16E−02 6.20E−03
800	8.97E-03	8.42E-03	3.51E−03 2.51E−03	7.77E−03 4.16E−03
1000	4.16E-03	8.78E-03	1.63E−03 1.16E−03	3.60E−03 1.93E−03
1200	2.25E-03	2.01E-03	8.80E−04 6.28E−04	1.94E−03 1.04E−03
1400	1.59E-03	2.60E-03	6.22E−04 4.44E−04	1.38E−03 7.36E−04
1500	1.34E-03	2.82E-03	5.27E−04 3.76E−04	1.16E−03 6.23E−04
1600	1.06E-03	2.24E-03	4.13E−04 2.95E−04	9.13E−04 4.89E−04
1800	6.27E-04	5.97E-04	2.46E−04 1.75E−04	5.43E−04 2.91E−04
2000	5.45E-04	6.11E-04	2.13E−04 1.52E−04	4.72E−04 2.52E−04
2400	4.61E-04	5.54E-04	1.81E−04 1.29E−04	3.99E−04 2.14E−04
2600	3.80E-04	3.96E-04	1.49E−04 1.06E−04	3.29E−04 1.76E−04
3000	2.41E-04	1.84E-04	9.42E−05 6.72E−05	2.08E−04 1.11E−04
3500	1.81E-04	1.47E-04	7.09E−05 5.06E−05	1.57E−04 8.39E−05
4000	1.60E-04	1.20E-04	6.27E−05 4.48E−05	1.39E−04 7.42E−05
4500	1.71E-04	1.39E-04	6.71E−05 4.79E−05	1.48E−04 7.94E−05
5000	1.65E-04	1.41E-04	6.47E−05 4.61E−05	1.43E−04 7.65E−05

Table B.12: A summary of exclusion limits for Radion VBF from WW/ZZ fit.

M[GeV]	Observed [pb]	Expected [pb]	$\pm1\sigma$ [pb]	$\pm2\sigma$ [pb]
300	3.60E+00	1.30E+00	1.41E+00 1.01E+00	3.11E+00 1.67E+00
400	5.16E-01	2.08E-01	2.02E−01 1.44E−01	4.47E−01 2.39E−01
600	9.67E-02	1.28E-01	3.79E−02 2.70E−02	8.37E−02 4.48E−02
700	6.29E-02	8.14E-02	2.46E−02 1.76E−02	5.45E−02 2.91E−02
800	4.17E-02	3.38E-02	1.63E−02 1.16E−02	3.61E−02 1.93E−02
1000	2.05E-02	2.82E-02	8.02E−03 5.72E−03	1.77E−02 9.49E−03
1200	1.03E-02	4.92E-03	4.04E−03 2.89E−03	8.94E−03 4.78E−03
1500	5.02E-03	4.16E-03	1.97E−03 1.40E−03	4.35E−03 2.33E−03
1800	3.20E-03	2.77E-03	1.25E−03 8.94E−04	2.77E−03 1.48E−03
2000	2.01E-03	3.14E-03	7.86E−04 5.61E−04	1.74E−03 9.30E−04
2400	1.19E-03	1.52E-03	4.65E−04 3.31E−04	1.03E−03 5.49E−04
2600	8.96E-04	8.17E-04	3.51E−04 2.50E−04	7.75E−04 4.15E−04
3000	6.15E-04	3.96E-04	2.41E−04 1.72E−04	5.33E−04 2.85E−04
3500	4.08E-04	3.33E-04	1.60E−04 1.14E−04	3.53E−04 1.89E−04
4000	3.05E-04	2.19E-04	1.19E−04 8.52E−05	2.64E−04 1.41E−04
4500	2.69E-04	2.18E-04	1.05E−04 7.52E−05	2.33E−04 1.25E−04
5000	2.60E-04	2.20E-04	1.02E−04 7.27E−05	2.25E−04 1.20E−04

Table B.13: A summary of exclusion limits for RSG from WW/ZZ fit.

M[GeV]	Observed [pb]	Expected [pb]	$\pm1\sigma$ [pb]	$\pm2\sigma$ [pb]
300	4.29E-01	2.79E-01	1.68E−01 1.20E−01	3.72E−01 1.99E−01
400	2.97E-01	1.83E-01	1.16E−01 8.30E−02	2.57E−01 1.38E−01
500	1.06E-01	9.17E-02	4.13E−02 2.95E−02	9.14E−02 4.89E−02
600	4.78E-02	4.27E-02	1.87E−02 1.34E−02	4.14E−02 2.22E−02
700	2.70E-02	2.44E-02	1.06E−02 7.56E−03	2.34E−02 1.25E−02
800	1.78E-02	1.72E-02	6.96E−03 4.96E−03	1.54E−02 8.23E−03
1000	7.72E-03	1.59E-02	3.02E−03 2.16E−03	6.68E−03 3.58E−03
1200	4.11E-03	4.01E-03	1.61E−03 1.15E−03	3.56E−03 1.90E−03
1500	2.27E-03	4.80E-03	8.90E−04 6.35E−04	1.97E−03 1.05E−03
1600	1.79E-03	3.52E-03	7.00E−04 4.99E−04	1.55E−03 8.28E−04
1800	1.02E-03	8.70E-04	4.01E−04 2.86E−04	8.85E−04 4.74E−04
2000	8.57E-04	9.71E-04	3.36E−04 2.39E−04	7.42E−04 3.97E−04
2400	7.32E-04	9.15E-04	2.87E−04 2.05E−04	6.34E−04 3.39E−04
2600	6.14E-04	6.22E-04	2.41E−04 1.72E−04	5.32E−04 2.84E−04
3000	3.67E-04	2.79E-04	1.44E−04 1.03E−04	3.18E−04 1.70E−04
3500	2.82E-04	2.35E-04	1.10E−04 7.87E−05	2.44E−04 1.30E−04
4000	2.44E-04	1.79E-04	9.55E−05 6.81E−05	2.11E−04 1.13E−04
4500	2.40E-04	2.02E-04	9.40E−05 6.71E−05	2.08E−04 1.11E−04
5000	2.22E-04	1.94E-04	8.70E−05 6.21E−05	1.92E−04 1.03E−04

Table B.14: A summary of exclusion limits for RSG VBF from WW/ZZ fit.

Appendix C

Impact of systematic uncertainties

The relative uncertainties in the best-fit μ value from the leading sources of systematic uncertainty are shown in Table C.1 for ggF and VBF HVT W' signal with $m(X) = 600$ GeV and 2 TeV, respectively.

Table C.1: Ranking of the nuisance parameter impact on the expected exclusion limits on ggF HVT W' with $m(X) = 600$ GeV and $\sigma(pp \to X) \times \mathrm{BR}(X \to WZ) = 0.01$ pb, ggF HVT W' with $m(X) = 2000$ GeV and $\sigma(pp \to X) \times \mathrm{BR}(X \to WZ) = 0.002$ pb, VBF HVT W' with $m(X) = 600$ GeV and $\sigma(pp \to X) \times \mathrm{BR}(X \to WZ) = 0.01$ pb and VBF HVT W' with $m(X) = 2$ TeV and $\sigma(pp \to X) \times \mathrm{BR}(X \to WZ) = 0.002$ pb.

ggF HVT W'			
600 GeV		2000 GeV	
Source	$\Delta\mu$	Source	$\Delta\mu \times 10^{-3}$
Large-R jet p_{T} scale	0.058	V+jets Generator difference	1.08
MC statistical uncertainty	0.056	Boson tag SF b-tag efficiency SF	0.65
NonClosure ttbar	0.028	Large-R jet p_{T} scale	0.61
V+jets Generator difference	0.026	MC statistical uncertainty	0.42
Small-R jet JER	0.025	Boson tag SF ttbar Modeling	0.42
VV RFScale	0.021	Boson tag SF Gamma+jets	0.20
Large-R jet JER	0.019	Boson tag SF other	0.19
Z+jets cross-section	0.018	VV RFScale	0.14
VV cross-section	0.011	NonClosure ttbar	0.12
Boson tag SF Gamma+jets	0.010	Boson tag SF dijet	0.10

VBF HVT W'			
600 GeV		2000 GeV	
Source	$\Delta\mu$	Source	$\Delta\mu \times 10^{-3}$
Z+jets cross-section	0.0288	Large-R jet p_{T} scale	0.68
MC statistical uncertainty 0.0247	MC statistical uncertainty	0.65	
Large-R jet p_{T} scale	0.0093	Boson tag SF b-tag efficiency SF	0.54
VV EWcontribution	0.0077	Boson tag SF other	0.19
Small-R jet JER	0.0072	V+jets Generator difference	0.16
W+jets cross-section	0.0047	Small-R jet JER	0.12
Boson tag SF ttbar Modeling	0.0043	ttbar PH7	0.09
Large-R jet JER	0.0038	ttbar ISR/FSR	0.08
MET	0.0037	ttbar cross-section	0.07
VV RFScale	0.0036	NonClosure ttbar	0.06

The relative uncertainties in the best-fit μ value from the leading sources of systematic uncertainty are shown in Table C.2 for ggF and VBF Graviton signal with $m(X) = 600$ GeV and 2 TeV, respectively.

Table C.2: Ranking of the nuisance parameter impact on the expected exclusion limits on ggF Graviton with $m(X) = 600$ GeV and $\sigma(pp \to X) \times \mathrm{BR}(X \to VV) = 0.01$ pb, ggF Graviton with $m(X) = 2000$ GeV and $\sigma(pp \to X) \times \mathrm{BR}(X \to VV) = 0.002$ pb, VBF Graviton with $m(X) = 600$ GeV and $\sigma(pp \to X) \times \mathrm{BR}(X \to VV) = 0.01$ pb and VBF Graviton with $m(X) = 2$ TeV and $\sigma(pp \to X) \times \mathrm{BR}(X \to VV) = 0.002$ pb.

ggF Graviton			
600 GeV		2000 GeV	
Source	$\Delta\mu$	Source	$\Delta\mu \times 10^{-3}$
V+jets Generator difference	0.0409	V+jets Generator difference	1.465
Z+jets	0.0223	Boson tag SF b-tag efficiency SF	0.635
Large-R jet p_{T} scale	0.0204	MC statistical uncertainty	0.523
MC statistical uncertainty	0.0153	Large-R jet p_{T} scale	0.469
VV RFScale	0.0141	Boson tag SF ttbar Modeling	0.463
Small-R jet JER	0.0139	Boson tag SF other	0.184
Small-R jet b-tag efficiency SF	0.0129	VR track jet b-tag efficiency SF	0.167
Large-R jet JER	0.0088	Boson tag SF Gamma+jets	0.157
VV cross-section	0.0083	VV RFScale	0.112
ttbar cross-section	0.0074	Boson tag SF dijets	0.109

VBF Graviton			
600 GeV		2000 GeV	
Source	$\Delta\mu$	Source	$\Delta\mu \times 10^{-3}$
Small-R jet JER	0.0154	Large-R jet p_{T} scale	0.517
V+jets Generator difference	0.0128	Boson tag SF b-tag efficiency SF	0.474
Z+jets cross-section	0.0116	Boson tag SF ttbar Modeling	0.306
Large-R jet p_{T} scale	0.0112	V+jets Generator difference	0.169
VV EWcontribution	0.0074	Boson tag SF other	0.168
W+jets cross-section	0.0073	Small-R jet JER	0.113
MC statistical uncertainty	0.0039	MC statistical uncertainty	0.113
Boson tag SF b-tag efficiency SF	0.0028	VR track jet b-tag efficiency SF	0.083
MET	0.0027	ttbar PH7	0.068
Small-R jet Pileup	0.0025	ttbar ISR/FSR	0.051

References

[1] ATLAS Collaboration. "Observation of a new particle in the search for the Standard Model Higgs boson with the ATLAS detector at the LHC". In: *Phys. Lett. B* 716 (2012), p. 1. DOI: 10.1016/j.physletb.2012.08.020. arXiv: 1207.7214 [hep-ex].

[2] CMS Collaboration. "Observation of a new boson at a mass of 125 GeV with the CMS experiment at the LHC". In: *Phys. Lett. B* 716 (2012), p. 30. DOI: 10.1016/j.physletb.2012.08.021. arXiv: 1207.7235 [hep-ex].

[3] G. 't Hooft. "Naturalness, chiral symmetry, and spontaneous chiral symmetry breaking". In: *NATO Sci. Ser. B 59 (1980), pp. 135–157* (1980).

[4] W.-Y. Keung V.D. Barger and E. Ma. "A gauge model with light W and Z bosons". In: *Phys. Rev. D 22 (1980) 727* (1980).

[5] Gia Dvali Nima Arkani-Hamed Savas Dimopoulos. "The Hierarchy Problem and New Dimensions at a Millimeter". In: *Phys.Lett.B429:263-272,1998* (1998).

[6] I. Antoniadis et al. "New Dimensions at a Millimeter to a Fermi and Superstrings at a TeV". In: *Phys.Lett.B436:257-263,1998* (1998).

[7] S. Weinberg. "Implications of dynamical symmetry breaking: An addendum". In: *Phys. Rev. D 19, 1277* (1979).

[8] Leonard Susskind. "Dynamics of spontaneous symmetry breaking in the Weinberg-Salam theory". In: *Phys. Rev. D 20, 2619* (1979).

[9] S. L. Glashow. "Partial Symmetries of Weak Interactions". In: *Nucl. Phys. 22 (1961), 579–588* (1961).

[10] S. Weinberg. "A Model of Leptons". In: *Phys. Rev. Lett. 19 (1967), 1264–1266* (1967).

[11] A. Salam and J. C. Ward. "Weak and electromagnetic interactions". In: *Nuovo Cim. 11 (1959), 568–577* (1959).

[12] F. Englert and R. Brout. "Broken Symmetry and the Mass of Gauge Vector Mesons". In: *Phys. Rev. Lett. 13 (1964) 321* (1964).

[13] P. W. Higgs. "Broken symmetries, massless particles and gauge fields". In: *Phys. Lett. 12 (1964) 132* (1964).

[14] P. W. Higgs. "Broken Symmetries and the Masses of Gauge Bosons". In: *Phys. Rev. Lett. 13 (1964) 508* (1964).

[15] C. Hagen G. Guralnik and T. Kibble. "Global Conservation Laws and Massless Particles". In: *Phys. Rev. Lett. 13 (1964) 585* (1964).

[16] Frank Wilczek David J. Gross. "Ultraviolet Behavior of Nonabelian Gauge Theories". In: *Phys.Rev.Lett. 30 (1973) 1343-1346* (1973).

[17] H.David Politzer. "Reliable Perturbative Results for Strong Interactions?" In: *Phys.Rev.Lett. 30 (1973) 1346-1349* (1973).

[18] "Particle Data Group". In: *The Review of Particle Physics* ().

[19] ATLAS and CMS Collaborations. "Combined Measurement of the Higgs Boson Mass in pp Collisions at $\sqrt{s} = 7$ and 8 TeV with the ATLAS and CMS Experiments". In: *Phys. Rev. Lett.* 114 (2015), p. 191803. DOI: 10.1103/PhysRevLett.114.191803. arXiv: 1503.07589 [hep-ex].

[20] ATLAS Collaboration. "Measurements of gluon-gluon fusion and vector-boson fusion Higgs boson production cross-sections in the $H \to WW^* \to e\nu\mu\nu$ decay channel in pp collisions at $\sqrt{s} = 13$ TeV with the ATLAS detector". In: *Phys. Lett. B* 789 (2019), p. 508. DOI: 10.1016/j.physletb.2018.11.064. arXiv: 1808.09054 [hep-ex].

[21] ATLAS Collaboration. "Measurement of the Higgs boson mass in the $H \to ZZ^* \to 4\ell$ and $H \to \gamma\gamma$ channels with $\sqrt{s} = 13\,\text{TeV}$ pp collisions using the ATLAS detector". In: *Phys. Lett. B* 784 (2018), p. 345. DOI: 10.1016/j.physletb.2018.07.050. arXiv: 1806.00242 [hep-ex].

[22] the L3 Collaboration the OPAL Collaboration the SLD Collaboration the LEP Electroweak Working Group the SLD electroweak heavy flavour groups The ALEPH Collaboration the DELPHI Collaboration. "Precision Electroweak Measurements on the Z Resonance". In: *Phys.Rept.427:257-454,2006* (2006).

[23] V. C. Rubin and Jr. W. K. Ford. "Rotation of the Andromeda Nebula from a Spectroscopic Survey of Emission Regions". In: *Astrophisical Journal, vol. 159, p.379* (1970).

[24] R. H. Sandlers K. G. Begeman A. H. Broeils. "Extended rotation curves of spiral galaxies: dark haloes and modified dynamics". In: *Mon. Not. Roy. Astron. Soc. 249 (1991) 523* (1991).

[25] P. A. R. Ade et al. Planck Collaboration. "Planck 2015 results. XIII. Cosmological parameters". In: *Astron. Astrophys. 594 (2016) A13* (2016).

[26] D. Volkov and V. Akulov. "Is the neutrino a goldstone particle?" In: *Physics Letters B 46 no. 1, (1973) 109 – 110* (1973).

[27] C. R. Nappi and B. A. Ovrut. "Supersymmetric extension of the SU(3) SU(2) U(1) model". In: *Physics Letters B 113 no. 2, (1982) 175 – 179* (1982).

[28] J. Wess and B. Zumino. "Supergauge transformations in four dimensions". In: *Nuclear Physics B 70 no. 1, (1974) 39 – 50* (1974).

[29] J. Wess and B. Zumino. "Supergauge invariant extension of quantum electrodynamics". In: *Nuclear Physics B 78 no. 1, (1974) 1 – 13* (1974).

[30] S. Ferrara and B. Zumino. "Supergauge invariant Yang-Mills theories". In: *Nuclear Physics B 79 no. 3, (1974) 413 – 421* (1974).

[31] A. Salam and J. Strathdee. "Super-symmetry and non-Abelian gauges". In: *Physics Letters B 51 no. 4, (1974) 353 – 355* (1974).

[32] Alex Pomarol Kaustubh Agashe Roberto Contino. "The minimal composite Higgs model". In: *arXiv:hep-ph/0412089* (2005).

[33] A Large Mass Hierarchy from a Small Extra Dimension. "Lisa Randall, Raman Sundrum". In: *Phys.Rev.Lett.83:3370-3373,1999* (1999).

[34] Michael E. Peskin and Tatsu Takeuchi. "New constraint on a strongly interacting Higgs sector". In: *Phys. Rev. Lett. 65, 964* (1990).

[35] Juan M. Maldacena. "The Large N Limit of Superconformal Field Theories and Supergravity". In: *arXiv:hep-th/9711200* (1998).

[36] A.M. Polyakov S.S. Gubser I.R. Klebanov. "Gauge Theory Correlators from Non-Critical String Theory". In: *arXiv:hep-th/9802109* (1998).

[37] Edward Witten. "Anti De Sitter Space And Holography". In: *arXiv:hep-th/9802150* (1998).

[38] John M. Cornwall, David N. Levin, and George Tiktopoulos. "Derivation of gauge invariance from high-energy unitarity bounds on the S matrix". In: *Phys. Rev. D 10, 1145* (1974).

[39] G. J. Gounaris et al. "Relationship between longitudinally polarized vector bosons and their unphysical scalar partners". In: *Phys. Rev. D 34, 3257* (1986).

[40] Michael S.ChanowitzMary K.Gaillard. "The TeV physics of strongly interacting W's and Z's". In: *Nuclear Physics B Volume 261, 1985, Pages 379-431* (1985).

[41] J. Alwall et al. "The automated computation of tree-level and next-to-leading order differential cross sections, and their matching to parton shower simulations". In: *Alwall:2014hca* (2014).

[42] H. Davoudiasl, J. L. Hewett, and T. G. Rizzo. "Phenomenology of the Randall-Sundrum Gauge Hierarchy Model". In: *Phys. Rev. Lett. 84, 2080* (2000).

[43] Y. Grossman and M. Neubert. "Neutrino masses and mixings in non-factorizable geometry". In: *Phys. Lett. B 474, 361 (2000)* (2000).

[44] Sanghyeon Chang et al. "Bulk standard model in the Randall-Sundrum background". In: *Phys. Rev. D 62, 084025* (2000).

[45] Alex Pomarol Tony Gherghetta. "Bulk Fields and Supersymmetry in a Slice of AdS". In: *Nucl.Phys.B586:141-162,2000* (2000).

[46] Mark B. Wise Walter D. Goldberger. "Modulus Stabilization with Bulk Field". In: *Phys.Rev.Lett. 83 (1999) 4922-4925* (1999).

[47] Alexandra Carvalho. "Gravity particles from Warped Extra Dimensions, predictions for LHC". In: *arXiv:1404.0102* (2014).

[48] Muneyuki Ishida Vernon Barger. "Randall-Sundrum Reality at the LHC". In: *arXiv:1110.6452* (2011).

[49] Csaba Csáki, Jay Hubisz, and Seung J. Lee. "Radion Phenomenology in Realistic Warped Space Models". In: *Phys.Rev.D76:125015,2007* (2007).

[50] Tao Han, Joseph D. Lykken, and Ren-Jie Zhang. "On Kaluza-Klein States from Large Extra Dimensions". In: *Phys.Rev.D59:105006,1999* (1999).

[51] ATLAS Collaboration. "Combination of searches for heavy resonances decaying into bosonic and leptonic final states using 36 fb^{-1} of proton–proton collision data at $\sqrt{s} = 13$ TeV with the ATLAS detector". In: *Phys. Rev. D* 98 (2018), p. 052008. DOI: 10.1103/PhysRevD.98.052008. arXiv: 1808.02380 [hep-ex].

[52] ATLAS Collaboration. "Search for new phenomena in high-mass diphoton final states using 37 fb^{-1} of proton–proton collisions collected at $\sqrt{s} = 13$ TeV with the ATLAS detector". In: *Phys. Lett. B* 775 (2017), p. 105. DOI: 10.1016/j.physletb.2017.10.039. arXiv: 1707.04147 [hep-ex].

[53] Lyndon Evans and Philip Bryant. "LHC Machine". In: *Journal of Instrumentation, Volume 3, August 2008* (2008).

[54] Service graphique. "Overall view of the LHC". In: *CERN Photos* (2016).

[55] Mobs and Esma. "The CERN accelerator complex". In: *CERN Photos* (2016).

[56] ATLAS Collaboration. *Luminosity determination in pp collisions at* $\sqrt{s} = 13$ *TeV using the ATLAS detector at the LHC*. ATLAS-CONF-2019-021. 2019. URL: https://cds.cern.ch/record/2677054.

[57] G. Avoni et al. "The new LUCID-2 detector for luminosity measurement and monitoring in ATLAS". In: *JINST 13 (2018) P07017* (2018).

[58] ATLAS Collaboration. "Luminosity determination in *pp* collisions at $\sqrt{s} = 8$ TeV using the ATLAS detector at the LHC". In: *Eur. Phys. J. C* 76 (2016), p. 653. DOI: 10.1140/epjc/s10052-016-4466-1. arXiv: 1608.03953 [hep-ex].

[59] ATLAS Collaboration. "Luminosity determination in *pp* collisions at $\sqrt{s} = 7$ TeV using the ATLAS detector at the LHC". In: *Eur. Phys. J. C* 71 (2011), p. 1630. DOI: 10.1140/epjc/s10052-011-1630-5. arXiv: 1101.2185 [hep-ex].

[60] ATLAS collaboration. "ATLAS LuminosityPublicResultsRun2". In: *ATLAS LuminosityPublicResultsRun2* ().

[61] ATLAS Collaboration. "The ATLAS Experiment at the CERN Large Hadron Collider". In: *JINST* 3 (2008), S08003. DOI: 10.1088/1748-0221/3/08/S08003.

[62] J. Pequenao. "Computer generated image of the whole ATLAS detector". In: *CERN Photos* (2008).

[63] G. Aad et al. "ATLAS pixel detector electronics and sensors". In: *JINST 3 (2008) P07007* (2008).

[64] ATLAS Collaboration. *ATLAS Insertable B-Layer Technical Design Report*. ATLAS-TDR-19. 2010. URL: https://cds.cern.ch/record/1291633.

[65] ATLAS Collaboration. ATLAS-TDR-19-ADD-1. 2012. URL: https://cds.cern.ch/record/1451888.

[66] A. Ahmad et al. "The silicon microstrip sensors of the ATLAS semiconductor tracker". In: *ELSEVIER, volume 578, issue 1* (2007).

[67] E. Abat et al. "The ATLAS Transition Radiation Tracker (TRT) proportional drift tube: design and performance". In: *2008 JINST 3 P02013* (2008).

[68] ATLAS collaboration. "ATLAS liquid-argon calorimeter : Technical Design Report". In: *CERN-LHCC-96-041* (1996).

[69] ATLAS collaboration. "ATLAS tile calorimeter : Technical Design Repor". In: *CERN-LHCC-96-042* (1996).

[70] The ATLAS Muon Collaboration. "The ATLAS Muon Spectromter technical design report". In: *CERN, 1997. - 513 p.* (1997).

[71] C. Adorisio et al. "System test of the ATLAS Muon spectrometer in the H8 beam at the CEARN SPS". In: *Nucl. Instrum. Meth. A 593, 232–254* (2008).

[72] C. Adorisio et al. "Study of the ATLAS MDT spectrometer using high energy CERN combined test beam data". In: *Nucl. Instrum. Meth. A 598, 400–415* (2009).

[73] ATLAS Collaboration. "Performance of the ATLAS trigger system in 2015". In: *Eur. Phys. J. C* 77 (2017), p. 317. DOI: 10.1140/epjc/s10052-017-4852-3. arXiv: 1611.09661 [hep-ex].

[74] ATLAS Collaboration. "Luminosity determination in pp collisions at $\sqrt{13}$ TeV using the ATLAS detector at the LHC". In: *ATLAS-CONF-2019-021* (2019).

[75] ATLAS collaboration. "ATLAS computing: Technical design report". In: *CERN-LHCC-2005-022, ATLAS-TRD-017* (2005).

[76] S. Hoche. "Introduction to parton-shower event generators". In: *Proceedings, Theor- etical Advanced Study Institute in Elementary Particle Physics: Journeys Through the Precision Frontier: Amplitudes for Colliders (TASI 2014): Boulder, Colorado, June 2-27, 2014. 2015, pages 235–295* (2014).

[77] P.Z. Skands. "QCD for Collider Physics". In: *arXiv:1104.2863* (2012).

[78] M.A. Dobbs et al. "Les Houches Guidebook to Monte Carlo Generators for Hadron Collider Physics". In: *arXiv:hep-ph/0403045* (2004).

[79] Simone Alioli et al. "A general framework for implementing NLO calculations in shower Monte Carlo programs: the POWHEG BOX". In: *Alioli:2010xd* (2010).

[80] Enrico Bothmann et al. "Event Generation with Sherpa 2.2". In: *arXiv:1905.09127* (2019).

[81] S. Frixione V. Hirschi F. Maltoni O. Mattelaer H.S. Shao T. Stelzer P. Torrielli J. Alwall R. Frederix. "The automated computation of tree-level and next-to-leading order differential cross sections, and their matching to parton shower simulations". In: *JHEP 07(2014)079* (2014).

[82] Y.L. Dokshitzer. "Calculation of the Structure Functions for Deep Inelastic Scattering and $e+e-$ Annihilation by Perturbation Theory in Quantum Chromodynamics". In: *Sov. Phys. JETP 46* (1977).

[83] V. N. Gribov and L. N. Lipatov. "Deep inelastic *ep* scattering in perturbation theory". In: *Sov. J. Nucl. Phys. 15 (1972) 438* (1972).

[84] G. Altarelli and G. Parisi. "Asymptotic freedom in parton language". In: *Nuclear Physics B 126 (1977) p. 298* (1977).

[85] V. V. Sudakov. "Vertex parts at very high-energies in quantum electrodynamics". In: *Sov. Phys. JETP 3* (1965).

[86] S. Catani et al. "QCD Matrix Elements + Parton Showers". In: *Journal of High Energy Physics 2001* (2001).

[87] F. Krauss N. Lavesson L. Lonnblad F.Maltoni M.L.Mangano M.Moretti C.G. Papadopoulos F. Piccinini S. Schumann M. Treccani J.Winter M. J. Alwall S. Hoche. "Comparative study of various algorithms for the merging of parton showers and matrix elements in hadronic collisions". In: *Eur. Phys. J. C 53 (2008) p. 473* (2008).

[88] B. Andersson et al. "Parton fragmentation and string dynamics". In: *Physics Reports 97 (1983) p. 31* (1983).

[89] D.J. Lange. "The EvtGen particle decay simulation package". In: *Nucl. Instrum. Meth. A462 (2001), 152–155* (2001).

[90] GEANT4 Collaboration. "GEANT4: A Simulation toolkit". In: *Nucl. Instrum. Meth. A506 (2003), 250–303* (2002).

[91] ATLAS Collaboration. *The simulation principle and performance of the ATLAS fast calorimeter simulation FastCaloSim*. ATL-PHYS-PUB-2010-013. 2010. URL: https://cds.cern.ch/record/1300517.

[92] ATLAS collaboration. "Measurement of the Inelastic Proton-Proton Cross Section at $\sqrt{s} = 13$ TeV with the ATLAS Detector at the LHC". In: *Phys. Rev. Lett., 117(18):182002, 2016.* (2016).

[93] W. Buttinger. "Using Event Weights to account for differences in Instantaneous Luminosity and Trigger Prescale in Monte Carlo and Data". In: *tech. rep. ATL-COM-SOFT-2015-119, CERN, 2015* (2015).

[94] Torbjörn Sjöstrand et al. "Introduction to Pythia 8.2". In: *arXiv:1410.3012* (2015).

[95] T. Gleiberg et al. "Event generation with SHERPA 1.1". In: *Gleisberg:2008ta* (2008).

[96] Steffen Schumann. "W+jets as a background to top physics: The Quest for many jets". In: *Gleisberg:2008fv* (2008).

[97] Bellm.Johannes et al. "Herwig 7.1 Release Note". In: *Cascioli:2011va* (2011).

[98] Winter.Jan, Skands.Peter Z, and Webber.Bryan R. "Monte Carlo event generators & the top quark forward–backward asymmetry". In: *chumann:2007mg* (2007).

[99] Marek Schonherr. "Vector boson plus multijet production". In: *Hoeche:2012yf* (2012).

[100] Sergey Alekhin, Johannes Bluemlein, and Sven-Olaf Moch. "NNLO Parton Distributions for the LHC". In: *Ball:2014uwa* (2014).

[101] Kirill Melnikov Frank Petriello Charalampos Anastasiou Lance Dixon. "High-precision QCD at hadron colliders: electroweak gauge boson rapidity distributions at NNLO". In: *Phys.Rev.D69:094008,2004* (2003).

[102] Olivier Mattelaerc Pierre Artoisenet Rikkert Frederix and Robbert Rietkerk. "Automatic spin-entangled decays of heavy resonances in Monte Carlo simulations". In: *Artoisenet:2012st* (2012).

[103] ATLAS collaboration. "Search for Supersymmetry at the high luminosity LHC with the ATLAS experiment". In: *ATL-PHYS-PUB-2014-02* (2014).

[104] ATLAS Collaboration. "Measurement of total and differential W+W- production cross sections in proton-proton collisions at $\sqrt{s}$=8 TeV with the ATLAS detector and limits on anomalous triple-gauge-boson couplings". In: *Czakon:2011xx* (2011).

[105] Andrea Giammanco. "Single top quark production at the LHC". In: *Kidonakis:2011wy* (2011).

[106] ATLAS Collaboration. *Studies on top-quark Monte Carlo modelling for Top2016*. ATL-PHYS-PUB-2016-020. 2016. URL: https://cds.cern.ch/record/2216168.

[107] G Altarelli. "Experimental Tests of Perturbative QCD". In: *Altarelli:1989ff* (1989).

[108] Cornelissen.T et al. "Concepts, Design and Implementation of the ATLAS New Tracking (NEWT)". In: *ATL-SOFT-PUB-2007-007 ; ATL-COM-SOFT-2007-002* (2007).

[109] Akmal Rakhmadi et al. "Connected Component Labeling Using Components Neighbors-Scan Labeling Approach". In: *J. ACM 13, 471-494* (1966).

[110] The ATLAS collaboration. "A neural network clustering algorithm for the ATLAS silicon pixel detector". In: *JINST 9 (2014) P09009* (2014).

[111] R.Frühwirth. "Application of Kalman filtering to track and vertex fitting". In: *Nucl. Instrum. Methods A 262, 444 (1987)* (1987).

[112] Daniel Wicke. "A New Algorithm For Solving Tracking Ambiguities". In: *DELPHI 98-163, PROG 236 TRACK 92, 1998* (1998).

[113] J. Illingworth and J. Kittler. "A survey of the Hough transform". In: *Comp. Vis. Graph. Image Proc. 44 (1988) 87* (1988).

[114] ATLAS Collaboration. "Reconstruction of primary vertices at the ATLAS experiment in Run 1 proton–proton collisions at the LHC". In: *Eur. Phys. J. C* 77 (2017), p. 332. DOI: 10.1140/epjc/s10052-017-4887-5. arXiv: 1611.10235 [hep-ex].

[115] ATLAS Collaboration. *Characterization of Interaction-Point Beam Parameters Using the pp Event-Vertex Distribution Reconstructed in the ATLAS Detector at the LHC*. ATLAS-CONF-2010-027. 2010. URL: https://cds.cern.ch/record/1277659.

[116] ATLAS Collaboration. "Topological cell clustering in the ATLAS calorimeters and its performance in LHC Run 1". In: *Eur. Phys. J. C* 77 (2017), p. 490. DOI: 10.1140/epjc/s10052-017-5004-5. arXiv: 1603.02934 [hep-ex].

[117] ATLAS Collaboration. "Electronic calibration of the ATLAS LAr calorimeter". In: *ATL-LARG-PROC-2009-001* (2009).

[118] ATLAS Collaboration. "ATLAS Tile calorimeter calibration and monitoring systems". In: *arXiv:1806.09156* (2018).

[119] Matteo Cacciar, Gavin P. Salam, and Gregory Soyez. "The anti-kt jet clustering alogithm". In: *JHEP 0804:063,2008* (2008).

[120] J. Thaler D. Krohn and L.-T. Wang. "Jet Trimming". In: *JHEP 02 (2010) 084* (2010).

[121] ATLAS Collaboration. *Variable Radius, Exclusive-k_T, and Center-of-Mass Subjet Reconstruction for Higgs($\to b\bar{b}$) Tagging in ATLAS*. ATL-PHYS-PUB-2017-010. 2017. URL: https://cds.cern.ch/record/2268678.

[122] Ian Moult Andrew J. Larkoski and Duff Neill. "Power Counting to Better Jet Observables". In: *arXiv:1409.6298v1* (2014).

[123] Jesse Thaler Andrew J. Larkoski Gavin P. Salam. "Energy Correlation Functions for Jet Substructure". In: *JHEP06(2013)108* (2013).

[124] Andrew J. Larkoski and Ian Moult2. "The Singular Behavior of Jet Substructure Observables". In: *Phys. Rev. D 93, 014017* (2016).

[125] ATLAS Collaboration. *Jet Calibration and Systematic Uncertainties for Jets Reconstructed in the ATLAS Detector at $\sqrt{s} = 13$ TeV*. ATL-PHYS-PUB-2015-015. 2015. URL: https://cds.cern.ch/record/2037613.

[126] ATLAS Collaboration. *Pile-up subtraction and suppression for jets in ATLAS*. ATLAS-CONF-2013-083. 2013. URL: https://cds.cern.ch/record/1570994.

[127] ATLAS Collaboration. "Jet energy measurement and its systematic uncertainty in proton-proton collisions at sqrt(s)=7 TeV with the ATLAS detector". In: *Eur.Phys.J. C75.1 (2015) 17* (2015).

[128] ATLAS Collaboration. *Jet global sequential corrections with the ATLAS detector in proton–proton collisions at $\sqrt{s} = 8$ TeV*. ATLAS-CONF-2015-002. 2015. URL: https://cds.cern.ch/record/2001682.

[129] ATLAS Collaboration. "In situ calibration of large-radius jet energy and mass in 13 TeV proton–proton collisions with the ATLAS detector". In: *Eur. Phys. J. C* 79 (2019), p. 135. DOI: 10.1140/epjc/s10052-019-6632-8. arXiv: 1807.09477 [hep-ex].

[130] M. Cacciari and G. P. Salam. "Pileup subtraction using jet areas". In: *Phys. Lett. B 659, 119* (2008).

[131] ATLAS Collaboration. "Jet energy measurement with the ATLAS detector in proton–proton collisions at $\sqrt{s} = 7$ TeV". In: *Eur. Phys. J. C* 73 (2013), p. 2304. DOI: 10.1140/epjc/s10052-013-2304-2. arXiv: 1112.6426 [hep-ex].

[132] ATLAS Collaboration. "Jet energy measurement and its systematic uncertainty in proton–proton collisions at $\sqrt{s} = 7$ TeV with the ATLAS detector". In: *Eur. Phys. J. C* 75 (2015), p. 17. DOI: 10.1140/epjc/s10052-014-3190-y. arXiv: 1406.0076 [hep-ex].

[133] ATLAS Collaboration. "Performance of jet substructure techniques for large-R jets in proton–proton collisions at $\sqrt{s} = 7$ TeV using the ATLAS detector". In: *JHEP* 09 (2013), p. 076. DOI: 10.1007/JHEP09(2013)076. arXiv: 1306.4945 [hep-ex].

[134] ATLAS Collaboration. "Tagging and suppression of pileup jets with the ATLAS detector". In: *ATLAS-CONF-2014-018* (2014).

[135] ATLAS Collaboration. *Expected performance of the ATLAS b-tagging algorithms in Run-2*. ATL-PHYS-PUB-2015-022. 2015. URL: https://cds.cern.ch/record/2037697.

[136] G Piacquadio and C Weiser. "A new inclusive secondary vertex algorithm for b-jet tagging in ATLA". In: *J. Phys. Conf. Ser. Vol. 119. 3. 2008, p. 032032* (2008).

[137] Walter Lampl et al. *Calorimeter Clustering Algorithms: Description and Performance*. ATL-LARG-PUB-2008-002. 2008. URL: https://cds.cern.ch/record/1099735.

[138] D. Lelas P. Loch H. Ma S. Menke S. Rajagopalan D. Rousseau S. Snyder G. Unal W. Lampl S. Laplace. "Calorimeter clustering algorithms: Description and performance". In: *ATL-LARG-PUB-2008-002* (2008).

[139] ATLAS Collaboration. *Improved electron reconstruction in ATLAS using the Gaussian Sum Filter-based model for bremsstrahlung*. ATLAS-CONF-2012-047. 2012. URL: https://cds.cern.ch/record/1449796.

[140] ATLAS Collaboration. "Electron reconstruction and identification in the ATLAS experiment using the 2015 and 2016 data". In: *Eur. Phys. J. C 79 (2019) 639* (2019).

[141] ATLAS Collaboration. "Electron efficiency measurements with the ATLAS detector using 2012 LHC proton–proton collision data". In: *Eur. Phys. J. C* 77 (2017), p. 195. DOI: 10.1140/epjc/s10052-017-4756-2. arXiv: 1612.01456 [hep-ex].

[142] ATLAS Collaboration. *Electron efficiency measurements with the ATLAS detector using the 2015 LHC proton–proton collision data*. ATLAS-CONF-2016-024. 2016. URL: https://cds.cern.ch/record/2157687.

[143] ATLAS Collaboration. *Electron and photon energy calibration with the ATLAS detector using data collected in 2015 at* $\sqrt{s} = 13$ *TeV*. ATL-PHYS-PUB-2016-015. 2016. URL: https://cds.cern.ch/record/2203514.

[144] ATLAS Collaboration. "Muon reconstruction performance of the ATLAS detector in proton–proton collision data at $\sqrt{s} = 13$ TeV". In: *Eur. Phys. J. C* 76 (2016), p. 292. DOI: 10.1140/epjc/s10052-016-4120-y. arXiv: 1603.05598 [hep-ex].

[145] ATLAS Collaboration. "Measurement of the muon reconstruction performance of the ATLAS detector using 2011 and 2012 LHC proton–proton collision data". In: *Eur. Phys. J. C* 74 (2014), p. 3130. DOI: 10.1140/epjc/s10052-014-3130-x. arXiv: 1407.3935 [hep-ex].

[146] ATLAS Collaboration. "Performance of missing transverse momentum reconstruction with the ATLAS detector using proton–proton collisions at $\sqrt{s} = 13$ TeV". In: *Eur. Phys. J. C* 78 (2018), p. 903. DOI: 10.1140/epjc/s10052-018-6288-9. arXiv: 1802.08168 [hep-ex].

[147] ATLAS Collaboration. "Search for WW/WZ resonance production in $\ell\nu qq$ final states in pp collisions at $\sqrt{s} = 13$ TeV with the ATLAS detector". In: *JHEP* 03 (2018), p. 042. DOI: 10.1007/JHEP03(2018)042. arXiv: 1710.07235 [hep-ex].

[148] ATLAS Collaboration. "Searches for heavy ZZ and ZW resonances in the $\ell\ell qq$ and $\nu\nu qq$ final states in pp collisions at $\sqrt{s} = 13$ TeV with the ATLAS detector". In: *JHEP* 03 (2018), p. 009. DOI: 10.1007/JHEP03(2018)009. arXiv: 1708.09638 [hep-ex].

[149] ATLAS Collaboration. *Improving jet substructure performance in ATLAS using Track-CaloClusters*. ATL-PHYS-PUB-2017-015. 2017. URL: https://cds.cern.ch/record/2275636.

[150] ATLAS Collaboration. "Performance of the ATLAS track reconstruction algorithms in dense environments in LHC Run 2". In: *Eur. Phys. J. C* 77 (2017), p. 673. DOI: 10.1140/epjc/s10052-017-5225-7. arXiv: 1704.07983 [hep-ex].

[151] J. Thaler D. Krohn and L.T. Wang. "Jet trimming". In: *JHEP 02 (2010) 084* (2010).

[152] ATLAS Collaboration. *Search for diboson resonances in hadronic final states in* 79.8 fb^{-1} *of pp collisions at* $\sqrt{s} = 13$ *TeV with the ATLAS detector*. ATLAS-CONF-2018-016. 2018. URL: https://atlas.web.cern.ch/Atlas/GROUPS/PHYSICS/CONFNOTES/ATLAS-CONF-2018-016/.

[153] ATLAS Collaboration. *Impact of Alternative Inputs and Grooming Methods on Large-R Jet Reconstruction in ATLAS*. ATL-PHYS-PUB-2017-020. 2017. URL: https://cds.cern.ch/record/2297485.

[154] ATLAS Collaboration. "Performance of top-quark and W-boson tagging with ATLAS in Run 2 of the LHC". In: *Eur. Phys. J. C* 79 (2019), p. 375. DOI: 10.1140/epjc/s10052-019-6847-8. arXiv: 1808.07858 [hep-ex].

[155] ATLAS Collaboration. *Selection of jets produced in* 13 *TeV proton–proton collisions with the ATLAS detector*. ATLAS-CONF-2015-029. 2015. URL: https://cds.cern.ch/record/2037702.

[156] ATLAS Collaboration. *Photon identification in 2015 ATLAS data*. ATL-PHYS-PUB-2016-014. 2016. URL: https://cds.cern.ch/record/2203125.

[157] J. Henderson1 A. Dafinca and A.R. Weidberg. "Single event upset studies using the ATLAS SCT". In: *JINST 9 C01050* (2014).

[158] The ATLAS collaboration. "Monitoring and data quality assessment of the ATLAS liquid argon calorimeter". In: *Journal of Instrumentation, Volume 9, July 2014* (2014).

[159] The ATLAS collaboration. "LArCaloPublicResults2015". In: *LArCaloPublicResults2015* ().

[160] Sepp Hochreiter and Jurgen Schmidhuber. "Long Short-Term memory". In: *Neural computation, 9(8):1735-1780* (1997).

[161] ATLAS Collaboration. "Measurement of differential production cross-sections for a Z boson in association with b-jets in 7 TeV proton–proton collisions with the ATLAS detector". In: *JHEP* 10 (2014), p. 141. DOI: 10.1007/JHEP10(2014)141. arXiv: 1407.3643 [hep-ex].

[162] ATLAS Collaboration. "Measurement of the Inelastic Proton–Proton Cross Section at $\sqrt{s} = 13\,\text{TeV}$ with the ATLAS Detector at the LHC". In: *Phys. Rev. Lett.* 117 (2016), p. 182002. DOI: 10.1103/PhysRevLett.117.182002. arXiv: 1606.02625 [hep-ex].

[163] ATLAS Collaboration. "Electron reconstruction and identification in the ATLAS experiment using the 2015 and 2016 LHC proton–proton collision data at $\sqrt{s} = 13\,\text{TeV}$". In: *Eur. Phys. J.* (2019). arXiv: 1902.04655 [hep-ex].

[164] ATLAS Collaboration. *Search for the Standard Model Higgs boson produced in association with a vector boson and decaying to a $b\bar{b}$ pair in pp collisions at 13 TeV using the ATLAS detector*. ATLAS-CONF-2016-091. 2016. URL: https://cds.cern.ch/record/2206813.

[165] ATLAS Collaboration. "Jet energy scale measurements and their systematic uncertainties in proton–proton collisions at $\sqrt{s} = 13\,\text{TeV}$ with the ATLAS detector". In: *Phys. Rev. D* 96 (2017), p. 072002. DOI: 10.1103/PhysRevD.96.072002. arXiv: 1703.09665 [hep-ex].

[166] ATLAS Collaboration. *Measurement of b-tagging efficiency of c-jets in $t\bar{t}$ events using a likelihood approach with the ATLAS detector*. ATLAS-CONF-2018-001. 2018. URL: https://cds.cern.ch/record/2306649.

[167] ATLAS Collaboration. *E_T^{miss} performance in the ATLAS detector using 2015–2016 LHC pp collisions*. ATLAS-CONF-2018-023. 2018. URL: https://cds.cern.ch/record/2625233.

[168] M. Bahr et al. "Herwig++ Physics and Manual". In: *Eur.Phys.J.C58:639-707,2008* (2008).

[169] John M. Campbell, R. Keith Ellis, and Ciaran Williams. "Vector boson pair production at the LHC". In: *JHEP* 07 (2011), p. 018. DOI: 10.1007/JHEP07(2011)018. arXiv: 1105.0020 [hep-ph].

[170] Eilam Gross Ofer Vitells Glen Cowan Kyle Cranmer. "Asymptotic formulae for likelihood-based tests of new physics". In: *Eur.Phys.J.C71:1554,2011* (2010).

[171] A L Read. "Modified frequentist analysis of search results (the CLs method)". In: *CERN-OPEN-2000-205* (2000).

[172] A. Wald. "Tests of Statistical Hypotheses Concerning Several Parameters When the Number of Observations is Large". In: *Transactions of the American Mathematical Society, Vol. 54, No. 3 (Nov., 1943), pp. 426-482* (1943).

[173] Christine Beeston Roger Barlow. "Fitting using finite Monte Carlo samples". In: *Volume 77, Issue 2, October 1993, Pages 219-228* (1993).

[174] George ; Moneta Lorenzo ; Shibata Akira ; Verkerke Wouter Cranmer Kyle ; Lewis. "HistFactory: A tool for creating statistical models for use with RooFit and RooStats". In: *CERN-OPEN-2012-016* (2012).